HYBRID COMPUTATIONAL APPROACHES FOR FLAGELLAR WAVEFORM DEVELOPMENT IN COMPLEX FLUIDS WITH APPLICATION TO HUMAN SPERM PROPULSION

by

CARA VICTORIA NEAL

A thesis submitted to

The University of Birmingham

for the degree of

DOCTOR OF PHILOSOPHY

School of Mathematics

College of Engineering and Physical Sciences

University of Birmingham

December 2021

UNIVERSITY OF
BIRMINGHAM

University of Birmingham Research Archive

e-theses repository

This unpublished thesis/dissertation is copyright of the author and/or third parties. The intellectual property rights of the author or third parties in respect of this work are as defined by The Copyright Designs and Patents Act 1988 or as modified by any successor legislation.

Any use made of information contained in this thesis/dissertation must be in accordance with that legislation and must be properly acknowledged. Further distribution or reproduction in any format is prohibited without the permission of the copyright holder.

Abstract

The journey of the human spermatozoa to the ovum is a complex and essential process, fraught with challenges that successful fertilisers must overcome. Sperm cells must traverse the intricate geometry of the female reproductive tract, generating active bending to progress through cervical mucus – a polymer suspension exhibiting complex, non-Newtonian properties. In general, only a dozen cells will reach the egg, with the situation even worse for the one in six couples worldwide with fertility issues. Thus, it is becoming increasingly important to study how human sperm swim and what can influence this process.

We examine how mathematical modelling can provide insight into how two aspects of this complex fluid-structure problem can impact the propulsion of human sperm. Firstly, we explore the effect of the sperm flagellar end piece – a region of depleted axoneme structure occupying the most-distal few microns of the human sperm flagellum. Lacking the organised "9+2" axoneme structure predominant in the rest of the flagellum, the end piece is unlikely to have the ability to generate active bending. Through elastohydrodynamic modelling, we demonstrate that the end piece gives rise to increased swimming speed and efficiency compared to cells with a fully active flagellum. The beneficial effect of the end piece on these statistics can be as large as 430%, with the optimal inactive length being between 2–18% of the total length, and depending on both wavenumber and viscous-elastic ratio.

Out of the non-Newtonian properties exhibited by cervical mucus, shear-thinning rheology, in which fluid viscosity decreases with increased shear rates, has been comparatively under-explored. Thus, we develop a hybrid computational approach for solving the non-linear equations associated with modelling human sperm in three-dimensional shear-thinning fluids. This approach utilises known Newtonian solution techniques to approximate the rapidly varying flow surrounding a swimmer, with a non-Newtonian correction term obtained through solving using the finite element method over a coarse mesh. Combined with a model of swimmer elasticity, we present a first study on the effects of shear-thinning rheology on the propulsion of human sperm with flexible elastic flagella. We uncover that shear-thinning rheology tends to hinder cell progress, although propulsion can also be enhanced, depending on a balance of fluid and swimmer properties. We suggest that the mechanism by which propulsion of sperm cells is hindered in a shear-thinning fluid is via shape changes due to fluid-flagellum interactions, resulting in the development of sub-optimal waveforms for progression.

Acknowledgements

Firstly, I would like to greatly thank my supervisors, Prof. David Smith and Dr Meurig Gallagher, for their patience, guidance and support. Their knowledge and enthusiasm has inspired me throughout my Ph.D., and I am incredibly grateful for the time and effort they have invested in my development. Secondly, I would like to thank my co-supervisors, Dr Jackson Kirkman-Brown and Dr Thomas Montenegro-Johnson, for their passion, insight, and suggestions that significantly impacted my research.

I would also like to thank all of the friends I made at the University of Birmingham – particularly Euan and John – for making the program such an enjoyable experience. Furthermore, a huge thank you is owed to Atticus, those support both as a colleague and as a friend has been paramount in the completion of this thesis. I am incredibly grateful to have had someone there through every step of my Ph.D. experience and a place to ask any questions without judgement.

For his constant moral assistance, I would like to thank my fiancé Chris. Thank you for celebrating with me through my successes and cheering me up when I was struggling. Finally, I would like to thank my family, particularly my parents and grandparents, for encouraging me to pursue science from a young age and for their confidence in my ability, especially when I lacked it in myself.

I gratefully acknowledge the receipt of an EPSRC doctoral training scholarship which funded the work in this thesis.

List of publications

Doing more with less: The flagellar end piece enhances the propulsive effectiveness of human spermatozoa. Neal, C.V., Hall-McNair, A.L., Kirkman-Brown, J., Smith, D.J. and Gallagher, M.T. 2020. Phys. Rev. Fluids, 5(7), p.073101.

This paper explores the effect of the inactive flagellar end piece on the propulsion of human spermatozoa. My contribution involved developing the elastohydrodynamic method used to simulate cells (see the statement of collaborative work below), running simulations, and writing all sections along with Hall-McNair, Kirkman-Brown, Smith and Gallagher.

Portions of this paper are used in the discussion of the effect of the flagellar end piece provided in Chapter 2 of this thesis, as well as in the discussion of sperm structure in Chapter 1. This work is used without obtaining prior permission from APS, as permitted through the APS copyright policy for the use of an APS-published article in a thesis or dissertation as an author of the published work. All images taken from this paper are referenced accordingly.

A hybrid computational approach for studying sperm motility in shear-thinning fluids. Neal, C.V., Gallagher, M.T., and Smith, D.J. *Unpublished.*

This paper will present the hybrid approach for solving non-linear swimming problems presented in Chapter 3 of this thesis. This method will then be used to study the effect of shear-thinning rheology on the propulsion of human sperm with flexible elastic flagella (see Chapter 4). This paper is intended for submission following the completion of this thesis.

Statement of collaborative work

Over the course of this Ph.D. program I have worked closely with fellow Ph.D. student Atticus Hall-McNair. For clarity, the elastohydrodynamic formulation discussed in Chapter 2 is an extension of the EIF method developed by Hall-McNair et al. (2019), to model active and passive filaments in Stokes flow. Including a sperm head in this formulation was a collaborative effort by myself and Atticus. Following this, I formulated and implemented the problem involving varying elastic stiffness and an inactive distal region. I also performed the simulations and analysis of the effect of the flagellar end piece.

Contents

1 Introduction **1**
- 1.1 Motivation . . . 1
- 1.2 Sperm structure and environment . . . 2
  - 1.2.1 The journey of human sperm . . . 5
  - 1.2.2 The rheology of cervical mucus . . . 6
  - 1.2.3 Sperm propulsion in non-Newtonian fluids . . . 7
- 1.3 Dynamics of flow . . . 10
  - 1.3.1 Newtonian fluids . . . 11
  - 1.3.2 Generalised Newtonian fluids . . . 13
- 1.4 Fundamental hydrodynamic methods for Stokes flow . . . 16
  - 1.4.1 The fundamental singularity of Stokes flow . . . 17
  - 1.4.2 The boundary integral equations for Stokes flow . . . 18
  - 1.4.3 The method of regularised stokeslets . . . 20
- 1.5 Studies of microscopic swimming . . . 22
  - 1.5.1 Microswimmer propulsion in Newtonian fluids . . . 23
  - 1.5.2 Microswimmer propulsion in Non-Newtonian fluids . . . 24
- 1.6 Overview of this thesis . . . 46

2 The flagellar end piece enhances the propulsive effectiveness of human spermatozoa **49**
- 2.1 Introduction . . . 49
- 2.2 Model setup . . . 51
  - 2.2.1 The elastohydrodynamic integral formulation . . . 52
  - 2.2.2 Problem non-dimensionalisation . . . 56
  - 2.2.3 Problem discretisation . . . 58
- 2.3 Results . . . 63
  - 2.3.1 Choice of parameters . . . 64
  - 2.3.2 Simulations actuated for optimal velocity . . . 68
  - 2.3.3 Simulations actuated for optimal efficiency . . . 70
  - 2.3.4 Effect of the end piece on waveform and trajectory . . . 71
  - 2.3.5 Effect of the end piece on surrounding fluid flow . . . 73
- 2.4 Discussion . . . 75

3 Swimming in shear-thinning fluids: a non-linear finite element approach **80**
- 3.1 Introduction . . . 80
- 3.2 The finite element method for generalised Newtonian flows . . . 82
  - 3.2.1 Formulation . . . 83

3.2.2 Implementation . . . 87
3.3 Validating the generalised Newtonian solver . . . 92
3.3.1 Deriving a semi-analytic solution . . . 93
3.3.2 Comparison of the FEM and semi-analytic solutions . . . 95
3.4 The hybrid method for a single embedded force in a generalised Newtonian fluid . . . 99
3.4.1 The boundary value problem . . . 100
3.4.2 Formulation . . . 101
3.4.3 Implementation for the Hookean spring problem . . . 104
3.4.4 Results . . . 113
3.5 The hybrid method for sperm-like swimmers in generalised Newtonian fluids . 116
3.5.1 Problem formulation . . . 118
3.5.2 The dimensionless system . . . 121
3.5.3 Solution method . . . 122
3.5.4 Discretisation . . . 124
3.5.5 Implementation . . . 128
3.5.6 Numerical solver parameters and convergence . . . 134

4 How does shear-thinning rheology affect the propulsion of human sperm? 140
4.1 The effect of shear-thinning rheology on propulsion for fixed viscoelastic parameter $\mathcal{S}$ . . . 141
4.1.1 Waveform development in shear-thinning fluids . . . 148
4.1.2 Velocity fields and flagellar force generation . . . 154
4.1.3 Prescribed flagellar beat comparisons . . . 155
4.2 The effect of shear-thinning rheology on propulsion with varying viscoelastic parameter $\mathcal{S}$ . . . 160
4.3 The effect of the inactive end piece on propulsion in shear-thinning fluids . . . 167
4.4 Discussion . . . 172

5 Conclusion 177
5.1 Summary of methodology and results . . . 177
5.2 Future directions . . . 181

Appendices 200

A Basis function mapping from the reference element in the finite element solver 201

B Velocity basis functions on the reference element in the finite element solver 204

C Element-wise construction of the global matrix blocks in the finite element solver 206

D Calculation of stokeslet velocity derivatives in the hybrid solver 208

E Solving problems involving prescribed flagellar motion using the nearest-neighbour method 211

List of Figures

1.1 Schematic of an idealised sperm cell, showing the typical dimensions of the gross structural components. Cross sections (redrawn from Neal et al. (2020) and Zabeo et al. (2019)) show internal flagellar structure at several points across the flagellum. A tapering fibrous sheath surrounds the axoneme core, which thins towards the distal end of the flagellum. 3

1.2 A cross-section of the 9+2 axoneme, consisting of 9 doublet microtubules surrounding a central pair. The central pair is connected to the outer microtubules via radial links, and each pair of microtubules is connected to its neighbours via nexin bridges. The central pair is surrounded by an inner sheath, and the entire structure is encased in a plasma membrane. 4

1.3 Diagram showing an overview of the female reproductive system. Sperm cells are deposited in the vagina and travel through the various organs to reach the egg, which is located in one/both ovaries. 5

1.4 Characteristic flagellar beats of human sperm in (a) Newtonian semen and, (b) non-Newtonian cervical mucus. The flagellar shape in mucus displays higher frequency, smaller wavelength and amplitude, and less pitching of the head compared to swimming in a Newtonian fluid. Figure redrawn from the characteristic flagellar beats observed in Katz et al. (1978). . 8

1.5 The viscosity $\mu(\dot{\gamma}(\boldsymbol{u}))$ calculated from the constitutive law (1.14) over a range of shear rates $\dot{\gamma}(\boldsymbol{u})$ and for $n \in [0.2, 0.9]$. Here $\mu_0 = 1$, $\mu_\infty = 0.5$ and $\lambda = 1$. 15

1.6 The variety of swimmer types studied in viscoelastic fluids from both an experimental and theoretical perspective. (a) A infinite almost-cylindrical swimmer with prescribed beating motion in the azimuthal direction (Fu et al., 2009), (b) a rotating helical swimmer (Spagnolie et al., 2013; Liu et al., 2011), (c) an infinite two-dimensional waving sheet (Lauga, 2007; Riley and Lauga, 2014), (d) a two-dimensional sperm cell consisting of spherical head and flagellum with sinusodial beat (Fulford et al., 1998), (e) a finite-length undulatory swimmer (Teran et al., 2010; Thomases and Guy, 2014; Shen and Arratia, 2011). Red arrows indicate the direction of swimming. 27

2.1 A sketch of the model sperm highlighting the position of the centreline $\boldsymbol{X}(s,t)$ (parametrised by arclength $s \in [0, L]$ and tangent angle $\theta(s,t)$), head surface (∂H, blue ellipsoid), head angle ($\phi(t)$), and flagellum/neck junction ($\boldsymbol{X}_0(t)$). The active component of the flagellum ($s \in [0, \ell]$) is shown in dark yellow, with the inactive distal end ($s \in [\ell, L]$) shown black dashed. A tapering fibrous sheath surrounds the flagellum. Image taken

from Neal et al. (2020). 51
2.2 The forces and moments acting on a segment of the flagellum of length Δs. Here, $-\boldsymbol{f}(s)$ is the force per unit length exerted by the surrounding fluid onto the flagellum, $m(s)$ is an active moment per unit length and $\boldsymbol{N}(s)$ and $M(s)$ represent contact forces and moments respectively. The dependence on time has been dropped for clarity. 54
2.3 Discretisation of the flagellum into $Q = N - 1$ straight-line segments of equal length Δs. The end points of each segment are denoted $\{\boldsymbol{X}^{[n]}\}_{n=1}^{N}$, with midpoints $\{\tilde{\boldsymbol{X}}^{[n]}\}_{n=1}^{Q}$ and tangent angles to each segment $\{\tilde{\theta}^{[n]}\}_{n=1}^{Q}$. The dependence on time has been omitted for brevity. 57
2.4 Discretisation of an ellipsoidal sperm head with radii $r_x = 0.0444$, $r_y = 0.0356$ and $r_z = 0.0222$, shown in (a) the xy-plane and, (b) three-dimensions. The fine quadrature discretisation consists of $M_Q = 1536$ nodes (blue), with the coarse traction discretisation consisting of $M_T = 384$ nodes (red). . . . 64
2.5 Comparison between simulated and experimental data to verify the choice of elastic stiffness parameters. (a) The mean absolute value of curvature for both a progressive human sperm cell simulated with $(\mathcal{S}, k) = (18, 5\pi)$ (blue) and an experimentally tracked cell (magenta) are plotted against arclength. A waveform comparison is shown for the (b) simulated and (c) experimental cell (tracked with FAST (Gallagher et al., 2019a), scale bar denotes 5 μm). In the case of the simulated waveform, the inactive end piece is shown in orange. Image taken from Neal et al. (2020). 65
2.6 The change in the dimensionless elastic stiffness function $E(s)$ with dimensionless arclength s, representing the tapering fibrous sheath surrounding the core of the flagellum. Here, $\rho = 36.4$ is the proximal-distal stiffness ratio, $d = 0.65$ and $\ell = 0.85$. 66
2.7 Values of the actuation parameter $\mathcal{M}$, optimising (a) swimming speed (VAL) and (b) the Lighthill efficiency (η) for $\mathcal{S} \in [9, 18]$ and $k \in [3\pi, 5\pi]$. Colour represents the magnitude of the optimising parameters $\mathcal{M}_{\text{VAL}}$ and $\mathcal{M}_\eta$ for (a) and (b) respectively. Image taken from Neal et al. (2020). 67
2.8 The effect of the inactive end piece length on swimming speed and efficiency of propulsion, for simulations actuated with $\mathcal{M} = \mathcal{M}_{\text{VAL}}$ (a) The swimming speed (VAL), (b) the Lighthill efficiency (η). (c, d) The relative increase in VAL and η respectively, when comparing the optimally-active and fully-active flagella, for viscous-elastic parameter choices $\mathcal{S} \in [9, 18]$ and wavenumbers $k \in [3\pi, 5\pi]$. Image taken from Neal et al. (2020). 68
2.9 (a) Normalised VAL and (b) normalised Lighthill efficiency (η) for $\mathcal{S} \in [9, 18]$ versus $\ell \in [0.5, 1]$, shown for five choices of dimensionless wavenumber k. Values in each subplot are normalised with respect to either (a) the maximum VAL or (b) the maximum η for each $(\mathcal{S}, k)$ pair. The optimal choices of ℓ are highlighted as red dots. (c) The active length that optimises VAL (ℓ_{VAL}) and (d) the active length that optimises the Lighthill efficiency (ℓ_η), for $\mathcal{S} \in [9, 18]$, $k \in [3\pi, 5\pi]$ where surface colour represents the magnitude of the parameters ℓ_{VAL} and ℓ_η for (c) and (d) respectively. Simulations are actuated with $\mathcal{M} = \mathcal{M}_{\text{VAL}}$. Image taken from Neal et al. (2020). 69

2.10 The effect of the inactive end piece length on swimming speed and efficiency of propulsion, for simulations actuated with $\mathcal{M} = \mathcal{M}_\eta$ (a) The swimming speed (VAL), (b) the Lighthill efficiency (η). (c, d) The relative increase in VAL and η respectively, when comparing the optimally-active and fully-active flagella, for viscous-elastic parameter choices $\mathcal{S} \in [9, 18]$ and wavenumbers $k \in [3\pi, 5\pi]$. Image taken from Neal et al. (2020). 71
2.11 (a) Normalised VAL and (b) normalised Lighthill efficiency (η) for $\mathcal{S} \in [9, 18]$ versus $\ell \in [0.5, 1]$, shown for five choices of dimensionless wavenumber k. Values in each subplot are normalised with respect to either (a) the maximum VAL or (b) the maximum η for each $(\mathcal{S}, k)$ pair. The optimal choices of ℓ are highlighted as red dots. (c) The active length that optimises VAL (ℓ_{VAL}) and (d) the active length that optimises the Lighthill efficiency (ℓ_η), for $\mathcal{S} \in [9, 18]$, $k \in [3\pi, 5\pi]$ where surface colour represents the magnitude of the parameters ℓ_{VAL} and ℓ_η for (c) and (d) respectively. Simulations are actuated with $\mathcal{M} = \mathcal{M}_\eta$. Image taken from Neal et al. (2020). 72
2.12 The swimming track following the head for both fully-active and optimally-inactive sperm (top and bottom of each pair respectively) for a selection of parameter pairs $(\mathcal{S}, k)$ actuated with $\mathcal{M} = \mathcal{M}_{\text{VAL}}$ and simulated for 10 cycles of the active moment. In each pair the sperm is plotted at the final time point with the optimally-inactive length $\ell = \ell_{\text{VAL}}$, shown in orange. Image taken from Neal et al. (2020). 73
2.13 The flagellar waveform for a fully-active and optimally-inactive sperm (left and right of each pair respectively), simulated for a selection of parameter pairs $(\mathcal{S}, k)$, and actuated with $\mathcal{M} = \mathcal{M}_{\text{VAL}}$. The color of the flagellum indicates progression through a single beat, from blue to yellow. For each pair the sperm are plotted with the optimally-inactive length ℓ_{VAL} shown in orange. Image taken from Neal et al. (2020). 74
2.14 The swimming track following the head for both fully-active and optimally-inactive sperm (top and bottom of each pair respectively) for a selection of parameter pairs $(\mathcal{S}, k)$ actuated with $\mathcal{M} = \mathcal{M}_\eta$ and simulated for 10 cycles of the active moment. For each pair the sperm are plotted at the final time point with the optimally-inactive length ($\ell = \ell_\eta$) shown in orange. Image taken from Neal et al. (2020). 74
2.15 The flagellar waveform for a fully-active and optimally-inactive sperm (left and right of each pair respectively) simulated for a selection of parameter pairs $(\mathcal{S}, k)$, and actuated with $\mathcal{M} = \mathcal{M}_\eta$. The color of the flagellum indicates progression through a single beat, from blue to yellow. For each pair the sperm are plotted with the optimally-inactive length $\ell = \ell_\eta$, shown in orange. Image taken from Neal et al. (2020). 75
2.16 Comparison of the flow fields around a simulated sperm actuated with $\mathcal{M} = \mathcal{M}_{\text{VAL}}$ with $\mathcal{S} = 13.5$ and $k = 4\pi$, for (a) a cell with a fully-active flagellum, and (b) an optimally-inactive cell, each shown at five time points in the final simulated beat. (c) The difference between flow fields, with positive values corresponding to the optimally-inactive case having a faster fluid velocity. (a,b) Instantaneous fluid streamlines are shown in white

with arrows indicating direction, and the fluid magnitude in indicated by the colourbar for each panel. In (b) the inactive part of the flagellum is shown in black. Image taken from Neal et al. (2020). 76
2.17 Comparison of the flow fields around a simulated sperm actuated with $\mathcal{M} = \mathcal{M}_\eta$ with $\mathcal{S} = 13.5$ and $k = 4\pi$, for (a) a cell with a fully-active flagellum, and (b) an optimally-inactive cell, each shown at five time points in the final simulated beat. (c) The difference between flow fields, with positive values corresponding to the optimally-inactive case having a faster fluid velocity. (a,b) Instantaneous fluid streamlines are shown in white with arrows indicating direction, and the fluid magnitude in indicated by the colourbar for each panel. In (b) the inactive part of the flagellum is shown in black. Image taken from Neal et al. (2020). 77

3.1 Schematic of an example cylindrical domain $\Omega \in \mathbb{R}^3$. The curved surface and pipe 'inlet' form the boundary $\partial\Omega_D$, with the remaining circular 'oulet' forming the boundary $\partial\Omega_N$. The outward pointing unit normal n is shown on one of the circular faces. 83
3.2 Examples of (a) a structured mesh and, (b) an unstructured mesh of a cylindrical pipe of radius $a = 1$ and length $L = 10$. Whilst only the element faces on the outside of the cylinder are shown, the entire volume of the pipes is also meshed with the same pattern. 88
3.3 The reference hexahedron element with twenty-seven velocity nodes (black points) and eight pressure nodes (black circles). In (a), the coordinates of the pressure nodes are indicated in reference to the Cartesian coordinate system (ξ_1, ξ_2, ξ_3). In (b), the ordering of the velocity (blue) and pressure (red) nodes are shown within the element. 89
3.4 Schematic of a cylindrical pipe of radius a and length L in the cylindrical coordinate system (r, θ, z). 93
3.5 Schematic of the domain Ω, which is a cylindrical pipe of length L and radius a. The surface of the cylinder is split into three parts, Γ_1, Γ_2 and Γ_3 where Γ_1 is the pipe 'inlet', Γ_2 is the pipe 'outlet' and Γ_3 is the curved surface of the cylinder. 95
3.6 Velocity profiles for the flow of a BCC4p fluid in a cylindrical pipe of radius $a = 1$ and length $L = 10$, obtained using the finite element solver. Here the fluid parameters are $\mu_0 = 1$, $\mu_\infty = 0.5$ and $\lambda = 1$. We observe how different values of $n \in [0.5, 1.5]$ affect the axial velocity component u_3. . . 96
3.7 Comparison between the finite element (red dots) and semi-analytic (blue) solutions for the (a) axial velocity u_3 and, (b) shear rate $\dot{\gamma}(\boldsymbol{u})$ of the flow of a BCC4p fluid with shear-thinning index $n = 0.5$ in a cylindrical pipe of radius $a = 1$ and length $L = 10$. 97
3.8 Relative error between the finite element and semi-analytic velocity solutions for the cylindrical pipe flow problem for varying degrees of mesh refinement in the finite element solution (blue solid line). A line of best fit is shown in blue dashed, with the gradient of this line given by m. Here the fluid is modelled using the BCC4p constitutive law with $n = 0.5$ and the cylindrical pipe is of radius $a = 1$ and length $L = 10$. 98

3.9 A spring of resting length ℓ and stiffness K within the cuboidal domain Ω with boundary $\partial\Omega$. The spring is attached to the wall of the domain at the point $\boldsymbol{y}_W \in \partial\Omega$ and extends to the point $\boldsymbol{y} \in \Omega$. 105
3.10 Value of the integral given in equation (3.52), calculated numerically using Q quadrature points per direction for the 18^{th} basis function and where $i = 1$. The integral is calculated using standard Gauss-Legendre quadrature (blue) and using the sinh transform (black). 110
3.11 The velocity solutions $\boldsymbol{u}_S$, $\boldsymbol{\mathcal{U}}$ and $\boldsymbol{u}$, in the plane $x_3 = 0.5$ for a regularised force of strength $\boldsymbol{f} = (1, 0, 0)$ at the point $\boldsymbol{y} = (0.5, 0.5, 0.5)$ within a shear-thinning fluid. Here, $\epsilon = 0.01$ and the fluid parameters are $\beta_0 = 2$, $\mathrm{De} = 1$ and $n = 0.5$. The domain is the unit cube $\Omega = [0, 1] \times [0, 1] \times [0, 1]$ which is meshed using $N_e = 216$ elements. Solutions are shown for three difference choices of β_S, (a-c) $\beta_S = \langle \mu(\dot{\gamma}(\boldsymbol{\mathcal{U}}(\boldsymbol{x}) + \boldsymbol{u}_S(\boldsymbol{x}))) \rangle$ where $\boldsymbol{x} \in \left\{ \boldsymbol{x} : (x_1 - y_1)^2 + (x_2 - y_2)^2 + (x_3 - y_3)^2 = \epsilon^2 \right\}$, (d-f) $\beta_S = \mu_\infty/\mu_\infty = 1$, and (g-i) $\beta_S = \mu_0/\mu_\infty = 2$. 114
3.12 Relaxation of a single Hookean spring, located within the domain $\Omega = [0, 1]\times[0, 1]\times[0, 1]$ and with resting length $l = 0.25$. The spring is attached to the wall of the domain at the point $\boldsymbol{y}_W = (0, 0.5, 0.5)$, and extends to a point $\boldsymbol{y} = (0.5, 0.5, 0.5)$ within the fluid. In (a), the x_1 component of the position of the free end of the spring y_1 is plotted over time for 10 equally spaced values of $n \in [0.1, 1]$. In (b), the absolute value of the velocity in the x_1 direction at the free end of the spring $|u_1(\boldsymbol{y})|$ is plotted over time for the values of n considered in (a). In (c) and (d), the equivalent figures as (a) and (b) are plotted, but for 13 equally spaced values of $\mathrm{De} \in [0, 3]$. Finally, in (e) and (f), the analogous plots as (a) and (b) are plotted, but for 13 equally spaced values of $\beta_0 \in [1, 4]$. In all cases, the Newtonian solution ($n = 1$, $\mathrm{De} = 0$ or $\beta_0 = 1$) is shown in blue, ranging to the most shear-thinning simulation in yellow. The remaining two shear-thinning parameters are fixed in each case, as indicated in the plot titles. 117
3.13 View in the xy-plane of an example hexahedron mesh of the domain $\Omega = [0, 10] \times [0, 5] \times [0, 5]$. The domain contains a sperm cell with a flagellum of dimensionless length $L = 1$ and dimensionless head radii $r_x = 0.0444$ and $r_y = 0.0356$. The mesh is more refined in a box surrounding the cell, the dimensions of which are give in equation (3.84). 129
3.14 Convergence of the volume integrals (3.87) and (3.89) over a mesh of the domain $\Omega = [0, 10] \times [0, 5] \times [0, 5]$, consisting of $N_e = 13718$ elements and shown in the xy-plane. For the head integrals (3.89), the colour of each element in (a) shows the number of quadrature points per direction required to reduce the absolute error in approximating the integral using Gauss-Legendre quadrature to 1×10^{-9}, where the integral is summed over all basis functions and head points. Similarly, (b) shows the equivalent but for integrals approximated using the sinh method. (c) and (d) show convergence of the integrals over the flagellum segments, i.e. (3.87), summed over all basis function and flagellum segments and calculated using Gauss-Legendre and the sinh method respectively. Values are shown after one beat cycle, i.e. at $t = 2\pi$. 133

3.15 Convergence of the velocity solution (at $t = 2\pi$) over all mesh points with the number of mesh elements, corresponding to simulating a sperm cell within the domain $\Omega = [0, 10] \times [0, 10] \times [0, 10]$, with cell parameters $\mathcal{S} = 13$, $\mathcal{M} = 0.027$ and $\ell = 0.95$. For a fine mesh ($N_e = 67500$ elements), the plot shows the sum of the error over all refined mesh nodes, between the velocity solutions in this case and the interpolated velocity solutions for a less refined mesh with N_e elements. In (a), the fluid is Newtonian with parameters $(\mathrm{De}, \beta_0, n) = (1, 2, 1)$. In (b), the fluid is shear-thinning with $(\mathrm{De}, \beta_0, n) = (1, 2, 0.2)$. 135

3.16 Convergence of the velocity solution with the number of head nodes N_h and number of flagellum segments Q. The plots show the root-mean-square-error (RMSE) between the velocity solution corresponding to a refined head/flagellum ($N_h = 125$ or $Q = 160$), and the solution calculated using a coarser head/flagellum discretisation, interpolated to the refined head/flagellum points. The velocity solution corresponds to $t = 2\pi$ and is that for a sperm cell within the domain $\Omega = [0, 10] \times [0, 10] \times [0, 10]$ with $\mathcal{S} = 13$, $\mathcal{M} = 0.027$ and $\ell = 0.95$. In (a), the fluid is Newtonian with parameters $(\mathrm{De}, \beta_0, n) = (1, 2, 1)$ and the convergence is shown with N_h. In (b), the fluid is shear-thinning with $(\mathrm{De}, \beta_0, n) = (1, 2, 0.2)$ and again convergence is shown with number of head nodes N_h. In (a) and (b) we set $Q = 60$. Finally, (c) and (d) show the equivalent plots but for convergence with the number of flagellar segments Q. Here we fix $N_h = 45$. 136

3.17 The instantaneous velocity solutions (plotted at $t = 2\pi$) (a) $\boldsymbol{u}_S(\boldsymbol{x}, t)$, the stokeslet solution, and, (b) $\boldsymbol{\mathcal{U}}(\boldsymbol{x}, t)$, the correction field, shown in the plane $z = 2.5$ surrounding a sperm cell with parameters $\mathcal{S} = 13$, $\mathcal{M} = 0.027$ and $\ell = 0.95$ where β_S is chosen as described in Section 3.5.5. The shear-thinning fluid is defined by the parameters $(\mathrm{De}, \beta_0, n) = (1, 2, 0.5)$. The solution $\boldsymbol{u}_S(\boldsymbol{x}, t)$ is rapidly varying across the fluid domain, however the perturbation solution $\boldsymbol{\mathcal{U}}(\boldsymbol{x}, t)$ is slowly varying by construction. Additional perturbation solutions are plotted for the same cell where now (c) $\beta_S = \mu_\infty/\mu_\infty = 1$, (d) $\beta_S = \mu_0/\mu_\infty = 2$, to demonstrate that the solutions in these cases are still slowly varying. 137

3.18 The variation in the Newtonian-infinite shear rate viscosity ratio $\beta_S = \mu_S/\mu_\infty$ with arclength s across the flagellum and the corresponding flagellar beat and surrounding flow fields (at $t = 10\pi$). (a) For each segment, the value β_S is approximated based on the average of the viscosity over a cylinder of radius $\epsilon = 0.01$ surrounding the segment. This value is plotted against arclength for a flagellum with $Q = 60$ segments. (b) The fluid magnitude surrounding the simulated sperm cell is indicated with a colourbar, with instantaneous fluid streamlines shown in white with arrows indicating direction. 138

4.1 Results exploring the effect of shear-thinning rheology on the propulsion of a single human sperm cell with a flexible elastic flagellum. The impact of the shear-thinning index $n \in [0.2, 1]$ on (a) the swimming speed (VAL) and (b) the Lighthill efficiency (η) of the cell. Equivalently, (c) and

(d) examine the effect of changing Deborah number De $\in [0, 3]$ on swimming speed and efficiency, and (e) and (f) provide results for varying zero-infinite shear rate viscosity ratio $\beta_0 \in [1, 6]$. The Newtonian solutions, indicated by red dots, correspond to $n = 1$, De $= 0$ and β_0. Across (a–f), $\mathcal{S} = 13$, $\mathcal{M} = 0.027$ and $\ell = 0.95$ and the remaining shear-thinning parameters are fixed as $n = 0.5$, De $= 1$, or $\beta_0 = 2$ as appropriate. Panels (g) and (h) indicate the variation in VAL and η over $\beta_0 \in [1, 6]$ respectively for a cell with $\mathcal{S} = 15.46$ and $\mathcal{M} = 0.0135$ (remaining parameters fixed as in (a–f)). In this case the Newtonian solution $\beta_0 = 1$ is equivalence to that in (a–d). 142

4.2 Results exploring the effect of shear-thinning rheology on average work done by a single human sperm cell and average distal flagellar curvature over $t \in [8\pi, 10\pi]$. The impact of the shear-thinning index $n \in [0.2, 1]$ on (a) the average work done by the cell over the fifth period $\overline{W}$ and (b) the average of the distal curvature over the fifth period ($\langle \kappa_d \rangle$). Equivalently, (c) and (d) examine the effect of changing Deborah number De $\in [0, 3]$ on average work done and curvature, and (e) and (f) provide results for varying zero-infinite shear rate viscosity ratio $\beta_0 \in [1, 6]$. The Newtonian solutions, indicated by red dots, correspond to $n = 1$, De $= 0$ and $\beta_0 = 1$. Across (a–f), $\mathcal{S} = 13$, $\mathcal{M} = 0.027$ and $\ell = 0.95$ and the remaining shear-thinning parameters are fixed as $n = 0.5$, De $= 1$, or $\beta_0 = 2$ as appropriate. Panels (g) and (h) indicate the variation in $\overline{W}$ and $\langle \kappa_d \rangle$ over $\beta_0 \in [1, 6]$ respectively for a cell with $\mathcal{S} = 15.46$ and $\mathcal{M} = 0.0135$ (remaining parameters fixed as in (a–f)). In this case the Newtonian solution $\beta_0 = 1$ is equivalence to that in (a–d). 146

4.3 Results exploring the effect of shear-thinning rheology on swimming speed (VAL) and the relationship between the parameters $n \in [0.2, 1]$, De $\in [0, 3]$ and $\beta_0 \in [1, 6]$ and VAL. (a) The change in swimming speed VAL over n and β_0 and, (b) the change in VAL over n and De. In each case, swimming speed VAL is indicated by a colorbar with yellow corresponding to higher swimming speeds. Here, $\mathcal{S} = 13$, $\mathcal{M} = 0.027$ and $\ell = 0.95$ and the remaining shear-thinning parameters are fixed as $n = 0.5$, De $= 1$, or $\beta_0 = 2$ as appropriate 147

4.4 Results exploring the effect of shear-thinning rheology on flagellar waveform and the distribution of tangent angles over the beat $t \in [8\pi, 10\pi]$. (a) The flagellar waveform is shown for the best and worst swimmers (maximum and minimum VAL respectively) over $n \in [0.2, 1]$. The colour of the flagellum indicates progress through the beat, from blue to yellow, with the final waveform shown in black at $t = 10\pi$. In (b) the distribution of flagellar tangent angles across the beat are shown for the best and worst swimmers plotted in (a). In (c) and (d), the equivalent results are shown for the best and worst swimmers over De $\in [0, 3]$. Finally, in (e) and (f), the same is shown over $\beta_0 \in [1, 6]$. Across all simulations $\mathcal{S} = 13$, $\mathcal{M} = 0.027$ and $\ell = 0.95$ and the remaining shear-thinning parameters are fixed as $n = 0.5$, De $= 1$, or $\beta_0 = 2$ as appropriate. 149

4.5 The flagellar waveform during the beat $t \in [8\pi, 10\pi]$, over parameter

ranges (a) $n \in [0.2, 1]$, (b) De $\in [0, 3]$ and (c) $\beta_0 \in [1, 6]$. In each case, the waveform in the Newtonian case is shown in yellow, corresponding to $n = 1$, De $= 0$ or $\beta_0 = 1$ respectively. These waveforms are plotted ranging to blue, corresponding to the strongest shear-thinning effects and parameters $n = 0.2$, De $= 3$ or $\beta_0 = 6$. In each panel, a magnified image of distal flagellum is shown at $t = 10\pi$. Across all simulations $\mathcal{S} = 13$, $\mathcal{M} = 0.027$ and $\ell = 0.95$ and the remaining shear-thinning parameters are fixed as $n = 0.5$, De $= 1$, or $\beta_0 = 2$ as appropriate. 151

4.6 The flagellar curvature $\partial\theta(s,t)/\partial s$ for the best and worst swimmer (maximum and minimum VAL respectively), over the parameters (a) $n \in [0.2, 1]$, (b) De $\in [0, 3]$ and (c) $\beta_0 \in [1, 6]$. The curvature is plotted over a single beat $t \in [8\pi, 10\pi]$. Across all simulations $\mathcal{S} = 13$, $\mathcal{M} = 0.027$ and $\ell = 0.95$ and the remaining shear-thinning parameters are fixed as $n = 0.5$, De $= 1$, or $\beta_0 = 2$ as appropriate. 152

4.7 The variation in the trajectories of sperm cells and the maximum flagellar amplitude over shear-thinning parameters (a) $n \in [0.2, 1]$, (b) De $\in [0, 3]$ and (c) $\beta_0 \in [1, 6]$. In each case, the trajectory is plotted over the beat $t \in [8\pi, 10\pi]$ (left), where x and y represent the displacement of $\boldsymbol{X}_0(t)$ from $\boldsymbol{X}_0(t = 8\pi)$. The Newtonian case is plotted in black, with the remaining paths plotted from least shear-thinning (dark blue) to most shear-thinning (yellow). Maximum flagellar amplitude over the beat $t \in [8\pi, 10\pi]$ (right) is plotted via calculating the maximum displacement of the flagellum in the y direction from the y component of the head-flagella joint $\boldsymbol{X}_0(t)$ in the cell body frame. Across all simulations, the remaining shear-thinning parameters are fixed as $n = 0.5$, De $= 1$, or $\beta_0 = 2$ as appropriate. 153

4.8 Comparison of the flow fields around a simulated sperm for best and worst swimmer (maximum and minimum VAL respectively), over the parameters (a) $n \in [0.2, 1]$, (b) De $\in [0, 3]$ and (c) $\beta_0 \in [1, 6]$. The top of each column shows the best swimmer, with fluid magnitude indicated by the colorbar, and instantaneous fluid streamlines shown in white with arrows indicating direction. The middle of each column shows the worst swimmer, with fluid magnitude and streamlines indicated as above. The difference between flow fields is shown in the bottom of each column, where positive values correspond to the best swimmer having faster fluid velocity. Here the best and worst swimmers (heads and flagella) are plotted in pink and black respectively. Across all simulations $\mathcal{S} = 13$, $\mathcal{M} = 0.027$ and $\ell = 0.95$ and the remaining shear-thinning parameters are fixed as $n = 0.5$, De $= 1$, or $\beta_0 = 2$ as appropriate. 155

4.9 Comparison of the force generation of the flagellum for the best and worst swimmer (maximum and minimum VAL respectively), over the parameters (a) $n \in [0.2, 1]$, (b) De $\in [0, 3]$ and (c) $\beta_0 \in [1, 6]$. In (a), force generation is indicated by arrows showing strength and direction for a cell with $n = 1$ (top left) and $n = 0.2$ (bottom left). Arrows are scaled equally in the top and bottom diagrams. The magnitude of the flagellar force ($|\boldsymbol{f}|$) is plotted over arclength s (right). Similarly, (b) shows the same as (a) but for the cells corresponding to De $= 0$ (top left) and De $= 3$ (bottom left). The same

is also true of (c), for cells corresponding to $\beta_0 = 2$ (top left) and $\beta_0 = 6$ (bottom left). Across all simulations $\mathcal{S} = 13$, $\mathcal{M} = 0.027$ and $\ell = 0.95$ and the remaining shear-thinning parameters are fixed as $n = 0.5$, De $= 1$, or $\beta_0 = 2$ as appropriate. 156

4.10 Results exploring the effect of shear-thinning rheology on propulsion of a sperm cell with fixed flagellar beat. (a) The effect of the shear-thinning index $n \in [0.2, 1]$ on swimming speed ($\mathrm{VAL}_{\mathrm{ST}}$) for a cell simulated using the HANS method (blue). For each n, the swimming speed ($\mathrm{VAL}_{\mathrm{STb\text{-}Nf}}$) of a cell with prescribed flagellar beat corresponding to the beat obtained via the HANS method and simulated within a Newtonian fluid is plotted in red. (b) The difference in swimming speeds between a cell simulated with shear-thinning index n and a cell with the same waveform within a Newtonian fluid. Panels (c) and (d) show analogous results to (a),(b) but over De $\in [0, 3]$. Similarly, (e) and (f) show the corresponding results for $\beta_0 \in [1, 6]$. Across all simulations $\mathcal{S} = 13$, $\mathcal{M} = 0.027$ and $\ell = 0.95$ and the remaining shear-thinning parameters in the HANS simulation are fixed as $n = 0.5$, De $= 1$, or $\beta_0 = 2$ as appropriate. 158

4.11 The viscosity $\mu(\dot{\gamma}(\boldsymbol{u}))$ surrounding a simulated sperm cell for (a) $n = 0.2$, (b) $n = 0.5$ and (c) $n = 0.8$. Here, the colorbar corresponds to the fluid viscosity, with lower viscosity regions indicated in black, and higher viscosity regions in white. For each value of n, the cell waveform and the surrounding viscosity is plotted in the planes $z = \bar{z}$ (left), $y = \bar{y}$ (middle) and $x = \bar{x}$ (right) where $\bar{x}$, $\bar{y}$ and $\bar{z}$ represent the mean position across the flagellum in each direction (values indicated in each panel). Across all simulations, $\mathcal{S} = 13$, $\mathcal{M} = 0.027$ and $\ell = 0.95$ and the remaining shear-thinning parameters are fixed as De $= 1$ and $\beta_0 = 2$. The waveform and viscosity are plotted at $t = 10\pi$ (after five beats). 160

4.12 The viscosity $\mu(\dot{\gamma}(\boldsymbol{u}))$ surrounding a simulated sperm cell for (a) De $= 3$, (b) De $= 1.5$ and (c) De $= 0.5$. Here, the colorbar corresponds to the fluid viscosity, with lower viscosity regions indicated in black, and higher viscosity regions in white. For each value of De, the cell waveform and the surrounding viscosity is plotted in the planes $z = \bar{z}$ (left), $y = \bar{y}$ (middle) and $x = \bar{x}$ (right) where $\bar{x}$, $\bar{y}$ and $\bar{z}$ represent the mean position across the flagellum in each direction (values indicated in each panel). Across all simulations, $\mathcal{S} = 13$, $\mathcal{M} = 0.027$ and $\ell = 0.95$ and the remaining shear-thinning parameters are fixed as $n = 0.5$ and $\beta_0 = 2$. The waveform and viscosity are plotted at $t = 10\pi$ (after five beats). 161

4.13 The viscosity $\mu(\dot{\gamma}(\boldsymbol{u}))$ surrounding a simulated sperm cell for (a) $\beta_0 = 2$, (b) $\beta_0 = 4$ and (c) $\beta_0 = 6$. Here, the colorbar corresponds to the fluid viscosity, with lower viscosity regions indicated in black, and higher viscosity regions in white. For each value of β_0, the cell waveform and the surrounding viscosity is plotted in the planes $z = \bar{z}$ (left), $y = \bar{y}$ (middle) and $x = \bar{x}$ (right) where $\bar{x}$, $\bar{y}$ and $\bar{z}$ represent the mean position across the flagellum in each direction (values indicated in each panel). Across all simulations, $\mathcal{S} = 13$, $\mathcal{M} = 0.027$ and $\ell = 0.95$ and the remaining shear-thinning parameters are fixed as $n = 0.5$ and De $= 1$. The waveform and

viscosity are plotted at $t = 10\pi$ (after five beats). 162
4.14 The variation in the viscosity ratio β_S with arclength s along the flagellum over shear-thinning parameters (a) $n \in [0.2, 1]$, (b) De $\in [0, 3]$ and (c) $\beta_0 = [1, 6]$. Results are plotted at $t = 10\pi$ for a cell with $\mathcal{S} = 13$, $\mathcal{M} = 0.027$ and $\ell = 0.95$. In each panel, yellow represents the most strongly shear-thinning case, ranging to blue for the Newtonian solution. Arrows are plotted to show the change in the shear-thinning parameters across each panel. Across all panels, the remaining shear-thinning parameters are fixed as $n = 0.5$, De $= 1$ and $\beta_0 = 2$ as appropriate. 163
4.15 The effect of shear-thinning rheology on the propulsion of a single human sperm over varying viscous-elastic parameter values $\mathcal{S} \in [9, 18]$. (a) The swimming speed (VAL, left panel) and the Lighthill efficiency (η, right panel) over $\mathcal{S} \in [9, 18]$, plotted for nine values of $n \in [0.2, 1]$. Here, the solutions for a Newtonian fluid (where $n = 1$) are plotted in black, with the solutions for the remaining values of $n \in [0.2, 0.9]$ plotted from yellow ($n = 0.2$) to dark blue ($n = 0.9$). In (b), the difference between the maximum and minimum VAL across all values of n is plotted over $\mathcal{S} \in [9, 18]$ (left panel). Similarly, the difference between the maximum and minimum observed efficiency η across all values of n is plotted over $\mathcal{S} \in [9, 18]$ (right panel). The remaining shear-thinning parameters are fixed as De $= 1$ and $\beta_0 = 2$. 164
4.16 The effect of shear-thinning rheology on flagellar waveform over varying viscous-elastic parameter values $\mathcal{S} \in [9, 18]$. At two points over the beat (a) $t = 9\pi$ and (b) $t = 10\pi$, the variation in flagellar shape over $n \in [0.2, 1]$ is plotted for ten values of $\mathcal{S} \in [9, 18]$. For each $(\mathcal{S}, t)$ pair, the waveform in the Newtonian case ($n = 1$) is shown in yellow, ranging to the waveform in a strongly shear-thinning fluid ($n = 0.2$), which is plotted in blue. The remaining shear-thinning parameters are fixed as De $= 1$ and $\beta_0 = 2$. 166
4.17 The effect of shear-thinning rheology on the propulsion of a single human sperm cell with a fixed flagellar beat over varying viscous-elastic parameter values $\mathcal{S} \in [9, 18]$. For each of the simulations in Figure 4.15a, i.e. for every combination of $n \in [0.2, 1]$ and $\mathcal{S} \in [9, 18]$, the flagellar beat is extracted between $t \in [0, 10\pi]$. The extracted beat is used to prescribe the flagellar motion in the body frame of a sperm cell in a Newtonian fluid. The difference in swimming speed between the results plotted in Figure 4.15a and for the same waveform in a Newtonian fluid, $\text{VAL}_{\text{ST}} - \text{VAL}_{\text{STb-Nf}}$, is plotted over $\mathcal{S} \in [9, 18]$ for nine values of $n \in [0.2, 1]$. The results for $n \in [0.2, 0.9]$ are plotted from yellow ($n = 0.2$) to dark blue ($n = 0.9$). When $n = 1$, the two solutions methods coincide (shown in black). 167
4.18 The effect of the flagellar end piece on the propulsion of a single human sperm cell in a shear-thinning fluid. (a) The effect of shear-thinning index $n \in [0.2, 1]$ on the swimming speed (VAL, left plot) and the Lighthill efficiency (η, right plot) are plotted for a fully-active cell (red) and a cell with an inactive end piece of length $L - \ell = 0.05$ (blue). Here, $\mathcal{S} = 13$. Panel (b) shows the equivalent results for swimming speed and efficiency for a cell with $\mathcal{S} = 18$. The remaining shear-thinning parameters are fixed as

De = 1 and $\beta_0 = 2$, and VAL and η are calculated after five cycles of the active moment. 169
4.19 The flagellar waveform for fully-active ($\ell = 1$) cells and cells with an inactive end piece ($\ell = 0.95$) for three value of the shear-thinning index $n \in \{1, 0.6, 0.2\}$ and (a) $\mathcal{S} = 13$ and (b) $\mathcal{S} = 18$. The color of the flagellum indicates progress through a single beat ($t \in [8\pi, 10\pi]$), from blue to yellow, with the final waveform shown in black at $t = 10\pi$. The remaining shear-thinning parameters are set as De = 1 and $\beta_0 = 2$. 170
4.20 Comparison of the flow fields around a simulated sperm cell with and without an inactive end piece for three values of the shear-thinning index (a) $n = 1$, (b) $n = 0.6$ and (c) $n = 0.2$. In each case, the top panel indicates a cell with $\ell = 0.95$ and the bottom panel indicates a fully-active cell with $\ell = 1$. Fluid magnitude is indicated by a colorbar, and instantaneous fluid streamlines are shown in white with arrows indicating direction. The difference between flow fields is shown in the bottom of each panel, where positive values correspond to the cell with the inactive end piece having faster fluid velocity. Here, $\mathcal{S} = 13$ and the remaining shear-thinning parameters are set as De = 1 and $\beta_0 = 2$. 171
4.21 Comparison of the flow fields around a simulated sperm cell with and without an inactive end piece for three values of the shear-thinning index (a) $n = 1$, (b) $n = 0.6$ and (c) $n = 0.2$. In each case, the top panel indicates a cell with $\ell = 0.95$ and the bottom panel indicates a fully-active cell with $\ell = 1$. Fluid magnitude is indicated by a colorbar, and instantaneous fluid streamlines are shown in white with arrows indicating direction. The difference between flow fields is shown in the bottom of each panel, where positive values correspond to the cell with the inactive end piece having faster fluid velocity. Here, $\mathcal{S} = 18$ and the remaining shear-thinning parameters are set as De = 1 and $\beta_0 = 2$. 172

List of Tables

1.1 Order of the characteristic Reynolds number for a variety of systems (Vogel, 2020). 12
1.2 Summary of the key studies discussed in the review of swimming in viscoelastic fluids. The author of the study, type of swimmer, type of study and fluid constitutive law are indicated. The conclusion indicates whether viscoelasticity decreases (red), increases (green) or has no effect on (yellow) the swimming speed of the swimmer compared to that in a Newtonian fluid, where in some studies multiple effects are uncovered. The papers are split into theoretical and experimental studies and are listed in ascending order with date. 26
1.3 Summary of the key studies discussed in the review of swimming in shear-thinning fluids. The author of the study, type of swimmer, type of study and actuation method are indicated. The conclusion indicates whether shear-thinning rheology decreases (red), increases (green) or has no effect on (yellow) the swimming speed of the swimmer compared to that in a Newtonian fluid, where in some studies multiple effects are uncovered. Studies indicated with an asterisk (*) include both shear-thinning and viscoelastic effects. The papers are split into theoretical and experimental studies and are listed in ascending order with date. 38

2.1 Approximate sperm number S for spermatozoa of various mammalian species (Cummins and Woodall, 1985). 65

Chapter 1

Introduction

1.1 Motivation

In sexual reproduction, the male and female gametes must meet for fertilisation to occur. Whilst this may seem like a simple proposition, the journey of the male gamete (the spermatozoon) to reach the female gamete (the ovum/egg) is fraught with challenges that successful sperm must overcome. Of the millions of sperm present in the ejaculate, only a few thousand will reach the fallopian tubes, and in general, only around a dozen cells will reach the site of the egg (Suarez and Pacey, 2006).

For many couples, the situation can be even worse. Approximately one in six couples worldwide are subfertile (Boivin et al., 2007), with male infertility accounting for at least 50% of these cases (Barratt et al., 2009). For this reason, it is becoming increasingly important to understand how sperm swim and what can affect their propulsive characteristics. A better understanding of sperm motility could result in improved diagnosis of fertility problems and better-targeted treatment for patients suffering from fertility issues.

Sperm cells are a principal example of monoflagellated swimmers, which push themselves through the surrounding fluid by beating a single elastic flagellum. Sperm encounter many different fluids in their journey toward the female gamete, including cervical mucus – a highly viscous polymer suspension. The development of the flagellar beat in such fluids depends on the complex interactions between the active elastic flagellum, the fluid itself, and the con-

voluted geometry encountered in regions of the female reproductive system. Changing one aspect of this fluid-structure system can profoundly affect cell propulsion. This motivates the need to develop biologically realistic modelling to understand problems involving sperm motility in their entirety.

In the first part of this thesis, we model the internal structure of the human sperm flagellum to provide insight into how a mechanically inactive flagellar end piece contributes to the effective propulsion of cells. We then develop a new computational approach for simulating sperm cells with flexible elastic flagella in rheologically complex fluids. We will study the effect of the fluid environment on propulsion and flagellar waveform development and discuss the physical mechanisms responsible for the computational predictions.

In the remainder of this chapter, we discuss the physiology of human sperm and experimental observations of how different fluid properties can lead to differences in flagellar waveform and propulsion of cells. Following this, we discuss the derivation of the relevant fluid equations for the problems considered in this thesis. We then outline several fundamental hydrodynamic techniques applicable to sperm motility and summarise the literature surrounding microscopic swimming in non-Newtonian fluids.

1.2 Sperm structure and environment

The precise morphology, or shape, of sperm cells can vary significantly between species (Anderson and Personne, 1975; Fawcett, 1975; Austin, 1995; Werner and Simmons, 2008; Nelson et al., 2010; Mafunda et al., 2017). However, in gross structural terms, several conserved features can be observed in the sperm of humans, most mammals, and many of our evolutionary ancestors (Cummins and Woodall, 1985). In particular, healthy sperm cells consist of two main components – the sperm head and flagellum. The head of the sperm cell contains a nucleus packed with haploid DNA, as well as the acrosome, which holds the enzymes required for penetrating the ovum (see Figure 1.1). A typical human sperm head is of a flattened ellipsoidal shape, approximately 5–6 μm long and 3 μm wide (Cummins and Woodall, 1985). Common

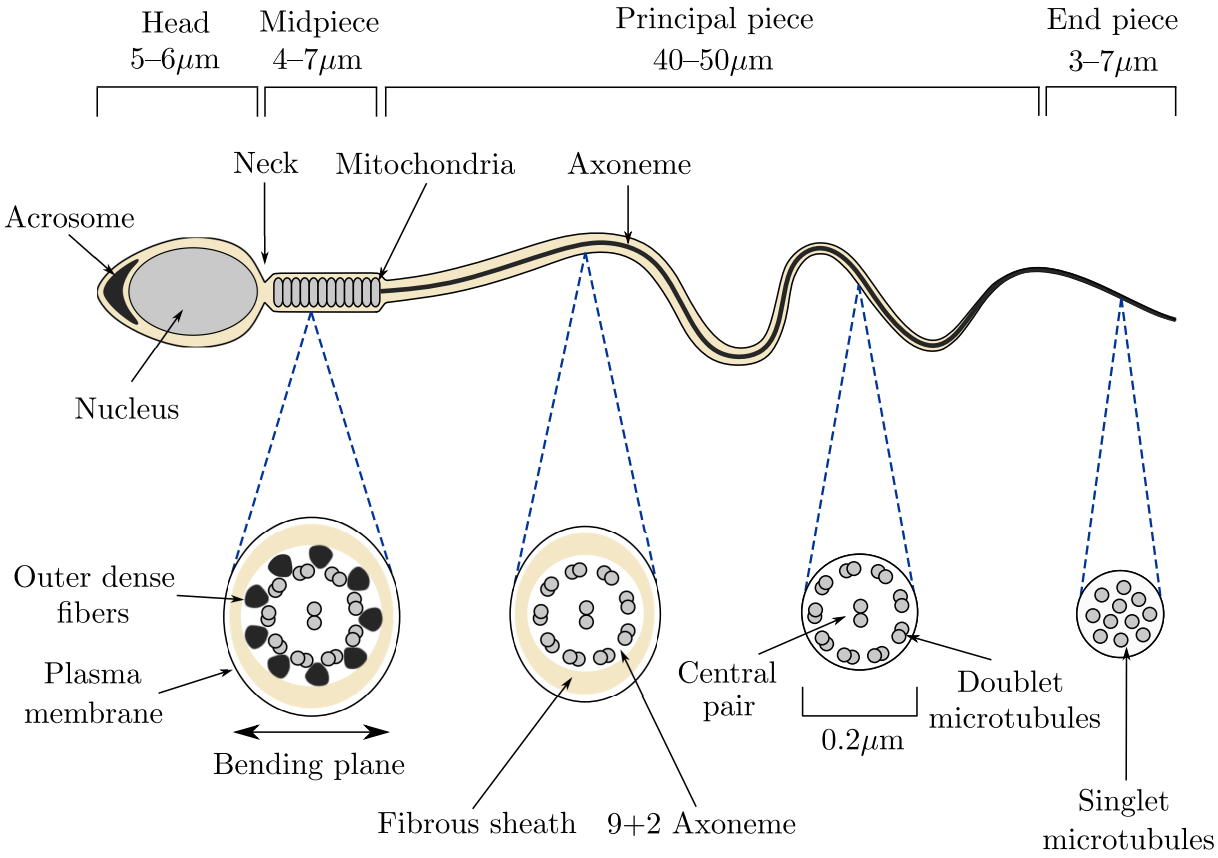


Figure 1.1: Schematic of an idealised sperm cell, showing the typical dimensions of the gross structural components. Cross sections (redrawn from Neal et al. (2020) and Zabeo et al. (2019)) show internal flagellar structure at several points across the flagellum. A tapering fibrous sheath surrounds the axoneme core, which thins towards the distal end of the flagellum.

head abnormalities which may affect propulsion include heads that are too large, too small or spherical (WHO, 2010).

The head is connected to the flagellum at a location referred to as the neck (or connecting piece). In contrast to prokaryotic organisms, which generate bending only at this head-flagellum joint (Berg, 2003), sperm flagella induce bending across the majority of their length (Machin, 1958). The role of the flagellar neck has been proposed to be that of initialising the flagellum beat, as well as alternating the direction of bend propagation along the flagellum (Vernon and Woolley, 2004; Woolley et al., 2008; Gaffney et al., 2011).

The flagellum is a motile piece, capable of propelling the sperm cell through the fluid by utilising a collection of molecular motors called dyneins, that induce shear and bending throughout the length of the flagellum. At the core of the flagellum is the axoneme, a structure

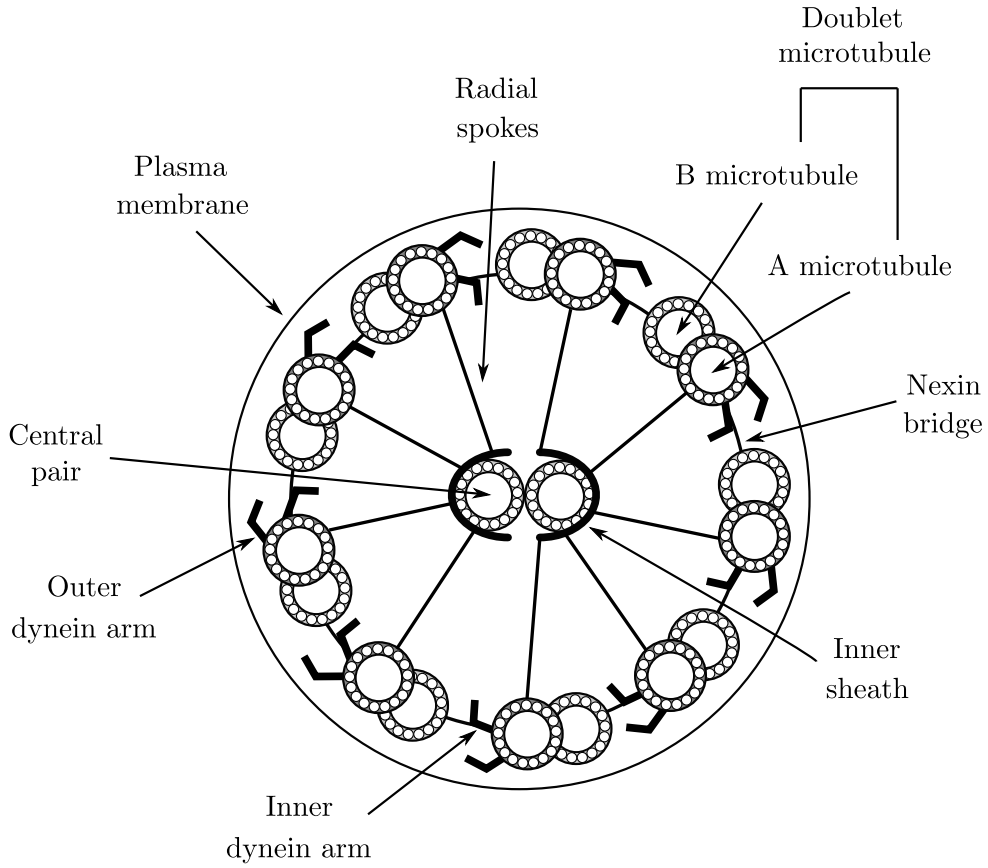


Figure 1.2: A cross-section of the 9+2 axoneme, consisting of 9 doublet microtubules surrounding a central pair. The central pair is connected to the outer microtubules via radial links, and each pair of microtubules is connected to its neighbours via nexin bridges. The central pair is surrounded by an inner sheath, and the entire structure is encased in a plasma membrane.

comprising nine doublet microtubules surrounding a central pair of microtubules, commonly referred to as the 9+2 axoneme. Radial links connect the central pair of microtubules to the surrounding nine pairs, and nexin bridges connect the nine outer microtubules (see Figure 1.2). The sliding between microtubule pairs is produced through the extension, binding and detaching of dyneins between neighbouring pairs of microtubules. In human sperm, the active axoneme structure is encompassed by a fibrous sheath that confers additional mechanical stiffness and thins towards the distal end of the flagellum. Human sperm flagella are typically between 40–60 μm long and beat at a frequency of approximately 10–20 Hz. This corresponds to an angular frequency of $\omega \approx 60$–120 Rads s^{-1} (Yeung et al., 1994).

The flagella of humans and most mammals comprise of three distinct regions – the midpiece, principal piece and end piece (see Figure 1.1). The midpiece of the flagellum contains the

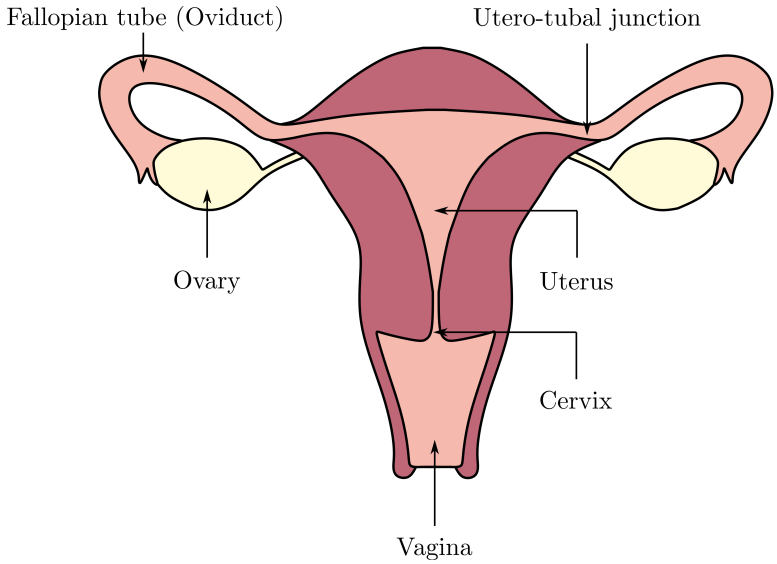


Figure 1.3: Diagram showing an overview of the female reproductive system. Sperm cells are deposited in the vagina and travel through the various organs to reach the egg, which is located in one/both ovaries.

ATP-generating mitochondria, and, in the case of human sperm, is approximately 4–7 μm in length. The principal piece, typically 40–50 μm, contains the 9+2 axoneme core and is where bending waves are produced and propagated across the flagellum. Finally, the end piece, which is typically a few microns in length, contains disorganised singlet microtubules only (Zabeo et al., 2019). Lacking the predominant 9+2 axoneme structure, it appears unlikely that the end piece is a site of molecular motor activity. This hypothesis forms the basis of our study in Chapter 2 of this thesis.

1.2.1 The journey of human sperm

Following ejaculation, sperm cells accumulate at the cervical mucus boundary, a mucus barrier located in the narrow region that forms a canal between the uterus and vagina (see Figure 1.3). To progress to the uterus, cells must penetrate this mucus layer, which presents the first major challenge for successful fertilisers to overcome (Sobrero and MacLeod, 1962). The ease of progression has been shown to depend on several factors, including sperm numbers, motility, and the hydration of the mucus itself (Wolf et al., 1978). On average, around 10% of the cells initially deposited in the vagina penetrate the cervical mucus barrier and enter the uterus.

Cells that enter the uterus must then travel towards one of the two oviducts, known as the fallopian tubes. Sperm exit the uterus via the utero-tubal junction – a narrow channel approximately 300μm in diameter containing viscous mucus exhibiting complex, non-Newtonian properties (Suarez and Pacey, 2006). From here, cells progress to the oviduct, the epithelium of which is lined with motile cilia. Sperm swim along the oviduct walls and against the flow of mucus to reach the ovum (Katz et al., 1989), navigating a convoluted geometry as they do so.

Throughout their journey through the female reproductive system, sperm encounter many highly viscous, non-Newtonian fluids such as cervical mucus, the fluid at the utero-tubal junction and in the oviduct. Even when sperm reach the ovum, located in one of the two ovaries (see Figure 1.3), cells must penetrate the cumulus oophorus, a non-Newtonian hyaluronic acid gel that forms the outer layer of the egg (Drobnis et al., 1988). In Chapter 3 and Chapter 4 of this thesis, we focus on modelling sperm swimming in non-Newtonian fluids exhibiting similar properties to cervical mucus, the composition of which we discuss in detail in the next section.

1.2.2 The rheology of cervical mucus

On the scale of a single cell, human cervical mucus is not a continuous fluid; rather, it is a network of polymer chains suspended within solution (Lai et al., 2009). These polymer chains, known as mucins, form a complex mesh with an interfibre spacing of approximately 100 nm (Olmsted et al., 2001). This mesh presents a significant obstacle to propulsion for sperm cells which are between $40 - 60\,\mu$m in length, much larger than the typical distance between fibres. Cells must burrow through the mesh, and in doing so, significantly alter the structure through the stretching and compressing of fibres (Yudin et al., 1989). Despite this obstacle, sperm progress remarkably quickly through the mucus, with speeds as high as $25 - 45\,\mu\text{m}\,s^{-1}$ observed, similar to the speeds recorded for sperm in much lower viscosity fluids such as semen (Katz et al., 1989). The ability for cells to progress so rapidly is likely partly because cervical mucus and mammalian sperm have co-evolved together, so that whilst sperm can ad-

vance quickly, many other foreign pathogens cannot.

Properties such as the viscosity and degree of alignment of the fibres in cervical mucus can vary considerably based on factors including the stage of the female menstrual cycle (Odeblad, 1968). In particular, at the time of ovulation, high levels of oestrogen promotes a less viscous mucus, with fibres typically aligning parallel to the direction of travel between the vagina and uterus (Ceric et al., 2005). Contrastingly, high levels of progesterone result in a dry and viscous mucus, the composition of which hinders sperm progression (Wolf et al., 1977).

The structure of cervical mucus endows the fluid with complex, non-Newtonian properties. Cervical mucus can be described as a 'viscoelastic fluid' due to both its viscous and elastic properties, resulting from the behaviour of the polymer mesh whilst undergoing deformations. The fluid also exhibits 'shear-thinning rheology', in which the viscosity of the fluid reduces with increased fluid shear. This reduction in viscosity results from fibres within the mesh aligning with shear flow within the fluid. In the next section, we discuss experimental observations of the effect of viscoelasticity and shear-thinning rheology on human sperm.

1.2.3 Sperm propulsion in non-Newtonian fluids

Early experimental observations of the effect of cervical mucus on the movement characteristics of human sperm were conducted by Katz et al. (1978). Compared to locomotion in semen, a Newtonian fluid, sperm in non-Newtonian cervical mucus possess distinct swimming properties. Whilst Katz et al. (1978) noted that swimming speed appeared unchanged in these different fluids, they recorded that sperm swam with straighter trajectories in mucus and exhibited distinct flagellar beats. In particular, cells in cervical mucus possessed a higher beat frequency, lower amplitude beats and smaller wavelength. Katz et al. (1978) also noted that bending was confined to the distal half of the flagellum, with less pitching of the head observed compared to in a Newtonian fluid. Two example characteristic beats, redrawn based on the observations in Katz et al. (1978), are shown in Figure 1.4.

Katz et al. (1981) subsequently studied the behaviour of bull sperm in cervical mucus. In particular, they compared the swimming speed and flagellar waveforms of cells swimming

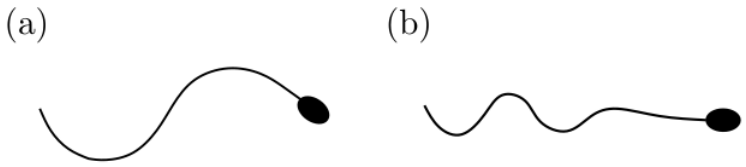


Figure 1.4: Characteristic flagellar beats of human sperm in (a) Newtonian semen and, (b) non-Newtonian cervical mucus. The flagellar shape in mucus displays higher frequency, smaller wavelength and amplitude, and less pitching of the head compared to swimming in a Newtonian fluid. Figure redrawn from the characteristic flagellar beats observed in Katz et al. (1978).

through the centre of a rectangular capillary tube and close to the wall. In both of these cases, Katz et al. (1981) observed that the sperm cell swimming in front of all other cells (the 'vanguard' cell), swam more rapidly than any subsequent cells, likely as a result of alternations in the properties of the mucus resulting from the motion of the vanguard cell. Katz et al. (1981) also observed that cells swam faster near the tube boundary, with lower beat frequencies and substantial differences in beat shape compared to swimming in the bulk fluid. In cervical mucus, sperm cells exhibited an essentially planar beat, whereas cells in the bulk fluid possessed a more three-dimensional swimming gait. Katz et al. (1981) noted that these changes may be due to the higher shear close to the boundaries of the tube, which likely alters the fluid properties.

Sperm undergo a set of changes in preparation for fertilisation, which are collectively referred to as capacitation (Yanagimachi, 1994). One such change is known as hyperactivation, which involves a shift in cell motility, specifically flagellar beat pattern, the precise manifestation of which depends on the surrounding fluid viscosity. For cells in low viscosity fluids, hyperactivation typically involves the development of a high-amplitude flagellar beat that results in a non-progressive star-spin motility pattern (Burkman, 1995). Experimental observations of hyperactivated mouse sperm in viscoelastic media demonstrate that cells show increased progression compared to cells exhibiting normal (activated) motility, unlike in Newtonian fluids where hyperactivation impedes progress (Suarez and Dai, 1992).

More recent experimental observations of bovine sperm in shear-thinning viscoelastic fluids, chosen to exhibit similar rheological properties to mammalian cervical mucus, again

demonstrate that complex rheology can affect cell motility and flagellar waveform (Hyakutake et al., 2019). In particular, Hyakutake et al. (2019) demonstrated that shear-thinning viscoelasticity increases the swimming speed of cells and yields flagellar waveforms with higher curvature towards the distal end of the flagellum, similar to the observed waveforms of Katz et al. (1978) (see Figure 1.4). Hyakutake et al. (2019) additionally found that thrust efficiency in shear-thinning viscoelastic fluids is larger than in Newtonian fluids and that the propulsive thrust of cells increases with the measured curvature of the flagellum tip.

These experimental observations of sperm in non-Newtonian fluids demonstrate that complex fluid rheology can have a pronounced effect on flagellar waveform development and propulsion of cells. In addition to human sperm, many other microscopic swimmers progress through non-Newtonian fluids, including bacteria swimming through mucosal media in the human body (Kimsey and Spielman, 1990; Gómez and Prince, 2007; Montecucco and Rappuoli, 2001) and nematodes such as *C. elegans* progressing through saturated soil (Jung, 2010). This interest in locomotion in non-Newtonian fluids from many aspects of biology has led to numerous theoretical techniques developed to better explore the mechanisms behind the observed changes in swimmer behaviour.

From a fluid mechanics perspective, the locomotion of microswimmers in viscoelastic fluids has been studied substantially more than swimming in shear-thinning rheology. In particular, the effect of viscoelasticity on propulsion has been examined for swimmers including waving sheets (Lauga, 2007; Riley and Lauga, 2014), helical swimmers (Spagnolie et al., 2013), undulatory swimmers (Teran et al., 2010; Thomases and Guy, 2014, 2017) and spermatozoa (Fulford et al., 1998). The effect of swimmer elasticity, where waveform emerges as a result of interactions between the elastic swimmer and surrounding fluid properties, has also been explored (Riley and Lauga, 2014; Thomases and Guy, 2014, 2017). A similar variety of swimmers have been studied theoretically in shear-thinning fluids (Montenegro-Johnson, 2013; Vélez-Cordero and Lauga, 2013; Li and Ardekani, 2015; Riley and Lauga, 2017; Demir et al., 2020; Qin et al., 2021). However, there has been little explanation of the effects of shear-thinning rheology on the propulsion of flexible swimmers, such as the flexible elastic flagellum of hu-

man sperm. Moreover, many methods make simplifying assumptions, such as small amplitude motion (Vélez-Cordero and Lauga, 2013; Riley and Lauga, 2014; Qin et al., 2021) or two-dimensional fluid dynamics (Montenegro-Johnson, 2013). This motivates the development of further methods to explore the effect of shear-thinning rheology on microswimmers, which forms the main focus of this thesis.

In the next section, we discuss the derivation of the relevant fluid equations for modelling both Newtonian and shear-thinning fluids as well as key techniques for solving such problems. Following this, we further review the literature surrounding experimental and theoretical studies of swimming in both Newtonian and non-Newtonian fluids (see Section 1.5). Finally, we outline the specific problems we will focus on throughout this thesis in Section 1.6.

1.3 Dynamics of flow

Through applying conservation of momentum and conservation of mass to an arbitrary volume of fluid of density ρ and velocity $\boldsymbol{u}$, we derive the fluid flow equations

$$\rho\left[\frac{\partial \boldsymbol{u}}{\partial t} + [\boldsymbol{u}\cdot\nabla]\boldsymbol{u}\right] = \nabla\cdot\boldsymbol{\sigma} + \boldsymbol{F}, \tag{1.1a}$$

$$\frac{\partial \rho}{\partial t} + \nabla\cdot[\rho\boldsymbol{u}] = 0, \tag{1.1b}$$

where $\boldsymbol{F}$ is the body force per unit volume acting on the fluid and $\boldsymbol{\sigma}$ is the stress tensor. If the fluid is assumed to be incompressible (as is the case for the fluids in this thesis), equation (1.1b) reduces to

$$\nabla\cdot\boldsymbol{u} = 0, \tag{1.2}$$

which is the continuity equation for an incompressible fluid.

The form of the stress tensor $\boldsymbol{\sigma}$ in the above system of equations depends on the type of fluid being modelled. In this thesis, we will consider both Newtonian and shear-thinning fluids. In particular, shear-thinning fluids are a subclass of the broader category of generalised-

Newtonian fluids, in which viscosity depends on the shear rate of the fluid. We now discuss the choice of the stress tensor in both the Newtonian and generalised-Newtonian cases, as well as the resulting fluid equations and their key properties.

1.3.1 Newtonian fluids

In the case of a Newtonian fluid, stress is proportional to strain, and the form of the stress tensor is given by

$$\boldsymbol{\sigma} = -p\mathbf{I} + 2\mu\,\boldsymbol{\varepsilon}(\boldsymbol{u}). \tag{1.3}$$

Here, p is fluid pressure, $\mathbf{I}$ is the identity tensor, and μ is the dynamic viscosity of the fluid. The strain rate tensor is defined as

$$\boldsymbol{\varepsilon}(\boldsymbol{u}) = \frac{1}{2}\left[\nabla\boldsymbol{u} + [\nabla\boldsymbol{u}]^T\right], \tag{1.4}$$

where $[\nabla\boldsymbol{u}]^T$ is the transpose of the velocity gradient tensor $\nabla\boldsymbol{u}$.

Choosing this form of the stress tensor, the conservation of momentum equation (1.1a) can be non-dimensionalised via scalings

$$\boldsymbol{u} = U\hat{\boldsymbol{u}}, \quad \nabla = L\hat{\nabla}, \quad t = \frac{L}{U}\hat{t}, \quad \boldsymbol{\sigma} = \frac{\mu U}{L}\hat{\boldsymbol{\sigma}}, \quad \boldsymbol{F} = \frac{\mu U}{L^2}\hat{\boldsymbol{F}}, \tag{1.5}$$

where U is the characteristic velocity of the fluid and L is a characteristic length-scale of the problem. In terms of the dimensionless variables (denoted with a hat $\hat{\cdot}$), the equation becomes

$$\frac{\rho UL}{\mu}\left[\frac{\partial\hat{\boldsymbol{u}}}{\partial\hat{t}} + [\hat{\boldsymbol{u}}\cdot\hat{\nabla}]\hat{\boldsymbol{u}}\right] = \hat{\nabla}\cdot\hat{\boldsymbol{\sigma}} + \hat{\boldsymbol{F}}, \tag{1.6}$$

from which we retrieve the dimensionless group

$$\mathrm{Re} = \frac{\rho UL}{\mu}, \tag{1.7}$$

which is known as the Reynolds number of the fluid and describes the ratio of inertial and

Table 1.1: Order of the characteristic Reynolds number for a variety of systems (Vogel, 2020).

Type	Re
Blue whale	$\mathcal{O}(10^8)$
Tuna fish	$\mathcal{O}(10^7)$
Human swimming	$\mathcal{O}(10^6)$
Butterfly flying	$\mathcal{O}(10^1)$
C. elegans	$\mathcal{O}(10^{-1})$
Sea urchin spermatozoa	$\mathcal{O}(10^{-2})$
Human spermatozoa	$\mathcal{O}(10^{-2})$
E. coli	$\mathcal{O}(10^{-5})$

viscous forces in the problem. The Reynolds number for a variety of self-propelled organisms in their natural environments are given in Table 1.1.

For $\mathrm{Re} \ll 1$, dropping the hat notation for brevity, the dimensionless form of the system (1.1) with the Newtonian form of the stress tensor (1.3) reduces to

$$\nabla^2 \boldsymbol{u} - \boldsymbol{\nabla} p + \boldsymbol{F} = \boldsymbol{0}, \tag{1.8a}$$

$$\boldsymbol{\nabla} \cdot \boldsymbol{u} = 0, \tag{1.8b}$$

which are the Stokes flow equations for the motion of a continuous Newtonian incompressible fluid in an inertialess regime.

The Stokes flow equations (1.8) have several properties that have important consequences when modelling microswimmers. The first of these properties is linearity. That is, for two solutions to these equations given by $(\boldsymbol{u}_1, p_1)$ and $(\boldsymbol{u}_2, p_2)$ respectively, we have that

$$\nabla^2 \left[\boldsymbol{u}_1 + \boldsymbol{u}_2\right] - \nabla \left[p_1 + p_2\right] = \left[\nabla^2 \boldsymbol{u}_1 - \nabla p_1\right] + \left[\nabla^2 \boldsymbol{u}_2 - \nabla p_2\right] = \boldsymbol{0}, \tag{1.9a}$$

$$\boldsymbol{\nabla} \cdot \left[\boldsymbol{u}_1 + \boldsymbol{u}_2\right] = \boldsymbol{\nabla} \cdot \boldsymbol{u}_1 + \boldsymbol{\nabla} \cdot \boldsymbol{u}_2 = 0, \tag{1.9b}$$

and thus $(\boldsymbol{u}, p) = (\boldsymbol{u}_1 + \boldsymbol{u}_2, p_1 + p_2)$ is also a solution. This true for any finite number of sums of solutions to the system (1.8).

The Stokes flow equations are also reversible, meaning that $(\boldsymbol{u}, p)$ is a solution to the problem (1.8) if and only if $(-\boldsymbol{u}, -p)$ is also a solution (with suitably adjusted boundary conditions). This limits the types of motion that can generate a net displacement in Stokes flow to swimming strokes that are irreversible. For example, Purcell's scallop theorem states that a scallop cannot swim through the clapping of its shell in a fluid obeying the Stokes flow equations (1.8), as this will always be time-reversible (Purcell, 1977).

In this thesis, we consider problems involving a single human sperm swimming in fluids of a range of characteristic viscosities. The typical length scale of a sperm cell is approximately 50 μm, with cells typically swimming no more than one body length per second. In this way, typical velocities are in the region $\mathcal{O}(10^{-5} - 10^{-4})\,\mathrm{m\,s^{-1}}$, fluid densities are of order $\mathcal{O}(10^{3})\,\mathrm{kg\,m^{-3}}$ and viscosities are $\mathcal{O}(10^{-3})\,\mathrm{Pa\,s}$ or greater. Therefore, an upper bound for the Reynolds number is $\mathcal{O}(10^{-2}) \ll 1$.

Despite the focus of the majority of this thesis on swimming in shear-thinning fluids, the Stokes flow equations and their subsequent solution form a crucial part of many of the methods we develop. Consequently, in Section 1.4, we outline several of the fundamental techniques for solving problems involving swimmers in fluids obeying these equations. Prior to this, we discuss the derivation of the generalised-Newtonian fluid flow equations in the next section.

1.3.2 Generalised Newtonian fluids

In a generalised-Newtonian fluid, the viscosity μ is instantaneously dependent on the shear rate of the fluid $\dot{\gamma}(\boldsymbol{u})$. We define the shear rate via

$$\dot{\gamma}(\boldsymbol{u}) = [2\boldsymbol{\varepsilon}(\boldsymbol{u}) : \boldsymbol{\varepsilon}(\boldsymbol{u})]^{\frac{1}{2}}, \tag{1.10}$$

where the double-dot product between two second-order tensors A and B is defined as

$$\mathrm{A} : \mathrm{B} = \sum_{i,j} \mathrm{A}_{ij}\mathrm{B}_{ij}. \tag{1.11}$$

The form of the stress tensor in a generalised-Newtonian fluid is given by

$$\boldsymbol{\sigma} = -p\mathbf{I} + 2\mu(\dot{\gamma}(\boldsymbol{u}))\,\boldsymbol{\varepsilon}(\boldsymbol{u}), \tag{1.12}$$

where to model a shear rate dependent rheology, the viscosity μ (units Pa s) should change as the shear rate $\dot{\gamma}(\boldsymbol{u})$ (units s^{-1}) increases. The simplest model for this behaviour is given by the power law

$$\mu(\dot{\gamma}(\boldsymbol{u})) = K\dot{\gamma}(\boldsymbol{u})^{n-1}, \tag{1.13}$$

where K (units Pa s^n) and n (unitless) are the consistency index and power law index respectively. When $n < 1$, this model describes shear-thinning fluids. If $n > 1$, then the model depicts a shear-thickening fluid, for example a suspension of corn starch in water. If $n = 1$, the model reduces to the Newtonian case of Stokes flow as in system (1.8). The power law has several drawbacks when modelling biological fluids. For example, if $n < 1$, the power law dictates that the viscosity approaches zero as the shear rate is increased indefinitely. Also, the viscosity in the expression (1.13) tends to infinity as the shear rate approaches zero. Biological fluids cannot attain a zero or infinite viscosity, and as such the power law is only applicable over a restricted range of shear rates. A more accurate constitutive model for describing biological fluids such as mucus is given by

$$\mu(\dot{\gamma}(\boldsymbol{u})) = \mu_\infty + [\mu_0 - \mu_\infty]\left[1 + [\lambda\dot{\gamma}(\boldsymbol{u})]^2\right]^{\frac{n-1}{2}}. \tag{1.14}$$

Here, the viscosities μ_0 and μ_∞ are referred to as the zero and infinite shear rate viscosities respectively, and λ (units s) is the relaxation time of the fluid. The choice of the parameter n (unitless), the shear-thinning index, characterises whether the fluid is Newtonian ($n = 1$), shear-thinning ($0 < n < 1$) or shear-thickening ($n > 1$), as in the power law case. For a shear-thinning fluid, $\mu_0 > \mu_\infty$, and the viscosity, as described by the constitutive law (1.14), decreases monotonically with shear rate from μ_0 (units Pa·s) to μ_∞ (units Pa·s) (see Figure 1.5).

This constitutive law (1.14) is referred to by a variety of names in the literature, as high-

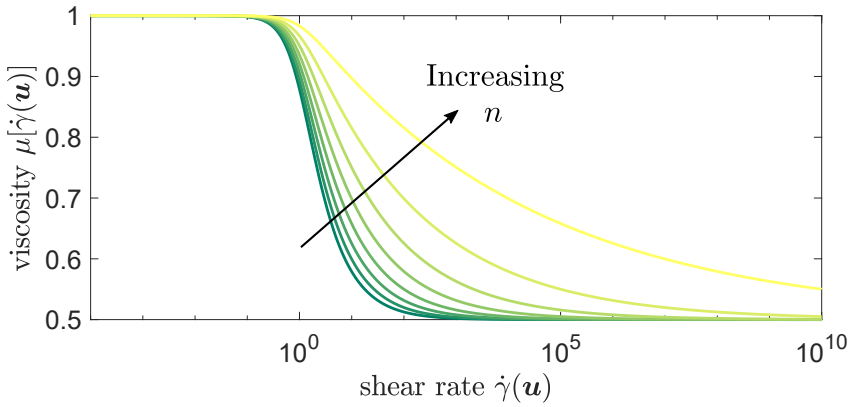


Figure 1.5: The viscosity $\mu(\dot{\gamma}(\boldsymbol{u}))$ calculated from the constitutive law (1.14) over a range of shear rates $\dot{\gamma}(\boldsymbol{u})$ and for $n \in [0.2, 0.9]$. Here $\mu_0 = 1$, $\mu_\infty = 0.5$ and $\lambda = 1$.

lighted by Gallagher et al. (2019b). For example, it is often referred to as the Carreau model, despite the fact that it differs from the original constitutive law proposed by Carreau (1972) due to the inclusion of the infinite shear rate viscosity μ_∞. In fact, this constitutive law is a hybrid of those proposed by Bird et al. (1987), Carreau (1972) and Cross (1965), with Bird et al. (1987) suggesting the five parameter model

$$\mu(\dot{\gamma}(\boldsymbol{u})) = \mu_\infty + [\mu_0 - \mu_\infty]\,[1 + [\lambda\dot{\gamma}(\boldsymbol{u})]^a]^{\frac{n-1}{a}} \tag{1.15}$$

Here the parameter a, a contribution of Yasuda (1979), was included to better describe the transition between the low shear and power law regimes. We consider a specific case in which $a = 2$, meaning that our constitutive law may be described as a 'Bird-Carreau-Cross four parameter model', which we will refer to as the BCC4p model going forward to avoid ambiguity.

We substitute the expression for the stress tensor (1.12) with the form of $\mu(\dot{\gamma}(\boldsymbol{u}))$ given in equation (1.14) into the system (1.1). For a flow involving a swimmer with beat frequency ω, we non-dimensionalise via the scalings given in equation (1.5) but with characteristic timescale ω^{-1} and characteristic viscosity μ_∞. For $\mathrm{Re} \ll 1$, dropping the hat notation for brevity, this yields the equations of flow for an inertialess generalised-Newtonian fluid modelled using the BCC4p constitutive law

$$\nabla \cdot [2\mu(\dot{\gamma}(\boldsymbol{u}))\boldsymbol{\varepsilon}(\boldsymbol{u})] - \nabla p + \boldsymbol{F} = \boldsymbol{0}, \tag{1.16a}$$

$$\nabla \cdot \boldsymbol{u} = 0, \tag{1.16b}$$

where

$$\mu(\dot{\gamma}) = 1 + \left[\frac{\mu_0}{\mu_\infty} - 1\right]\left[1 + [\lambda\omega\dot{\gamma}]^2\right]^{\frac{n-1}{2}}. \tag{1.17}$$

Unlike the Stokes equations (1.8), these equations are non-linear, due to the dependence of the viscosity on the shear-rate of the fluid. This restricts the number of methods that can be used to solve the system (1.16), and in particular motivates the use of numerical techniques which may be used to solve such systems using an iterative approach.

The goal of Chapter 3 of this thesis is to develop a new numerical method which allows for the efficient simulation of human sperm in shear-thinning fluids. This will then allow for the study of the effect of a shear-thinning rheology on the propulsion of sperm in Chapter 4. Before focusing on locomotion in complex fluids, we review some of the fundamental techniques for solving problems involving the Stokes flow equations (1.8) in the next section.

1.4 Fundamental hydrodynamic methods for Stokes flow

Whilst the work conducted in Chapter 3 and 4 of this thesis involves simulations in non-Newtonian fluids, Newtonian solution methods form an important part of the techniques we develop throughout. Here, in Section 1.4.1, we discuss the fundamental solution to the Stokes flow equations in the presence of a single point force. Following this, we describe the boundary integral formulation for Stokes flow in Section 1.4.2. Finally, we discuss the method of regularised stokeslets, a key numerical approach for solving biologically problems involving moving boundaries in Stokes flow, in Section 1.4.3.

1.4.1 The fundamental singularity of Stokes flow

Consider a single point force of magnitude $\boldsymbol{g}$ acting at the point $\boldsymbol{y} \in \mathbb{R}^3$ within a fluid obeying the Stokes flow equations (1.8). The total body force per unit volume acting at a point $\boldsymbol{x} \in \mathbb{R}^3$ is given by

$$\boldsymbol{F}(\boldsymbol{x}) = \boldsymbol{g}\delta(\boldsymbol{x} - \boldsymbol{y}), \tag{1.18}$$

where δ is the three-dimensional Dirac delta distribution (units m^{-3}), which is infinite at $\boldsymbol{x} = \boldsymbol{y}$ and zero otherwise and where

$$\iiint_D \delta(\boldsymbol{x} - \boldsymbol{y})d\boldsymbol{x} = \begin{cases} 1 & \text{if } \boldsymbol{y} \in D \subset \mathbb{R}^3, \\ 0 & \text{if } \boldsymbol{y} \notin D. \end{cases} \tag{1.19}$$

The velocity and pressure solutions to the Stokes flow equations with $\boldsymbol{F}$ defined as in (1.18) are given by

$$u_i(\boldsymbol{x}) = S_{ij}(\boldsymbol{x}, \boldsymbol{y})g_j(\boldsymbol{y}), \tag{1.20a}$$

$$p(\boldsymbol{x}) = P_j(\boldsymbol{x}, \boldsymbol{y})g_j(\boldsymbol{y}), \tag{1.20b}$$

which are known as the Stokeslet solutions. In these expressions, repeated indices are summed over and

$$S_{ij}(\boldsymbol{x}, \boldsymbol{y}) = \frac{1}{8\pi\mu}\left[\frac{\delta_{ij}}{r} + \frac{r_i r_j}{r^3}\right], \quad P_j(\boldsymbol{x}, \boldsymbol{y}) = \frac{1}{4\pi}\left[\frac{r_j}{r^3}\right], \tag{1.21}$$

for a fluid of viscosity μ, where $r_i = x_i - y_i$ and $r = |\boldsymbol{x} - \boldsymbol{y}|$. The rank-2 tensor $\boldsymbol{S}$ is known as the Stokeslet (or the Oseen tensor), a term first coined by Hancock (1953). The Stokeslet is singular at $r = 0$, which presents a challenge when considering numerical approaches to solving problems formulated in this way, the resolution of which will be discussed in Section 1.4.3. The Stokeslet solution has many important applications in the modelling of slender bodies such as cilia and flagella which will be discussed later.

In addition to the velocity and pressure solutions discussed above, the stress field associated

with the flow can be defined in a similar way via

$$\sigma_{ik}(\boldsymbol{x}) = T_{ijk}(\boldsymbol{x}, \boldsymbol{y}) f_j, \tag{1.22}$$

where the rank-3 stress tensor $\boldsymbol{T}$ is given by

$$T_{ijk}(\boldsymbol{x}, \boldsymbol{y}) = -\delta_{ik} P_j(\boldsymbol{x}, \boldsymbol{y}) + \mu \left[\frac{\partial S_{ij}(\boldsymbol{x}, \boldsymbol{y})}{\partial x_k} + \frac{\partial S_{kj}(\boldsymbol{x}, \boldsymbol{y})}{\partial x_i} \right] = -\frac{3}{4\pi} \frac{r_i r_j r_k}{r^5}, \tag{1.23}$$

which is known as the Stresslet[1]. This solution again forms an important part of many methods for modelling microswimmers. One such method is discussed in the next section.

1.4.2 The boundary integral equations for Stokes flow

In this thesis, we consider problems involving moving boundaries, such as the beating sperm flagellum, within both Newtonian and non-Newtonian fluids. For the Newtonian case where the fluid obeys the the Stokes flow equations (1.8), we formulate the boundary integral representation of this problem in this section.

Consider an object immersed within the fluid where the object may be described via a surface D. The derivation of the boundary integral formulation begins with the application of Lorentz reciprocal theorem (Lorentz, 1896), which states that

$$\frac{\partial}{\partial x_k} \left(u'_i \sigma_{ik} - u_i \sigma'_{ik} \right) = 0, \tag{1.24}$$

for two non-singular flows with velocities $\boldsymbol{u}$ and $\boldsymbol{u}'$ and stress tensors $\boldsymbol{\sigma}$ and $\boldsymbol{\sigma}'$.

If the flow with velocity $\boldsymbol{u}'$ is driven by a point force of strength $\boldsymbol{g}$ at the location $\boldsymbol{y}$, we may express the velocity $\boldsymbol{u}'$ and stress tensor $\boldsymbol{\sigma}'$ in terms of the Stokeslet and Stresslet kernels,

[1]The name 'Stresslet' may also be given to mean the velocity field due to a symmetric stokes doublet (see Blake and Chwang (1974)), which is slightly different to what we have defined here.

as in equations (1.20) and (1.22) respectively. In terms of the reciprocal theorem, this yields

$$\frac{\partial}{\partial x_k}\left(S_{ij}(\boldsymbol{x},\boldsymbol{y})\sigma_{ik} - u_i T_{ijk}(\boldsymbol{x},\boldsymbol{y})\right) = 0, \tag{1.25}$$

where we note that we have also divided by the strength of the force $\boldsymbol{g}$.

We choose a volume V which is bounded by the surface D and choose $\boldsymbol{y} \notin V$. In this case, the expression (1.24) is non-singular over V. Integrating over V and following the derivation outlined in Pozrikidis (1992) yields the boundary integral equation for Stokes flow

$$u_j(\boldsymbol{y}) = -\int_D S_{ij}(\boldsymbol{x},\boldsymbol{y}) f_i(\boldsymbol{x}) dS_{\boldsymbol{x}} + \int_D u_i(\boldsymbol{x}) T_{ijk}(\boldsymbol{x},\boldsymbol{y}) n_k(\boldsymbol{x}) dS_{\boldsymbol{x}}, \tag{1.26}$$

where $\boldsymbol{n}$ is the outward facing normal to D and $f_i = \sigma_{ik} n_k$ is the force per unit area exerted by the surface onto the fluid. This expression is valid for $\boldsymbol{y} \notin D$, whereas if $\boldsymbol{y} \in D$ then the left hand side of equation (1.26) is replaced by $u_j(\boldsymbol{y})/2$. Equation (1.26) provides a representation of the flow in terms of the Stokeslet, Stresslet, and force distribution. The first term on the right hand side of this expression is called the 'single-layer potential' and the second term the 'double-layer potential'.

For problems involving a stationary domain and the translation or rotation of a rigid immersed body, if $\boldsymbol{y} \in D$ then the double-layer integral yields $-u_j(\boldsymbol{y})/2$, meaning that equation (1.26) reduces to the single-layer formulation for Stokes flow

$$u_j(\boldsymbol{y}) = -\int_D S_{ij}(\boldsymbol{x},\boldsymbol{y}) f_i(\boldsymbol{x}) dS_{\boldsymbol{x}}. \tag{1.27}$$

Alternatively, under the condition that

$$\int_D \boldsymbol{u} \cdot \boldsymbol{n} dS = 0, \tag{1.28}$$

it can also be shown that the double-layer potential can be eliminated in equation (1.26) through an adjusted density.

1.4.3 The method of regularised stokeslets

The boundary integral equation (1.26) contains singular integrals that can be problematic when applying a numerical approach to biological flow problems due to the rapidly varying nature of the fluid flow around these points. A popular approach that alleviates this complication is the method of regularised stokeslets, proposed by Cortez (2001).

The regularised stokeslet is the solution to the Stokes flow equations (1.8), with body force given by a spatially-smoothed force per unit volume, i.e.

$$\boldsymbol{F}(\boldsymbol{x}) = \boldsymbol{f}\phi_\epsilon(\boldsymbol{x}-\boldsymbol{y}). \tag{1.29}$$

The function $\phi_\epsilon(\boldsymbol{x})$, otherwise known as the blob function, satisfies the property

$$\int_{\mathbb{R}^3} \phi_\epsilon(\boldsymbol{x})\mathrm{d}\boldsymbol{x} = 1, \tag{1.30}$$

and tends to the Dirac delta distribution as $\epsilon \to 0$. A popular choice in three-dimensions is given by

$$\phi_\epsilon(\boldsymbol{x}) = \frac{15\epsilon^4}{8\pi[r^2+\epsilon^2]^{7/2}}, \tag{1.31}$$

where the regularisation parameter $0 < \epsilon \ll 1$ controls the radius of the smoothed blob over which the force is applied. For this choice of blob function, an analogue of the stokeslet solution (1.21), the regularised stokeslet, can be derived. In this case, the regularised stokeslet velocity and pressure tensors are given by

$$S^\epsilon_{ij}(\boldsymbol{x},\boldsymbol{y}) = \frac{1}{8\pi\mu}\left[\delta_{ij}\frac{r^2+2\epsilon^2}{[r^2+\epsilon^2]^{3/2}} + \frac{r_i r_j}{[r^2+\epsilon^2]^{3/2}}\right], \tag{1.32a}$$

$$P^\epsilon(\boldsymbol{x},\boldsymbol{y}) = \frac{1}{4\pi}\left[r_j\frac{2r^2+5\epsilon^2}{[r^2+\epsilon^2]^{5/2}}\right], \tag{1.32b}$$

where $r_i = x_i - y_i$ and $r = |\boldsymbol{x}-\boldsymbol{y}|$. Similarly, the regularised form of the stress tensor (1.23) is given by

$$T^\epsilon_{ijk}(\boldsymbol{x},\boldsymbol{y}) = \frac{1}{8\pi}\left[\frac{-6r_i r_j r_k}{[r^2+\epsilon^2]^{5/2}} - \frac{3\epsilon[r_i\delta_{jk}+r_j\delta_{ik}+r_k\delta_{ij}]}{[r^2+\epsilon^2]^{5/2}}\right]. \tag{1.33}$$

The regularised stokeslet counterpart of the full boundary integral equation (1.26) is given by

$$u_j(\boldsymbol{y}) \approx -\int_D S_{ij}^{\epsilon}(\boldsymbol{x},\boldsymbol{y}) f_i(\boldsymbol{x}) dS_x + \int_D u_i(\boldsymbol{x}) T_{ijk}^{\epsilon}(\boldsymbol{x},\boldsymbol{y}) n_k(\boldsymbol{x}) dS_x, \tag{1.34}$$

which again is valid for $\boldsymbol{y} \notin D$, with the left hand side reducing to $u_j(\boldsymbol{y})/2$ if $\boldsymbol{y} \in D$. The error in the approximation in equation (1.34) is $\mathcal{O}(\epsilon^2)$ when $\boldsymbol{y}$ is further than $\sqrt{5\epsilon/2}$ away from the boundary D, and is $\mathcal{O}(\epsilon)$ otherwise (Cortez et al., 2005). Neglecting the double-layer potential following the same argument as in Section 1.4.2, we have that

$$u_j(\boldsymbol{y}) \approx -\int_D S_{ij}^{\epsilon}(\boldsymbol{x},\boldsymbol{y}) f_i(\boldsymbol{x}) dS_x. \tag{1.35}$$

Due to the symmetry of the regularised stokeslet kernel $S_{ij}^{\epsilon}(\boldsymbol{x},\boldsymbol{y}) = S_{ji}^{\epsilon}(\boldsymbol{y},\boldsymbol{x})$ and via relabelling, we rewrite the single-layer potential as

$$u_i(\boldsymbol{x}) = -\int_D S_{ij}^{\epsilon}(\boldsymbol{x},\boldsymbol{y}) f_j(\boldsymbol{y}) dS_y. \tag{1.36}$$

This relation is written as exact here and in what follows, however we note the previously discussed error associated with the regularised stokeslet approximation.

In many applications involving simulating swimmers in Stokes flow, the above equation must be numerically discretised. This can be achieved through approximating the integral in equation (1.36) via a quadrature rule with nodes $\{\boldsymbol{x}^{[1]}, \boldsymbol{x}^{[2]}, \dots, \boldsymbol{x}^{[N]}\}$ and corresponding weights $\{w^{[1]}, w^{[2]}, \dots, w^{[N]}\}$. If the surface metric is denoted by $dS_y(\boldsymbol{x}^{[n]})$, then the area associated with each node is given by $A^{[n]} := w^{[n]} dS_y(\boldsymbol{x}^{[n]})$ and (1.36) is approximated by

$$u_i(\boldsymbol{x}^{[n]}) = \sum_{m=1}^{N} S_{ij}^{\epsilon}(\boldsymbol{x}^{[n]}, \boldsymbol{x}^{[m]}) f_j^{[m]} A^{[m]}, \quad n = 1, \dots, N, \tag{1.37}$$

where $f_j^{[n]} := -f_j(\boldsymbol{x}^{[n]})$. This discretisation is often referred to as the Nyström discretisation as it arises from an application of the classical method by Nyström (1930). In practical applications, we define the unknown force distribution in the problem via $F_j^{[n]} := f_j^{[n]} A^{[n]}$ i.e. we

absorb the quadrature weights and surface metric into the unknown force rather than choosing them explicitly.

For prescribed body motion, we may apply the no-slip condition on the surface D so that $\boldsymbol{u}(\boldsymbol{x}^{[n]}) = \dot{\boldsymbol{x}}^{[n]}$. Thus equation (1.37) reduces to a problem to solve for the unknown forces $\{\boldsymbol{f}^{[n]}\}_{n=1}^{N}$, otherwise known as a 'resistance problem'. Alternatively, if the motion is known up to rigid body motion and the total force and moment on the body are also known, the expression becomes a 'motility problem' for the unknown rigid body velocity $\boldsymbol{U}$, angular velocity $\boldsymbol{\Omega}$, and force distribution.

In this section, we have discussed some of the fundamental techniques for solving problems involving the Stokes flow equations (1.8) in the presence of driving forces to represent, for example, the forces exerted by a swimmer on the surrounding fluid. These methods will form a useful basis for many of the techniques developed throughout this thesis. In the next section, we review the literature surrounding microscopic swimming in Newtonian, viscoelastic and shear-thinning fluids. Following this and based on our review, we define the precise problems we will explore in this thesis in Section 1.6.

1.5 Studies of microscopic swimming

The study of microscopic swimming, from both a theoretical and experimental perspective, has been a particular area of interest in the last 60 years (nearly 9,000 results for a search of 'Microswimmers' via Google Scholar), with many publications in this area more recently (95% of the aforementioned results published over the last 10 years). This may in part be due to the developments in experimental methods of tracking cells, as well as the collaboration of experimentalists with mathematical modellers. The classic problem that generated significant interest in the field was when Taylor calculated the flow induced by propagating travelling waves on a two-dimensional sheet, immersed in a viscous fluid (Taylor, 1951). Further classical contributions include those Gray and Hancock (1955) and Hancock (1953), including the development of slender body theory (SBT), a method based on modelling slender swimmers

through distributions of force singularities.

1.5.1 Microswimmer propulsion in Newtonian fluids

An approach that underpins much current research in the field of microswimmers involves representing a swimmer through a line distribution of forces. These so-called singularity-based approaches were first applied to swimming problems by Hancock (1953), who represented a headless flagellum through a force weighted distribution of Stokeslets and source dipoles (higher order singularities) along its center, where the flagellum in this case is modelled as a cylinder.

The fundamental propulsive mechanism for sperm was first explained by Gray and Hancock (1955). They showed that for a slender body, one can employ a local force-velocity relation in Stokes flow, with anisotropic coefficients for the normal (C_N) and tangential drag (C_T), such that $C_N/C_T \approx 2$. This was derived using the resistive-force theory (RTF) developed by Hancock (1953). Thus, they explained how a propagating flagellar wave results in propulsion in Stokes flow, as it generates a propulsive force that is balanced by the drag on the head of the cell, resulting in zero total force and torque on the swimmer. Applying this approach to a flagellar beat with wavelength λ leads to the drag coefficients

$$C_T = \frac{2\pi\mu}{\ln\frac{2\lambda}{a} - \frac{1}{2}}, \tag{1.38a}$$

$$C_N = \frac{4\pi\mu}{\ln\frac{2\lambda}{a} + \frac{1}{2}}, \tag{1.38b}$$

where a is the radius of the flagellum and μ is the viscosity of the fluid. The derivation of these parameters was later refined by Lighthill (1970), resulting in new coefficients

$$C_T = \frac{2\pi\mu}{\ln\frac{2q}{a}}, \tag{1.39a}$$

$$C_N = \frac{4\pi\mu}{\ln\frac{2q}{a} + \frac{1}{2}}, \tag{1.39b}$$

with $q = 0.09\Lambda$ where Λ is the wavelength measured along the centerline of the flagellum. These approaches compare well with experimental observations for example those of Dresdner and Katz (1981) and Friedrich et al. (2010), but have several drawbacks. The methods are inaccurate for flagella near boundaries, with very high curvature, with large bodies and interacting with each other (Johnson and Brokaw, 1979). They are also inaccurate at the ends of the flagellum, as they assume that the flagellum is slender, which is invalid at these locations. This problem can be improved upon by replacing the cylindrical model with a prolate ellipsoid, the solutions for which were derived by Chwang and Wu (1975) and applied to a flagellum by Johnson (1980) through constructing matched asymptotic expansions. Smith et al. (2007) compared the errors in these cases and showed that the prolate ellipsoid case greatly reduced these endpoint errors.

Youngren and Acrivos (1975) first applied the boundary element method (BEM), a method that does not assume slenderness of the flagellum, to Stokes flow. This method was then first used to model flagella by Phan-Thien et al. (1987), and compared to the existing slender body theory by Ramia et al. (1993). In this case, we consider surface distributions of singularities. Through the application of the boundary element method, we determine the fluid forces acting on a body with prescribed boundary conditions, from which we find the swimming velocity as well as the flow field. In particular Phan-Thien et al. (1987) used the BEM to study the swimming behaviour of a microswimmer exhibiting helical waves across its flagellum, and uncovered the optimum flagellar length $L/A = 10$ (L flagellar length, A radius of cell body/head), optimal wave properties $\alpha k \approx 1$ (beat amplitude α, wavenumber k), and optimal head aspect ratios $B/A \approx 0.7$ and $C/A \approx 0.3$ (A, B, C radii of the ellipsoid), for cell propulsion.

1.5.2 Microswimmer propulsion in Non-Newtonian fluids

As discussed previously, in many biological systems, microswimmers progress through complex, non-Newtonian fluids. Polymer suspensions such as mucus display rheological proper-

ties such as viscoelasticity and shear-thinning rheology (Lai et al., 2009), both of which can significantly modify propulsion. While most experimental and theoretical studies concentrate on the effect of one of these complex rheologies, several studies focus on their combined influence. This section provides an overview of important work conducted in the field of microswimmer locomotion in non-Newtonian fluids. In particular, we focus on outlining studies which examine how complex fluids can modify the swimming speed and efficiency of swimmers. We start by reviewing the effect of viscoelasticity on propulsion. Although we will not be modelling viscoelastic fluids in this thesis, many of these methods provide insight into the mechanisms behind swimming in complex fluids. Following this, we outline several important studies exploring the effect of shear-thinning rheology on microswimmer propulsion. In all cases, rather than focusing only on studies exploring the effects of complex rheology on sperm, we extend our view to that of a wide variety of microswimmers. This is because, in many cases, the techniques developed for other classes of swimmers may still provide insight into the effect of non-Newtonian fluids on human sperm propulsion.

Viscoelastic fluids

Compared to the effect of shear-thinning rheology, substantially more studies have focused on the impact of viscoelasticity on propulsion. These include experimental and theoretical investigations and consider a wide variety of microswimmers, including waving sheets, helical swimmers, undulatory swimmers, and spermatozoa (see Table 1.2 and Figure 1.6).

Initially, Newtonian resistive-force-theory was used to approximate the behaviour of sperm in viscoelastic fluids (Baltz et al., 1988; Drobnis et al., 1988), however a significant early development in modelling techniques for viscoelastic fluids was the generalisation of resistive-force-theory for linear viscoelastic fluids by Fulford et al. (1998). In this case, the viscoelastic behaviour of the fluid may be described by the constitutive law

$$\left[1 + \lambda \frac{\partial}{\partial t}\right] \boldsymbol{\tau} = 2\mu \boldsymbol{\varepsilon}, \tag{1.40}$$

Table 1.2: Summary of the key studies discussed in the review of swimming in viscoelastic fluids. The author of the study, type of swimmer, type of study and fluid constitutive law are indicated. The conclusion indicates whether viscoelasticity decreases (red), increases (green) or has no effect on (yellow) the swimming speed of the swimmer compared to that in a Newtonian fluid, where in some studies multiple effects are uncovered. The papers are split into theoretical and experimental studies and are listed in ascending order with date.

Author	Swimmer type	Study type	Constitutive model	Conclusion
Fulford et al. (1998)	Spermatozoa	Theory	Linear Maxwell	🟡
Lauga (2007)	Infinite waving sheet	Theory/asymptotic analysis	Oldroyd-B	🔴
Fu et al. (2009)	Infinite cylindrical swimmer	Theory/asymptotic analysis	Oldroyd-B	🔴
Teran et al. (2010)	Finite waving sheet	Theory/numerical	Oldroyd-B	🔴🟢
Spagnolie et al. (2013)	Rigid helix	Theory/numerical	Oldroyd-B	🔴🟢
Riley and Lauga (2014)	Flexible infinite waving sheet	Theory	Oldroyd-B	🔴🟢
Thomases and Guy (2014)	Undulatory swimmers	Theory/numerical	Oldroyd-B	🔴🟢
Thomases and Guy (2017)	Undulatory swimmers	Theory/asymptotic analysis	Oldroyd-B	🔴🟢
Shen and Arratia (2011)	*Caenorhabditis elegans*	Living micro-organisms	N/A	🔴
Liu et al. (2011)	Rigid helix	Physical systems	N/A	🔴🟡🟢
Espinosa-Garcia et al. (2013)	Head + flexible helix	Physical systems	N/A	🟢
Godínez et al. (2015)	Head + various tails	Physical systems	N/A	🔴🟡🟢
Qin et al. (2015)	*Chlamydomonas reinhardtii*	Living micro-organisms	N/A	🔴
Angeles et al. (2021)	Head and rigid helix	Physical systems	N/A	🔴🟡🟢

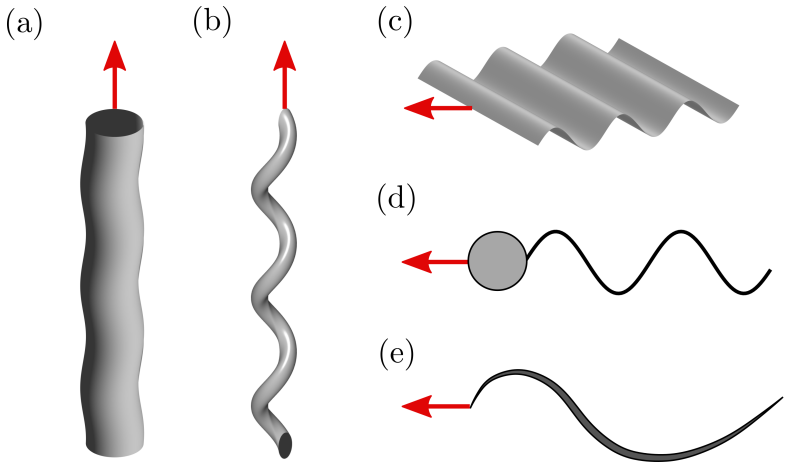


Figure 1.6: The variety of swimmer types studied in viscoelastic fluids from both an experimental and theoretical perspective. (a) A infinite almost-cylindrical swimmer with prescribed beating motion in the azimuthal direction (Fu et al., 2009), (b) a rotating helical swimmer (Spagnolie et al., 2013; Liu et al., 2011), (c) an infinite two-dimensional waving sheet (Lauga, 2007; Riley and Lauga, 2014), (d) a two-dimensional sperm cell consisting of spherical head and flagellum with sinusodial beat (Fulford et al., 1998), (e) a finite-length undulatory swimmer (Teran et al., 2010; Thomases and Guy, 2014; Shen and Arratia, 2011). Red arrows indicate the direction of swimming.

where $\boldsymbol{\tau}$ is the deviatoric stress tensor, which is related to the Cauchy stress tensor $\boldsymbol{\sigma}$ via $\boldsymbol{\sigma} = -p\boldsymbol{I} + \boldsymbol{\tau}$. Fluids modelled using the constitutive law (1.40) are known as linear Maxwell fluids, with the model initially developed by Maxwell (1867) to describe the elastic and viscous response of air, although it has since been applied to many other fluids. For a spermatazoon swimming in a fluid modelled using the above constitutive law, Fulford et al. (1998) found that the hydrodynamic force per unit length exerted by the fluid on the flagellum satisfies

$$\lambda \frac{\partial f_T}{\partial t}(s,t) + f_T(s,t) = -C_T U_T(s,t), \tag{1.41a}$$

$$\lambda \frac{\partial f_N}{\partial t}(s,t) + f_N(s,t) = -C_N U_N(s,t). \tag{1.41b}$$

Here, s represents arclength along the flagellum, t is time, λ is the fluid elastic relaxation time, U_T and U_N are the tangential and normal components of the flagellar velocity respectively, and similarly, f_T and f_N are the tangential and normal force components. The parameters C_T and C_N represent the Newtonian resistive-force-theory resistance coefficients.

For a sperm cell with a spherical head and small amplitude sinusoidal flagellar beat, Fulford

et al. (1998) observed no change in propulsive velocity for a viscoelastic fluid compared to a Newtonian fluid. However, Fulford et al. (1998) demonstrated that the rate of work decreases as fluid relaxation time increases, thus predicting that sperm cells can swim faster in a linear viscoelastic fluid with the same energy expenditure as for a Newtonian fluid.

Further examples of the use of the linear Maxwell equations as a constitutive model for linear viscoelasticity are the works of Smith et al. (2009a), Ishimoto and Gaffney (2017) and Ishimoto and Gaffney (2018). Smith et al. (2009a) derived the fundamental solution for linear viscoelastic flow. This 'viscoelastic Stokeslet' was subsequently used to develop a viscoelastic slender-body theory and applied to cilia-driven linear viscoelastic flow.

Ishimoto and Gaffney (2017) developed a boundary element formulation for linear Maxwell flows in which only surface integrals are required. Ishimoto and Gaffney (2017) demonstrated that for force and torque-free swimmers, the swimming dynamics in a Maxwell fluid are identical to those in Newtonian Stokes flow. However, linear viscoelasticity can significantly impact dynamics for forced swimmers such as magnetised helical swimmers under the effect of a rotating magnetic field. Finally, Ishimoto and Gaffney (2018) demonstrated via simulations that linear viscoelasticity aides clustering of sperm cells, a behaviour previously observed experimentally (Tung et al., 2017).

Despite the value of these studies in developing our knowledge of swimming in viscoelastic fluids, the linear Maxwell fluid model has one serious drawback – the expression is not frame-invariant (Morozov and Spagnolie, 2015). Thus, in general, more complex fluid constitutive laws are considered. Of the many possibilities, arguably the most popular is the Oldroyd-B fluid model. In this case, the deviatoric stress is expressed via $\boldsymbol{\tau} = \boldsymbol{\tau}^s + \boldsymbol{\tau}^p$, where $\boldsymbol{\tau}^s$ is the Newtonian contribution from the solvent, $\boldsymbol{\tau}^s = 2\mu_s\boldsymbol{\varepsilon}$, and $\boldsymbol{\tau}^p$ is the polymeric contribution to the stress. Here $\boldsymbol{\varepsilon}$ is the strain rate tensor as defined in Section 1.3.

To obtain the Oldroyd-B model, we assume that the polymeric stress obeys the upper-convected Maxwell equation

$$\boldsymbol{\tau}^p + \lambda\overset{\triangledown}{\boldsymbol{\tau}}^p = 2\mu_p\boldsymbol{\varepsilon}, \tag{1.42}$$

where λ is the polymer relaxation time, and the upper-convective derivative of a tensor $\boldsymbol{T}$, $\overset{\triangledown}{\boldsymbol{T}}$,

is defined via

$$\overset{\triangledown}{\boldsymbol{T}} = \frac{\partial \boldsymbol{T}}{\partial t} + \boldsymbol{u} \cdot \nabla \boldsymbol{T} - \left[[\nabla \boldsymbol{u}]^T \cdot \boldsymbol{T} + \boldsymbol{T} \cdot [\nabla \boldsymbol{u}] \right]. \tag{1.43}$$

This represents the time derivative of the tensor $\boldsymbol{T}$ within a fluid with velocity $\boldsymbol{u}$, built to ensure that the relation is frame-invariant (Morozov and Spagnolie, 2015). The Oldroyd-B model for the total deviatoric stress can then be derived as

$$\boldsymbol{\tau} + \lambda_1 \overset{\triangledown}{\boldsymbol{\tau}} = \mu [\boldsymbol{\varepsilon} + \lambda_2 \overset{\triangledown}{\boldsymbol{\varepsilon}}], \tag{1.44}$$

where $\mu = \mu_s + \mu_p$ is the total viscosity composed of solvent and polymer components, $\lambda_1 = \lambda$ and $\lambda_2 = \lambda[\mu_s/\mu]$ is the retardation time (Lauga, 2007).

One such study that utilises the Oldroyd-B constitutive law was conducted by Lauga (2007) who studied the propulsion of an infinite waving sheet in a non-linear viscoelastic fluid. Through asymptotic analysis, Lauga (2007) demonstrated that the leading-order swimming velocity of the sheet U is related to the Newtonian swimming speed U_N via

$$\frac{U}{U_N} = \frac{1 + \mathrm{De}^2 \mu_s/\mu}{1 + \mathrm{De}^2}. \tag{1.45}$$

Here, De is the Deborah number, defined as the product of wave frequency and fluid relaxation time. Crucially, $\mu \geq \mu_s$ by definition and hence $U \leq U_N$. Therefore, Lauga (2007) conclude that an infinite waving sheet with a prescribed small-amplitude swimming gait always swims slower in a viscoelastic fluid. Lauga (2007) also derived a similar expression for the leading-order work done by the waving sheet, finding that

$$\frac{W}{W_N} = \frac{\mu/\mu_S + \mathrm{De}^2}{1 + \mathrm{De}^2}, \tag{1.46}$$

and concluding that swimming in a viscoelastic fluid requires more work than in a Newtonian fluid. This is in contrast to the observations of Fulford et al. (1998), and thus the inclusion of non-linear terms in the fluid constitutive law (using the Olydroyd-B model rather than linear Maxwell) results in different predictions in terms of swimming speed and work.

Fu et al. (2009) also performed an asymptotic study of the effects of non-linear viscoelasticity on propulsion. Fu et al. (2009) considered an infinite cylindrical swimmer with prescribed small-amplitude beating motion in the azimuthal direction. Deriving an expression for the swimming speed of the swimmer, Fu et al. (2009) found results in broad agreement with those of Lauga (2007). Further, Fu et al. (2009) applied their methodology to study what types of swimmers can produce a net translation in non-linear viscoelastic fluids. Whilst in a Newtonian fluid Purcell's scallop theorem dictates net swimmer progression cannot be achieved through time-reciprocal motion, Fu et al. (2009) demonstrated that net movement is possible in a viscoelastic fluid for a reciprocal stroke in which the backwards and forwards strokes occur at different rates.

Continuing the theme of theoretical methods for simulating swimming in non-linear viscoelastic fluids, Teran et al. (2010) developed a numerical approach based on the immersed boundary method and analysed the effect of viscoelasticity on several swimmer types. Returning to the infinite waving sheet problem, Teran et al. (2010) demonstrated that using their method the small-amplitude results of Lauga (2007) could be qualitatively recovered, namely that the swimming speed ratio U/U_N was less than one. The same framework was then applied to the simulation of finite-length two-dimensional swimming sheets with large tail undulations. In this case, the swimmer reaches a peak swimming speed at $\mathrm{De} \approx 1$, indicating that viscoelasticity aids propulsion. Teran et al. (2010) explain how the conflicting results in the infinite and finite cases lie in the development of regions of highly stressed fluid at the distal tip of the finite swimmer within a viscoelastic fluid. This stress build-up restricts backwards movement of the swimmer during portions of its swimming stroke, which leads to an increase in average speed.

The propulsion of finite-length undulatory swimmers in viscoelastic fluids has also been studied experimentally. Shen and Arratia (2011) explored the swimming behaviour of the nematode *Caenorhabditis elegans* in both a viscoelastic carboxymethylcellulose solution and Newtonian fluids over a range of viscosities (approximately 2 mPa s–400 mPa s). The swimming nematode was experimentally tracked, with the surrounding flow fields extracted using

particle tracking velocimetry. Similarly to Lauga (2007) and Fu et al. (2009), Shen and Arratia (2011) found increased fluid elasticity hinders propulsion, with swimming speed reductions of up to 35% observed compared to Newtonian solutions. However, these results are in contradiction to finite-swimmer results of Teran et al. (2010), a discontinuity that Shen and Arratia (2011) states is likely due to the differences in beat pattern. In particular, whilst the simulations of Teran et al. (2010) considered a prescribed travelling wave with increasing amplitude from the proximal to the distal end, the experiments of Shen and Arratia (2011) revealed a travelling wave swimming gait with an exponential decay of amplitude across the swimmer.

Along with experiments with living organisms, the effect of viscoelasticity on specially designed physical systems representing artificially constructed swimmers has also been examined. Liu et al. (2011) developed an experimental set-up in which a helical swimmer is simultaneously rotated at a constant rate and translated within a viscoelastic solution in such a way as to enforce zero total force and moment on the swimmer. Specifically, to calculate the force-free swimming speed, the translational speed was adjusted until the net hydrodynamic force vanished, allowing swimming speed to be calculated as a function of the rotation rate. Liu et al. (2011) compared their results using this technique in the Newtonian case to theoretical predictions using methods such as slender-body-theory and the boundary element method, showing good agreement.

Liu et al. (2011) demonstrated that Newtonian and viscoelastic swimming speeds are similar when the relaxation time of the fluid is short compared to the rotation period of the helical swimmer. This corresponds to small Deborah number De, defined via $\mathrm{De} = \Omega\lambda/(2\pi)$, where $\Omega/(2\pi)$ is the rotation frequency of the swimmer. However, as the relaxation time increases (increased De), the viscoelastic swimming speed grows compared to the Newtonian rate, leading to enhanced propulsion in a viscoelastic fluid with a peak value of the swimming speed obtained at $\mathrm{De} = 1$ (similar to the peak observed by Teran et al. (2010)). Eventually, increasing the relaxation time past a critical value leads to the swimming speed falling below the Newtonian threshold. These results contrast with those of Shen and Arratia (2011), indicating that the nature of the dependence of swimming speed on relaxation time depends strongly on the

swimmer type in question.

Whilst the helical swimmer considered by Liu et al. (2011) was rigid, the effect of viscoelasticity on a flexible helical swimmer has also been studied experimentally. Espinosa-Garcia et al. (2013) constructed a swimmer consisting of a magnetic head and flexible tail, actuated via an external magnetic field to produce helical motion. Espinosa-Garcia et al. (2013) observed a monotonic increase in swimming speed with increasing Deborah number, in qualitative agreement with the results of Teran et al. (2010) and Liu et al. (2011) for $\mathrm{De} \leq 1$. However, the results of Espinosa-Garcia et al. (2013) do not exhibit a critical Deborah number at which swimming speed is maximised as in these previous studies, and therefore do not agree with the results of Teran et al. (2010) and Liu et al. (2011) for $\mathrm{De} > 1$. To explore this discrepancy in results, Espinosa-Garcia et al. (2013) used particle image velocimetry to visualise the flow fields surrounding the swimmer and found that there is a significant variation in the shear experienced at the back and front of the swimmer's head. The presence of shear deformations in a viscoelastic fluid leads to additional normal stresses, since this stretches the polymers in the suspension along the direction of flow (Barnes et al., 1989). Espinosa-Garcia et al. (2013) postulated that the presence of these non-Newtonian normal stresses leads to net elastic force in the direction of swimming and a subsequent increase in swimming rate.

In addition to being studied experimentally, the effect of viscoelasticity on helical swimmers has also been studied numerically. Spagnolie et al. (2013) showed that viscoelasticity could either enhance or reduce the swimming speed and efficiency of a rigid helical swimmer, depending on the body geometry, fluid characteristics and the rotation rate of the helix. Comparing first to the results of Fu et al. (2009), Spagnolie et al. (2013) demonstrated that increasing the thickness of the helix yields monotonic convergence of the swimming speed to the values presented by Fu et al. (2009). As a consequence, Fu et al. (2009) showed that viscoelasticity again hinders swimming speed for small-amplitude motion. For high pitch angles, Spagnolie et al. (2013) recovered the results of Liu et al. (2011), namely that there exists a critical Deborah number at which the swimming speed is higher in a viscoelastic fluid than in a Newtonian fluid.

Spagnolie et al. (2013) further demonstrated that the thickness of the helical swimmer can influence swimming speed. In particular, slender filaments appear to swim faster than thicker filaments for the same pitch angle. Spagnolie et al. (2013) also showed that reducing thickness for filaments of intermediate pitch angle introduces a new regime in which viscoelastic effects aid propulsion.

Returning now to the infinite waving sheet problem, Riley and Lauga (2014) conducted a theoretical study to explore the effect of viscoelasticity on propulsion of a flexible waving sheet. Here, rather than prescribing the shape of the waveform, Riley and Lauga (2014) solved for the waveform as a balance between fluid stresses and the internal driving and resisting forces. Using asymptotic analysis, Riley and Lauga (2014) demonstrated that the ratio between the Newtonian and viscoelastic swimming speeds can be expressed as

$$\frac{U}{U_N} = \frac{[1 + 4\mathcal{S}^6][1 + \beta \mathrm{De}^2]}{1 + \mathrm{De}^2 + 4\mathcal{S}^3 \mathrm{De}[1 - \beta] + 4\mathcal{S}^6[1 + \beta^2 \mathrm{De}^2]}, \tag{1.47}$$

where $\beta = \mu_s/\mu$ is the ratio between the Newtonian and viscoelastic viscosity and $\mathcal{S}$ is a dimensionless group quantifying the ratio of fluid to bending stresses in the problem. In the stiff limit, $\mathcal{S} \ll 1$, this expression simplifies to equation (1.45), derived by Lauga (2007) for a rigid infinite waving sheet. In this case, the swimming speed ratio decreases monotonically with increasing Deborah number. In the limit where $\mathcal{S} \gg 1$, corresponding to a very 'floppy' filament, equation (1.47) becomes

$$\frac{U}{U_N} = \frac{1 + \beta \mathrm{De}^2}{1 + \beta^2 \mathrm{De}^2}. \tag{1.48}$$

Here, the swimming speed ratio increases monotonically with Deborah number up to a value of $1/\beta$ when $\mathrm{De} \gg 1$. Thus, Riley and Lauga (2014) demonstrate the transition from hindered to enhanced propulsion depends on swimmer flexibility.

Thomases and Guy (2014) developed a computational model of finite-length undulatory swimmers in viscoelastic fluids, in order to examine the origin of the effect of fluid elasticity on propulsion. In particular, Thomases and Guy (2014) explored two distinct swimming gaits;

one with large head undulations and one with large tail undulations, referred to as burrowers and kickers respectively. They described the motion of the swimmer via a curvature function and used the immersed boundary method to solve for the coupled motion of the fluid and swimmer. Thomases and Guy (2014) studied the swimmer for both low and high bending stiffness, referred to as 'soft' and 'stiff' swimmers, respectively.

The results of Thomases and Guy (2014) demonstrated that whilst swimming speed depends on the type of swimming stroke employed by the swimmer, it is also sensitive to both fluid and swimmer elasticity. Thomases and Guy (2014) found that in general viscoelasticity hinders swimmers, but that speed boosts can be gained for soft swimmers and kickers due to favourable changes in the swimming gait and asymmetries in the polymer stress distribution respectively. Significant enhancements are are only observed when these two mechanisms concur together, as seen in the case of soft kickers in which a maximum swimming speed is achieved at approximately $\mathrm{De} = 1$, similar to the peak observed by Liu et al. (2011). Whilst the swimming stroke used by Thomases and Guy (2014) was based on the experimental data of Shen and Arratia (2011), Thomases and Guy (2014) demonstrated that the finite-length results of Teran et al. (2010), which are contradictory to Shen and Arratia (2011), can be reproduced by changing the direction of the wave.

Whilst the results of Thomases and Guy (2014) agree with previous observations that fluid elasticity aids swimming speed up to a critical Deborah number, they do not explain the experimental results of Espinosa-Garcia et al. (2013) in which fluid elasticity leads to monotonic gains in swimming speed for flexible swimmers. Again considering finite-length undulatory swimmers, Thomases and Guy (2017) sought to bridge this gap between these, as well as other, theoretical and experimental observations, by exploring how shape changes in flexible swimmers can lead to speed boosts in viscoelastic fluids.

Thomases and Guy (2017) considered three distinct values of the flagellum stiffness B, representing 'very soft', 'moderately soft' and 'stiff' swimmers, and studied the resultant swimming speeds using the same computational framework as Thomases and Guy (2014). Thomases and Guy (2017) demonstrated that for very soft swimmers, monotonic boosts in swimming

speed are observed, similar those of Espinosa-Garcia et al. (2013). For moderately soft swimmers and stiff swimmers, the results of Thomases and Guy (2014) are recovered, namely non-monotonic speed-up and slow-down for the different swimmer types respectively. Therefore, changes in swimmer stiffness determine which of these regimes a swimmer belongs to.

It is evident from the literature that whether a swimmer is enhanced or hindered by viscoelasticity is dependent on several factors, including swimming gait and swimmer elasticity. To explore this hypothesis further, Godínez et al. (2015) experimentally investigated the locomotion of three distinct artificial swimmers in viscoelastic fluids. These swimmers consisted of a rigid head and three flagellum types: a rigid helical tail, a planar flexible tail and a flexible helical tail.

For rigid helical swimmers, no change is observed in the swimming speed. This observation is likely due to the intermediate helical pitch angle, which yields results that fall between the small-amplitude theoretical predictions of Fu et al. (2009) and high-amplitude results of Spagnolie et al. (2013). Cells with a planar flexible tail exhibit faster propulsion, possibly as a result of the normal stress difference across the cell head observed by Espinosa-Garcia et al. (2013). Finally, flexible helical swimmers are consistently impeded by viscoelasticity. Godínez et al. (2015) also note that viscoelasticity has little effect on the kinematics of the flexible flagella considered, although they postulate that shear-thinning effects could influence flagellar shape much more significantly.

Qin et al. (2015) conducted an experimental study to uncover the effects of viscoelastcity on the propulsion of the the bi-flagellated algae *Chlamydomonas reinhardtii*. Qin et al. (2015) demonstrated through direct experimental measurements that fluid elasticity and viscosity can strongly influence the beat pattern and propulsion of *Chlamydomonas*. They observed that both beating frequency and wave speed are enhanced by fluid elasticity; however, viscoelasticity always hinders swimming speed.

Through examining the curvature of the flagella in both the viscoelastic and Newtonian cases, Qin et al. (2015) postulate localised polymer stress regions at both the distal and proximal end of the flagella, similar to observations by Thomases and Guy (2014). Examining the

power and recovery stroke independently, Qin et al. (2015) concluded that these polymer stress regions, along with an increase in beat frequency, lead to enhanced speed during the recovery stroke in a viscoelastic fluid resulting in increased backward movement. Contrastingly, these effects work against each other during the power stroke. The net results is a reduction in speed of the swimmer. The results of Qin et al. (2015) are further supported by those of Li et al. (2017), who used the experimentally tracked swimming gaits from Qin et al. (2015) as inputs to their numerical simulations in order to decouple the effects of swimming gait and fluid elasticity on locomotion.

To conclude our review of the effect of viscoelasticity on propulsion, we examine the recent experimental work of Angeles et al. (2021) on force-free magnetically driven rigid helical swimmers in Newtonian and viscoelastic fluids. The swimmer constructed by Angeles et al. (2021) resembled that of Godínez et al. (2015), that is, it consists of an elongated plastic head and a rigid helical tail. A magnet is located inside the head, and actuation is achieved through the action of a rotating magnetic field.

Angeles et al. (2021) explored the effect of varying the size of the swimmer body and helical flagellum and demonstrated a critical dependence of the swimming speed in a viscoelastic fluid on the swimmer geometry. Fluid elasticity can lead to significant increases in swimming speed, a similar decrease, or no effect on swimming speed. Combining the experimental results with theoretical modelling using restive-force-theory, Angeles et al. (2021) demonstrated a so called 'snowman-like' effect, in which the front-back asymmetry of the swimmer leads to elastic forces that may help or hinder the cell. This effect was previously reported for magnetically actuated rigid dumbbell swimmers (Puente-Velázquez et al., 2019), and results in swimmers with smaller heads than flagella swimming faster, whereas cells with heads larger than their tails decrease in swimming speed with increasing fluid elasticity. These results again demonstrate how the effect of viscoelasticty on cell propulsion is strongly dependent on the exact morphology of the swimmer.

In this section, we have reviewed the literature surrounding swimming in viscoelastic fluids. Both experimental and theoretical studies indicate that fluid elasticity can have a pro-

nounced effect on the propulsion of microswimmers, influencing factors such as swimming speed and efficiency (see Table 1.2). We have considered a variety of different swimmers including waving sheets (Lauga, 2007; Riley and Lauga, 2014), helical swimmers (Spagnolie et al., 2013), undulatory swimmers (Teran et al., 2010; Thomases and Guy, 2014, 2017) and spermatozoa (Fulford et al., 1998). In particular, the studies most relevant to sperm are those that consider finite length planar swimmers (Teran et al., 2010; Shen and Arratia, 2011; Thomases and Guy, 2014, 2017), as well as those that include swimmer flexibility/elasticity (Riley and Lauga, 2014; Thomases and Guy, 2014, 2017). Whilst we will not be considering the effects of fluid viscoelasticity in this thesis, these studies, which indicate that swimmer type, swimming gait, swimmer elasticity and fluid properties are important, provide a basis for exploration in shear-thinning fluids. In the next section, we review the literature surrounding swimming in shear-thinning fluids.

Shear-thinning fluids

In a shear-thinning fluid, viscosity decreases with increased shear rates, resulting from polymers within the suspension aligning with the shear flow, which allows them to slide past each other more readily (Barnes et al., 1989). Until more recently, compared to studies of viscoelasticity, the effects of shear-thinning rheology on propulsion have been largely overlooked. However, several investigations reveal situations where the swimming velocity of various swimmers can increase, decrease, or stay the same relative to their speed in a Newtonian fluid (see Table 1.3). In this section, we discuss these works, some of which study the combined effect of both viscoelasticity and shear-thinning rheology.

Table 1.3: Summary of the key studies discussed in the review of swimming in shear-thinning fluids. The author of the study, type of swimmer, type of study and actuation method are indicated. The conclusion indicates whether shear-thinning rheology decreases (red), increases (green) or has no effect on (yellow) the swimming speed of the swimmer compared to that in a Newtonian fluid, where in some studies multiple effects are uncovered. Studies indicated with an asterisk (*) include both shear-thinning and viscoelastic effects. The papers are split into theoretical and experimental studies and are listed in ascending order with date.

Author	Swimmer type	Study type	Actuation type	Conclusion
Montenegro-Johnson et al. (2013)	Conceptual microswimmers, squirmers, sperm	Theory/numerical	Prescribed flagellar shear angle	🟢
Vélez-Cordero and Lauga (2013)	Infinite waving sheet	Theory/asymptotic analysis	Prescribed sinusoidal travelling waveform	🟡🟢
Li and Ardekani (2015)*	Infinite waving sheet	Theory/numerical	Prescribed sinusoidal travelling waveform	🔴🟢
Riley and Lauga (2017)	Infinite waving filament	Theory	Prescribed sinusoidal travelling waveform	🔴
Demir et al. (2020)	Rigid helical swimmer	Theory/numerical	Prescribed helical beat	🟢
Qin et al. (2021)	Mechanically actuated flexible filaments	Theory	Oscillating magnetic field	🔴🟢
Dasgupta et al. (2013)*	Cylindrical waving sheet	Physical systems	Deformations via mechanically driven rollers	🔴🟢
Gagnon et al. (2014)	*Caenorhabditis elegans*	Living micro-organisms	N/A	🟡
Gómez et al. (2017)	Rigid helical swimmer	Physical systems	Magnetic actuation	🟢
Qu and Breuer (2020)*	*Escherichia coli*	Living micro-organisms	N/A	🟢

Montenegro-Johnson et al. (2012, 2013) developed the 'method of femlets' for modelling various types of swimmers within shear-thinning fluids. This numerical technique involved representing swimmers through a distribution of concentrated regularised forces of unknown strength and direction. The surrounding fluid flow was solved for using the finite element method over a body-fitted mesh, in conjunction with the unknown forces. Montenegro-Johnson et al. (2012, 2013) considered two-dimensional fluid dynamics and swimmers, and explored the effect of shear-thinning rheology on squirmers (spherical swimmers driven by tangential deformations at their surface), sperm-like swimmers and the Najafi-Golestanian conceptual microswimmer (three co-linear spheres exhibiting periodic sliding motion). In all cases, the fluid was modelled via the BCC4p constitutive law (termed 'Carreau' in these works).

Focusing here on results for sperm, (Montenegro-Johnson et al., 2012) found that for a cell with a prescribed gait specified via a prescribed flagellar tangent angle, shear-thinning rheology enhances propulsion compared to swimming in a Newtonian fluid. Further to this, this effect persists across various cell morphologies, with cells with a particular prescribed flagellar beat but various head morphologies always enhanced by shear-thinning rheology (Montenegro-Johnson et al., 2013). Montenegro-Johnson et al. (2013) also noted that sperm cells in shear-thinning fluids generate a thinned corridor of fluid surrounding the cell where viscosity is reduced. This effect also results in a gradient of thick to thin fluid across the flagellum, leading to a flattening of swimming trajectories and an increase in swimming speed.

To explore waving flagellar motion and ciliary transport via metachronal waves in shear-thinning fluids, Vélez-Cordero and Lauga (2013) examined the effect of shear-dependent viscosity on the propulsion of an infinite two-dimensional waving sheet. Using a scaling argument, Vélez-Cordero and Lauga (2013) demonstrated that small-amplitude oscillations of the sheet in a BCC4p fluid result in approximately identical net flow in the Newtonian and shear-thinning cases at leading order. At the next non-trivial order, non-Newtonian effects come into operation. Vélez-Cordero and Lauga (2013) displayed that for a sheet deforming in the directions parallel and perpendicular to the direction of the wave (an extensible sheet), shear-thinning rheology results in a non-zero flow induced in the far field. On the other hand,

for an inextensible sheet, the non-Newtonian contribution to the flow is again zero. Vélez-Cordero and Lauga (2013) demonstrated that in a shear-thinning fluid, the rate of work of the swimmer is always reduced. Therefore Vélez-Cordero and Lauga (2013) showed that for a flagellum, which is inextensible, shear-thinning rheology has no effect on swimming speed, although it does decrease rate of work and correspondingly increase swimmer efficiency. This result is consistent with the experimental observations of Gagnon et al. (2014) for the swimming nematode *C. elegans*, where swimming speed remains unchanged in a shear-thinning and Newtonian fluid. Through comparing the magnitude of the shear-thinning contributions with past work on viscoelastic fluids, Vélez-Cordero and Lauga (2013) also suggested that shear-dependent viscosity is likely more important than fluid elasticity in modifying propulsion.

Dasgupta et al. (2013) experimentally investigated the combined effects of viscoelasticity and shear-thinning rheology on the velocity of a cylindrical sheet. The sheet represents a cylindrical version of the infinite two-dimensional waving sheet problem, with propagating waves travelling across the sheet in the azimuthal direction (similar to Figure 1.6a). For a sheet immersed in a Newtonian fluid, calculations are consistent with theoretical computations using the Stokes flow equations. In the case of a Boger fluid, which displays viscoelastic properties but minimal shear-thinning effects, Dasgupta et al. (2013) observe an increase in swimming speed compared to the Newtonian case. In contrast, measurements in shear-thinning viscoelastic fluids lead to a reduction in swimming speeds.

This relationship between fluid elasticity and swimming velocity is in stark contrast to the theoretical predictions of Lauga (2007), namely the proposed swimming speed ratio given in equation (1.45). However, Dasgupta et al. (2013) note a qualitative similarity in the shear-thinning viscoelastic case. The results of Dasgupta et al. (2013) for both fluid types are, nevertheless, consistent with previous observations. These include the enhanced propulsion of rigid helical swimmers in viscoelastic fluids observed by Liu et al. (2011), and the decrease in swimming velocity of *C. elegans* in shear-thinning viscoelastic carboxymethylcellulose witnessed by Shen and Arratia (2011).

Returning to theoretical observations as well as the infinite two-dimensional waving sheet

problem, Li and Ardekani (2015) numerically explored the effects of both shear-thinning rheology and viscoelasticity on swimmers of this type. For arbitrary prescribed beat amplitude, Li and Ardekani (2015) demonstrated that both swimming speed and power consumption decrease with increasing Deborah number in a viscoelastic fluid. In the purely shear-thinning fluid case, speed enhancements are observed, the magnitude of which depend on the beat frequency and the amplitude of oscillation.

Li and Ardekani (2015) also considered the combined effects of viscoelasticity and shear-thinning rheology, finding that including the presence of both fluid properties always hinders propulsion. The fluid in this case was modelled via the Giesekus constitutive relation (Giesekus, 1982). In this case, while the solvent contribution to the deviatoric stress tensor is given by $\boldsymbol{\tau}^s = 2\beta_s\boldsymbol{\varepsilon}$, the polymer contribution satisfies

$$\boldsymbol{\tau}^p + \mathrm{De}\overset{\triangledown}{\boldsymbol{\tau}^p} + \frac{De\,\alpha}{1-\beta_s}[\boldsymbol{\tau}^p]^2 = 2[1-\beta_s]\boldsymbol{\varepsilon}, \tag{1.49}$$

where $\beta_s = \mu_s/\mu_p$, which is also equal to the ratio between the infinite and zero shear rate viscosities of the fluid. The parameter α represents the anisotropic drag exerted by the solute molecules on the polymer molecules, with $\alpha = 0$ reducing the problem to that of the Oldyrold-B equations. Finally, Li and Ardekani (2015) considered the BCC4p constitutive law so that $\boldsymbol{\tau} = 2\beta_e(\dot{\gamma})\boldsymbol{\varepsilon}$ where β_e is given by the dimensionless form of the BCC4p equation (1.14).

Many studies of non-Newtonian swimming, including the works of Montenegro-Johnson et al. (2012, 2013), consider two-dimensional fluid dynamics due to the computational expense of solving problems concerning three-dimensional non-linear fluids. However, it has since been shown that failing to account for out-of-plane effects when calculating fluid shear rate is inaccurate, which in turn has a significant effect on computations performed with shear-dependent viscosity.

Montenegro-Johnson et al. (2016) first demonstrated the origin of this shear rate error for the case of Newtonian fluids. Using a mixture of experimental and numerical techniques, the flow field and kinematics of *C. elegans* were extracted over a two-dimensional slice at the

swimmers' midplane. The extracted velocity derivatives allow for the calculation of the two-dimensional shear rate via the expression

$$\dot{\gamma}_{2D} = \left[2\frac{\partial u}{\partial x}^2 + \left[\frac{\partial u}{\partial y} + \frac{\partial v}{\partial x} \right]^2 + 2\frac{\partial v}{\partial y}^2 \right]^{1/2}. \tag{1.50}$$

Alternatively, the three-dimensional shear rate can be calculated via

$$\dot{\gamma}_{3D} = \left[2\frac{\partial u}{\partial x}^2 + 2\frac{\partial v}{\partial y}^2 + 2\frac{\partial w}{\partial z}^2 + \left[\frac{\partial u}{\partial y} + \frac{\partial v}{\partial x} \right]^2 + \left[\frac{\partial u}{\partial z} + \frac{\partial w}{\partial x} \right]^2 + \left[\frac{\partial v}{\partial z} + \frac{\partial w}{\partial y} \right]^2 \right]^{1/2}, \tag{1.51}$$

where u, v and w are the x, y and z components of the fluid velocity. Due to the additional non-negative terms in $\dot{\gamma}_{3D}$, it is clear that by definitition $\dot{\gamma}_{3D} \geq \dot{\gamma}_{2D}$. Consequently, it follows that two-dimensional flow fields will always underestimate the true three-dimensional value of the shear rate. Through the assumption of planar kinematics and fluid incompressibility, the three-dimensional shear rate can be written in terms of known planar derivatives via

$$\dot{\gamma}_{3D} = \left[2\frac{\partial u}{\partial x}^2 + 2\frac{\partial v}{\partial y}^2 + \left[\frac{\partial u}{\partial y} + \frac{\partial v}{\partial x} \right]^2 + \left[\frac{\partial u}{\partial v} + \frac{\partial v}{\partial y} \right]^2 \right]^{1/2}, \tag{1.52}$$

and can thus be calculated from two-dimensional experimental data.

In the Newtonian case, Montenegro-Johnson et al. (2016) found that calculating $\dot{\gamma}_{2D}$ compared to $\dot{\gamma}_{3D}$ results in a relative error of between 25–40%. Gagnon and Montenegro-Johnson (2018) further showed that failing to account for the out-of-plane effects for *C. elegans* in a shear-thinning fluid results in an overestimate of fluid viscosity surrounding the swimmer, and consequently, an overestimate of the power that the swimmer expends. In particular, Gagnon and Montenegro-Johnson (2018) found that for a nemotode the relative error in the power depends linearly on the shear-thinning index of the fluid n via

$$\frac{P_{3D} - P_{2D}}{P_{3D}} \approx [n-1] \left[\frac{\dot{\gamma}_{3D}}{\dot{\gamma}_{2D}} - 1 \right], \tag{1.53}$$

which is valid for *C. elegans* assuming $\mu_0 \gg \mu_\infty$ and $\lambda\dot{\gamma} \gg 1$.

The results of Montenegro-Johnson et al. (2016) and Gagnon and Montenegro-Johnson (2018) demonstrate the importance of including out-of-plane derivatives for accurate calculations of shear rate. This conclusion motivates both fully three-dimensional computational approaches to swimming problems and the advancement of experimental techniques for capturing out-of-plane flow quantities.

Returning to further studies of swimming in shear-thinning fluids, Riley and Lauga (2017) adapted Newtonian resistive-force-theory to study the locomotion of slender filaments within shear-thinning fluids. Modelling the fluid using the BCC4p constitutive law, Riley and Lauga (2017) proposed a correction term of the form

$$R_C = \left[1 + [\lambda \dot{\gamma}_{\text{avg}}]^2\right]^{\frac{n-1}{2}}. \tag{1.54}$$

Here, λ denotes the relaxation time of the fluid, n the shear-thinning index and $\dot{\gamma}_{\text{avg}}$ the average local shear rate, given for a filament of radius a via

$$\dot{\gamma}_{\text{avg}} = \frac{\sqrt{C_N^2 U_N^2 + 2C_T^2 U_T^2}}{2\sqrt{2}a\pi\mu_0}, \tag{1.55}$$

where μ_0 is the zero-shear-rate viscosity. Riley and Lauga (2017) demonstrated that the proposed shear-thinning resistive-force-theory is consistent with the Newtonian version if $n = 1$ or $\lambda = 0$. Using this approach, Riley and Lauga (2017) further illustrated that the swimming speed of an undulatory swimmer is systematically lowered in a shear-thinning fluid compared to a Newtonian fluid.

Further experimental studies, conducted by Gómez et al. (2017), explored the effect of shear-thinning rheology on helical swimmers. Gómez et al. (2017) constructed a synthetic swimmer, consisting of a rigid cylindrical head attached to a stiff helical tail, actuated via an external rotating magnetic field. Gómez et al. (2017) considered four non-Newtonian fluids, those behaviour could be fitted to a power law model (see equation (1.13)), with shear-rates within $0.1 < \dot{\gamma} < 100\,\text{s}^{-1}$, power law indices $0.47 < n < 0.83$ and consistency indices $0.321 < K < 3.979\,\text{Pa s}^n$. Gómez et al. (2017) noted that in both the Newtonian and shear-

thinning cases, the speed of the swimmer scales linearly with the actuation frequency of the swimmer. Gómez et al. (2017) revealed that the ratio U/U_N is always greater than one and varies as a function of the shear-thinning index n. Whilst the swimming speed increases from $n = 1$ to reach a peak at $n \approx 0.6$, it then decreases as n increases further, though never falling below the Newtonian swimming rate.

To explore why shear-thinning rheology leads to increased propulsion, Gómez et al. (2017) explored four distinct mechanisms. Via further experiments and simple scaling arguments, Gómez et al. (2017) ruled out swimming enhancement being a result of the impact of the head, the consequence of a wake, or the effect of contrast between viscosities across the head and tail. Gómez et al. (2017) instead proposed that the enhancement is due to a confinement-like effect, in which swimmers propel faster when contained within a region of low viscosity fluid, surrounded by a region of high viscosity fluid. This confinement effect was also uncovered in studies by Li and Ardekani (2015), Man and Lauga (2015) and Demir et al. (2020).

For rigid helical swimmers, Demir et al. (2020) demonstrated using theoretical and computational analysis that the speed enhancement reported by Gómez et al. (2017) is caused by shear-thinning rheology alone. In particular, the magnitude of the observed enhancement can be considerably more significant than the equivalent increase due to viscoelasticity (Liu et al., 2011; Spagnolie et al., 2013), indicating that modelling shear-thinning rheology is crucial in understand locomotion of microswimmers through non-Newtonian fluids.

Recent observations by Qu and Breuer (2020) have provided insight into the behaviour of the bacterium *E. coli* in fluids exhibiting both viscoelastic and shear-thinning properties. Exploring the relationship between swimming speed and fluid viscosity, Qu and Breuer (2020) find that whilst in the Newtonian case swimming speed decreases with viscosity, in the non-Newtonian case, it can lead to speed enhancements. For high viscosities, enhanced swimming is observed in non-Newtonian fluids compared to Newtonian media. Qu and Breuer (2020) infer that these improvements are due to shear-thinning effects rather than viscoelasticity.

Whilst the theoretical studies discussed previously have featured a prescribed swimming gait, the effect of swimmer elasticity on propulsion in shear-thinning fluids was explored re-

cently by Qin et al. (2021). Qin et al. (2021) augmented the resistive-force-theory approach developed by Riley and Lauga (2017) to explore how flexible, magnetically actuated filaments progress in shear-thinning media. In particular, they modelling the elasticity of the filament via an Euler-Bernoulli beam model with a prescribed energy functional (Landau and Lifshitz, 1986). Qin et al. (2021) demonstrated that shear-thinning rheology could either enhance or hinder propulsion, depending on an intricate balance between elastic and viscous forces in the problem, as well as the strength of actuation.

In this section, we have reviewed the literature surrounding swimming in shear-thinning fluids. Similarly to the viscoelastic case, shear-thinning rheology has been shown both experimentally and theoretically to have a substantial effect on the propulsion of microswimmers including infinite waving sheets/filaments (Vélez-Cordero and Lauga, 2013; Li and Ardekani, 2015; Riley and Lauga, 2017), helical swimmers (Gómez et al., 2017; Demir et al., 2020), undulatory swimmers (Gagnon et al., 2014; Qin et al., 2021) and spermatozoa (Montenegro-Johnson et al., 2013). Whether propulsion is enhanced or hindered in a shear-thinning fluid compared to a Newtonian fluid depends on the type of swimmer, swimming gait, and whether viscoelasticity effects are also included. For human sperm, studies in two-dimensional shear-thinning fluids indicate that shear-thinning rheology aids propulsion (Montenegro-Johnson et al., 2013; Gagnon and Montenegro-Johnson, 2018). However, the importance of three-dimensional fluid dynamics in the calculations of shear rate has also been demonstrated (Montenegro-Johnson et al., 2016), motivating the need for further study of sperm in three-dimensional shear-thinning fluids. In viscoelastic fluids, swimmer elasticity has been shown to have a substantial effect on whether swimming is enhanced or hindered compared to a Newtonian fluid (Riley and Lauga, 2014; Thomases and Guy, 2014, 2017). This effect has been comparatively under-explored in shear-thinning fluids, although it has been demonstrated that the elastic properties of flexible filaments in shear-thinning fluids can alter the swimmers propulsive properties (Qin et al., 2021). The effect of flagellar elasticity has not be explored for human sperm, despite the fact that it has been demonstrated that non-Newtonian fluids have a significant effect on the development of the flagellar waveform (Katz et al., 1978, 1981; Suarez and Dai, 1992; Hyakutake

et al., 2019) (see Figure 1.4 of Section 1.2.3). Therefore, in this thesis, we develop a method for modelling human sperm with flexible elastic flagella in three-dimensional shear-thinning fluids (see Chapter 3). In particular, we aim to propose a technique that is both computational efficient and extensible, so that simulations can be performed rapidly despite the three-dimensional nature of the fluid, and so that the method can potentially be extended in the future to model other swimmers/fluid types. We then use this method in Chapter 4 of this thesis to explore the effect of shear-thinning rheology on waveform development and propulsion of human sperm. An understanding of the role of shear-thinning rheology in sperm propulsion is likely relevant when designing artificial microswimmers and understanding how sperm cells adapt to swim in complex environments.

1.6 Overview of this thesis

In this thesis, we begin by focusing on Newtonian fluid dynamics. In Chapter 2, we study the effect of the mechanically inactive flagellar end piece on the propulsive effectiveness of human spermatozoa in fluids obeying the Stokes flow equations (1.8), as proposed in Section 1.2. We find that an inactive distal region enhances propulsion, through elastohydrodynamic modelling of human sperm with and without a passive end piece. In particular, we demonstrate an increase in both swimming speed and efficiency for cells with an inactive region compared to fully-active cells. We also examine the effect of the end piece on the development of the flagellar waveform, and we observe that the presence of the inactive region produces waveforms much more reminiscent of experimental data than the waveforms of fully-active cells. Following this, we discuss potential implications in terms of both evolutionary biology and clinical assessment.

In Chapter 3, we focus on the dynamics of sperm in non-Newtonian fluids. Specifically, we develop a numerical method to enable three-dimensional modelling of a sperm cell with a flexible elastic flagellum in a shear-thinning fluid. This approach, named the hybrid approach for non-linear swimming (HANS), utilises both the method of regularised stokeslets (Cortez, 2001)

and the finite element method (FEM) to solve three-dimensional fluid problems over a coarse non-body-fitted discretisation of the fluid domain. We begin by formulating the finite element method for the generalised-Newtonian fluid flow equations in the absence of immersed forces (in the absence of a swimmer driving the flow). This allows us to demonstrate the derivation and implementation of the FEM for flows of this type in the simplest possible case. We then discuss the implementation of the hybrid method for a single point force embedded within the generalised-Newtonian fluid domain. Finally, we extend the method to model sperm-like swimmers within shear-thinning fluids via combining the hybrid method with the elastohydrodynamic model derived in Chapter 2. We discuss the numerical implementation of this approach and provide convergence results.

In Chapter 4, we utilise the methods developed in Chapter 2 and Chapter 3 to study the effect of shear-thinning rheology on the propulsion of flexible elastic sperm-like swimmers. We uncover that shear-thinning rheology tends to hinder progress of cells with flexible flagella, with reductions in both swimming speed and efficiency observed, compared to swimming in a Newtonian fluid with the same zero shear-rate viscosity. However, propulsion can also be enhanced, depending on a balance of fluid and swimmer properties. We also find that the incorporation of shear-thinning effects enables predictions of flagellar waveforms that more closely correspond to experimental observations of human sperm in mucus analogues. We demonstrate that in the absence of swimmer elasticity, shear-thinning rheology always aids the propulsion of human sperm. Thus we suggest that the mechanism by which the propulsion of cells with flexible flagella tends to be hindered in a shear-thinning fluid is via shape changes due to the fluid-flagellum interactions, resulting in the development of sub-optimal waveforms for progression. Finally, exploring the combined effect of shear-thinning rheology and the inactive end piece, we find that whilst the end piece enhances propulsion for Newtonian and weakly shear-thinning fluids, this effect is reversed in strongly-shear thinning fluids. In all cases, we explore the potential mechanisms behind these changes as well as the possible implications.

A summary of our methodology and findings is provided in Chapter 5. We also discuss

future extensions and applications for the methods developed during this thesis.

Chapter 2

The flagellar end piece enhances the propulsive effectiveness of human spermatozoa

2.1 Introduction

In the discussion of the internal structure of the flagellum in Section 1.2, we noted the presence of the end piece, a region occupying the most distal $3 - 7\,\mu$m of the human sperm flagellum. An early recording of the existence of the end piece was provided by Gray (1955), who observed a portion of very thin filament when studying sea-urchin sperm. Recent experimental observations using cryo-electron tomography have shown that the internal structure of the end piece consists of disorganised singlet microtubules only (Zabeo et al., 2019), unlike in the rest of the flagellum, where the interior consists of the 9+2 axoneme structure. In the 9+2 axoneme, bending is produced through the extension, binding and detaching of molecular motors called dyneins between neighbouring microtubule pairs, as outlined previously in Section 1.2. The end piece, with its disorganised structure and lack of microtubule pairs, likely lacks the presence of dyenins and is therefore unlikely to be a site of molecular motor activity. The hypothesis that the end piece does not produce active bending like the majority of the flagellum forms the basis for our study in this chapter.

While the end piece can be observed through transmission electron and atomic force microscopy (Fawcett, 1975; Ierardi et al., 2008; Lin and Nicastro, 2018), live imaging of the region is is currently challenging due to the thinness of the depleted axoneme structure. Further-

more, because the end piece has been primarily considered not to have a role in propelling the cell, it has received relatively little attention. However, the presence of the end piece has been shown to have a significant effect on flagellar waveform towards the distal end. In particular, both experimental and numerical results show an apparent 'end effect' for cells where the end piece has been removed (Omoto and Brokaw, 1982). Whilst cells where the end piece is present exhibit a flagellar waveform which smoothly propagates off the end of the flagellum when observed over time, cells with the distal region removed demonstrate a rapid 'unbending of bends' that reach the distal end of the flagellum, that is, a reduction in amplitude and curvature of the flagellum towards the distal end.

The sperm flagellar waveform can have a significant impact on propulsion (Gallagher et al., 2019a). Moreover, changes to the waveform have an essential role in enabling cells to penetrate the highly viscous cervical mucus encountered in internal fertilisation (Smith et al., 2009b). Since the presence of the end piece can alter the flagellar waveform, it, therefore, seems likely that in turn it may affect propulsion.

In this chapter, we explore how the mechanically inactive region at the distal end of the sperm flagellum affects the cell's progressive motion in a Newtonian fluid. We achieve this through elastohydrodynamic modelling of human-like sperm via an extension of the framework proposed by Hall-McNair et al. (2019) for modelling passive and active slender filaments in Stokes flow. Along with the inclusion of the inactive end piece, we consider the addition of the ellipsoidal sperm head, as well as varying elastic stiffness across the flagellum, chosen to model the fibrous sheath surrounding the internal axoneme structure. Through comparing simulations of fully active cells (those with a flagellum that is actuated across the entire length) with those with an inactive end piece, we show that the presence of an inactive distal region confers significant advantages to propulsive thrust and swimming efficiency in a Newtonian fluid. Later on, we will also study the effect of the end piece on propulsion in shear-thinning fluids (see Chapter 4).

We note that throughout this study, the flagellum length is fixed, and rather the proportion of the flagellum that is active (and inactive) is altered. This approach differs from previous

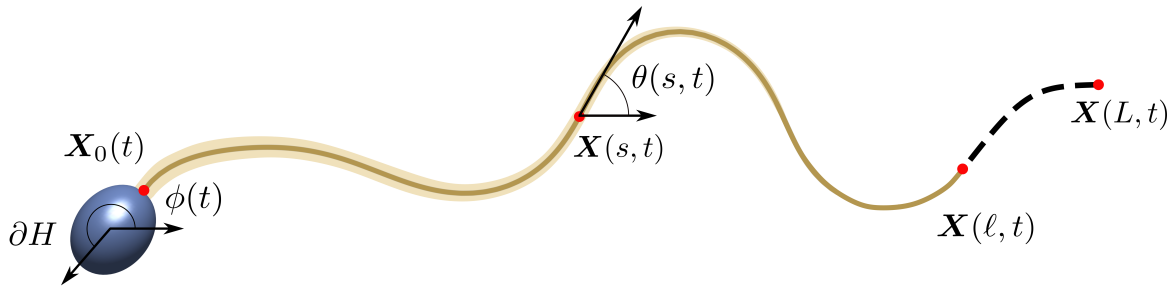


Figure 2.1: A sketch of the model sperm highlighting the position of the centreline $\boldsymbol{X}(s,t)$ (parametrised by arclength $s \in [0,L]$ and tangent angle $\theta(s,t)$), head surface (∂H, blue ellipsoid), head angle ($\phi(t)$), and flagellum/neck junction ($\boldsymbol{X}_0(t)$). The active component of the flagellum ($s \in [0,\ell]$) is shown in dark yellow, with the inactive distal end ($s \in [\ell,L]$) shown black dashed. A tapering fibrous sheath surrounds the flagellum. Image taken from Neal et al. (2020).

work, such as the experimental observations of Omoto and Brokaw (1982), in which the flagellar beat was compared for cells with a full flagellum and those with the end piece removed. We also note that since the end piece is assumed to be un-actuated, we will refer to it as 'inactive', noting that this does not mean it is necessarily ineffective. Correspondingly, the actuated principal piece will be referred to as 'active'.

2.2 Model setup

In this section, we develop a elastohydrodynamic model of a single sperm cell consisting of head and elastic flagellum (see Figure 2.1). The head is modelled as a rigid ellipsoidal surface ∂H, which is connected to the flagellum at the point $\boldsymbol{X}_0(t)$. The flagellum is parametrised by arclength s, where $s = 0$ corresponds to the head-flagellum joint $\boldsymbol{X}_0(t)$, and $s = L$ to the distal tip of the flagellum. In this way, the flagellum can be described via a time-varying curve $\boldsymbol{X}(s,t)$, where the length $s \in [0,\ell]$ will be considered active (representing the principal piece), and the remaining length $s \in [\ell,L]$ will be considered inactive (representing the end piece).

2.2.1 The elastohydrodynamic integral formulation

Since the waveforms of mammalian sperm flagella are approximately planar, especially upon approaching and collecting at surfaces (Woolley, 2003; Gallagher et al., 2018), the shape of the flagellum can be described via the angle between the tangent and the lab frame horizontal, $\theta(s,t)$. In this way, the entire cell can be described via the angle between the head centreline and the lab frame horizontal, $\phi(t)$, and the expression

$$\boldsymbol{X}(s,t) = \boldsymbol{X}_0(t) + \int_0^s [\cos\theta(s',t), \sin\theta(s',t), 0]^T \, ds'. \tag{2.1}$$

Differentiating with respect to time, the flagellar velocity is given by

$$\partial_t \boldsymbol{X}(s,t) = d_t \boldsymbol{X}_0(t) + \int_0^s \partial_t\theta(s',t)[-\sin\theta(s',t), \cos\theta(s',t), 0]^T \, ds'. \tag{2.2}$$

Modelling the head as undergoing rigid body motion about $\boldsymbol{X}_0(t)$ and applying the no-slip condition $\boldsymbol{u}(\boldsymbol{Y}(t),t) = d_t\boldsymbol{Y}(t)$, the surface velocity of a point on the head $\boldsymbol{Y}(t) \in \partial H$ is given by

$$d_t\boldsymbol{Y}(t) = d_t\boldsymbol{X}_0(t) + d_t\phi(t)\, \boldsymbol{e}_3 \times [\boldsymbol{Y}(t) - \boldsymbol{X}_0(t)]\,, \tag{2.3}$$

where $\boldsymbol{e}_3$ is a unit vector pointing perpendicular to the plane of beating. Equation (2.1) describes the geometry of the flagellum. Equations (2.2) and (2.3) describe the flagellum and head kinematics respectively.

Hydrodynamic model

At very low Reynolds number, neglecting non-Newtonian influences on the fluid, the hydrodynamics of the problem are described by the three-dimensional Stokes flow equations, given in system (1.8). The flow $u_i(\boldsymbol{x},t)$ produced by the flagellum $\boldsymbol{X}(s,t)$ exerting force per unit length $\boldsymbol{f}(s,t)$ on a fluid obeying the Stokes flow equations is given by the line integral $\int_0^L S^\epsilon_{ij}(\boldsymbol{x}, \boldsymbol{X}(s',t)) f_j(s',t)\, ds'$, where $\boldsymbol{S}^\epsilon$ is the regularised stokeslet kernel as given in equation (1.32a). Similarly, the flow due to the surface of the sperm head ∂H, exerting force per unit

area $\Phi(\boldsymbol{Y},t)$ for $\boldsymbol{Y}\in\partial H$, is given by the surface integral $\iint_{\partial H} S^{\epsilon}_{ij}(\boldsymbol{x},\boldsymbol{Y})\Phi_j(\boldsymbol{Y})\,dS_Y$. Thus the full boundary integral equation (Smith, 2009) for the hydrodynamics is given by

$$u_i(\boldsymbol{x},t)=\int_0^L S^{\epsilon}_{ij}(\boldsymbol{x},\boldsymbol{X}(s',t))f_j(s',t)\,ds'+\iint_{\partial H} S^{\epsilon}_{ij}(\boldsymbol{x},\boldsymbol{Y})\Phi_j(\boldsymbol{Y},t)\,dS_Y, \tag{2.4}$$

from which we have expressions for the velocity of points on the flagellum $\boldsymbol{X}(s,t)$ and head $\boldsymbol{Y}(t)$, given by

$$\partial_t X_i(s,t)=\int_0^L S^{\epsilon}_{ij}(\boldsymbol{X}(s,t),\boldsymbol{X}(s',t))f_j(s',t)\,ds'+\iint_{\partial H} S^{\epsilon}_{ij}(\boldsymbol{X}(s,t),\boldsymbol{Y})\Phi_j(\boldsymbol{Y},t)\,dS_Y, \tag{2.5}$$

and

$$d_t Y_i(t)=\int_0^L S^{\epsilon}_{ij}(\boldsymbol{Y}(t),\boldsymbol{X}(s',t))f_j(s',t)\,ds'+\iint_{\partial H} S^{\epsilon}_{ij}(\boldsymbol{Y}(t),\boldsymbol{Y})\Phi_j(\boldsymbol{Y},t)\,dS_Y, \tag{2.6}$$

where here we have applied the no-slip conditions $u_i(\boldsymbol{X}(s,t),t)=\partial_t X_i(s,t)$, $u_i(\boldsymbol{Y}(t),t)=d_t Y_i(t)$.

Flagellar elasticity model

Following Hall-McNair et al. (2019), we derive an expression for the elastic behaviour of the flagellum through considering force and moment balance over an infinitesimal segment of the filament. We consider the contact forces and moments, $\boldsymbol{N}(s,t)$ and $M(s,t)$ respectively, exerted by a distal section of the flagellum on a proximal segment (see Figure 2.2). We also consider the addition of an active moment per unit length $m(s,t)$ to model the internal sliding produced by dynein activity.

Since the distal tip of the flagellum is untethered, the boundary conditions at $s=L$ are given by the force and moment free conditions

$$\boldsymbol{N}(L,t)=\boldsymbol{0},\quad M(L,t)=0. \tag{2.7}$$

By considering force balance across the segment, we find that the hydrodynamic force per unit

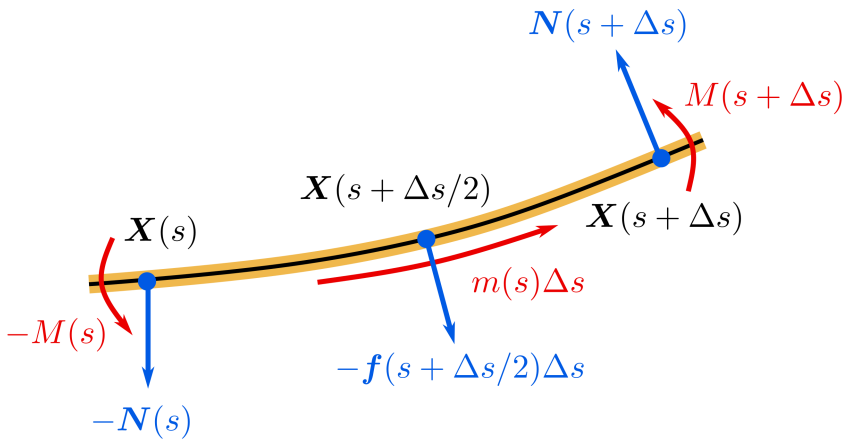


Figure 2.2: The forces and moments acting on a segment of the flagellum of length Δs. Here, $-\boldsymbol{f}(s)$ is the force per unit length exerted by the surrounding fluid onto the flagellum, $m(s)$ is an active moment per unit length and $\boldsymbol{N}(s)$ and $M(s)$ represent contact forces and moments respectively. The dependence on time has been dropped for clarity.

length $\boldsymbol{f}(s,t)$ is related to the contact force via

$$\partial_s \boldsymbol{N}(s,t) = \boldsymbol{f}(s,t). \tag{2.8}$$

Moment balance across the segment yields that

$$\partial_s M(s,t) = -\boldsymbol{e}_3 \cdot \partial_s \boldsymbol{X}(s,t) \times \boldsymbol{N}(s,t) - m(s,t), \tag{2.9}$$

which, through integrating across the distal segment $[s, L]$ and applying the moment boundary condition, leads to

$$M(s,t) = -\boldsymbol{e}_3 \cdot \int_s^L \left[\boldsymbol{X}(s',t) - \boldsymbol{X}(s,t)\right] \times \boldsymbol{f}(s',t) ds' + \int_s^L m(s',t) ds'. \tag{2.10}$$

Constitutively linear elasticity and bending in the xy-plane implies that the contact moment relates to the curvature via

$$M(s,t) = E(s)\partial_s \theta(s,t), \tag{2.11}$$

where $E(s)$ is a varying elastic stiffness function, chosen to model the tapering fibrous sheath surrounding the internal core of the flagellum. The form of this function is given via a modi-

fication of previous work (Gaffney et al., 2011), by

$$E(s) = \begin{cases} E_d[\rho - 1]\left[\frac{s-Ld}{Ld}\right]^2 + E_d & s \leq Ld, \\ E_d & s > Ld, \end{cases} \tag{2.12}$$

where E_d is the stiffness of the distal flagellum (at $s = L$). The dimensionless parameter ρ corresponds to the proximal-distal stiffness ratio, and d corresponds to the proportion of the flagellum over which the stiffness is a varying function. Equating equations (2.10) and (2.11) yields the elasticity integral equation

$$E(s)\,\partial_s\theta(s,t) + \boldsymbol{e}_3 \cdot \int_s^L \big[\boldsymbol{X}(s',t) - \boldsymbol{X}(s,t)\big] \times \boldsymbol{f}(s',t)\,ds' - \int_s^L m(s',t)\,ds' = 0. \tag{2.13}$$

Here, the active moment term $m(s,t)$ can be described to a first approximation by a sinusoidal travelling wave $m(s,t) = m_0\cos(ks - \omega t)$, where k is wavenumber and ω is radian frequency. The inactive end piece can be modelled by taking the product with a Heaviside function, so that $m(s,t) = m_0\cos(ks-\omega t)H(\ell - s)$, where $0 < \ell \leqslant L$ is the length of the active tail segment.

Since we are in an inertialess regime, the entire swimmer must be force and moment free. As such, we also have equations for total force and total moment balance across the cell respectively, given by

$$\int_0^L \boldsymbol{f}(s',t)ds' + \iint_{\partial H} \boldsymbol{\Phi}(\boldsymbol{Y},t)dS_Y = \boldsymbol{0}, \tag{2.14}$$

and

$$\boldsymbol{e}_3 \cdot \int_0^L \big[\boldsymbol{X}(s',t) - \boldsymbol{X}_0(t)\big] \times \boldsymbol{f}(s',t)ds' + \boldsymbol{e}_3 \cdot \iint_{\partial H} [\boldsymbol{Y} - \boldsymbol{X}_0(t)] \times \boldsymbol{\Phi}(\boldsymbol{Y},t)dS_Y = 0. \tag{2.15}$$

Finally, the head-flagellum coupling is enforced via the moment boundary condition

$$E(0)\kappa(0,t) - \boldsymbol{e}_3 \cdot \iint_{\partial H} [\boldsymbol{Y} - \boldsymbol{X}_0(t)] \times \boldsymbol{\Phi}(\boldsymbol{Y},t)dS_Y - \int_0^L m_0\cos(ks' - \omega t)H(\ell - s')\,ds' = 0, \tag{2.16}$$

where $\kappa(0,t)$ is the curvature evaluated at the head-flagellum joint, defined via

$$\kappa(0,t) := \partial_s \theta(0,t). \tag{2.17}$$

Equations (2.1), (2.2), (2.3), (2.5), (2.6), (2.13), (2.14), (2.15) and (2.16) form an elastohydrodynamic integral formulation for the evolution of a sperm cell with an inactive end piece of length $L - \ell$ in Stokes flow. The unknowns of this system are $\boldsymbol{X}_0(t)$, $\phi(t)$, $\theta(s,t)$, $\boldsymbol{f}(s,t)$ and $\Phi(Y,t)$.

2.2.2 Problem non-dimensionalisation

The model equations are non-dimensionalised with respect to characteristic length-scale L, time-scale ω^{-1} and force-scale $\mu\omega L^2$. The elastic stiffness function $E(s)$ is non-dimensionalised with respect to E_d, the distal value of the flagellum stiffness. The full dimensionless system (with dimensionless variables denoted by $\hat{\cdot}$) is given by

$$\begin{aligned}
0 &= \hat{E}(\hat{s})\,\partial_{\hat{s}}\theta(\hat{s},\hat{t}) + \boldsymbol{e}_3 \cdot \mathcal{S}^4 \int_{\hat{s}}^1 \left[\hat{\boldsymbol{X}}(\hat{s}',\hat{t}) - \hat{\boldsymbol{X}}(\hat{s},\hat{t})\right] \times \hat{\boldsymbol{f}}(\hat{s}',\hat{t})\, d\hat{s}' \\
&\quad - \mathcal{M}\mathcal{S}^4 \int_{\hat{s}}^1 \cos(\hat{k}\hat{s}' - \hat{t}) H(\hat{\ell} - \hat{s}')\, d\hat{s}', && \text{(2.18a)} \\
\mathbf{0} &= \int_0^1 \hat{\boldsymbol{f}}(\hat{s}',\hat{t}) d\hat{s}' + \iint_{\partial\hat{H}} \hat{\boldsymbol{\Phi}}(\hat{Y},\hat{t}) dS_{\hat{Y}}, && \text{(2.18b)} \\
0 &= \boldsymbol{e}_3 \cdot \int_0^1 \left[\hat{\boldsymbol{X}}(\hat{s}',\hat{t}) - \hat{\boldsymbol{X}}_0(\hat{t})\right] \times \hat{\boldsymbol{f}}(\hat{s}',\hat{t}) d\hat{s}' \\
&\quad + \boldsymbol{e}_3 \cdot \iint_{\partial\hat{H}} \left[\hat{Y} - \hat{\boldsymbol{X}}_0(\hat{t})\right] \times \hat{\boldsymbol{\Phi}}(\hat{Y},\hat{t}) dS_{\hat{Y}}, && \text{(2.18c)} \\
\partial_{\hat{t}}\hat{X}_i(\hat{s},\hat{t}) &= \int_0^1 S_{ij}^{\hat{\epsilon}}(\hat{\boldsymbol{X}}(\hat{s},\hat{t}), \hat{\boldsymbol{X}}(\hat{s}',\hat{t}))\hat{f}_j(\hat{s}',\hat{t})\, d\hat{s}' + \iint_{\partial\hat{H}} S_{ij}^{\hat{\epsilon}}(\hat{\boldsymbol{X}}(\hat{s},\hat{t}), \hat{Y})\hat{\Phi}_j(\hat{Y},\hat{t})\, dS_{\hat{Y}}, && \text{(2.18d)} \\
\partial_{\hat{t}}\hat{\boldsymbol{X}}(\hat{s},\hat{t}) &= d_{\hat{t}}\hat{\boldsymbol{X}}_0(\hat{t}) + \int_0^{\hat{s}} \partial_{\hat{t}}\theta(\hat{s}',\hat{t})[-\sin\theta(\hat{s}',\hat{t}), \cos\theta(\hat{s}',\hat{t}), 0]^T\, d\hat{s}', && \text{(2.18e)} \\
d_{\hat{t}}\hat{Y}_i(\hat{t}) &= \int_0^1 S_{ij}^{\hat{\epsilon}}(\hat{Y}(\hat{t}), \hat{\boldsymbol{X}}(\hat{s}',\hat{t}))\hat{f}_j(\hat{s}',\hat{t})\, d\hat{s}' + \iint_{\partial\hat{H}} S_{ij}^{\hat{\epsilon}}(\hat{Y}(\hat{t}), \hat{Y})\hat{\Phi}_j(Y,t)\, dS_{\hat{Y}}, && \text{(2.18f)} \\
d_{\hat{t}}\hat{Y}(\hat{t}) &= d_{\hat{t}}\hat{\boldsymbol{X}}_0(\hat{t}) + d_{\hat{t}}\hat{\phi}(\hat{t})\, \boldsymbol{e}_3 \times \left[\hat{Y}(\hat{t}) - \hat{\boldsymbol{X}}_0(\hat{t})\right], && \text{(2.18g)}
\end{aligned}$$

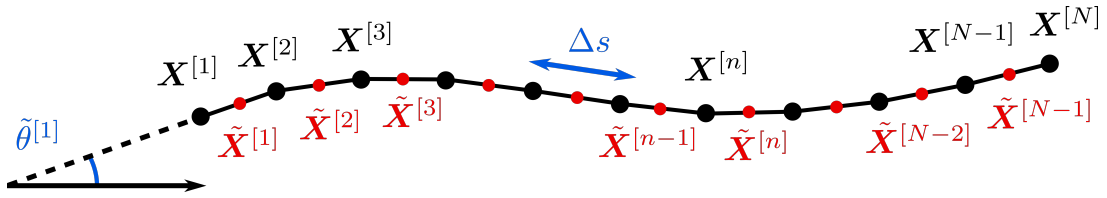


Figure 2.3: Discretisation of the flagellum into $Q = N-1$ straight-line segments of equal length Δs. The end points of each segment are denoted $\{\boldsymbol{X}^{[n]}\}_{n=1}^{N}$, with midpoints $\{\tilde{\boldsymbol{X}}^{[n]}\}_{n=1}^{Q}$ and tangent angles to each segment $\{\tilde{\theta}^{[n]}\}_{n=1}^{Q}$. The dependence on time has been omitted for brevity.

where $0 \leq \hat{s} \leq 1$ and $\hat{t} \geq 0$. Here, $\mathcal{S} = L(\mu\omega/E_d)^{1/4}$ is a dimensionless group comparing viscous and elastic forces (similar to the commonly-used 'sperm number' (Gadêlha et al., 2010; Montenegro-Johnson et al., 2015)), and $\mathcal{M} = m_0/\mu\omega L^2$ is a dimensionless group comparing active and viscous forces. Also, $\hat{\epsilon} = \epsilon/L$ is the dimensionless regularisation parameter, $\hat{\ell} = \ell/L$ is the dimensionless length of the active segment and $\hat{k} = kL$ is dimensionless wavenumber. The function $\hat{E}(\hat{s})$ is the dimensionless form of the stiffness function, defined via

$$\hat{E}(\hat{s}) = \frac{E(s)}{E_d}. \tag{2.19}$$

The dimensionless geometry equation is given via

$$\hat{\boldsymbol{X}}(\hat{s},\hat{t}) = \hat{\boldsymbol{X}}_0(\hat{t}) + \int_0^{\hat{s}} \left[\cos\theta(\hat{s}',\hat{t}), \sin\theta(\hat{s}',\hat{t}), 0\right]^T d\hat{s}'. \tag{2.20}$$

Finally, the dimensionless head-flagellum boundary condition is given by

$$\rho\hat{\kappa}(0,\hat{t}) - \boldsymbol{e}_3 \cdot \mathcal{S}^4 \iint_{\partial\hat{H}} \left[\hat{\boldsymbol{Y}} - \hat{\boldsymbol{X}}_0(\hat{t})\right] \times \hat{\boldsymbol{\Phi}}(\hat{\boldsymbol{Y}},\hat{t}) dS_{\hat{\boldsymbol{Y}}} \\ - \mathcal{M}\mathcal{S}^4 \int_0^1 \cos(\hat{k}\hat{s}' - \hat{t}) H(\hat{\ell} - \hat{s}')\, d\hat{s}' = 0, \tag{2.21}$$

where $\rho = \hat{E}(0)$ is the proximal-distal flagellum stiffness ratio, as defined previously. We drop the dimensionless 'hat' notation in what follows for clarity.

2.2.3 Problem discretisation

Following Hall-McNair et al. (2019), the flagellum is discretised into $Q = N - 1$ straight-line segments of equal length $\Delta s = 1/Q$ (see Figure 2.3), where the arclength at each of the end points is denoted as $s^{[n]}$ for $n = 1, 2, \dots, N$. The coordinates of the end points of the segments are defined by

$$\boldsymbol{X}^{[n]}(t) := \boldsymbol{X}((n-1)\Delta s, t), \quad n = 1, 2, \dots, N, \tag{2.22}$$

where $\boldsymbol{X}^{[1]}(t) := \boldsymbol{X}_0(t)$. The midpoints of each segment are denoted $\left\{\tilde{\boldsymbol{X}}^{[n]}(t)\right\}_{n=1}^{Q}$, where the force per unit length $\left\{\tilde{\boldsymbol{f}}^{[n]}(t)\right\}_{n=1}^{Q}$ on each segment is assumed to be acting at each of these midpoints. The angle connecting the end points $\boldsymbol{X}^{[n]}(t)$ and $\boldsymbol{X}^{[n+1]}(t)$ is denoted $\tilde{\theta}^{[n]}(t)$ for $n = 1, 2, \dots, Q$.

The head terms (integrals over the head surface ∂H) are discretised via the nearest-neighbour method outlined by Gallagher and Smith (2018). This method is implemented by first discretising the head into two sets of nodes $\{\boldsymbol{y}^{[1]}(t), \dots, \boldsymbol{y}^{[M_T]}(t)\}$ and $\{\boldsymbol{Y}^{[1]}(t), \dots, \boldsymbol{Y}^{[M_Q]}(t)\}$, referred to as the traction and quadrature discretisations respectively. The forces over the surface vary much more slowly than the rapidly varying regularised stokeslet kernel. Consequently, the traction discretisation can be much coarser than the quadrature discretisation ($M_T \ll M_Q$), thereby avoiding the construction of an excessively large dense linear system and associated assembly and inversion cost. The nearest-neighbour method is defined via the mapping $\mathcal{N} : \{1, 2, \dots, M_Q\} \to \{1, 2, \dots, M_T\}$ where

$$\mathcal{N}(q) = \arg \min_{m=1,2,\dots,M_T} |\boldsymbol{y}^{[m]}(t) - \boldsymbol{Y}^{[q]}(t)|, \tag{2.23}$$

so that $\Phi_j[\boldsymbol{Y}^{[q]}(t)]dS[\boldsymbol{Y}^{[q]}(t)] \approx \Phi_j(\boldsymbol{y}^{[\mathcal{N}(q)]})dS(\boldsymbol{y}^{[\mathcal{N}(q)]}) =: -\Psi_j^{[\mathcal{N}(q)]}A^{[\mathcal{N}(q)]}$ where $A^{[\mathcal{N}(q)]}$ is a quadrature weighting (Smith, 2018). The nearest-neighbour operator $\mathcal{N}$ can be defined via a

$M_Q \times M_T$ matrix

$$v^{[q,\hat{m}]} = \begin{cases} 1 & \text{if } \hat{m} = \arg\min_{m=1,\dots,M_T} |\boldsymbol{y}^{[m]}(t) - \boldsymbol{Y}^{[q]}(t)|, \\ 0 & \text{otherwise,} \end{cases} \tag{2.24}$$

so that $\Psi_i^{[\mathcal{N}(q)]} A^{[\mathcal{N}(q)]} = \sum_{m=1}^{M_T} v^{[q,m]} \Psi_i^{[m]} A^{[m]}$ (Gallagher and Smith, 2018; Smith, 2018). We may now fully discretise the system (2.18). The elasticity equation (2.18a) becomes

$$\begin{aligned} E(s^{[n+1]}) \left[\frac{\tilde{\theta}^{[n+1]}(t) - \tilde{\theta}^{[n]}(t)}{\Delta s} \right] & \\ + \delta_{i3} \mathcal{S}^4 \sum_{m=n}^{Q-1} \Delta s \varepsilon_{ijk} \left[\tilde{X}_j^{[m+1]}(t) - X_j^{[n+1]}(t) \right] \tilde{f}_k^{[m+1]} & \\ - \mathcal{M} \mathcal{S}^4 \int_{s^{[n+1]}}^{1} \cos(ks' - t) H(\ell - s') ds' = 0, & \end{aligned} \tag{2.25}$$

for $n = 1, 2, \dots, Q-1$, where ε_{ijk} is the Levi-Civita tensor, δ_{ij} is the Kronecker tensor and repeated indices are summed over. The active moment term is calculated analytically.

The total force and total moment balance equations (2.18b) and (2.18c) become

$$\sum_{n=1}^{Q} \Delta s \tilde{f}_i^{[n]}(t) + \sum_{m=1}^{M_T} \Psi_i^{[m]} A^{[m]} \sum_{q=1}^{M_Q} v^{[q,m]} = 0, \tag{2.26}$$

and

$$\delta_{i3} \sum_{n=1}^{Q} \Delta s \varepsilon_{ijk} \left[\tilde{X}_j^{[n]}(t) - X_{0j}(t) \right] \tilde{f}_k^{[n]} + \delta_{i3} \sum_{m=1}^{M_T} \Psi_k^{[m]} A^{[m]} \sum_{q=1}^{M_Q} \varepsilon_{ijk} \left[Y_j^{[q]}(t) - X_{0j}(t) \right] v^{[q,m]} = 0, \tag{2.27}$$

respectively for $i = 1, 2, 3$.

The position of the segment end points is given by the discretised version of the flagellum geometry equation (2.20)

$$\boldsymbol{X}^{[n+1]}(t) = \boldsymbol{X}_0(t) + \sum_{m=1}^{n} \Delta s \left[\cos \tilde{\theta}^{[m]}(t), \sin \tilde{\theta}^{[m]}(t), 0 \right]^T, \quad n = 1, \dots, Q. \tag{2.28}$$

In a similar way, the segment midpoints are given by

$$\tilde{\boldsymbol{X}}^{[n]}(t) = \boldsymbol{X}_0(t) + \sum_{m=1}^{n-1} \left\{ \Delta s \left[\cos\tilde{\theta}^{[m]}(t), \sin\tilde{\theta}^{[m]}(t), 0\right]^T \right\} + \frac{\Delta s}{2} \left[\cos\tilde{\theta}^{[n]}(t), \sin\tilde{\theta}^{[n]}(t), 0\right]^T, \quad (2.29)$$

for $n = 1, \dots, Q$. Through differentiating this equation, we find that flagellum segment midpoint velocities are given by

$$d_t\tilde{\boldsymbol{X}}^{[n]}(t) = d_t\boldsymbol{X}_0(t) + \sum_{m=1}^{n-1} \left\{ \Delta s d_t\tilde{\theta}^{[m]}(t) \left[-\sin\tilde{\theta}^{[m]}(t), \cos\tilde{\theta}^{[m]}(t), 0\right]^T \right\} + \frac{\Delta s}{2} d_t\tilde{\theta}^{[n]}(t) \left[-\sin\tilde{\theta}^{[n]}(t), \cos\tilde{\theta}^{[n]}(t), 0\right]^T, \quad (2.30)$$

for $n = 1, \dots, Q$, which is the discrete form of the flagellum kinematics equation (2.18e). The head kinematics equation (2.18g) becomes

$$d_t\boldsymbol{y}^{[m]}(t) = d_t\boldsymbol{X}_0(t) + d_t\phi(t)\boldsymbol{e}_3 \times [\boldsymbol{y}^{[m]}(t) - \boldsymbol{X}_0(t)], \quad (2.31)$$

for $m = 1, \dots, M_T$. The discretised hydrodynamics equations (2.18d) and (2.18f) are given by

$$d_t\tilde{X}_i^{[n]}(t) = \sum_{m=1}^{Q} I_{ij}^{[m]}\left(\tilde{\boldsymbol{X}}^{[n]}, t\right) \tilde{f}_j^{[m]}(t) + \sum_{m=1}^{M_T} \Psi_j^{[m]} A^{[m]} \sum_{q=1}^{M_Q} S_{ij}^{\epsilon}\left(\tilde{\boldsymbol{X}}^{[n]}, \boldsymbol{Y}^{[q]}\right) v^{[q,m]}, \quad (2.32)$$

for $n = 1, \dots, Q$, and

$$d_t y_i^{[m]}(t) = \sum_{n=1}^{Q} I_{ij}^{[n]}\left(\boldsymbol{y}^{[m]}, t\right) \tilde{f}_j^{[n]}(t) + \sum_{n=1}^{M_T} \Psi_j^{[n]} A^{[n]} \sum_{q=1}^{M_Q} S_{ij}^{\epsilon}\left(\boldsymbol{y}^{[m]}, \boldsymbol{Y}^{[q]}\right) v^{[q,n]}, \quad (2.33)$$

for $m = 1, \dots, M_T$ respectively, where

$$I_{ij}^{[n]}(\boldsymbol{x}, t) := \int_{(n-1)\Delta s}^{n\Delta s} S_{ij}^{\epsilon}\left(\boldsymbol{x}, \tilde{\boldsymbol{X}}^{[n]}(t) + [s' - \tilde{s}^{[n]}]\left[\cos\theta(\tilde{s}^{[n]}, t), \sin\theta(\tilde{s}^{[n]}, t), 0\right]^T\right) ds', \quad (2.34)$$

which can be calculated analytically (Smith, 2009; Hall-McNair et al., 2019).

The curvature at the head-flagellum joint $\kappa(0,t) = \partial_s\theta(0,t)$ is approximated through a

backwards finite difference approximation between the angle of the first flagellum segment $\tilde{\theta}^{[1]}(t)$ and the head angle $\phi(t)$, i.e. via

$$\kappa(0,t) \approx \frac{\tilde{\theta}^{[1]}(t) - \phi(t)}{\Delta s}. \tag{2.35}$$

In this way, the discrete form of the moment boundary condition at the head-flagellum joint (2.21) is given by

$$\rho \left[\frac{\tilde{\theta}^{[1]}(t) - \phi(t)}{\Delta s} \right] - \delta_{i3} \mathcal{S}^4 \sum_{m=1}^{M_T} \Psi_k^{[m]} A^{[m]} \sum_{q=1}^{M_Q} \varepsilon_{ijk} \left[Y_j^{[q]}(t) - X_{0\,j}(t) \right] v^{[q,m]} - \mathcal{M} \mathcal{S}^4 \int_0^1 \cos(ks' - t) H(\ell - s') ds' = 0. \tag{2.36}$$

Equating equations (2.30) and (2.32), along with equations (2.31) and (2.33) eliminates $\left\{ d_t \tilde{\boldsymbol{X}}^{[n]}(t) \right\}_{n=1}^{Q}$ and $\left\{ d_t \boldsymbol{y}^{[m]}(t) \right\}_{m=1}^{M_T}$ from the system. We can also eliminate $\{\boldsymbol{X}^{[n]}(t)\}_{n=1}^{N}$ and $\left\{ \tilde{\boldsymbol{X}}^{[n]}(t) \right\}_{n=1}^{Q}$ through the use of equations (2.28) and (2.29) respectively. The resulting system is linear in the unknowns $d_t \boldsymbol{X}_0(t)$, $\phi(t)$, $d_t \tilde{\theta}^{[1]}(t), \ldots, d_t \tilde{\theta}^{[Q]}(t)$, $\tilde{\boldsymbol{f}}^{[1]}(t), \ldots, \tilde{\boldsymbol{f}}^{[Q]}(t)$, and $\boldsymbol{\Psi}^{[1]}(t), \ldots, \boldsymbol{\Psi}^{[M_T]}(t)$.

Linear system

Given an initial discrete configuration of the cell

$$\boldsymbol{Z}_0 = \left[\boldsymbol{X}_0(0), \phi(0), \tilde{\theta}^{[1]}(0), \tilde{\theta}^{[2]}(0), \ldots, \tilde{\theta}^{[Q]}(0) \right]^T, \tag{2.37}$$

the full system can be expressed as an initial value problem

$$d_t \boldsymbol{Z} = \mathcal{F}(\boldsymbol{Z}, t), \quad \boldsymbol{Z}(0) = \boldsymbol{Z}_0, \tag{2.38}$$

where $\boldsymbol{Z}(t) := \left[\boldsymbol{X}_0(t), \phi(t), \tilde{\theta}^{[1]}(t), \tilde{\theta}^{[2]}(t), \ldots, \tilde{\theta}^{[Q]}(t) \right]^T$. Augmenting the problem with a vector of unknown head forces $\boldsymbol{\Psi}$, and unknown flagellum forces $\tilde{\boldsymbol{f}}$, yields a linear system to solve at

each timestep, given by

$$\mathrm{A}\begin{bmatrix} d_t Z \\ \boldsymbol{\Psi} \\ \tilde{\boldsymbol{f}} \end{bmatrix} = \boldsymbol{c}, \tag{2.39}$$

where

$$\mathrm{A} = \left[\begin{array}{c|c} 0 & \mathrm{A}_E \\ \hline \mathrm{A}_K & \mathrm{A}_H \end{array}\right], \tag{2.40}$$

$$\boldsymbol{c} = \left[0, \rho\left[\frac{\tilde{\theta}^{[1]}(t) - \phi(t)}{\Delta s}\right] - \Lambda^{[1]}(t), E\left(s^{[2]}\right)\left[\frac{\tilde{\theta}^{[2]}(t) - \tilde{\theta}^{[1]}(t)}{\Delta s}\right] - \Lambda^{[2]}(t), \dots, E\left(s^{[Q]}\right)\left[\frac{\tilde{\theta}^{[Q]}(t) - \tilde{\theta}^{[Q-1]}(t)}{\Delta s}\right] - \Lambda^{[Q]}(t), 0, 0, 0, \dots, 0\right]^T. \tag{2.41}$$

The matrix blocks A_E, A_K and A_H encode the elastics, kinematics and hydrodynamics of the system respectively. The block form of the system is the same as in Hall-McNair et al. (2019), however additionally A_E includes varying elastic stiffness, the modified actuation function, and the head-flagellum boundary condition. Also A_K incorporates the head kinematics and A_H the head hydrodynamics. The first component of the vector $\boldsymbol{c}$ corresponds to moment balance over the whole cell (equation (2.27)). The next component corresponds to the enforcement of the discrete form of the moment boundary condition at the head-flagellum joint (equation (2.36)), where

$$\Lambda^{[q]}(t) = \mathcal{M}\mathcal{S}^4 \int_{s^{[q]}}^{1} \cos(ks' - t) H(\ell - s') ds'. \tag{2.42}$$

The subsequent $Q - 1$ entries of the vector $\boldsymbol{c}$ correspond to moment balance about each interior flagellum joint (equation (2.25)). We then have the 2 entries corresponding to total force balance (equation (2.26)) in the x and y directions. The final $3Q + 3M_T$ zeros relate to equating the kinematic and hydrodynamic velocities for the flagellum and head points respectively (equating (2.30) and (2.31) with (2.32) and (2.33) respectively).

In this way, A is a $(Q + 3 + 3(Q + M_T)) \times (Q + 3 + 3(Q + M_T))$ matrix, $\boldsymbol{c}$ is a column vector of size $Q+3+3(Q+M_T)$, as is the vector of unknowns. Thus, given initial values $\boldsymbol{X}_0(0)$, $\{\tilde{\theta}^{[n]}(0)\}_{n=1}^{Q}$ and $\phi(0)$, the system can be solved at every time step using the MATLAB® backslash command '\', with $d_t\boldsymbol{Z}$ integrated using the built in MATLAB® function `ode23tb`. This stiff ODE solver has been chosen rather than a non-stiff solver such as `ode45` since it is more efficient in terms of computational time. This indicates that the problem does in fact exhibit some stiffness, as reported previously by Hall-McNair et al. (2019) when modelling filaments in Stokes flow using similar techniques. At any point in time, the sperm cell's position and shape can be reconstructed completely from $\boldsymbol{X}_0(t)$, $\{\tilde{\theta}^{[n]}(t)\}_{n=1}^{Q}$ and $\phi(t)$ through the discrete geometry equation (2.28) and the construction of the head from the point $\boldsymbol{X}_0(t)$ and angle $\phi(t)$.

2.3 Results

The impact of the length of the inactive end piece on propulsion is quantified by calculating the swimming speed and efficiency of simulated sperm cells. *Velocity Along a Line* (VAL) is used as a measure of swimming speed, calculated via

$$\mathrm{VAL}^{(j)} = \frac{|\boldsymbol{X}_0^{(j)} - \boldsymbol{X}_0^{(j-1)}|}{T}, \tag{2.43}$$

where $T = 2\pi$ is the period of the driving wave and $\boldsymbol{X}_0^{(j)}$ represents the position of the head-flagellum joint after j periods. *Lighthill Efficiency* (Lighthill, 1975) is calculated as

$$\eta^{(j)} = \frac{\left[\mathrm{VAL}^{(j)}\right]^2}{\overline{W}^{(j)}}, \tag{2.44}$$

where $\overline{W}^{(j)} = \left\langle \int_0^1 \boldsymbol{u} \cdot \boldsymbol{f} ds' + \iint_{\partial H} \boldsymbol{u}(\boldsymbol{Y}) \cdot \boldsymbol{\Phi}(\boldsymbol{Y}) \mathrm{d}S_Y \right\rangle$ is the average work done by the cell over the j^{th} period. In the following, j is chosen sufficiently large so that the cell has established a regular beat before its statistics are calculated (i.e. a beat which is approximately periodic). In what follows, $j = 5$ is sufficient.

In the remainder of this chapter, we will consider how varying the dimensionless groups

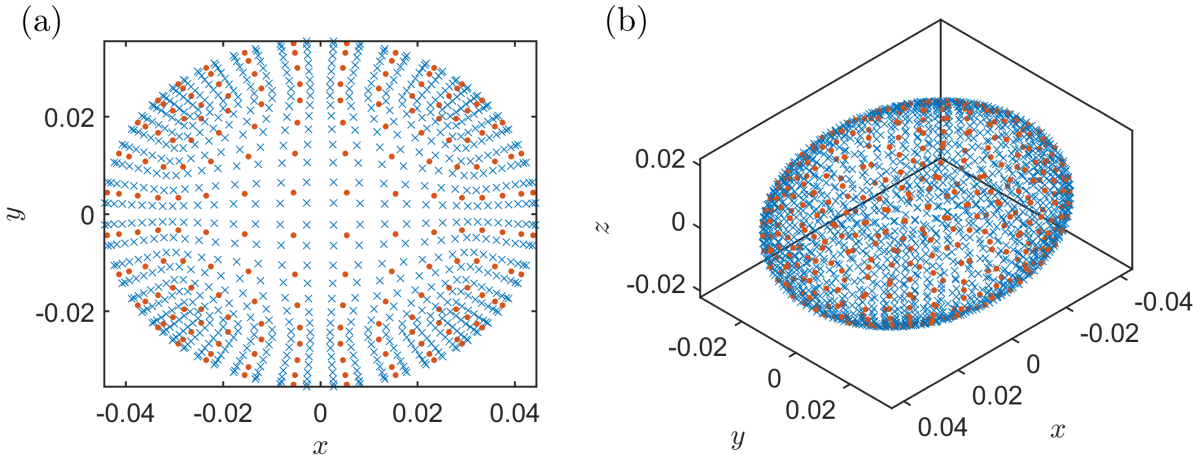


Figure 2.4: Discretisation of an ellipsoidal sperm head with radii $r_x = 0.0444$, $r_y = 0.0356$ and $r_z = 0.0222$, shown in (a) the xy-plane and, (b) three-dimensions. The fine quadrature discretisation consists of $M_Q = 1536$ nodes (blue), with the coarse traction discretisation consisting of $M_T = 384$ nodes (red).

$\mathcal{S}$, $\mathcal{M}$, and ℓ through appropriate physiological ranges can affect both swimming velocity and efficiency of simulated spermatozoa.

2.3.1 Choice of parameters

In what follows, simulated sperm cells are initialised with a flagellar shape in the form of a low-amplitude parabola, obtained by sampling a section of unit arclength from the curve $y = 0.1x^2$ centred about $x = 0$. The flagellum, which is of dimensionless length 1, is discretised via $Q = 100$ segments of length $\Delta s = 0.01$. We choose the dimensionless regularisation parameter $\epsilon = 0.01$ so that for a flagellum of length 50 μm, the corresponding flagellar radius is 0.5 μm. We consider the effect of varying the dimensionless active tail length between $\ell = 0.5$ and $\ell = 1$ so that the resulting simulations produce cells that are likely to be biologically realistic.

The head is modelled as an ellipsoid with dimensionless radii

$$r_x = 0.0444, \quad r_y = 0.0356, \quad r_z = 0.0222, \tag{2.45}$$

corresponding to a head with physical radii $R_x = 2.2\,\mu$m, $R_y = 1.78\,\mu$m and $R_z = 1.11\,\mu$m. To generate the head quadrature and traction discretisations, a sphere of unit radius is enclosed

Table 2.1: Approximate sperm number $\mathcal{S}$ for spermatozoa of various mammalian species (Cummins and Woodall, 1985).

Species	$\mathcal{S}$
Bull	10.5
Chocolate wattled bat	12.6
Rabbit	14.85
Cat	16.4
Dog	16.9
Dolphin	18

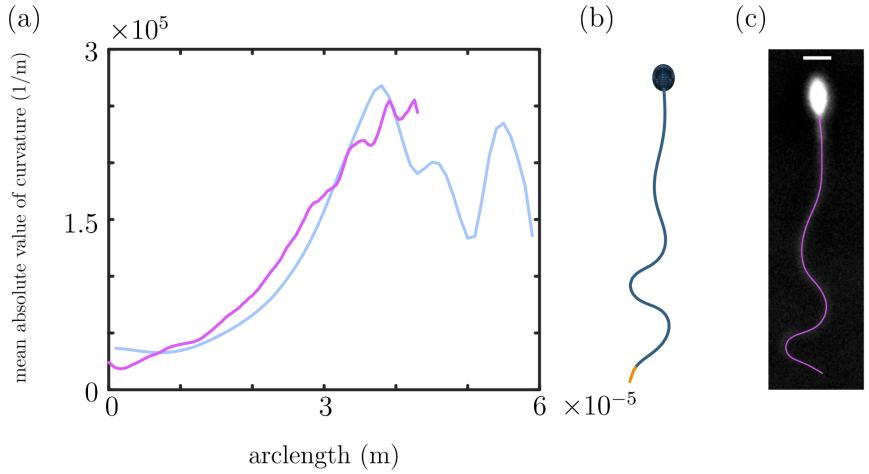


Figure 2.5: Comparison between simulated and experimental data to verify the choice of elastic stiffness parameters. (a) The mean absolute value of curvature for both a progressive human sperm cell simulated with $(\mathcal{S}, k) = (18, 5\pi)$ (blue) and an experimentally tracked cell (magenta) are plotted against arclength. A waveform comparison is shown for the (b) simulated and (c) experimental cell (tracked with FAST (Gallagher et al., 2019a), scale bar denotes 5 μm). In the case of the simulated waveform, the inactive end piece is shown in orange. Image taken from Neal et al. (2020).

by a cube whose sides are uniformly discretised. Projecting these points to the sphere and transforming to the appropriate ellipsoid via the scalings given in (2.45) leads to the required head discretisations. In what follows, each side of the cube is discretised via $m_Q = 16$ and $m_T = 8$ nodes for the quadrature and traction discretisations respectively, yielding $M_Q = 1536$ and $M_T = 384$ (see Figure 2.4).

The viscous-elastic parameter $\mathcal{S}$ is varied between 9 and 18, similar to the ranges considered in previous studies by Gadêlha et al. (2010) and Montenegro-Johnson et al. (2015),

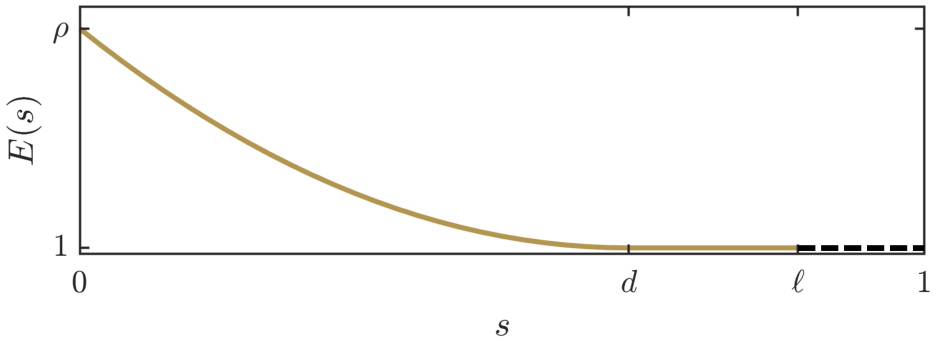


Figure 2.6: The change in the dimensionless elastic stiffness function $E(s)$ with dimensionless arclength s, representing the tapering fibrous sheath surrounding the core of the flagellum. Here, $\rho = 36.4$ is the proximal-distal stiffness ratio, $d = 0.65$ and $\ell = 0.85$.

and corresponding to the approximate physiological range for human spermatozoa migrating within the female reproductive tract. In particular, taking the typical flagellar length $L = 55\,\mu$m (Cummins and Woodall, 1985), distal flagellar stiffness $E_d = 2\times10^{-21}\,\mathrm{Nm}^2$ (Gaffney et al., 2011), angular beat frequency $\omega = 10 \times 2\pi\,s^{-1}$ (Gallagher et al., 2019a) and viscosity $\mu = 0.14\,\mathrm{Pa}\cdot\mathrm{s}$ (similar to mucus analogue (Smith et al., 2009b)) yields $\mathcal{S} = 14.1639$, which falls well within the range $\mathcal{S} \in [9, 18]$. Note that the sperm of many other mammalian species also exhibit similar values of $\mathcal{S}$ (see Table 2.1), and as such these results are likely applicable to a wide range of species. Dimensionless wavenumbers between $k = 3\pi$ and $k = 5\pi$ are considered as they are typical of mammalian sperm flagella in higher viscosity media (Smith et al., 2009b).

For the stiffness function $E(s)$ given in equation (2.12), we fix $d = 0.65$ so that $Ld = 39\,\mu$m for human sperm of length $L = 60\,\mu$m. This corresponds to the distance over which the accessory structures extend. We choose the proximal-distal stiffness ratio $\rho = 36.4$ in order to produce results that closely resemble experimentally observed waveforms of human spermatozoa. To validate this choice, the mean absolute value of the curvature of the flagellum is plotted against arclength of both a simulated (with $(\mathcal{S}, k) = (18, 5\pi)$) and experimental cell in Figure 2.5. The experimental data and waveform agree closely over the proximal $40\,\mu$m of the flagellum. Following this point, the flagellum is not visible in the experimental image (the magenta line terminates in Figure 2.5). This is due to the thinness of this region and the insufficient resolution of the imaging technique. It could also be due to the slight three-

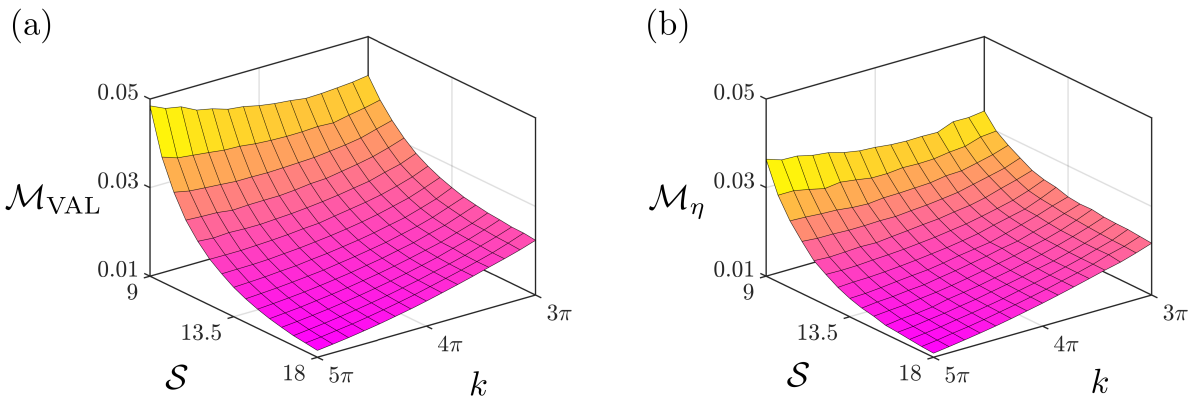


Figure 2.7: Values of the actuation parameter $\mathcal{M}$, optimising (a) swimming speed (VAL) and (b) the Lighthill efficiency (η) for $\mathcal{S} \in [9, 18]$ and $k \in [3\pi, 5\pi]$. Colour represents the magnitude of the optimising parameters $\mathcal{M}_{\mathrm{VAL}}$ and $\mathcal{M}_{\eta}$ for (a) and (b) respectively. Image taken from Neal et al. (2020).

dimensionality in the flagellar swimming stroke, which could shift the distal flagellum out of the plane of imaging. For these choices of parameters, a sketch of how the dimensionless form of the elastic stiffness $E(s)$ varies with arclength s can be seen in Figure 2.6.

The choice of the actuation parameter $\mathcal{M}$ in the simulations is not obvious, since direct estimation from experimental data is difficult (i.e. physical values of the actuation strength m_0 are hard to measure). Furthermore, very different values of $\mathcal{M}$ are required to produce realistic amplitude beats across all parameter pairs $(\mathcal{S}, k)$. We also require that our results are not an unintended consequence of the choice of $\mathcal{M}$. Therefore, for each pair $(\mathcal{S}, k)$, two variations on the actuation parameter $\mathcal{M}$ are investigated: the value $\mathcal{M}_{\mathrm{VAL}}$ that optimises VAL, and the value $\mathcal{M}_{\eta}$ that optimises Lighthill efficiency η, for the fully-active $\ell = 1$ case. This ensures any increase in velocity or efficiency as a consequence of varying ℓ is not a consequence of the specific value of $\mathcal{M}$ chosen. Indeed any increases in velocity and efficiency observed will therefore be lower bounds for what is possible if $\mathcal{M}$ is allowed to vary freely. Optimisation was carried out using the MATLAB® 1-dimensional optimisation algorithm `fminbnd`. Figure 2.7 shows the smooth variation in both $\mathcal{M}_{\mathrm{VAL}}$ and $\mathcal{M}_{\eta}$ as $\mathcal{S}$ and k are varied over $\mathcal{S} \in [9, 18]$ and $k \in [3\pi, 5\pi]$.

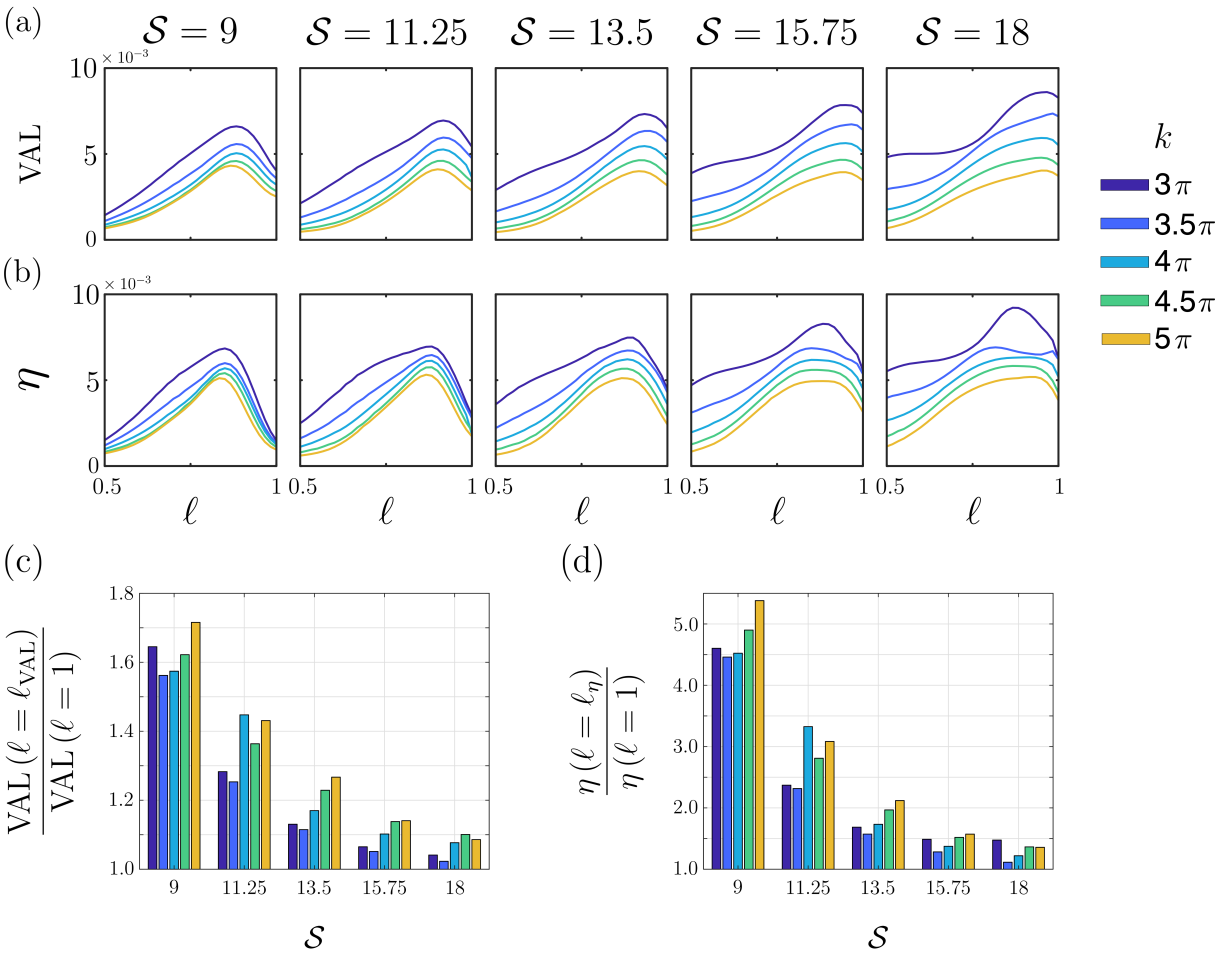


Figure 2.8: The effect of the inactive end piece length on swimming speed and efficiency of propulsion, for simulations actuated with $\mathcal{M} = \mathcal{M}_{\mathrm{VAL}}$ (a) The swimming speed (VAL), (b) the Lighthill efficiency (η). (c, d) The relative increase in VAL and η respectively, when comparing the optimally-active and fully-active flagella, for viscous-elastic parameter choices $\mathcal{S} \in [9, 18]$ and wavenumbers $k \in [3\pi, 5\pi]$. Image taken from Neal et al. (2020).

2.3.2 Simulations actuated for optimal velocity

The effects of varying the dimensionless active tail length on sperm swimming speed and efficiency are shown in Figure 2.8 for five choices of dimensionless wavenumber k and viscous-elastic parameter $\mathcal{S}$, actuated with $\mathcal{M} = \mathcal{M}_{\mathrm{VAL}}$. Here $\ell = 1$ corresponds to an entirely active flagellum and $\ell = 0$ to an entirely inactive flagellum, although only the range $0.5 \leq \ell \leq 1$ is investigated.

Optimal active lengths for swimming speed, ℓ_{VAL}, and efficiency, ℓ_{η}, occur for each parameter pair $(\mathcal{S}, k)$; crucially, as shown in Figures 2.8a and 2.8b, the optima are always less than 1, indicating that by either measure some length of inactive flagellum is always better than a

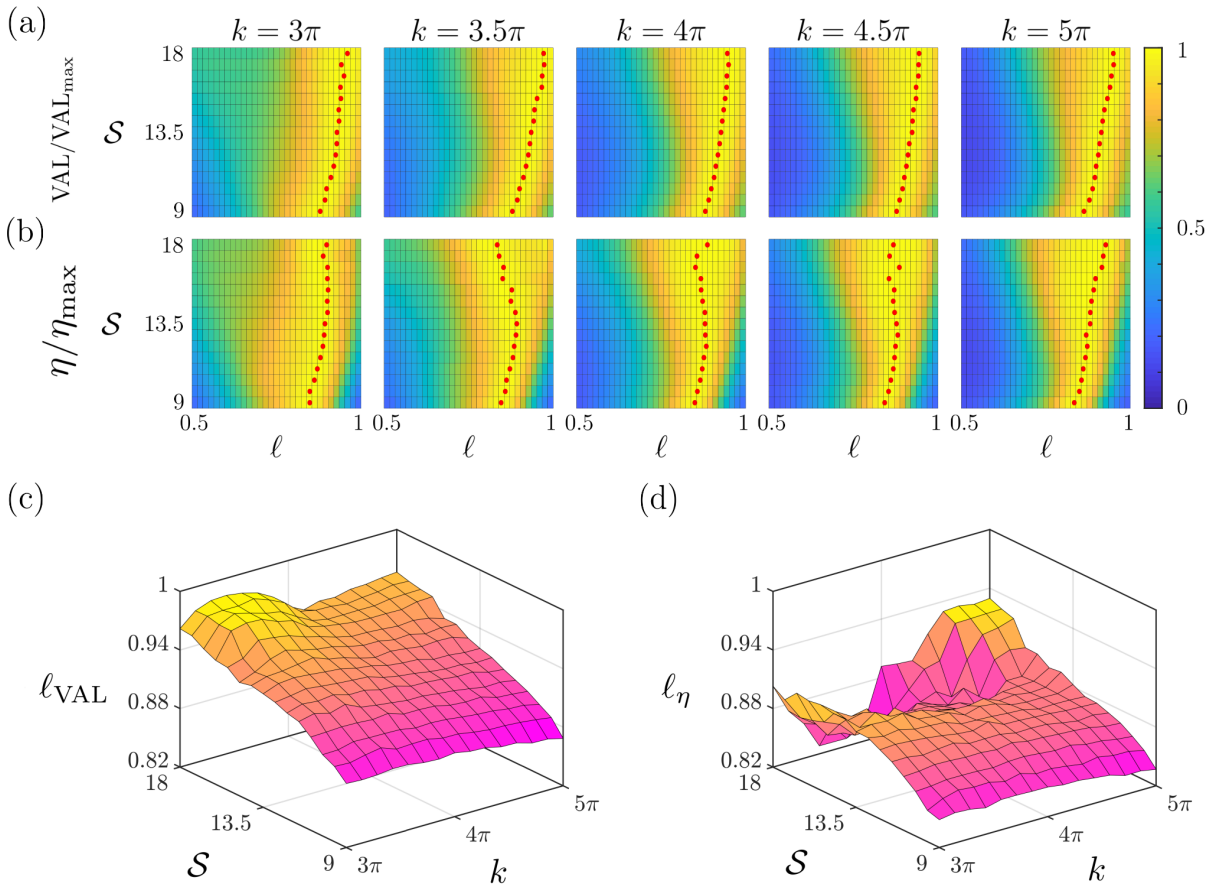


Figure 2.9: (a) Normalised VAL and (b) normalised Lighthill efficiency (η) for $\mathcal{S} \in [9, 18]$ versus $\ell \in [0.5, 1]$, shown for five choices of dimensionless wavenumber k. Values in each subplot are normalised with respect to either (a) the maximum VAL or (b) the maximum η for each $(\mathcal{S}, k)$ pair. The optimal choices of ℓ are highlighted as red dots. (c) The active length that optimises VAL (ℓ_{VAL}) and (d) the active length that optimises the Lighthill efficiency (ℓ_η), for $\mathcal{S} \in [9, 18]$, $k \in [3\pi, 5\pi]$ where surface colour represents the magnitude of the parameters ℓ_{VAL} and ℓ_η for (c) and (d) respectively. Simulations are actuated with $\mathcal{M} = \mathcal{M}_{\mathrm{VAL}}$. Image taken from Neal et al. (2020).

fully active flagellum. The relative effect of the end piece on VAL and η is larger for smaller values of $\mathcal{S}$. In particular, for $\mathcal{S} = 9$ the optimally-inactive flagellum results in an 56–72% increase in VAL over $k \in [3\pi, 5\pi]$ compared to a fully active flagellum (Figure 2.8c), decreasing to 2–9% when $\mathcal{S} = 18$. Physically this corresponds to the end piece effect being larger in magnitude for flagella that are stiffer relative to surrounding fluid. The end piece can have an extremely significant effect on the efficiency of cells (Figure 2.8d), with an 11–438% increase over the values of k and $\mathcal{S}$ considered.

A more detailed investigation of the relationship between optimum active flagellum length

and each of VAL and η is shown in Figures 2.9a and 2.9b by simulating cells over a finer gradation in $S \in [9, 18]$. The optimum values ℓ_{VAL} and ℓ_η are shown in Figures 2.9c and 2.9d; typically $\ell_{\mathrm{VAL}} \neq \ell_\eta$ for a given swimmer. For each metric, the optimum active length is smoothly varying for each choice of S and k. In the case of ℓ_η, we observe non-monotonic behaviour for the combination of larger values of S and smaller values of k. That is, if we fix S and increase k from $k = 3\pi$ to $k = 5\pi$ (or similarly if we fix k and increase S from $S = 9$ to $S = 18$), then the value of ℓ_η may both increase and decrease over the interval if it covers large values of S and small values of k. We postulate that this may be due to the development of a skewed beat pattern (see Figure 2.12), in which the peaks and troughs of the flagellar waveform lean in one particular direction, rather than being symmetrical. This skewness in beat occurs across similar parameter ranges to where we observe the non-monotonic behaviour in ℓ_η (high S, low k). Finally, overall we observe that relatively stiffer flagella benefit from longer inactive regions than relatively less stiff flagella.

2.3.3 Simulations actuated for optimal efficiency

In addition to the figures in Section 2.3.2, equivalent results can be produced for cells actuated with $\mathcal{M} = \mathcal{M}_\eta$. Figures 2.10a and 2.10b show the relationship between active tail length ℓ and swimming speed and efficiency (with finer detail shown in Figure 2.11a and 2.11b). Figures 2.10c and 2.10d highlight the relative benefit of an optimally-inactive flagellum compared to the fully-active case, showing an increase of 7–40% for swimming speed and 22–240% for efficiency. The optimum active length for both swimming speed and efficiency is shown in Figures 2.11c and 2.11d for $k \in [3\pi, 5\pi]$ and $S \in [9, 18]$. The qualitative similarities between Figures 2.10 and 2.11, and the analogous figures in Section 2.3.2 (Figures 2.8 and 2.9) highlight that the observed cell behaviours are not simply governed by the choice of actuation parameter $\mathcal{M}$.

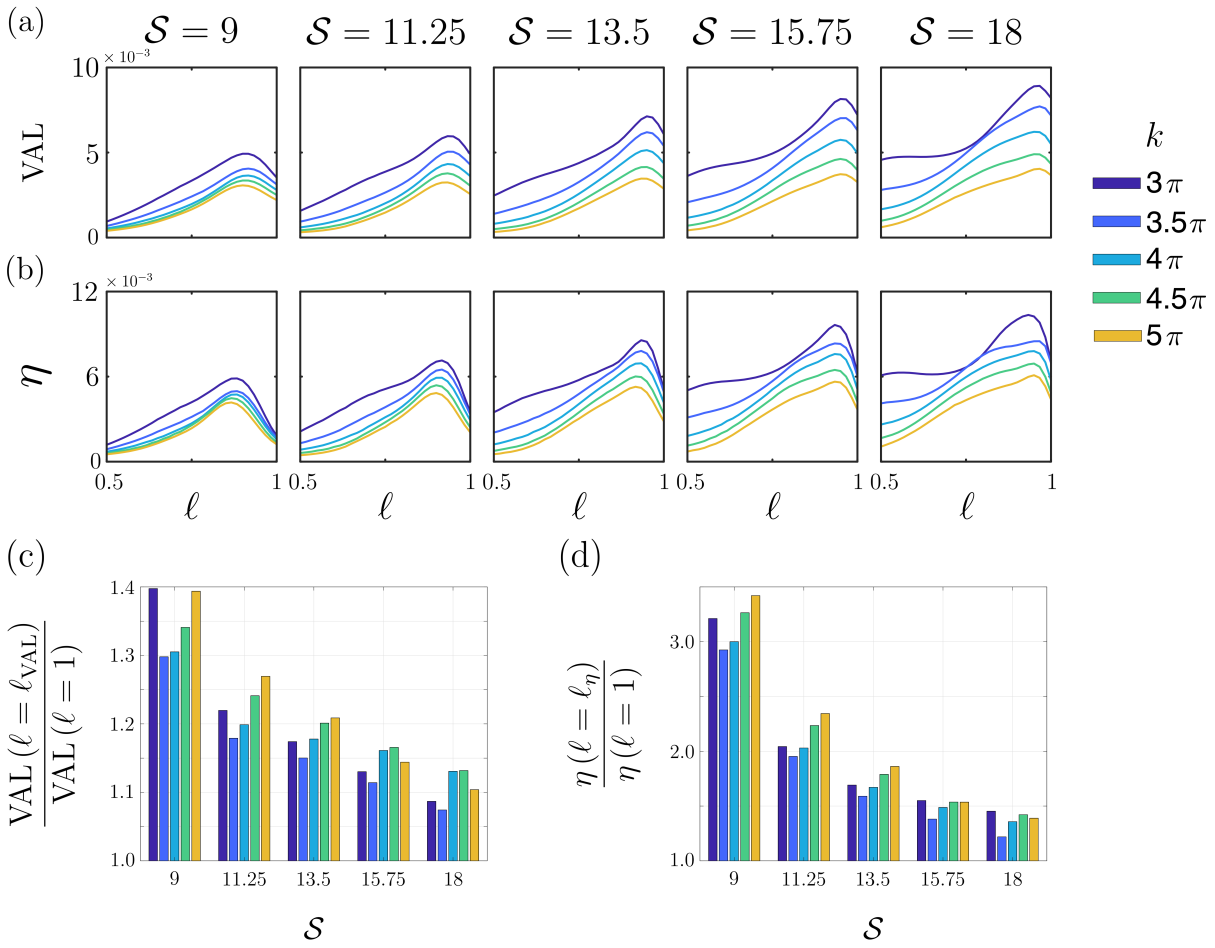


Figure 2.10: The effect of the inactive end piece length on swimming speed and efficiency of propulsion, for simulations actuated with $\mathcal{M} = \mathcal{M}_{\eta}$ (a) The swimming speed (VAL), (b) the Lighthill efficiency (η). (c, d) The relative increase in VAL and η respectively, when comparing the optimally-active and fully-active flagella, for viscous-elastic parameter choices $\mathcal{S} \in [9, 18]$ and wavenumbers $k \in [3\pi, 5\pi]$. Image taken from Neal et al. (2020).

2.3.4 Effect of the end piece on waveform and trajectory

The foregoing results establish the propulsive and efficiency advantages of an inactive distal flagellar region. To better understand why the inactive region yields these advantages we consider the flagellar waveforms and overall cell dynamics resulting from simulations with parameters $\mathcal{S} = \{9, 13.5, 18\}$ and $k = \{3\pi, 4\pi, 5\pi\}$. The tracks and shapes of swimming sperm actuated with $\mathcal{M} = \mathcal{M}_{\mathrm{VAL}}$ are shown in Figure 2.12, which compares the fully-active ($\ell = 1$) and optimally-inactive ($\ell = \ell_{\mathrm{VAL}}$) waveforms for each parameter pair. Simulations with an optimally-inactive region produce flagellar shapes and tracks that are more similar to experimental observations of flagellar waveform (see, for example, Gallagher et al. (2019a)) than

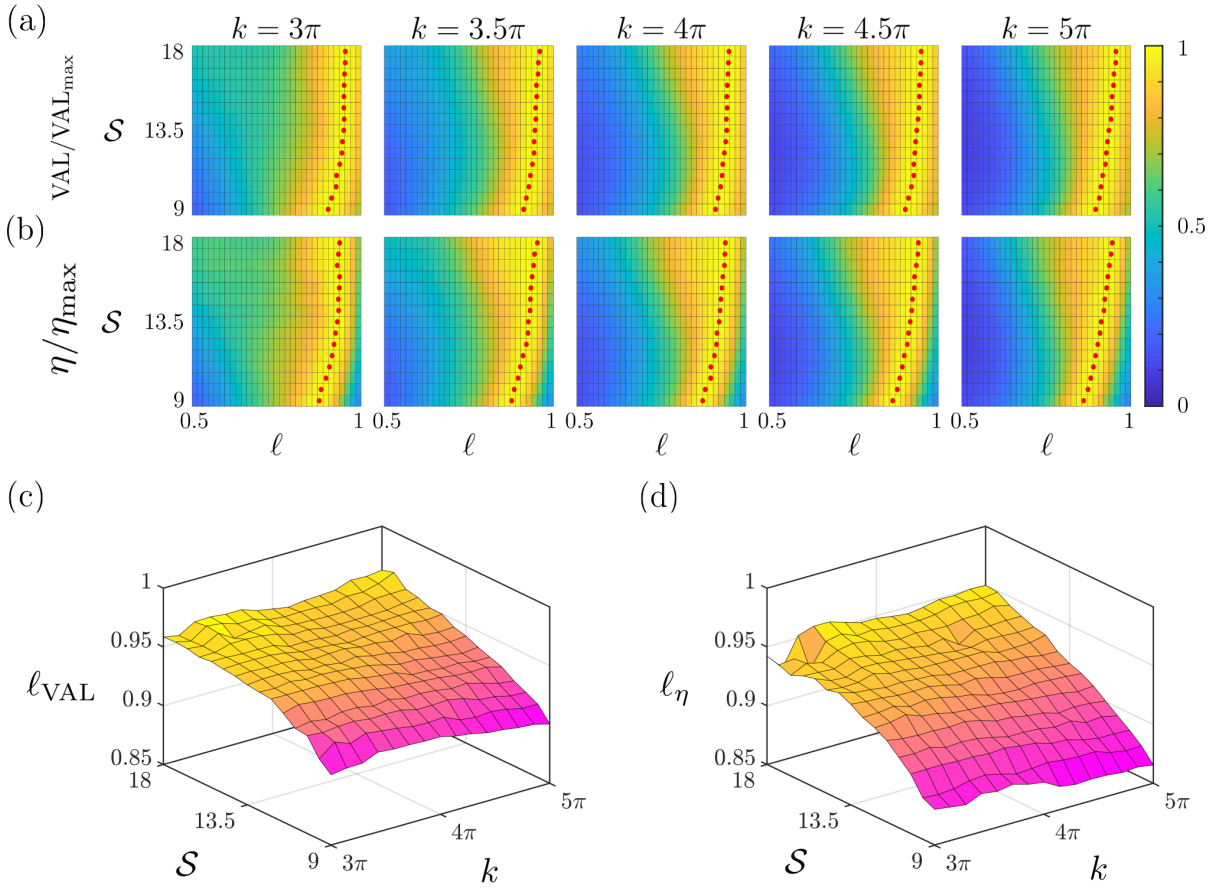


Figure 2.11: (a) Normalised VAL and (b) normalised Lighthill efficiency (η) for $\mathcal{S} \in [9, 18]$ versus $\ell \in [0.5, 1]$, shown for five choices of dimensionless wavenumber k. Values in each subplot are normalised with respect to either (a) the maximum VAL or (b) the maximum η for each $(\mathcal{S}, k)$ pair. The optimal choices of ℓ are highlighted as red dots. (c) The active length that optimises VAL (ℓ_{VAL}) and (d) the active length that optimises the Lighthill efficiency (ℓ_η), for $\mathcal{S} \in [9, 18]$, $k \in [3\pi, 5\pi]$ where surface colour represents the magnitude of the parameters ℓ_{VAL} and ℓ_η for (c) and (d) respectively. Simulations are actuated with $\mathcal{M} = \mathcal{M}_\eta$. Image taken from Neal et al. (2020).

those with an entirely active flagellum. More specifically, cells with an end piece exhibit decreased curvature and hence tangent angle in the distal flagellum. The change to the flagellar envelope is most clearly visible in the overlaid timelapse images of Figure 2.13. A similar effect is observed for cells actuated with $\mathcal{M} = \mathcal{M}_\eta$, whose cell tracks can be seen in Figure 2.14, and waveforms in Figure 2.15.

The velocity field associated with flagella that are fully-active and optimally-inactive for propulsion are shown in Figures 2.16 and 2.17 for parameter values $\mathcal{S} = 13.5$ and $k = 4\pi$, where cells are actuated with $\mathcal{M} = \mathcal{M}_{\mathrm{VAL}}$ and $\mathcal{M} = \mathcal{M}_\eta$ respectively. The qualitative features of both

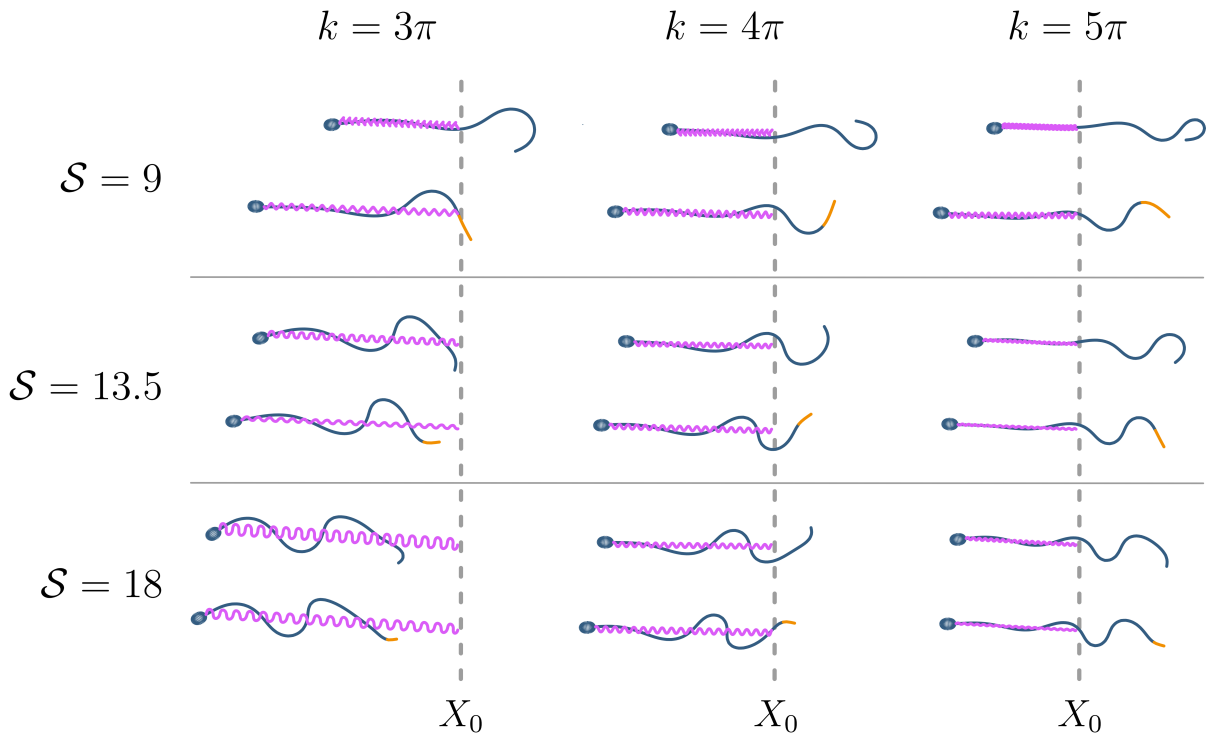


Figure 2.12: The swimming track following the head for both fully-active and optimally-inactive sperm (top and bottom of each pair respectively) for a selection of parameter pairs $(\mathcal{S}, k)$ actuated with $\mathcal{M} = \mathcal{M}_{\text{VAL}}$ and simulated for 10 cycles of the active moment. In each pair the sperm is plotted at the final time point with the optimally-inactive length $\ell = \ell_{\text{VAL}}$, shown in orange. Image taken from Neal et al. (2020).

waveform and the velocity field are similar in the fully-active and optimally-inactive cases, however the optimally-inactive flagellar waveforms have reduced curvature and tangent angle in the distal region, often resulting in an additional 'oblique' region (i.e. where $\theta - \phi \approx \pi/4$) that confers additional thrust to the cell when $\ell < 1$.

2.3.5 Effect of the end piece on surrounding fluid flow

In Figure 2.16, we compare the flow fields surrounding a fully-active sperm cell and an optimally-active sperm cell, actuated with $\mathcal{M} = \mathcal{M}_{\text{VAL}}$ and for $\mathcal{S} = 13.5$ and $k = 4\pi$. In Figure 2.16a, instantaneous fluid streamlines and fluid velocity magnitude are indicated at five time points over the interval $t \in [8\pi, 10\pi]$ for a cell with $\ell = 1$. Similarly, in Figure 2.16b, flow fields are plotted for the optimally-active case, corresponding here to $\ell = 0.93$. In Figure 2.16c, the difference between the flow fields in the $\ell = 1$ and $\ell = 0.93$ cases is plotted. Here, regions

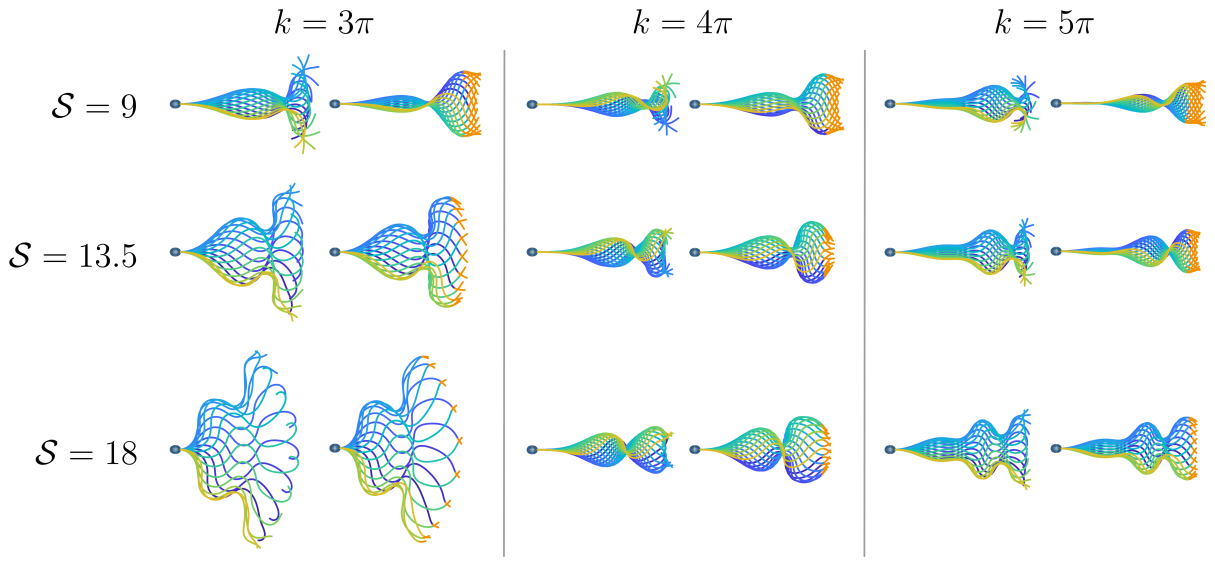


Figure 2.13: The flagellar waveform for a fully-active and optimally-inactive sperm (left and right of each pair respectively), simulated for a selection of parameter pairs (S, k), and actuated with $\mathcal{M} = \mathcal{M}_{\text{VAL}}$. The color of the flagellum indicates progression through a single beat, from blue to yellow. For each pair the sperm are plotted with the optimally-inactive length ℓ_{VAL} shown in orange. Image taken from Neal et al. (2020).

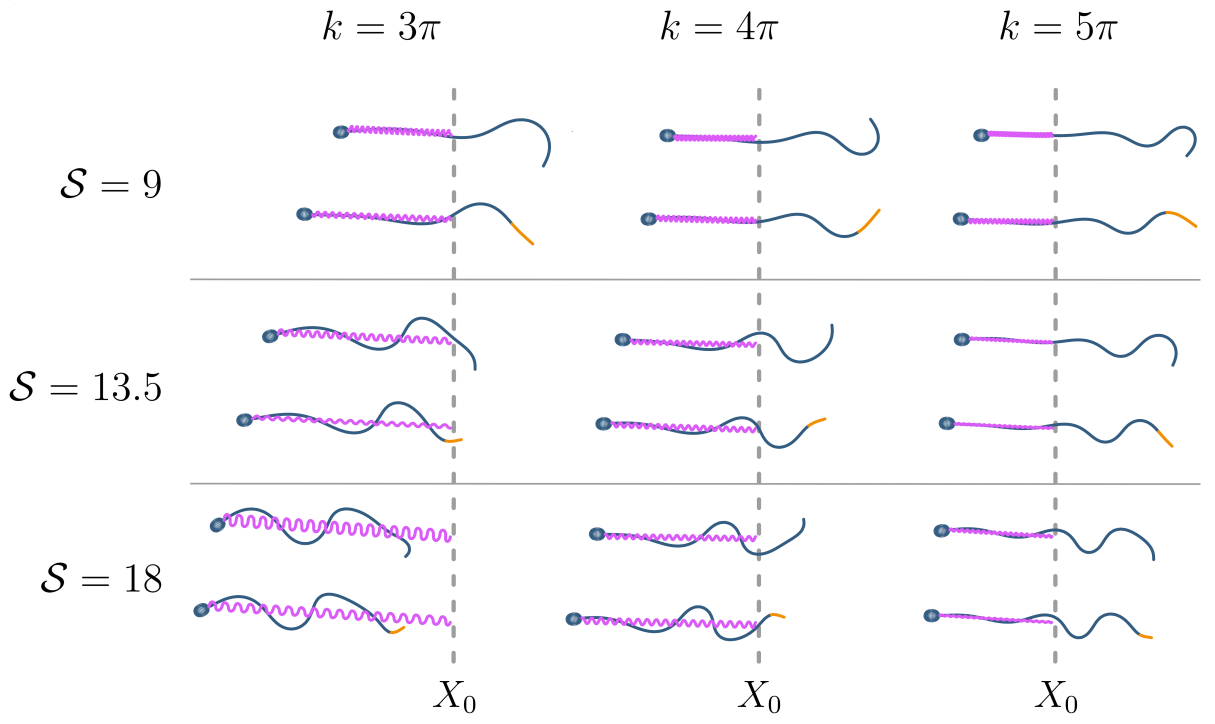


Figure 2.14: The swimming track following the head for both fully-active and optimally-inactive sperm (top and bottom of each pair respectively) for a selection of parameter pairs (S, k) actuated with $\mathcal{M} = \mathcal{M}_\eta$ and simulated for 10 cycles of the active moment. For each pair the sperm are plotted at the final time point with the optimally-inactive length $(\ell = \ell_\eta)$ shown in orange. Image taken from Neal et al. (2020).

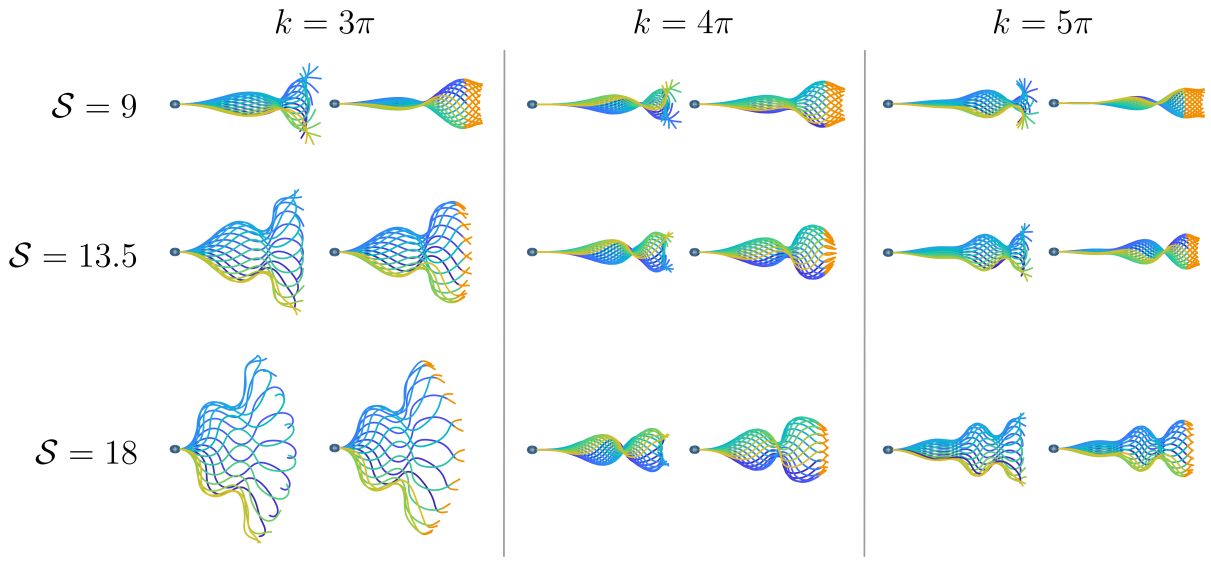


Figure 2.15: The flagellar waveform for a fully-active and optimally-inactive sperm (left and right of each pair respectively) simulated for a selection of parameter pairs (S, k), and actuated with $\mathcal{M} = \mathcal{M}_\eta$. The color of the flagellum indicates progression through a single beat, from blue to yellow. For each pair the sperm are plotted with the optimally-inactive length $\ell = \ell_\eta$, shown in orange. Image taken from Neal et al. (2020).

in which the fluid velocity magnitude in both cases is equal are indicated in white. Regions where the velocity magnitude in the optimally-active is larger than the fully-active case are indicated in pink, with the opposite shown in black. Whilst in the fully-active case there is a region of high fluid velocity at the tip of the flagellum, Figure 2.16c indicates that in general the fluid velocities associated with optimally-active cells tend to be higher than those for the fully-active case. In particular, it appears that these increases in fluid velocity can be attributed to regions of the flagellum in which the curvature and hence tangent angle of the flagellum are reduced compared to the fully-active case, resulting in sections of the flagellum that move 'obliquely' through the fluid. A similar conclusion can be drawn from the results presented in Figure 2.17, which again compare the flow fields surrounding a fully-active and optimally-active cell, but here actuated with $\mathcal{M} = \mathcal{M}_\eta$.

2.4 Discussion

These simulations provide evidence that those spermatozoa which feature a short, inactive region at the end of their flagellum swim faster and more efficiently than those without. For each

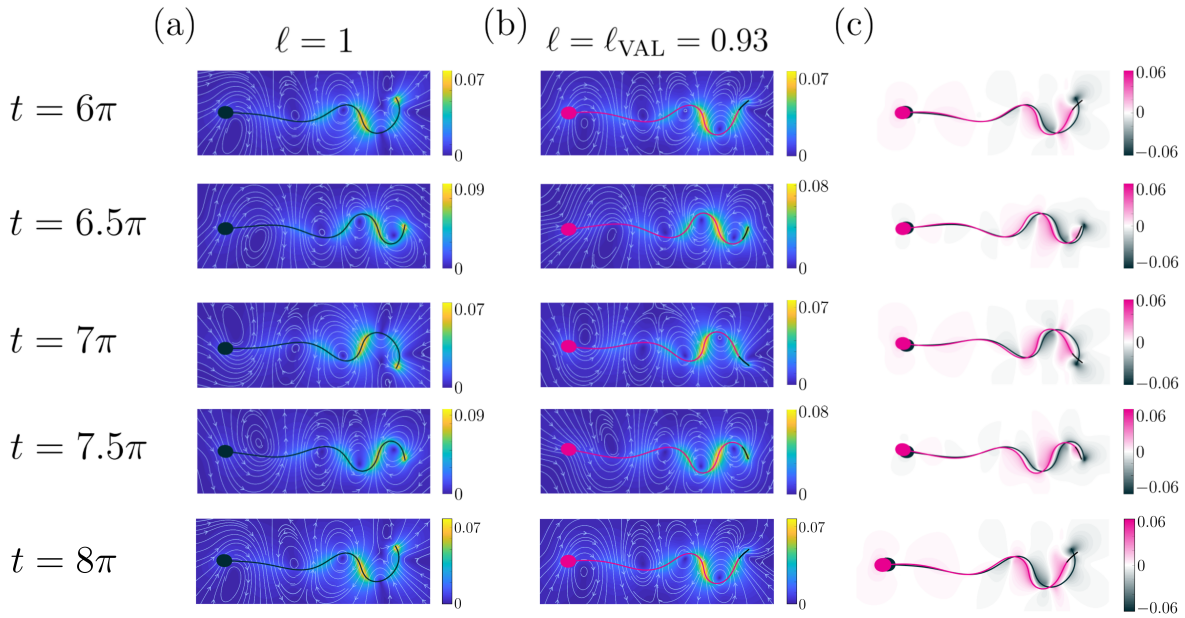


Figure 2.16: Comparison of the flow fields around a simulated sperm actuated with $\mathcal{M} = \mathcal{M}_{\mathrm{VAL}}$ with $\mathcal{S} = 13.5$ and $k = 4\pi$, for (a) a cell with a fully-active flagellum, and (b) an optimally-inactive cell, each shown at five time points in the final simulated beat. (c) The difference between flow fields, with positive values corresponding to the optimally-inactive case having a faster fluid velocity. (a,b) Instantaneous fluid streamlines are shown in white with arrows indicating direction, and the fluid magnitude in indicated by the colourbar for each panel. In (b) the inactive part of the flagellum is shown in black. Image taken from Neal et al. (2020).

simulation, cell motility is optimised when 2–18% of the distal flagellum is inactive, regardless of parameter choices. For the larger values of $\mathcal{S}$, representative of cells in the human female reproductive tract, the optimally inactive length for velocity and efficiency (Figures 2.9c and 2.11d) lies between 2–10%. Experimental measurements of human sperm indicate an average combined length of the midpiece and principal piece of $\approx$ 54 μm and an average end piece length of $\approx$ 3 μm (Cummins and Woodall, 1985), suggesting that the effects uncovered in this work are biologically relevant.

The modelling method has been validated by comparing the mean absolute value of curvature along the flagellum, for the case $\mathcal{S} = 18$, $k = 5\pi$, with that of an experimentally captured sperm. The consistency between simulated cells and experimental data lends further confidence that the modelling choices made are biophysically reasonable; future investigation may assess the robustness of the conclusions to more intricate models of flagellar structure and regulation.

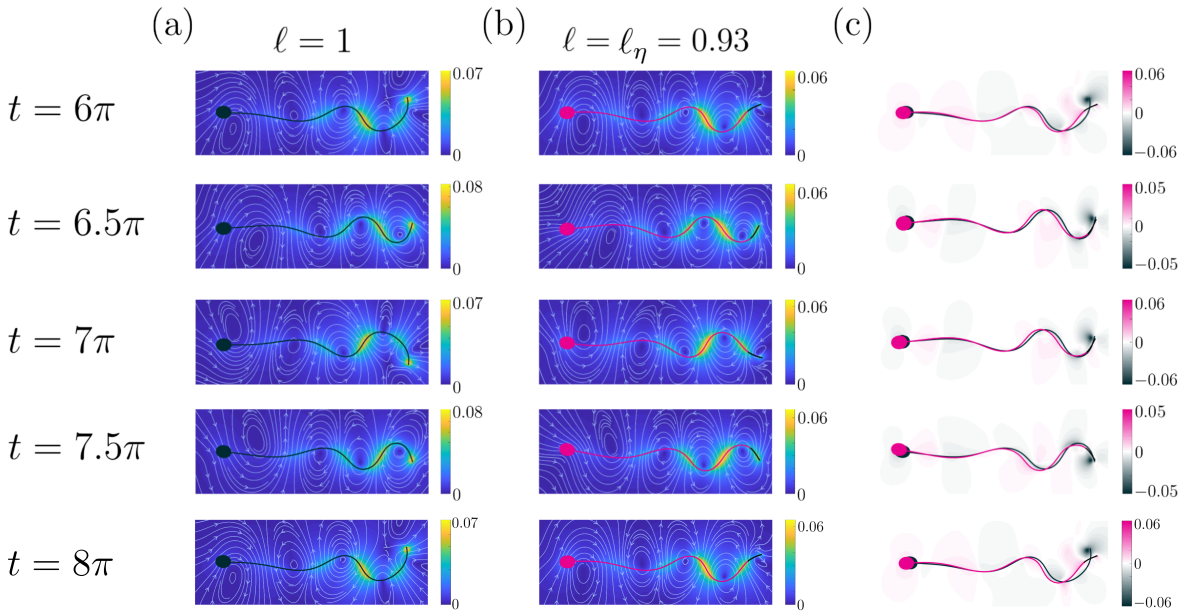


Figure 2.17: Comparison of the flow fields around a simulated sperm actuated with $\mathcal{M} = \mathcal{M}_\eta$ with $\mathcal{S} = 13.5$ and $k = 4\pi$, for (a) a cell with a fully-active flagellum, and (b) an optimally-inactive cell, each shown at five time points in the final simulated beat. (c) The difference between flow fields, with positive values corresponding to the optimally-inactive case having a faster fluid velocity. (a,b) Instantaneous fluid streamlines are shown in white with arrows indicating direction, and the fluid magnitude in indicated by the colourbar for each panel. In (b) the inactive part of the flagellum is shown in black. Image taken from Neal et al. (2020).

Sperm move through a variety of fluids during migration, in particular encountering a step change in viscosity when penetrating the interface between semen and cervical mucus, and having to swim against physiological flows (Tung et al., 2015). Cells featuring an optimally-sized inactive end piece may form better candidates for fertilisation, being able to swim faster and for longer when traversing the female reproductive tract (Holt and Fazeli, 2015).

The basic mechanism by which the flagellar wave produces propulsion is through the interaction of segments of the filament moving obliquely through the fluid (Gray and Hancock, 1955), with the angle relative to the direction of propulsion being between $-\pi/2$ and $\pi/2$. Analysis of the flow fields (Figures 2.16 and 2.17) suggest that the lower curvature and hence tangent angle associated with the inactive end piece maintains such regions towards the end of the flagellum, preventing the flagellum from 'overturning' (Figures 2.12 and 2.14).

An inactive region of flagellum is not a feature unique to human gametes – its presence can also be observed in the sperm of other species (Fawcett, 1975), as well as other microorganisms.

In particular, the axonemal structures of the biflagellated algae *Chlamydomonas reinhardtii* deplete at the distal tips (Jeanneret et al., 2016), suggesting the presence of an inactive region. The contribution to swimming speed and cell efficiency due to the inactive distal section in these cases remains unknown. By contrast, the tip of the 9+2 cilium is a more organised 'crown' structure (Kuhn III and Engleman, 1978), which will interact differently with fluid than the flagellar end piece modelled here. The structure and actuation of the motile 9+0 cilia found in the embryonic node (see for example Nonaka et al. (1998)) is less well-characterised. Understanding this distinction between cilia and flagella, as well as the role of the inactive region in other microorganisms, may provide further insight into underlying biological phenomena, such as chemotaxis (Alvarez et al., 2014) and synchronisation (Guo et al., 2018; Goldstein et al., 2016). Further work should investigate how this phenomenon changes when more detailed models of the flagellar ultrastructure are considered, taking into account the full 9+2 structure (Ishijima, 2019), sliding resistance associated with filament connections (Coy and Gadêlha, 2017), and the interplay of these factors with biochemical signalling in the cell (Carichino and Olson, 2018).

The ability to qualitatively assess and model the inactive end piece of a human spermatozoon could have important clinical applications. In live imaging for diagnostic purposes, the end piece is often hard to resolve due to its depleted axonemal structure. Lacking more sophisticated imaging techniques, which are often expensive or impractical in a clinical environment, modelling of the end piece combined with flagellar tracking software, such as FAST (Gallagher et al., 2019a), could enable more accurate sperm analysis. Such software tracks the principal piece of the flagellum, and mathematical modelling of the end piece could help infer its movement, yielding more precise measurements of propulsive efficiency which could help improve cell selection in assisted reproductive technologies. The difficulty in capturing the end piece may be a significant explanatory factor to why previous works have only been able to reconstruct the qualitative features of the swimming tracks, even when high quality flagellar waveform data is available (Ishimoto et al., 2017). Furthermore, knowledge of the function of an inactive distal region has wider applications across synthetic microbiology, particularly

in the design of artificial swimmers (Dreyfus et al., 2005) and flexible filament microbots used in targeted drug delivery (Montenegro-Johnson, 2018).

Following the findings of this chapter, several additional questions may now be posed. For example, how does the presence of the inactive end piece affect propulsion in non-Newtonian fluids such as cervical mucus? Also, does the end piece confer an advantage to cells penetrating between semen and cervical mucus, which involves a step-change in viscosity? In the next chapter, we develop a hybrid method for modelling sperm-like swimmers within shear-thinning fluids. This methodology will enable both investigation of the effect of shear thinning rheology per se, and also its interaction with the flagellar end piece effect.

Chapter 3

Swimming in shear-thinning fluids: a non-linear finite element approach

3.1 Introduction

In Chapter 1, we discussed the journey of human sperm through the female reproductive tract, and specifically cells encounters with fluids which exhibit complex, non-Newtonian properties. In this chapter, we focus on modelling sperm in shear-thinning fluids, in which fluid viscosity decreases with increased shear rate.

In order to solve problems involving human sperm in fluids with shear-dependent viscosity, we develop a hybrid approach for non-linear swimming (HANS) in this chapter. The HANS method utilises a Newtonian approximation to the fluid flow surrounding a model swimmer, along with a correction term obtained through solving the appropriate boundary value problem using the finite element method (FEM). In this way, the overall outcome is an accurate solution to the full non-linear flow problem. The Newtonian approximation to the flow is computed via the method of regularised stokeslets (Cortez, 2001) and is the first application of this method to non-Newtonian flow problems. Since the regularised stokeslet solution accounts for the rapidly varying nature of the flow close to the swimmer, the correction term is slowly varying across the computational domain. Consequently, the finite element solver can be formulated on a coarse mesh rather than a body-fitted mesh as required by previous FEM solvers for swimmers in non-Newtonian fluids (Montenegro-Johnson et al., 2012, 2013).

This approach alleviates the need for complex re-meshing as the swimmer evolves and reduces computational costs due to a reduction in system size from fewer mesh nodes.

The finite element method (FEM) is a numerical method used to approximate the solution of boundary and initial value problems described by partial differential equations. To solve a given problem, the FEM involves constructing a spatial discretisation of the computational domain into non-overlapping subdomains called finite elements, a process referred to as meshing the domain. Over each subdomain, the unknown solution function is calculated at a number of nodal points, often (but not always exclusively) located on the boundaries between elements. Interpolation functions are defined on each element to interpolate the nodal solution values to non-nodal points within the element. The FEM was first applied to fluid flow problems by Zienkiewicz and Cheung (1965), with solutions to the Navier-Stokes and Stokes equations found using this approach by Oden (1969, 1970) and Crouzeix and Raviart (1973) respectively. Prior to this, it was common practice to solve fluid flow problems using numerical methods such as the finite difference method (FDM). The FEM is often used to solve flow problems today due to, amongst other factors, its ease of application to irregular geometries.

The finite element method can be used to solve non-linear equations, including boundary value problems involving the generalised-Newtonian fluid flow equations (Baranger and Najib, 1990; Barrett and Liu, 1993). Despite its uses in solving flow problems of this type, there are only a few cases where the finite element method has been applied to simulating swimming in generalised-Newtonian fluids. For example, Montenegro-Johnson et al. (2012, 2013) utilised the finite element method when developing the 'method of femlets' for modelling various swimmers with prescribed kinematics within two-dimensional shear-thinning fluids. In this case, swimmers were represented through a distribution of unknown regularised forces, with the surrounding fluid flow and the value of the forces solved for using the FEM over a body-fitted mesh. In this chapter, we solve problems involving two-dimensional swimmers in three-dimensional computational domains over a non-body-conforming mesh.

Before outlining the HANS method, we first show how the equations of flow for a generalised-Newtonian fluid can be solved using the finite element method without immersed forces. This

solution method will later be built upon to form part of the HANS method for simulating swimmers within generalised-Newtonian fluids. After formulating this method, we validate the solution via comparison to the solution produced through a semi-analytic method for the pressure-driven flow of a BCC4p fluid in a cylindrical pipe.

After outlining the solution process without immersed forces, we formulate the HANS method for modelling swimmers within shear-thinning fluids. This is done in several stages: firstly, we consider how a single elastic Hookean spring behaves in a shear-thinning fluid. This simple 'toy problem' allows us to demonstrate the formulation and implementation of the HANS method. Finally, we describe how the HANS method is formulated to simulate sperm-like swimmers with flexible elastic flagella in shear-thinning fluids. In Chapter 4, this method is used to study the effect of shear-thinning rheology on the propulsion of human sperm.

3.2 The finite element method for generalised Newtonian flows

In this section, we demonstrate how the equation of flow for a generalised-Newtonian fluid without the presence of a swimmer (i.e. $\boldsymbol{F} = \mathbf{0}$ in equation (1.16)) can be solved using the finite element method. Whilst the FEM solution to this problem has previously been derived by Barrett and Liu (1993) (for BCC4p and power law fluids), we recap the formulation and implementation here to later build upon when developing the HANS method.

We begin by formulating the boundary value problem for a generalised-Newtonian fluid within a three-dimensional computational domain with a mixture of Neumann and Dirichlet boundary conditions. Following this, we discuss the derivation of the finite element weak formulation and the linearisation of the non-linear flow problem via a Picard iterative process. We then discuss the implementation of the solution method, including the generation of the finite element mesh and numerical integral calculation. Following this, in Section 3.3, we verify the formulation and implementation of the finite element procedure by comparing the

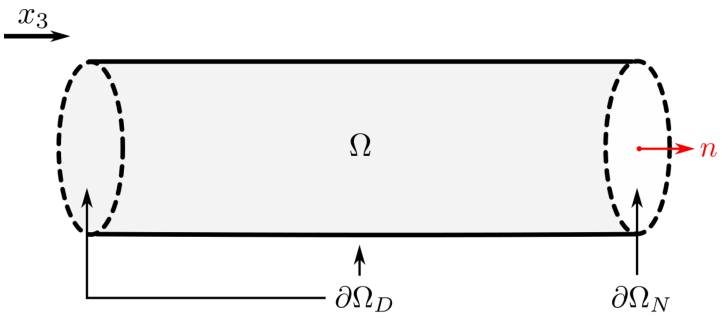


Figure 3.1: Schematic of an example cylindrical domain $\Omega \in \mathbb{R}^3$. The curved surface and pipe 'inlet' form the boundary $\partial\Omega_D$, with the remaining circular 'oulet' forming the boundary $\partial\Omega_N$. The outward pointing unit normal n is shown on one of the circular faces.

solution to that produced through a semi-analytic method for the specific problem of pressure-driven flow of a BCC4p fluid within a cylindrical pipe.

3.2.1 Formulation

We consider a bounded domain $\Omega \subset \mathbb{R}^3$ with boundary $\partial\Omega$, which has an outward-pointing unit normal $\boldsymbol{n}$. We assume that the boundary can be decomposed into two disjoint parts $\partial\Omega_N$ and $\partial\Omega_D$, where Neumann and Dirichlet boundary conditions are applied respectively (see Figure 3.1). The domain contains a generalised-Newtonian fluid where no external body force is exerted on the fluid, i.e. $\boldsymbol{F} = \boldsymbol{0}$ in equation (1.16a). The boundary value problem is given by

$$\nabla \cdot [2\mu(\dot{\gamma}(\boldsymbol{u}))\boldsymbol{\varepsilon}(\boldsymbol{u})] - \nabla p = \boldsymbol{0} \text{ in } \Omega, \tag{3.1a}$$

$$\nabla \cdot \boldsymbol{u} = 0 \text{ in } \Omega, \tag{3.1b}$$

$$[-p\mathbf{I} + 2\mu\left(\dot{\gamma}\left(\boldsymbol{u}\right)\right)\boldsymbol{\varepsilon}\left(\boldsymbol{u}\right)] \cdot \boldsymbol{n} = \boldsymbol{0} \text{ on } \partial\Omega_N, \tag{3.1c}$$

$$\boldsymbol{u} = \boldsymbol{h} \text{ on } \partial\Omega_D. \tag{3.1d}$$

The Dirichlet boundary condition $\boldsymbol{u} = \boldsymbol{h}$ is applied on $\partial\Omega_D$ and the zero normal stress condition is applied on $\partial\Omega_N$. The form of the viscosity $\mu\left(\dot{\gamma}\left(\boldsymbol{u}\right)\right)$ is given via the BCC4p constitutive law defined in equation (1.14).

To derive the finite element weak formulation, we first consider the function spaces

$$W(\Omega) = \left\{ \boldsymbol{v} \in H^1\left(\Omega; \mathbb{R}^3\right) \,:\, \boldsymbol{v} = \boldsymbol{0} \text{ on } \partial\Omega_D \right\}, \tag{3.2a}$$

$$V(\Omega) = \left\{ \boldsymbol{v} \in H^1\left(\Omega; \mathbb{R}^3\right) \,:\, \boldsymbol{v} = \boldsymbol{h} \text{ on } \partial\Omega_D \right\}, \tag{3.2b}$$

$$L_0^2(\Omega) = \left\{ q \in L^2\left(\Omega; \mathbb{R}^3\right) \,:\, \int_\Omega q d\boldsymbol{x} = 0 \right\}, \tag{3.2c}$$

where $H^1\left(\Omega; \mathbb{R}^3\right)$ is the Sobolev space of order 1 and $L^2\left(\Omega; \mathbb{R}^3\right)$ is the space of square-integrable functions on $\Omega \subset \mathbb{R}^3$. Multiplying equations (3.1a) and (3.1b) by test functions $\boldsymbol{v} \in W(\Omega)$ and $q \in L_0^2(\Omega)$ respectively and integrating by parts yields the problem

$$\text{Find } (\boldsymbol{u}, p) \in V(\Omega) \times L_0^2(\Omega) \text{ such that } \forall (\boldsymbol{v}, q) \in W(\Omega) \times L_0^2(\Omega),$$

$$\int_\Omega 2\mu\left(\dot{\gamma}(\boldsymbol{u})\right)\left[\boldsymbol{\varepsilon}(\boldsymbol{u}) \,:\, \boldsymbol{\varepsilon}(\boldsymbol{v})\right] d\boldsymbol{x} - \int_\Omega p\left[\nabla \cdot \boldsymbol{v}\right] d\boldsymbol{x} = 0, \tag{3.3a}$$

$$\int_\Omega q\left[\nabla \cdot \boldsymbol{u}\right] d\boldsymbol{x} = 0, \tag{3.3b}$$

which is the weak formulation of the boundary value problem (3.1), as derived previously by Barrett and Liu (1993). Existence and uniqueness of the solution to the system (3.3) was shown by Baranger and Najib (1990) for fluids modelled using both the BCC4p and power law constitutive relations.

The system (3.3) is non-linear in $\boldsymbol{u}$ due to the dependence of the viscosity on the shear rate $\dot{\gamma}(\boldsymbol{u})$. It can be linearised using Picard's method, an iterative process commonly used for approximating solutions to systems of differential equations. Given an initial guess for the unknown velocity solution $\boldsymbol{u}^0$, the Picard iteration consists of constructing a sequence of functions $\boldsymbol{u}^1, \boldsymbol{u}^2, \ldots, \boldsymbol{u}^r$ representing approximate solutions to the system (3.3). The r^{th} function is calculated using the known $(r-1)^{\text{th}}$ solution, with the approximation becoming increasing accurate the more iterations used. The Picard iteration is applied to the system (3.3) via the following process:

1. Initilise with $r = 0$ and $\boldsymbol{u}^0 := \boldsymbol{u}^0(\boldsymbol{x}) = \boldsymbol{0}$ for every $\boldsymbol{x} \in \Omega$.

2. Set $r = r + 1$.

3. Find $(\boldsymbol{u}^r, p^r) \in V(\Omega) \times L_0^2(\Omega)$ such that $\forall (\boldsymbol{v}, q) \in W(\Omega) \times L_0^2(\Omega)$,

$$\int_\Omega 2\mu\left(\dot{\gamma}\left(\boldsymbol{u}^{r-1}\right)\right)\left[\boldsymbol{\varepsilon}(\boldsymbol{u}^r) : \boldsymbol{\varepsilon}(\boldsymbol{v})\right] d\boldsymbol{x} - \int_\Omega p^r\left[\nabla \cdot \boldsymbol{v}\right] d\boldsymbol{x} = 0, \tag{3.4a}$$

$$\int_\Omega q\left[\nabla \cdot \boldsymbol{u}^r\right] d\boldsymbol{x} = 0. \tag{3.4b}$$

4. Repeat steps 2–3 until converged, i.e. until the difference between successive solutions is small.

For each r this system is linear, since the viscosity is calculated from the velocity from the previous iteration $\boldsymbol{u}^{r-1}$. An appropriate metric for the convergence in Step 4 of the algorithm will be discussed following outlining the discretisation of the system (3.4).

Let Ω_h represent a partition of the domain Ω with mesh size h that consists of arbitrary polyhedra elements. Consider the finite-dimensional subspaces $W^h \subset W(\Omega)$, $Q^h \subset L_0^2(\Omega)$. We define

$$W^h := \operatorname{span}\{\varphi_1(\boldsymbol{x}), \varphi_2(\boldsymbol{x}), \ldots, \varphi_N(\boldsymbol{x})\}, \tag{3.5a}$$

$$Q^h := \operatorname{span}\{\psi_1(\boldsymbol{x}), \psi_2(\boldsymbol{x}), \ldots, \psi_M(\boldsymbol{x})\}, \tag{3.5b}$$

where $\{\varphi_n(\boldsymbol{x})\}_{n=1}^N$, $\{\psi_m(\boldsymbol{x})\}_{m=1}^M$ are suitable piecewise polynomial functions defined on Ω_h, referred to as the velocity and pressure basis functions respectively. The discrete form of the system (3.4) is written as

$$\text{Find } \left(\boldsymbol{u}_h^r, p_h^r\right) \in W^h \times Q^h \text{ such that } \forall (\boldsymbol{v}_h, q_h) \in W^h \times Q^h,$$

$$\int_{\Omega_h} 2\mu\left(\dot{\gamma}\left(\boldsymbol{u}_h^{r-1}\right)\right)\left[\boldsymbol{\varepsilon}\left(\boldsymbol{u}_h^r\right) : \boldsymbol{\varepsilon}(\boldsymbol{v}_h)\right] d\boldsymbol{x} - \int_{\Omega_h} p_h^r\left[\nabla \cdot \boldsymbol{v}_h\right] d\boldsymbol{x} = 0, \tag{3.6a}$$

$$\int_{\Omega_h} q_h\left[\nabla \cdot \boldsymbol{u}_h^r\right] d\boldsymbol{x} = 0. \tag{3.6b}$$

At each iteration r, we apply the velocity expansion

$$u_{ih}^{r}(\boldsymbol{x}) = \sum_{n=1}^{N} U_{in}^{r} \varphi_n(\boldsymbol{x}), \tag{3.7}$$

for each component of the discrete velocity solution $\boldsymbol{u}_h^r = \left(u_{1h}^r, u_{2h}^r, u_{3h}^r\right)$. Similarly, the pressure is expanded in terms of its basis functions via

$$p_h^r(\boldsymbol{x}) = \sum_{m=1}^{M} P_m^r \psi_m(\boldsymbol{x}). \tag{3.8}$$

Substituting the expansions for $\boldsymbol{u}_h^r$ and p_h^r into the discrete form of the Picard iteration (3.6) allows us to obtain the linear system given by

$$\underbrace{\begin{bmatrix} \mathrm{A}_{11}^{r-1} & \mathrm{A}_{12}^{r-1} & \mathrm{A}_{13}^{r-1} & -\mathrm{B}_1^T \\ \mathrm{A}_{21}^{r-1} & \mathrm{A}_{22}^{r-1} & \mathrm{A}_{23}^{r-1} & -\mathrm{B}_2^T \\ \mathrm{A}_{31}^{r-1} & \mathrm{A}_{32}^{r-1} & \mathrm{A}_{33}^{r-1} & -\mathrm{B}_3^T \\ \mathrm{B}_1 & \mathrm{B}_2 & \mathrm{B}_3 & 0 \end{bmatrix}}_{\mathrm{Z}} \underbrace{\begin{bmatrix} \boldsymbol{U}_1^r \\ \boldsymbol{U}_2^r \\ \boldsymbol{U}_3^r \\ \boldsymbol{P}^r \end{bmatrix}}_{\boldsymbol{c}} = \mathbf{0}. \tag{3.9}$$

Here, the solution vector $\boldsymbol{c}$ consists of the nodal values of the velocity and pressure, given by $\boldsymbol{U}_i^r = \left[U_{i1}^r, U_{i2}^r, \ldots, U_{iN}^r\right]^T$ and $P^r = [P_1^r, P_2^r, \ldots, P_M^r]^T$ respectively for $i = 1, 2, 3$. The stiffness matrix Z can be constructed from the blocks

$$\mathrm{A}_{11}^{r-1} = 2\mathrm{K}_{11}^{r-1} + \mathrm{K}_{22}^{r-1} + \mathrm{K}_{33}^{r-1}, \tag{3.10a}$$

$$\mathrm{A}_{22}^{r-1} = 2\mathrm{K}_{22}^{r-1} + \mathrm{K}_{11}^{r-1} + \mathrm{K}_{33}^{r-1}, \tag{3.10b}$$

$$\mathrm{A}_{33}^{r-1} = 2\mathrm{K}_{33}^{r-1} + \mathrm{K}_{11}^{r-1} + \mathrm{K}_{22}^{r-1}, \tag{3.10c}$$

$$\mathrm{A}_{ij}^{r-1} = \mathrm{K}_{ij}^{r-1} \text{ for } i \neq j, \tag{3.10d}$$

where

$$[K_{ij}^{r-1}]_{nm} = \int_{\Omega_h} \mu\left(\dot{\gamma}\left(\boldsymbol{u}^{r-1}\right)\right) \frac{\partial \varphi_n}{\partial x_j} \frac{\partial \varphi_m}{\partial x_i} d\boldsymbol{x}, \quad n, m = 1, 2, \ldots, N, \tag{3.11a}$$

$$[B_i]_{nm} = \int_{\Omega_h} \psi_n \frac{\partial \varphi_m}{\partial x_i} d\boldsymbol{x}, \quad n = 1, 2, \ldots, M, \quad m = 1, 2, \ldots, N, \tag{3.11b}$$

and $i, j = 1, 2, 3$. Note that $[K_{ij}^{r-1}]_{nm}$ represents the $(n, m)^{\text{th}}$ entry of the matrix K_{ij}^{r-1}, and similarly $[B_i]_{nm}$ the $(n, m)^{\text{th}}$ entry of the matrix B_i. Finally, the right-hand-side vector in the system (3.9) is a zero vector of length $3N + M$.

Constructing and solving the linear system (3.9) at each iteration r allows us to calculate $\boldsymbol{u}_h^r$ and p_h^r. The Picard iteration is deemed converged when $\|\boldsymbol{c}^r - \boldsymbol{c}^{r-1}\|_2 < \delta_{\text{tol}}$. Here $\boldsymbol{c}^r$ denotes the solution vector in the system (3.9) at the iteration r, $\|\cdot\|_2$ represents the Euclidean norm (2-norm) and δ_{tol} is a small tolerance, set in what follows to $\delta_{\text{tol}} = 1 \times 10^{-9}$. Once converged, the Picard iteration provides solutions $\boldsymbol{u}$ and p of the non-linear problem (3.1). In what follows, the linear system (3.9) is termed [DGN]. To construct [DGN], we must choose a suitable mesh, the form of the velocity and pressure basis functions, and how to calculate the required volume integrals in the system (3.11).

3.2.2 Implementation

The domain is divided into hexahedron elements to form a mesh. We generate structured meshes (Figure 3.2a), defined as meshes with a regular pattern of connectivity of nodes. A structured mesh has many advantages over the alternative, an unstructured mesh (Figure 3.2b). Due to the uniform pattern of the elements, each node in a structured mesh can be identified by a unique index vector (I, J, K). The physical location of the nodes can be stored in a table, and neighbours can be identified by adding or subtracting one from each of the three indices. In an unstructured mesh, each node is assigned an arbitrary number since the lack of any pattern in the node organisation does not allow for any specific ordering. This means that the connectivity of the nodes needs to be stored in addition to their locations to identify neighbours. For this reason, the generation of an unstructured mesh is more computationally complicated

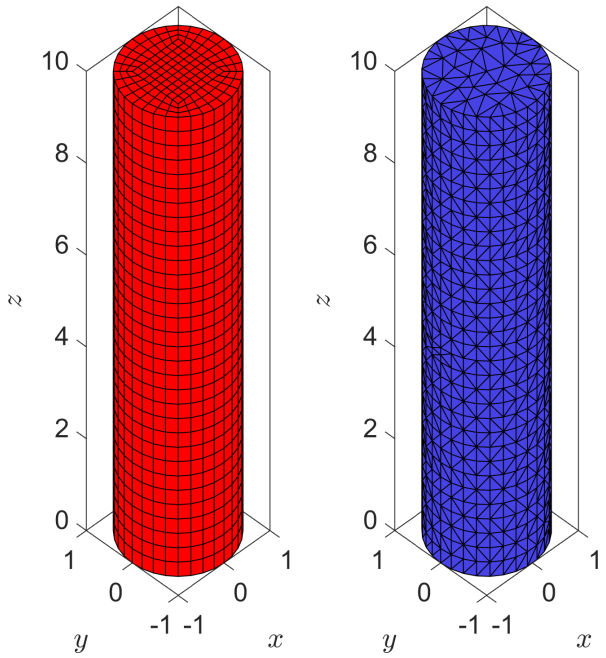


Figure 3.2: Examples of (a) a structured mesh and, (b) an unstructured mesh of a cylindrical pipe of radius $a = 1$ and length $L = 10$. Whilst only the element faces on the outside of the cylinder are shown, the entire volume of the pipes is also meshed with the same pattern.

and costly than a structured mesh. We will be considering cuboidal domains throughout the majority of this thesis, which are very simple to mesh using a uniform pattern of hexahedral elements.

Basis functions

To discretise the problem, we must choose the finite element subspaces $W^h \subset W(\Omega)$ and $Q^h \subset L^2_0(\Omega)$. The stability of the finite element discretisation requires the inf-sup condition of the theory of mixed methods to be satisfied (Babuška, 1973; Brezzi, 1974), that is, there exists $\beta_h \in \mathbb{R}$ such that

$$\inf_{q \in Q^h} \sup_{\boldsymbol{v} \in W^h} \frac{\int_{\Omega_h} q_h \boldsymbol{\nabla} \cdot \boldsymbol{v}_h d\boldsymbol{x}}{\|\boldsymbol{v}_h\|_{W(\Omega_h)} \|q_h\|_{L^2_0(\Omega_h)}} \geq \beta_h > 0. \tag{3.12}$$

One particular popular choice of approximations that satisfies this condition was introduced by Taylor and Hood (1973). In this case, the velocity basis functions contained within the spanning set of W^h are chosen to be piecewise quadratic (or tri-quadratic), with the pressure

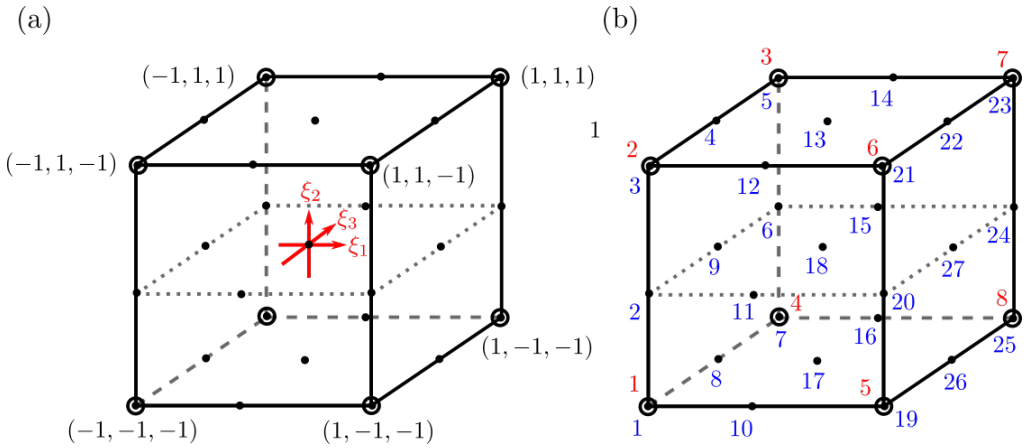


Figure 3.3: The reference hexahedron element with twenty-seven velocity nodes (black points) and eight pressure nodes (black circles). In (a), the coordinates of the pressure nodes are indicated in reference to the Cartesian coordinate system (ξ_1, ξ_2, ξ_3). In (b), the ordering of the velocity (blue) and pressure (red) nodes are shown within the element.

basis functions forming Q^h chosen to be piecewise linear (tri-linear). The general form of the velocity basis functions $\{\varphi_n(\boldsymbol{x})\}_{n=1}^N$ are given by

$$\varphi_n(\boldsymbol{x}) = \left[a_1 + a_2 x_1 + a_3 x_1^2\right]\left[a_4 + a_5 x_2 + a_6 x_2^2\right]\left[a_7 + a_8 x_3 + a_9 x_3^2\right], \tag{3.13}$$

for suitable constants $a_1, a_2, \ldots, a_9$ where $\boldsymbol{x} = [x_1, x_2, x_3]^T$. The general form of the basis functions for pressure $\{\psi_m(\boldsymbol{x})\}_{m=1}^M$ are given by

$$\psi_m(\boldsymbol{x}) = [b_1 + b_2 x_1]\,[b_3 + b_4 x_2]\,[b_5 + b_6 x_3], \tag{3.14}$$

for suitable constants $b_1, b_2, \ldots, b_6$. We consider a mapping from each element $E^{(e)}$ of the mesh to the reference element $\hat{E} = [-1, 1] \times [-1, 1] \times [-1, 1]$, centred at the origin of the Cartesian coordinate system (ξ_1, ξ_2, ξ_3). All basis functions are calculated on the reference element and subsequently mapped to all other elements when required (for details, see Appendix A). This drastically reduces computational time compared to calculating the basis functions explicitly on each element, and is common practice in most finite element routines (Anderson and Wendt, 1995; Kuzmin and Hämäläinen, 2015). For tri-quadratic velocity and tri-linear pressure basis functions, the reference hexahedron element contains twenty-seven velocity nodes

$\left\{\boldsymbol{\xi}_a^{(v)}\right\}_{a=1}^{27}$ and eight pressure nodes $\left\{\boldsymbol{\xi}_b^{(p)}\right\}_{b=1}^{8}$. These nodes can be seen in Figure 3.3a, with their ordering within the element shown in Figure 3.3b. The basis functions on the reference element should satisfy

$$\hat{\varphi}_a\left(\boldsymbol{\xi}_b^{(v)}\right) = \delta_{ab} \text{ for } a, b = 1, 2, \ldots, 27, \tag{3.15a}$$

$$\hat{\psi}_a\left(\boldsymbol{\xi}_b^{(p)}\right) = \delta_{ab} \text{ for } a, b = 1, 2, \ldots, 8, \tag{3.15b}$$

where δ_{ab} is the Kronecker delta function

$$\delta_{ab} = \begin{cases} 1 \text{ if } a = b, \\ 0 \text{ if } a \neq b. \end{cases} \tag{3.16}$$

Here, $\left\{\hat{\varphi}_a(\boldsymbol{\xi})\right\}_{a=1}^{27}$ and $\left\{\hat{\psi}_b(\boldsymbol{\xi})\right\}_{b=1}^{8}$ represent the basis functions on the reference element for velocity and pressure respectively. The b^{th} pressure basis function on the reference element which satisfies (3.15b) is given by

$$\hat{\psi}_b(\boldsymbol{\xi}) = \frac{1}{8}\left[1 + \xi_{1b}^{(p)}\xi_1\right]\left[1 + \xi_{2b}^{(p)}\xi_2\right]\left[1 + \xi_{3b}^{(p)}\xi_3\right] \text{ for } b = 1, 2, \ldots, 8. \tag{3.17}$$

Such a concise formula does not exist for the a^{th} velocity basis function on the reference element satisfying (3.15a). These functions can be found in Appendix B for reference.

The blocks of the algebraic system [DGN] are constructed using an element-wise integration procedure. In this way, the integrals over Ω_h are split into a sum of the contributions from each element. For example, consider the integral

$$[B_1]_{nm} = \int_{\Omega_h} \psi_n \frac{\partial \varphi_m}{\partial x_1} d\boldsymbol{x}, \quad n = 1, 2, \ldots, M, \quad m = 1, 2, \ldots, N. \tag{3.18}$$

We split this integral into the sum over the element integrals via

$$[B_1]_{nm} = \int_{\Omega_h} \psi_n \frac{\partial \varphi_m}{\partial x_1} d\boldsymbol{x} = \sum_e \left[B_1^{(e)}\right]_{nm}, \quad \left[B_1^{(e)}\right]_{nm} = \int_{E^{(e)}} \psi_n \frac{\partial \varphi_m}{\partial x_1} d\boldsymbol{x}, \tag{3.19}$$

where $\left[B_1^{(e)}\right]_{nm} \neq 0$ if and only if the nodes with indices n and m also belong to the element $E^{(e)}$. Further details of the implementation of this procedure can be found in Appendix C.

Numerical integration schemes

In order to construct the system [DGN], we need to be able to evaluate the element-wise form of the integrals (3.11a) and (3.11b). Integrals of this type can easily be calculated numerically using a three-dimensional Gauss-Legendre quadrature rule with Q points per direction for a total of $P := Q^3$ points. In this case, for a general function on the reference element $f(\xi_1, \xi_2, \xi_3)$ we have that

$$\int_{\hat{E}} f(\xi_1, \xi_2, \xi_3) d\boldsymbol{\xi} = \sum_{p=1}^{P} w^{[p]} f\left(\xi_1^{[p]}, \xi_2^{[p]}, \xi_3^{[p]}\right), \tag{3.20}$$

where $w^{[p]}$ are the weights associated with the quadrature points $\left\{ \left(\xi_1^{[p]}, \xi_2^{[p]}, \xi_3^{[p]}\right) \right\}_{p=1}^{P}$. In what follows, $P = 125$ (or $Q = 5$) is appropriate for calculating all integrals required for the construction of [DGN]. In particular, this choice is exact for the integral of the quadratic basis functions in (3.11b), and is approximate for the calculation of (3.11a) due to the presence of the viscosity $\mu\left(\dot{\gamma}\left(\boldsymbol{u}^{r-1}\right)\right)$.

In equation (3.11a), the viscosity must be evaluated at the quadrature points associated with the Gauss-Legendre quadrature rule. To do this, we first calculate the shear rate at these points, which requires the derivatives of the velocity $\boldsymbol{u}^{r-1}$ present in $\boldsymbol{\varepsilon}(\boldsymbol{u}^{r-1})$. To calculate these derivatives at general point $(z_1, z_2, z_3) \in E^{(e)}$ we first transform the point to the reference element $\hat{E}$ to give coordinates $(\zeta_1, \zeta_2, \zeta_3) \in \hat{E}$ in terms of the Cartesian coordinate system (ξ_1, ξ_2, ξ_3). We can then calculate the velocity derivatives via

$$\begin{aligned} \frac{\partial u_i^{r-1}(z_1, z_2, z_3)}{\partial x_b} = \sum_{a=1}^{27} U_{ia}^{r-1} \Bigg\{ & \left[\left(J^{(e)}(\zeta_1, \zeta_2, \zeta_3) \right)^{-1} \right]_{b1} \frac{\partial \hat{\varphi}_a(\zeta_1, \zeta_2, \zeta_3)}{\partial \xi_1} \\ & + \left[\left(J^{(e)}(\zeta_1, \zeta_2, \zeta_3) \right)^{-1} \right]_{b2} \frac{\partial \hat{\varphi}_a(\zeta_1, \zeta_2, \zeta_3)}{\partial \xi_2} \\ & + \left[\left(J^{(e)}(\zeta_1, \zeta_2, \zeta_3) \right)^{-1} \right]_{b3} \frac{\partial \hat{\varphi}_a(\zeta_1, \zeta_2, \zeta_3)}{\partial \xi_3} \Bigg\}, \end{aligned} \tag{3.21}$$

for $b = 1, 2, 3$, where $J^{(e)}$ is the Jacobian matrix of the transformation from $\hat{E} \to E^{(e)}$ and

$\left\{U_{ia}^{r-1}\right\}_{a=1}^{27}$ are the nodal values of the i^{th} velocity component on the element $E^{(e)}$ (at iteration $r-1$). We can also find $\boldsymbol{u}^r(z_1, z_2, z_3)$ and $p^r(z_1, z_2, z_3)$ in a similar way using the interpolation rules

$$u_i^r(z_1, z_2, z_3) = \sum_{a=1}^{27} U_{ia}^r \hat{\varphi}_a(\zeta_1, \zeta_2, \zeta_3), \tag{3.22a}$$

$$p^r(z_1, z_2, z_3) = \sum_{b=1}^{8} P_b^r \hat{\psi}_b(\zeta_1, \zeta_2, \zeta_3), \tag{3.22b}$$

where $\left\{P_b^r\right\}_{b=1}^{8}$ are the nodal values of the pressure on the element $E^{(e)}$ (at iteration r).

The system [DGN] is constructed at each iteration using the procedures discussed above, namely the chosen form of the basis functions and the numerical calculation of the required integrals. It can then be solved using the MATLAB® backslash command '\' in order to acquire the velocity and pressure solutions at all mesh nodes. Once the Picard iterations converge, the formulas (3.22a) and (3.22b) can be used to find the velocity and pressure solutions at any point within the domain if desired.

3.3 Validating the generalised Newtonian solver

In the previous section, we recapped the derivation and implementation of the finite element method for the generalised-Newtonian fluid flow equations (1.16) with no external body force. This solver will later form a crucial part of our method for simulating human sperm within shear-thinning fluids, and as such it is important that we verify our implementation through comparison with an alternative solution method. To do this, we will apply the method to the specific problem of the unidirectional pressure-driven flow of a BCC4p fluid in a cylindrical pipe. Whilst this problem does not have a known analytic solution, we can derive a semi-analytic solution which can be used to validate the output of the finite element solver. In particular, we wish to verify that the velocities and shear rates calculated via the two methods agree, and to explore the effect of shear-thinning rheology on the resultant flow profile.

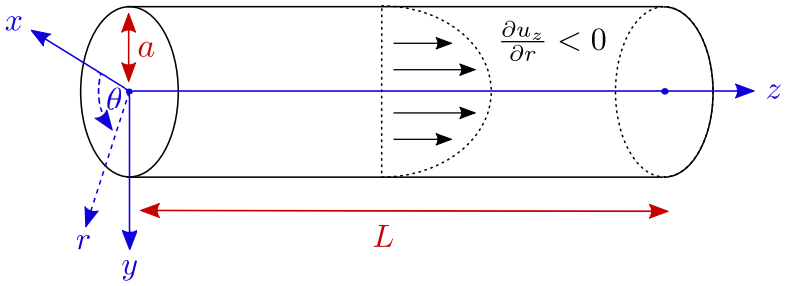


Figure 3.4: Schematic of a cylindrical pipe of radius a and length L in the cylindrical coordinate system (r, θ, z).

3.3.1 Deriving a semi-analytic solution

We begin by deriving the semi-analytic solution for the problem. Consider a cylindrical pipe of radius a and length L which extends in the z direction in the cylindrical coordinate system (r, θ, z) (see Figure 3.4). The flow of a BCC4p fluid within the pipe is driven by an imposed pressure gradient dp/dz. We assume that the flow is steady, unidirectional and axisymmetric, which yields the continuity equation

$$\frac{\partial u_z}{\partial z} = 0. \tag{3.23}$$

Since $\partial u_z/\partial\theta = 0$ by axisymmetry, the axial velocity u_z is a function of the radial component r only. The axial momentum equation is therefore given by

$$\frac{1}{r}\frac{d}{dr}\left[\mu\left(\dot{\gamma}(\boldsymbol{u})\right) r \frac{\partial u_z}{\partial r}\right] - \frac{dp}{dz} = 0, \quad 0 \leq r \leq a, \tag{3.24}$$

where we require that the velocity on the surface of the cylinder is zero, $u_z(a) = 0$. Defining Δp as the pressure drop across the pipe means that we can write $-dp/dz = \Delta p/L > 0$. Integrating equation (3.24) with respect to r then dividing by r yields

$$\mu\left(\dot{\gamma}(\boldsymbol{u})\right)\frac{\partial u_z}{\partial r} + \frac{r\Delta p}{2L} + \frac{C}{r} = 0, \tag{3.25}$$

where the constant of integration C is equal to zero since we require $\partial u_z/\partial r$ to be finite at $r = 0$. Due to the assumptions of unidirectional ($u_r = u_\theta = 0$) and axisymmetric ($\partial(\cdot)/\partial\theta = 0$)

flow, the shear rate can be expressed as

$$\dot{\gamma}(\boldsymbol{u}) = -\frac{\partial u_z}{\partial r}. \tag{3.26}$$

In this way, equation (3.25) can be written in terms of the shear rate via

$$-\mu\left(\dot{\gamma}(\boldsymbol{u})\right)\dot{\gamma}(\boldsymbol{u}) + \frac{r\Delta p}{2L} = 0, \tag{3.27}$$

where the form of $\mu\left(\dot{\gamma}(\boldsymbol{u})\right)$ is given by the BCC4p constitutive rule (1.14). We wish to examine how the shear rate and velocity of the fluid vary with r. Since equation (3.27) is non-linear in r, we cannot easily find an analytic solution $u_z(r)$. Instead, we discretise $0 \leq r \leq a$ via a sequence of $Q+1$ equally spaced nodes $\left\{r_q\right\}_{q=1}^{Q+1}$ where $r_q - r_{q-1} = \Delta r := a/Q$ for $q = 2, \ldots, Q+1$. We define the shear rate evaluated at these nodes $\dot{\gamma}_q(\boldsymbol{u})$ via

$$\dot{\gamma}_q(\boldsymbol{u}) = -\left.\frac{\partial u_z}{\partial r}\right|_{r_q}, \quad q = 1, 2, \ldots, Q+1. \tag{3.28}$$

Thus, for each node q, we have a non-linear algebraic equation in terms of $\dot{\gamma}_q(\boldsymbol{u})$ given by

$$-\mu\left(\dot{\gamma}_q(\boldsymbol{u})\right)\dot{\gamma}_q(\boldsymbol{u}) + \frac{r_q\Delta p}{2} = 0, \quad q = 1, 2, \ldots, Q+1, \tag{3.29}$$

i.e. the discrete form of (3.27). Given choices of the infinite shear-rate viscosity μ_∞, zero shear-rate viscosity μ_0, fluid relaxation time λ and shear-thinning index n, we may solve equation (3.29) for the shear rate at each node $\left\{r_q\right\}_{q=1}^{Q+1}$ using the built in MATLAB® non-linear equation solver `fsolve`. Following this, it remains to calculate the fluid velocity at these points. Approximating the derivative in the definition of the shear rate $\dot{\gamma}_q(\boldsymbol{u})$ via a backwards finite difference scheme yields

$$\frac{u_z(r_q) - u_z(r_{q-1})}{\Delta r} = -\dot{\gamma}_q(\boldsymbol{u}), \quad q = 1, 2, \ldots, Q+1. \tag{3.30}$$

The boundary condition $u_z(a) = 0$ means that we require that $u_z(r_{Q+1}) = 0$. Thus for $q = Q+1$

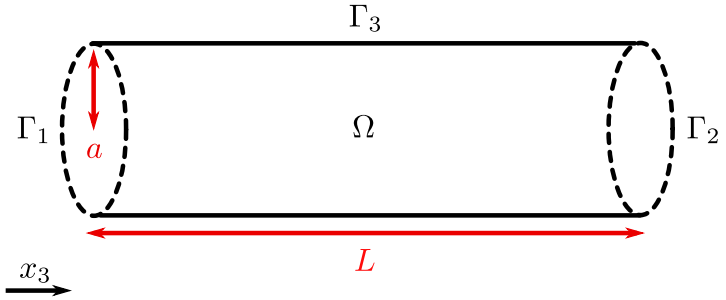


Figure 3.5: Schematic of the domain Ω, which is a cylindrical pipe of length L and radius a. The surface of the cylinder is split into three parts, Γ_1, Γ_2 and Γ_3 where Γ_1 is the pipe 'inlet', Γ_2 is the pipe 'outlet' and Γ_3 is the curved surface of the cylinder.

we have that

$$u_z(r_Q) = \dot{\gamma}_{Q+1}(\boldsymbol{u})\Delta r. \tag{3.31}$$

For the remaining q we calculate (in descending order of q)

$$u_z(r_q) = \dot{\gamma}_{q+1}(\boldsymbol{u})\Delta r + u_z(r_{q+1}). \tag{3.32}$$

This allows us to calculate the fluid velocity at each node $\left\{r_q\right\}_{q=1}^{Q+1}$ as required.

3.3.2 Comparison of the FEM and semi-analytic solutions

To solve the problem of the unidirectional flow of a BCC4p fluid in a cylindrical pipe using the finite element method, we again consider a cylindrical domain Ω which has length L and radius a. We define $\partial\Omega_D = \Gamma_1 \cup \Gamma_3$ and $\partial\Omega_N = \Gamma_2$ so that Dirichlet boundary conditions are applied on the curved face of the pipe and at the pipe inlet, and a Neumann boundary condition is applied at the outlet. A sketch of the geometry is shown in Figure 3.5 with the pipe extending in the x_3 direction in the Cartesian coordinate system (x_1, x_2, x_3) (equivalent to z in the cylindrical coordinate system (r, θ, z)). At the inlet, i.e. on Γ_1, we prescribe a Dirichlet boundary condition that specifies that the velocity is equal to the velocity calculated using the semi-analytic method discussed above. On the boundary Γ_2 we prescribe the Neumann

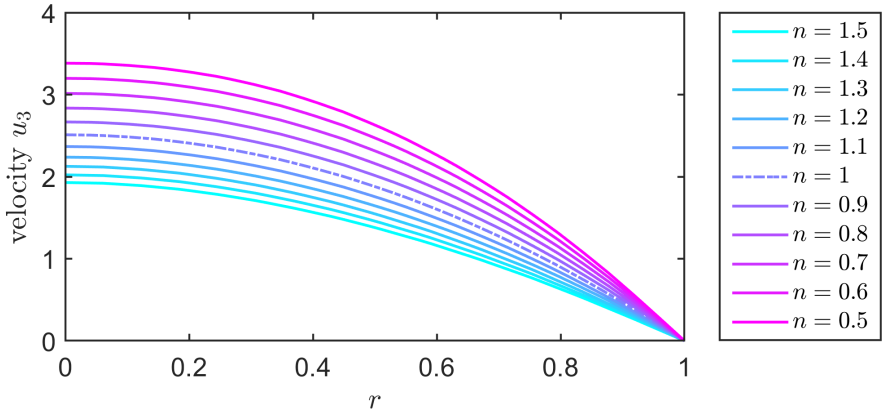


Figure 3.6: Velocity profiles for the flow of a BCC4p fluid in a cylindrical pipe of radius $a = 1$ and length $L = 10$, obtained using the finite element solver. Here the fluid parameters are $\mu_0 = 1$, $\mu_\infty = 0.5$ and $\lambda = 1$. We observe how different values of $n \in [0.5, 1.5]$ affect the axial velocity component u_3.

condition

$$\boldsymbol{\sigma} \cdot \boldsymbol{n} = [-p\mathbf{I} + 2\mu(\dot{\gamma}(\boldsymbol{u}))] \cdot \boldsymbol{n} = \mathbf{0}. \tag{3.33}$$

Finally, on Γ_3 we apply the no-slip boundary condition $\boldsymbol{u} = \mathbf{0}$, as in the semi-analytic case. We generate a mesh consisting of hexahedron elements following the criteria outlined in Section 3.2 (see Figure 3.2a).

For both methods, we set

$$L = 10, \quad a = 1, \quad \mu_0 = 1, \quad \mu_\infty = 0.5, \quad \lambda = 1, \quad \Delta p = 100, \tag{3.34}$$

and consider varying $n \in [0.5, 1.5]$. We calculate fluid velocities and shear rates via both methods at the pipe mid-plane ($x_3 = 5$ in the Cartesian coordinate system, or $z = 5$ in the cylindrical system).

In Figure 3.6, we show how the velocity profile over r produced from the finite element solver changes as the shear-thinning index n is varied between 0.5 (shear-thinning) and 1.5 (shear-thickening). This range of n is chosen in order to study a range of fluids from the strongly shear-thinning ($n = 0.5$) to weakly shear-thinning ($n = 0.9$), and even some shear-thickening ($n > 1$) fluids. We also plot the Newtonian ($n = 1$) case for comparison. The finite

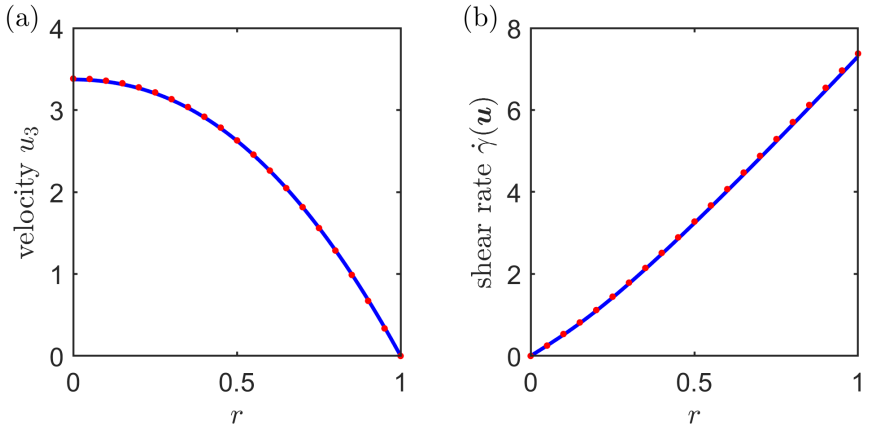


Figure 3.7: Comparison between the finite element (red dots) and semi-analytic (blue) solutions for the (a) axial velocity u_3 and, (b) shear rate $\dot{\gamma}(\boldsymbol{u})$ of the flow of a BCC4p fluid with shear-thinning index $n = 0.5$ in a cylindrical pipe of radius $a = 1$ and length $L = 10$.

element solution is calculated on a mesh consisting of $N_e = 6800$ elements. The Picard iterative method converges in between $N_{\text{it}} = 6$ and $N_{\text{it}} = 11$ iterations, with the number of iterations required reducing the closer n is to 1. We observe that the fluid velocity is higher at the crest of the velocity profile (at $r = 0$), the lower the value of n, or the more shear-thinning the fluid. Indeed, the fluid velocity is systematically higher the smaller the value of n, except on the boundary of the cylinder $r = 1$ where the velocity is zero in all cases due to the application of the no-slip boundary condition. Whilst we do not study shear-thickening fluids in this thesis, we note that the finite element method can also be used to solve the equations associated with this rheology. In particular, for shear-thickening fluids ($n > 1$), we observe that the fluid velocity is reduced at $r = 0$ compared to the velocity associated with a Newtonian fluid.

A comparison between the finite element and semi-analytic solutions for the velocity and shear rate with shear-thinning index $n = 0.5$ can be seen in Figure 3.7. Here, the semi-analytic solution is calculated over $N_r := Q + 1 = 1000$ equally spaced values of $0 \leq r \leq 1$. The finite element mesh again consists of $N_e = 6800$ elements, and the Picard iterative method converges after $N_{\text{it}} = 11$ iterations. Both the velocity and shear-rate are plotted against r, and the two solution methods show good agreement. The relative error between the finite element velocity

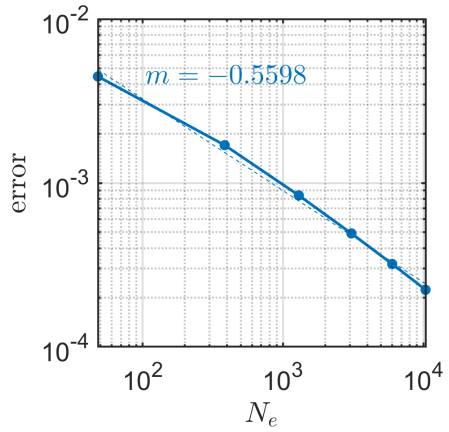


Figure 3.8: Relative error between the finite element and semi-analytic velocity solutions for the cylindrical pipe flow problem for varying degrees of mesh refinement in the finite element solution (blue solid line). A line of best fit is shown in blue dashed, with the gradient of this line given by m. Here the fluid is modelled using the BCC4p constitutive law with $n = 0.5$ and the cylindrical pipe is of radius $a = 1$ and length $L = 10$.

solution $\boldsymbol{u}_{\text{FEM}}$ and the semi-analytic velocity solution $\boldsymbol{u}_{\text{SA}}$ can be calculated via

$$\text{error} = \frac{\|\boldsymbol{u}_{\text{FEM}} - \boldsymbol{u}_{\text{SA}}\|_2}{\|\boldsymbol{u}_{\text{SA}}\|_2}. \tag{3.35}$$

In this case, the relative error between the solutions is 3.2037×10^{-4}, or approximately 0.03%.

To examine how mesh refinement affects the relative error, we calculate the finite element solution over various meshes with different numbers of elements ($48 \leq N_e \leq 10368$). The relative error between the finite element and semi-analytic solutions is calculated for each level of mesh refinement via equation (3.35). A plot of the error is given in Figure 3.8 for the case where $n = 0.5$. The error plotted on a log-log scale reduces approximately linearly with N_e, and therefore the finite element solution converges to the semi-analytic solution as the mesh is refined. For $N_e = 48$ elements in the finite element mesh, the relative error is equal to 4.46×10^{-3}, which reduces to 2.23×10^{-4} when $N_e = 10368$. As the shear-thinning parameter n is decreased, i.e. as shear-thinning effects are increased, the relative error between the semi-analytic and finite element solutions increases monotonically by a small amount. Thus, in the most shear-thinning case considered ($n = 0.1$), the relative errors are the largest over all $n \in [0.1, 1]$. Here, the error between the two solutions is 4.55×10^{-3} when $N_e = 48$ and reduces

to 2.28×10^{-4} when $N_e = 10368$. The smallest errors occur in the Newtonian case ($n = 1$), where the error is 4.41×10^{-3} when $N_e = 48$ and 2.16×10^{-4} when $N_e = 10368$. Clearly, the error for each N_e differs only slightly over $n \in [0.1, 1]$, and thus the error magnitudes presented in Figure 3.8 are typical of those observed over the whole parameter range.

We have verified that the finite element solver can be used to solve the fluid flow equations associated with a generalised-Newtonian fluid modelled using the BCC4p law. In particular, we have shown that the solution converges with successive mesh refinements to the semi-analytic solution when applied to the problem of unidirectional pressure-driven flow of a generalised-Newtonian fluid in a cylindrical pipe. Going forward, this solver will form an important part of our own novel method for simulating human sperm within shear-thinning fluids.

3.4 The hybrid method for a single embedded force in a generalised Newtonian fluid

In Section 3.2, we recapped how the finite element method can be used to solve the equations of flow associated with a generalised-Newtonian fluid with no external body force present ($\boldsymbol{F} = \boldsymbol{0}$ in system (1.16)). Following this discussion, in Section 3.3 we validated the formulation and our implementation by comparing the solution from the finite element solver with the solution produced via a semi-analytic solution method for the problem of pressure-driven flow of a shear-thinning fluid in a cylindrical pipe. The output of the FEM solver showed good agreement with the semi-analytic solver, with a relative error of approximately 0.03% for a suitably refined mesh consisting of $N_e = 6800$ hexahedron elements for a fluid with shear-thinning index $n = 0.5$.

In this section, we introduce the hybrid approach for non-linear swimming (HANS) for the case of modelling a single Hookean spring within a shear-thinning fluid. We begin by discussing the boundary value problem, following which we explain how the HANS method is formulated. We discuss the implementation of the technique, including deriving the linear system to solve at each timestep and iteration, along with discussions of dimensionless param-

eter groups, numerical integral calculation and an algorithm for the solution process. Finally, we provide results for how shear-thinning rheology affects the relaxation of the spring.

This simple example allows us to demonstrate the HANS method in the simplest possible case, where only one immersed force is present within the fluid domain, acting at the free end of the spring. Following this, in Section 3.5 we explain how the HANS method can be applied to the simulation of sperm-like swimmers in three-dimensional shear-thinning fluids. Finally, in Chapter 4 we will use this method to explore how shear-thinning rheology affects the propulsion of human sperm.

3.4.1 The boundary value problem

Consider a point force $\boldsymbol{f}$ acting at the location $\boldsymbol{y}$ within a fluid. The total force per unit volume exerted on the fluid at the point $\boldsymbol{x}$ is given by $\boldsymbol{F}(\boldsymbol{x}) = \boldsymbol{f}\delta(\boldsymbol{x}-\boldsymbol{y})$ where δ is a three-dimensional Dirac delta function, which satisfies

$$\int_{-\infty}^{\infty} f(\boldsymbol{x})\delta(\boldsymbol{x}-\boldsymbol{y})d\boldsymbol{x} = f(\boldsymbol{y}), \tag{3.36}$$

for any integrable function $f(\boldsymbol{x})$. The Dirac delta function can loosely be thought of as a function which is infinite at $\boldsymbol{x} = \boldsymbol{y}$ and zero elsewhere. Consequently, choosing $\boldsymbol{F}(\boldsymbol{x})$ in this way introduces a singularity into the flow when $\boldsymbol{x} = \boldsymbol{y}$. This can be problematic when considering numerical approaches to solving problems involving $\boldsymbol{F}(\boldsymbol{x})$, and as such we instead choose to represent $\boldsymbol{F}(\boldsymbol{x})$ via

$$\boldsymbol{F}(\boldsymbol{x}) = \boldsymbol{f}\phi_\epsilon(\boldsymbol{x}-\boldsymbol{y}), \tag{3.37}$$

where ϕ_ϵ is a regularised stokeslet cut-off function with the property that $\int_{\mathbb{R}^3}\phi_\epsilon(\boldsymbol{x})d\boldsymbol{x} = 1$, as discussed previously in Section 1.4.3. An appropriate choice of ϕ_ϵ is given in equation (1.31). In this way, $\boldsymbol{F}(\boldsymbol{x})$ remains finite throughout the fluid.

We assume that the force $\boldsymbol{f}$ acts at a point $\boldsymbol{y}$ that belongs to the bounded open domain $\Omega \subset \mathbb{R}^3$. This domain is occupied by a generalised-Newtonian fluid, where on the boundary of the domain $\partial\Omega$ we apply the no-slip boundary condition $\boldsymbol{u}(\boldsymbol{x},t) = \boldsymbol{0}$ for $t \geq 0$. The boundary

value problem is given by

$$\nabla \cdot [2\mu(\dot{\gamma}(\boldsymbol{u}(\boldsymbol{x},t)))\boldsymbol{\varepsilon}(\boldsymbol{u}(\boldsymbol{x},t))] - \nabla p(\boldsymbol{x},t) + \boldsymbol{f}\phi_\epsilon(\boldsymbol{x}-\boldsymbol{y}) = \boldsymbol{0} \text{ for } \boldsymbol{x} \in \Omega, \tag{3.38a}$$

$$\nabla \cdot \boldsymbol{u}(\boldsymbol{x},t) = 0 \text{ for } \boldsymbol{x} \in \Omega, \tag{3.38b}$$

$$\boldsymbol{u}(\boldsymbol{x},t) = \boldsymbol{0} \text{ for } \boldsymbol{x} \in \partial\Omega, \tag{3.38c}$$

where $t \geq 0$. This is the system (1.16) restricted to the computational domain Ω, with $\boldsymbol{F}$ chosen as in (3.37). Due to the presence of the regularised force in the domain, the solutions $\boldsymbol{u}(\boldsymbol{x},t)$ and $p(\boldsymbol{x},t)$ vary rapidly in particular in the vicinity of $\boldsymbol{y}$.

3.4.2 Formulation

To combat the issue of the rapidly varying solutions, we introduce the hybrid method. Here, at each point $\boldsymbol{x} \in \Omega$ we decompose the overall fluid velocity $\boldsymbol{u}(\boldsymbol{x},t)$ (and similarly the pressure $p(\boldsymbol{x},t)$) into two components $\boldsymbol{\mathcal{U}}(\boldsymbol{x},t)$ and $\boldsymbol{u}_S(\boldsymbol{x},t)$ via

$$\boldsymbol{u}(\boldsymbol{x},t) = \boldsymbol{\mathcal{U}}(\boldsymbol{x},t) + \boldsymbol{u}_S(\boldsymbol{x},t), \tag{3.39a}$$

$$p(\boldsymbol{x},t) = \mathcal{P}(\boldsymbol{x},t) + p_S(\boldsymbol{x},t). \tag{3.39b}$$

Note that we are not losing any part of the solutions $\boldsymbol{u}(\boldsymbol{x},t)$ and $p(\boldsymbol{x},t)$ by making this split, since the sum of $\boldsymbol{\mathcal{U}}(\boldsymbol{x},t)$ and $\boldsymbol{u}_S(\boldsymbol{x},t)$ equals $\boldsymbol{u}(\boldsymbol{x},t)$ by construction. The solutions $\boldsymbol{u}_S(\boldsymbol{x},t)$ and $p_S(\boldsymbol{x},t)$ are chosen to form a Newtonian approximation to the flow. Specifically, we choose $\boldsymbol{u}_S = \boldsymbol{S}^\epsilon \cdot \boldsymbol{f}$ and $p_S = \boldsymbol{P}^\epsilon \cdot \boldsymbol{f}$ (dependence on $\boldsymbol{x}$ and t dropped for clarity), which are the known regularised stokeslet solutions to the Newtonian problem in the infinite domain for a fluid with viscosity μ_S. This corresponds to the solution of the problem (1.8), with the form of $\boldsymbol{F}$ given as in equation (3.37). The kernels $\boldsymbol{S}^\epsilon$ and $\boldsymbol{P}^\epsilon$ are given in the system (1.32).

The solutions $\boldsymbol{u}_S(\boldsymbol{x},t)$ and $p_S(\boldsymbol{x},t)$, as described above, are by construction rapidly varying, particularly close to the point $\boldsymbol{y}$. In this way, they account for the majority of the rapidly varying nature of the overall fluid velocity $\boldsymbol{u}(\boldsymbol{x},t)$ and pressure $p(\boldsymbol{x},t)$ solutions over the domain

Ω. This means that the terms $\boldsymbol{\mathcal{U}}(\boldsymbol{x},t)$ and $\mathcal{P}(\boldsymbol{x},t)$, which correct for the non-Newtonian effects of the fluid, should be slowly varying across the domain. Later, we demonstrate that this is indeed the case. Whilst it is desirable that these solutions are slowly varying across the domain, we note that it is not a necessary condition for the implementation of the method. We will be employing the finite element method to solve for these unknown solutions, which in the case of slowly varying solutions can be computed over a coarse mesh of the fluid domain. However, the solutions $\boldsymbol{\mathcal{U}}(\boldsymbol{x},t)$ and $\mathcal{P}(\boldsymbol{x},t)$ could still be found if they varied more rapidly, but it would require a much finer mesh, particularly close to $\boldsymbol{y}$. Therefore, the slowly varying requirement is for computational efficiency and ease of implementation (for example, no requirement to generate meshes body-fitted to swimmers if the solution varies slowly), rather than for accuracy of the solution.

To form a system to solve for the unknown solutions $\boldsymbol{\mathcal{U}}(\boldsymbol{x},t)$ and $\mathcal{P}(\boldsymbol{x},t)$, we substitute the expressions for $\boldsymbol{u}(\boldsymbol{x},t)$ and $p(\boldsymbol{x},t)$ into the system (3.38). Dropping the dependence on $\boldsymbol{x}$ and t for brevity, this yields

$$\nabla\cdot[2\mu(\dot{\gamma}(\boldsymbol{\mathcal{U}}+\boldsymbol{u}_S))\boldsymbol{\varepsilon}(\boldsymbol{\mathcal{U}}+\boldsymbol{u}_S)]-\nabla[\mathcal{P}+p_S]+\boldsymbol{f}\phi_\epsilon(\boldsymbol{x}-\boldsymbol{y})=\boldsymbol{0}\text{ for }\boldsymbol{x}\in\Omega, \tag{3.40a}$$

$$\nabla\cdot[\boldsymbol{\mathcal{U}}+\boldsymbol{u}_S]=0\text{ for }\boldsymbol{x}\in\Omega, \tag{3.40b}$$

$$\boldsymbol{\mathcal{U}}+\boldsymbol{u}_S=\boldsymbol{0}\text{ for }\boldsymbol{x}\in\partial\Omega. \tag{3.40c}$$

To simplify this system, we exploit the linearity of the strain rate tensor, as well as the divergence and gradient operators. The momentum equation (3.40a) can be written as

$$\nabla\cdot[2\mu(\dot{\gamma}(\boldsymbol{\mathcal{U}}+\boldsymbol{u}_S))\boldsymbol{\varepsilon}(\boldsymbol{\mathcal{U}})]+\nabla\cdot[2\mu(\dot{\gamma}(\boldsymbol{\mathcal{U}}+\boldsymbol{u}_S))\boldsymbol{\varepsilon}(\boldsymbol{u}_S)]-\nabla\mathcal{P}-\nabla p_S+\boldsymbol{f}\phi_\epsilon(\boldsymbol{x}-\boldsymbol{y})=\boldsymbol{0}, \tag{3.41}$$

which is further simplified using equation (1.8a) with $\boldsymbol{F}$ chosen as in equation (3.37), yielding the simplified momentum equation

$$\nabla\cdot[2\mu(\dot{\gamma}(\boldsymbol{\mathcal{U}}+\boldsymbol{u}_S))\boldsymbol{\varepsilon}(\boldsymbol{\mathcal{U}})]+\nabla\cdot[2\mu(\dot{\gamma}(\boldsymbol{\mathcal{U}}+\boldsymbol{u}_S))\boldsymbol{\varepsilon}(\boldsymbol{u}_S)]-\nabla\mathcal{P}-\mu_S\nabla^2\boldsymbol{u}_S=\boldsymbol{0}\text{ for }\boldsymbol{x}\in\Omega. \tag{3.42}$$

The full system to solve for the unknown perturbation solutions $\boldsymbol{\mathcal{U}}$ and $\mathcal{P}$ is given by

$$\nabla \cdot [2\mu(\dot{\gamma}(\boldsymbol{\mathcal{U}} + \boldsymbol{u}_S))\boldsymbol{\varepsilon}(\boldsymbol{\mathcal{U}})] + \nabla \cdot [2\mu(\dot{\gamma}(\boldsymbol{\mathcal{U}} + \boldsymbol{u}_S))\boldsymbol{\varepsilon}(\boldsymbol{u}_S)]$$

$$-\nabla \mathcal{P} - \mu_S \nabla^2 \boldsymbol{u}_S = \boldsymbol{0} \qquad \text{for } \boldsymbol{x} \in \Omega, \tag{3.43a}$$

$$\nabla \cdot \boldsymbol{\mathcal{U}} = 0 \qquad \text{for } \boldsymbol{x} \in \Omega, \tag{3.43b}$$

$$\boldsymbol{\mathcal{U}} = -\boldsymbol{u}_S \quad \text{for } \boldsymbol{x} \in \partial\Omega, \tag{3.43c}$$

where the continuity equation has also been simplified via equation (1.8b). This system is similar to the boundary value problem (3.1), with several important differences. Firstly, the shear rate $\dot{\gamma}$ now depends on the velocity summation $\boldsymbol{\mathcal{U}} + \boldsymbol{u}_S$, where $\boldsymbol{u}_S$ is known and $\boldsymbol{\mathcal{U}}$ is unknown and must be solved for. Secondly, whilst equation (3.1a) contains only two terms, one involving the strain rate tensor of the unknown velocity and one involving the gradient of the unknown pressure, equation (3.43a) contains two additional terms concerning the same operations applied to the known regularised stokeslet velocity $\boldsymbol{u}_S$ and pressure p_S solutions. These are the 2$^{\text{nd}}$ and 4$^{\text{th}}$ terms on the left-hand-side of equation (3.43a), and differ from the other terms since, following the application of a Picard iterative process similar to in Section 3.2.1 for the unknown velocity $\boldsymbol{\mathcal{U}}$, they will concern only known quantities at each iteration. Finally, for simplicity we choose to apply only Dirichlet boundary conditions on the domain boundary $\partial\Omega$, rather than a mixture of Dirichlet and Neumann boundary conditions as in the problem (3.1).

To solve the boundary value problem (3.43), we adopt a similar finite element approach to that in Section 3.2 in order to solve for the unknowns $\boldsymbol{\mathcal{U}}$ and $\mathcal{P}$. For a particular choice of the force $\boldsymbol{f}$ acting at the point $\boldsymbol{y}$, the weak formulation of the boundary value problem (3.43) is given by

$$\begin{aligned}
&\text{Find } (\boldsymbol{\mathcal{U}}, \mathcal{P}) \in V(\Omega) \times L_0^2(\Omega) \text{ such that } \forall (\boldsymbol{v}, q) \in W(\Omega) \times L_0^2(\Omega), \\
&\int_\Omega 2\mu\left(\dot{\gamma}\left(\boldsymbol{\mathcal{U}} + \boldsymbol{u}_S\right)\right)\left[\boldsymbol{\varepsilon}(\boldsymbol{\mathcal{U}}) : \boldsymbol{\varepsilon}(\boldsymbol{v})\right] d\boldsymbol{x} - \int_\Omega \mathcal{P}\left[\nabla \cdot \boldsymbol{v}\right] d\boldsymbol{x} \\
&\qquad + \int_\Omega \left\{2\mu\left(\dot{\gamma}\left(\boldsymbol{\mathcal{U}} + \boldsymbol{u}_S\right)\right)\left[\boldsymbol{\varepsilon}(\boldsymbol{u}_S) : \boldsymbol{\varepsilon}(\boldsymbol{v})\right] - \mu_S\left[\nabla \boldsymbol{u}_S : \nabla \boldsymbol{v}\right]\right\} d\boldsymbol{x} = \boldsymbol{0},
\end{aligned} \tag{3.44a}$$

$$\int_\Omega q\,[\nabla \cdot \boldsymbol{\mathcal{U}}]\,d\boldsymbol{x} = 0, \tag{3.44b}$$

for function spaces $W(\Omega)$, $V(\Omega)$ and $L^2_0(\Omega)$ as defined in system (3.2), where $\boldsymbol{v} \in W(\Omega)$ and $q \in L^2_0(\Omega)$ are finite element test functions. This system is non-linear in the unknown velocity $\boldsymbol{\mathcal{U}}$. Given known solutions $\boldsymbol{u}_S$ and p_S which can be pre-calculated based on the position and strength of the prescribed force, the system is linearised using a Picard iterative process outlined as follows:

1. Initialise with $r = 0$ and $\boldsymbol{\mathcal{U}}^{\boldsymbol{0}} := \boldsymbol{\mathcal{U}}^0(\boldsymbol{x}) = \boldsymbol{0}$ for every $\boldsymbol{x} \in \Omega$.

2. Set $r = r + 1$.

3. Find $(\boldsymbol{\mathcal{U}}^r, \mathcal{P}^r) \in V(\Omega) \times L^2_0(\Omega)$ such that $\forall (\boldsymbol{v}, q) \in W(\Omega) \times L^2_0(\Omega)$,

$$\begin{aligned} &\int_\Omega 2\mu\left(\dot\gamma\left(\boldsymbol{\mathcal{U}}^{r-1} + \boldsymbol{u}_S\right)\right)\left[\boldsymbol{\varepsilon}(\boldsymbol{\mathcal{U}}^r) : \boldsymbol{\varepsilon}(\boldsymbol{v})\right] d\boldsymbol{x} - \int_\Omega \mathcal{P}^r\left[\nabla \cdot \boldsymbol{v}\right] d\boldsymbol{x} \\ &+ \int_\Omega \left\{2\mu\left(\dot\gamma\left(\boldsymbol{\mathcal{U}}^{r-1} + \boldsymbol{u}_S\right)\right)\left[\boldsymbol{\varepsilon}(\boldsymbol{u}_S) : \boldsymbol{\varepsilon}(\boldsymbol{v})\right] - \mu_S\left[\nabla \boldsymbol{u}_S : \nabla \boldsymbol{v}\right]\right\} d\boldsymbol{x} = \boldsymbol{0}, \end{aligned} \tag{3.45a}$$

$$\int_\Omega q\,[\nabla \cdot \boldsymbol{\mathcal{U}}^r]\,d\boldsymbol{x} = 0. \tag{3.45b}$$

4. Calculate $\boldsymbol{u}^r = \boldsymbol{\mathcal{U}}^r + \boldsymbol{u}_S$ and $p^r = \mathcal{P}^r + p_S$.

5. Repeat steps 2–4 until converged.

At each iteration r, the above system is linear in the unknown velocity $\boldsymbol{\mathcal{U}}^r$ since the viscosity is calculated from the known velocity from the previous iteration $\boldsymbol{\mathcal{U}}^{r-1}$. In the next section, we outline the implementation of the HANS method for the specific example of modelling a single relaxing Hookean spring within a shear-thinning fluid.

3.4.3 Implementation for the Hookean spring problem

Consider a spring extending from a point $\boldsymbol{y}_W \in \partial\Omega$ on the wall of the domain Ω to the point $\boldsymbol{y} \in \Omega$ (see Figure 3.9). The domain Ω contains a generalised-Newtonian fluid whose viscosity

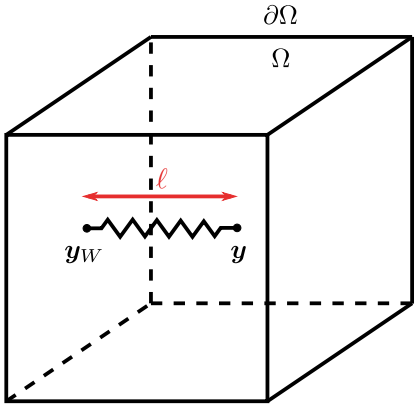


Figure 3.9: A spring of resting length ℓ and stiffness K within the cuboidal domain Ω with boundary $\partial\Omega$. The spring is attached to the wall of the domain at the point $\boldsymbol{y}_W \in \partial\Omega$ and extends to the point $\boldsymbol{y} \in \Omega$.

is modelled using the BCC4p constitutive law given in equation (1.14). A restoring force is exerted at the free end of spring $\boldsymbol{y}$, which can be prescribed using Hooke's law as

$$\boldsymbol{f}_H = -K[|\boldsymbol{y} - \boldsymbol{y}_W| - \ell]\bar{\boldsymbol{d}}, \tag{3.46}$$

where K is the stiffness constant of the spring, ℓ is the resting length of the spring and $\bar{\boldsymbol{d}}$ is a direction vector given by

$$\bar{\boldsymbol{d}} = \frac{\boldsymbol{y} - \boldsymbol{y}_W}{|\boldsymbol{y} - \boldsymbol{y}_W|}. \tag{3.47}$$

By Newton's third law, the forces at $\boldsymbol{y}$ balance so that $\boldsymbol{f}_H + [-\boldsymbol{f}] = 0$ where $-\boldsymbol{f}$ is the force that the fluid exerts on the spring at $\boldsymbol{y}$. Hence $\boldsymbol{f} = \boldsymbol{f}_H$ and we may calculate the regularised stokeslet velocity and pressure solutions using the force given by Hooke's law in equation (3.46).

We non-dimensionalise the system (3.45) with respect to characteristic length-scale L, unknown time-scale τ, force-scale KL, velocity-scale $L\tau^{-1}$ and pressure-scale $\mu_\infty\tau$. Choosing $\tau = L\mu_\infty/K$, the dimensionless weak formulation at iteration r is given by

$$\text{Find } (\boldsymbol{\mathcal{U}}^r, \mathcal{P}^r) \in V(\Omega) \times L_0^2(\Omega) \text{ such that } \forall (\boldsymbol{v}, q) \in W(\Omega) \times L_0^2(\Omega),$$
$$\int_\Omega 2\mu \left(\dot{\gamma}\left(\boldsymbol{\mathcal{U}}^{r-1} + \boldsymbol{u}_S\right)\right)[\boldsymbol{\varepsilon}(\boldsymbol{\mathcal{U}}^r) : \boldsymbol{\varepsilon}(\boldsymbol{v})]\, d\boldsymbol{x} - \int_\Omega \mathcal{P}^r [\nabla \cdot \boldsymbol{v}]\, d\boldsymbol{x}$$

$$+\int_{\Omega}\left\{2\mu\left(\dot{\gamma}\left(\boldsymbol{\mathcal{U}}^{r-1}+\boldsymbol{u}_S\right)\right)\left[\boldsymbol{\varepsilon}(\boldsymbol{u}_S):\boldsymbol{\varepsilon}(\boldsymbol{v})\right]-\beta_S\left[\nabla\boldsymbol{u}_S:\nabla\boldsymbol{v}\right]\right\}d\boldsymbol{x}=\boldsymbol{0}, \tag{3.48a}$$

$$\int_{\Omega} q\left[\nabla\cdot\boldsymbol{\mathcal{U}}^{r}\right]d\boldsymbol{x}=0, \tag{3.48b}$$

where the dimensionless form of the BCC4p constitutive law is given by

$$\mu\left(\dot{\gamma}\left(\boldsymbol{\mathcal{U}}^{r-1}+\boldsymbol{u}_S\right)\right)=1+\left[\beta_0-1\right]\left[1+\left(\mathrm{De}\,\dot{\gamma}(\boldsymbol{\mathcal{U}}^{r-1}+\boldsymbol{u}_S)\right)^2\right]^{\frac{n-1}{2}}, \tag{3.49}$$

where $\mathrm{De}=\lambda K/L\mu_\infty$, $\beta_0=\mu_0/\mu_\infty$ and $\beta_S=\mu_S/\mu_\infty$. The dimensionless regularised stokeslet solutions are given by

$$u_{Si}=\frac{1}{8\pi\beta_S}\left[\delta_{ij}\frac{r^2+2\epsilon^2}{[r^2+\epsilon^2]^{3/2}}+\frac{r_i r_j}{[r^2+\epsilon^2]^{3/2}}\right]f_j, \tag{3.50a}$$

$$p_S=\frac{1}{4\pi}\left[r_j\frac{2r^2+5\epsilon^2}{[r^2+\epsilon^2]^{5/2}}\right]f_j, \tag{3.50b}$$

with $\boldsymbol{f}=[|\boldsymbol{y}-\boldsymbol{y}_W|-l]\bar{\boldsymbol{d}}$.

The dimensionless groups in the problem are De, β_0, β_S, n and $l=\ell/L$. The regulation parameter ϵ is also scaled by L. The Deborah number De, along with the viscosity ratio β_0 and the shear-thinning index n determine the shear-thinning nature of the fluid. The group l represents the dimensionless resting length of the spring. Finally, the group β_S is chosen in order for the perturbations $\boldsymbol{\mathcal{U}}$ and $\mathcal{P}$ to be a small. Details regarding the appropriate choice of this parameter will be discussed later.

Let Ω_h represent a partition of the domain Ω with mesh size h that consists of arbitrary polyhedera elements. As in Section 3.2, we expand the velocity $\boldsymbol{\mathcal{U}}$ and pressure $\mathcal{P}$ in terms of piecewise polynomial basis functions $\{\varphi_n(\boldsymbol{x})\}_{n=1}^{N}$ and $\{\psi_m(\boldsymbol{x})\}_{m=1}^{M}$ respectively (see equations

(3.7) and (3.8)). We obtain the linear system

$$\underbrace{\begin{bmatrix} \mathrm{A}_{11}^{r-1} & \mathrm{A}_{12}^{r-1} & \mathrm{A}_{13}^{r-1} & -\mathrm{B}_1^T \\ \mathrm{A}_{21}^{r-1} & \mathrm{A}_{22}^{r-1} & \mathrm{A}_{23}^{r-1} & -\mathrm{B}_2^T \\ \mathrm{A}_{31}^{r-1} & \mathrm{A}_{32}^{r-1} & \mathrm{A}_{33}^{r-1} & -\mathrm{B}_3^T \\ \mathrm{B}_1 & \mathrm{B}_2 & \mathrm{B}_3 & 0 \end{bmatrix}}_{\mathrm{Z}} \underbrace{\begin{bmatrix} \boldsymbol{U}_1^r \\ \boldsymbol{U}_2^r \\ \boldsymbol{U}_3^r \\ \boldsymbol{P}^r \end{bmatrix}}_{\boldsymbol{c}} = \underbrace{\begin{bmatrix} \boldsymbol{G}_1^{r-1} \\ \boldsymbol{G}_2^{r-1} \\ \boldsymbol{G}_3^{r-1} \\ \boldsymbol{0} \end{bmatrix}}_{\boldsymbol{b}}, \tag{3.51}$$

which is the discrete form of the dimensionless weak formulation (3.48) to solve for the perturbation solutions $\boldsymbol{\mathcal{U}}^r$ and $\mathcal{P}^r$ at each iteration r, hereafter termed [DGNS].

The solution vector $\boldsymbol{c}$ consists of the nodal values of the velocity $\boldsymbol{\mathcal{U}}^r$ and pressure $\mathcal{P}^r$, given by $\boldsymbol{U}_i^r = [U_{i1}^r, U_{i2}^r, \dots, U_{iN}^r]^T$ and $P^r = [P_1^r, P_2^r, \dots, P_M^r]^T$ for $i = 1, 2, 3$. The stiffness matrix Z can be constructed in the same way as in Section 3.2, noting that the viscosity now depends on $\boldsymbol{u}^{r-1} = \boldsymbol{\mathcal{U}}^{r-1} + \boldsymbol{u}_S$. Finally, the load vector $\boldsymbol{b}$ consists of the vectors

$$[G_i^{r-1}]_n = \int_{\Omega_h} \left(\mu[\dot{\gamma}(\boldsymbol{\mathcal{U}}^{r-1} + \boldsymbol{u}_S)] - \beta_S\right) \sum_{j=1}^{3} \frac{\partial \varphi_n}{\partial x_j} \frac{\partial u_{Si}}{\partial x_j} + \mu[\dot{\gamma}(\boldsymbol{\mathcal{U}}^{r-1} + \boldsymbol{u}_S)] \sum_{j=1}^{3} \frac{\partial \varphi_n}{\partial x_j} \frac{\partial u_{Sj}}{\partial x_i} d\boldsymbol{x}, \quad n = 1, 2, \dots, N, \tag{3.52}$$

as well as a zero vector of length M.

The mesh and basis functions are generated as described in Section 3.2, with the calculation of the integrals required in the construction of [DGNS] also conducted as per Section 3.2. Solving the linear system [DGNS] at each iteration yields the velocity and pressure solutions $\boldsymbol{\mathcal{U}}^r$ and $\mathcal{P}^r$. Along with the regularised stokeslet solutions $\boldsymbol{u}_S$ and p_S, this allows us to calculate the solutions $\boldsymbol{u}^r$ and p^r. Once converged, i.e. when $\|\boldsymbol{c}^r - \boldsymbol{c}^{r-1}\|_2 < 1 \times 10^{-9}$ as in Section 3.2.1, this allows us to solve the boundary value problem (3.40).

Choice of β_S

The dimensionless groups De, β_0, n are fluid parameters, and thus are chosen in the model depending on the desired shear-thinning properties of the fluid. The dimensionless parameters l and ϵ, representing the dimensionless resting length of the spring and the dimensionless regularisation parameter respectively, are chosen based on the type of physical spring system being modelled. The remaining dimensionless group $\beta_S = \mu_S/\mu_\infty$, rather than being based on some physical property of the system, is rather a parameter of the numerical implementation, the value of which is now discussed.

To motivate the choice of β_S, first recall that solving for the perturbations $\mathcal{U}$ and $\mathcal{P}$ on a coarse mesh is only possible if the perturbations vary slowly across the domain. Near the free end of the spring the velocity and pressure vary rapidly, but the solutions $\boldsymbol{u}_S$ and p_S account for the majority of this variation. As such, the regularised stokeslet solutions should be the best approximation possible to the flow at the point where it varies rapidly, which is very close to $\boldsymbol{y}$. This informs our decision on how the viscosity ratio $\beta_S = \mu_S/\mu_\infty$ is chosen: we want the Newtonian viscosity μ_S to be as near to the true viscosity close to the regularised force as possible. Thus, we choose

$$\beta_S = \langle \mu\left(\dot{\gamma}(\boldsymbol{\mathcal{U}}(\boldsymbol{x}) + \boldsymbol{u}_S(\boldsymbol{x}))\right)\rangle\,, \tag{3.53}$$

for $\boldsymbol{x} \in \left\{\boldsymbol{x} : (x_1 - y_1)^2 + (x_2 - y_2)^2 + (x_3 - y_3)^2 = \epsilon^2\right\}$. Here, $\mu\left(\dot{\gamma}(\boldsymbol{\mathcal{U}}(\boldsymbol{x}) + \boldsymbol{u}_S(\boldsymbol{x}))\right)$ denotes the dimensionless viscosity at the point $\boldsymbol{x}$ and $\langle\cdot\rangle$ represents the average value. Thus, β_S is chosen to be the average of the dimensionless viscosity over the surface of a sphere of radius ϵ, centred at the point $\boldsymbol{y}$. We note that in order for the system (3.48) to be linear, we require that β_S is calculated from the velocity at the previous iteration. Therefore at each iteration r we choose

$$\beta_S^r = \left\langle \mu\left(\dot{\gamma}(\boldsymbol{\mathcal{U}}^{r-1}(\boldsymbol{x}) + \boldsymbol{u}_S(\boldsymbol{x};\, \beta_S^{r-1}))\right)\right\rangle\,, \tag{3.54}$$

where $\boldsymbol{u}_S(\boldsymbol{x};\, \beta_S^{r-1})$ denotes the dependence of $\boldsymbol{u}_S$ on β_S^{r-1}. At $r = 0$, we set $\beta_S^0 = \beta_0$.

Numerical integration schemes

The blocks of the stiffness matrix in the linear system [DGNS] can be calculated in the same way as those in the linear system [DGN], namely using Gauss-Legendre quadrature. The shear rate is computed via

$$\begin{aligned}\dot{\gamma}\left(\boldsymbol{\mathcal{U}}^{r-1}+\boldsymbol{u}_S\right) &= \left[2\varepsilon_{ij}\left(\boldsymbol{\mathcal{U}}^{r-1}+\boldsymbol{u}_S\right)\varepsilon_{ij}\left(\boldsymbol{\mathcal{U}}^{r-1}+\boldsymbol{u}_S\right)\right]^{\frac{1}{2}} \\ &= \left[2\left[\varepsilon_{ij}\left(\boldsymbol{\mathcal{U}}^{r-1}\right)+\varepsilon_{ij}\left(\boldsymbol{u}_S\right)\right]^2\right]^{\frac{1}{2}}. \end{aligned} \tag{3.55}$$

where the derivatives of the velocity perturbation $\boldsymbol{\mathcal{U}}^{r-1}$ can be calculated as before using interpolation via the velocity basis functions (see equation (3.21)). The derivatives of $\boldsymbol{u}_S$ can be directly calculated through differentiating equation (3.50a).

It remains to discuss how the load vector integrals in equation (3.52) can be calculated numerically. Integrals of this form over elements containing or close to the point $\boldsymbol{y}$ are rapidly varying due to the presence of the derivatives of the stokeslet velocity ∇u_{S_i}. The number of points required for accurate calculation of these integrals via Gauss-Legendre quadrature is large. For example, approximating the integral (3.52) over an element $E^{(e)} = [0, 0.1] \times [0, 0.1] \times [0, 0.1]$ containing a force of strength $\boldsymbol{f} = (1, 0, 0)$ at the center of the element requires $Q = 30$ quadrature points per direction ($P = 30^3$ points in total) to calculate the integral within an error of 1×10^{-6}. Since using large numbers of quadrature points considerably increases computational time, we seek to reduce the number of quadrature points required via an improved quadrature technique proposed by Muldowney and Higdon (1995). For a nearly singular integral of the form

$$\int_{-1}^{1} \frac{g(x)}{[[x-y]+\epsilon^2]^{\frac{a}{2}}}dx, \tag{3.56}$$

Muldowney and Higdon (1995) applied a mapping of the form $x = y + \epsilon \sinh(m \sinh^{-1}(X))$

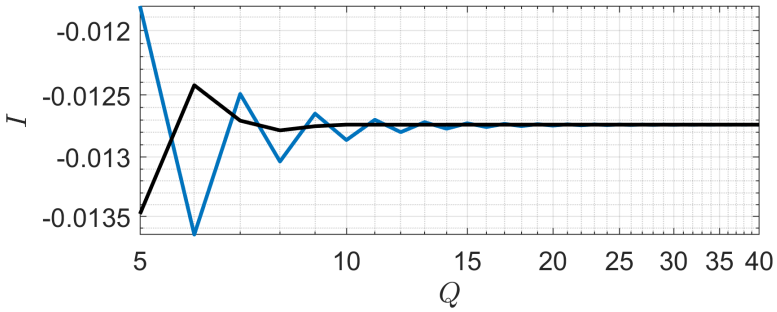


Figure 3.10: Value of the integral given in equation (3.52), calculated numerically using Q quadrature points per direction for the 18^{th} basis function and where $i = 1$. The integral is calculated using standard Gauss-Legendre quadrature (blue) and using the sinh transform (black).

where $m = \lfloor 1 + \ln(\alpha^{-1}) \rfloor$, with α defined as

$$\alpha = \begin{cases} \epsilon & \text{if } |y| < 1, \\ \min\{\epsilon, |y| - 1\} & \text{if } |y| > 1. \end{cases} \tag{3.57}$$

This approach moves the point of singularity away from the interval of integration, thereby reducing the number of points required for accurate evaluation, and can easily be extended to apply to three-dimensional integrals. In the HANS method, for integrals over elements that contain the point of near singularity $\boldsymbol{y} = (y_1, y_2, y_3)$, we map

$$x_i = y_i + \epsilon \sinh(m_i \sinh^{-1}(X_i)) \text{ for } i = 1, 2, 3, \tag{3.58}$$

with $m_i = \lfloor 1 + \ln(\alpha_i^{-1}) \rfloor$ and each α_i chosen as in equation (3.57) with $y = y_i$. Following the application of the mapping, we proceed using Gauss-Legendre quadrature to evaluate the mapped integrals.

To demonstrate the improved convergence obtained using this approach, we consider the calculation of the integral (3.52) for the 18^{th} basis function on the element (for $i = 1$). We calculate the integral over an element $E^{(e)} = [0, 0.1] \times [0, 0.1] \times [0, 0.1]$, which contains a point force of prescribed strength $\boldsymbol{f} = (1, 0, 0)$ at the location $\boldsymbol{y} = (0.05, 0.05, 0.05) \in E^{(e)}$. For fluid parameters $(n, \text{De}, \beta_0) = (1, 1, 2)$, the value of the integral for various numbers of quadrature

points per direction Q can be seen in Figure 3.10. To calculate the error in this approximation, we first calculate the value of the integral using both standard Gauss-Legendre quadrature and the sinh method using $Q = 200$ quadrature points per direction. This value I_{ref} represents an accurate representation of the true value of the integral. Calculating the error $|I - I_{\text{ref}}|$ for both methods for the range of Q shown in Figure 3.10 ($Q \in [5, 40]$), we find that the number of quadrature points per direction required to reduce the error to below 1×10^{-6} is $Q = 30$ for Gauss-Legendre quadrature and $Q = 10$ for the sinh method. This means calculating the value of the integral using the sinh method corresponds to a reduction in quadrature points of $\Delta P = 26000$ compared with performing calculations using the Gauss-Legendre method, for the same degree of error. As a result, the application of the sinh mapping greatly reduces the computational costs associated with calculating the integrals in (3.52). Going forward, we refer to this mapping as the 'sinh method' and use it to calculate all integrals in (3.52).

Time-stepping procedure

The evolution of a spring in a shear-thinning fluid is a time-dependent problem. Denoting the prescribed initial position of the free end of the spring as $\boldsymbol{y}_0$, the initial value problem for the evolution of the free end of the spring $\boldsymbol{y}(t)$ is given by

$$\frac{d\boldsymbol{y}(t)}{dt} = \boldsymbol{u}(\boldsymbol{y}(t), t), \quad \boldsymbol{y}(0) = \boldsymbol{y}_0, \tag{3.59}$$

where $\boldsymbol{u}(\boldsymbol{y}(t), t) = \boldsymbol{\mathcal{U}}(\boldsymbol{y}(t), t) + \boldsymbol{u}_S(\boldsymbol{y}(t), t)$ denotes the converged value of the velocity.

We denote the value of $\boldsymbol{y}(t)$ at the discrete times t_k via $\boldsymbol{y}_k \approx \boldsymbol{y}(t_k)$ where $t_k = k\Delta t$ for time-step size Δt. The first time-stepped value $\boldsymbol{y}_1 \approx \boldsymbol{y}(t_1)$ is computed using Euler's method

$$\boldsymbol{y}_1 = \boldsymbol{y}_0 + \Delta t\, \boldsymbol{u}(\boldsymbol{y}_0, t_0). \tag{3.60}$$

The remaining values are calculated via the two-step Adams-Bashforth method, which states that for $0 \leq k \in \mathbb{Z}$

$$\boldsymbol{y}_{k+2} = \boldsymbol{y}_{k+1} + \frac{3}{2}\Delta t\, \boldsymbol{u}(\boldsymbol{y}_{k+1}, t_{k+1}) - \frac{1}{2}\Delta t\, \boldsymbol{u}(\boldsymbol{y}_k, t_k). \tag{3.61}$$

This method does not incur any additional numerical costs compared to the Euler method since it only requires knowing the solution at times in the past, which have therefore already been calculated. Also, whilst the global error in the solution for the Euler method decays as $\mathcal{O}(\Delta t)$ (Iserles, 2009), the global error for the two-step Adams-Bashforth method decays as $\mathcal{O}(\Delta t^2)$, and thus by these metrics it is beneficial to use the two-step Adams-Bashforth method where possible, which is at any point other than the initial time-step.

Algorithm for the solution method

The HANS method for simulating a single Hookean spring in a generalised-Newtonian fluid is implemented via the steps:

1. Choose the domain $\Omega \in \mathbb{R}^3$ and generate a mesh consisting of hexahedron elements over the domain. Prescribe the initial configuration of the spring via choosing $\boldsymbol{y}_W \in \Omega$ and $\boldsymbol{y}(0) = \boldsymbol{y}_0 \in \partial\Omega$. Choose values for the dimensionless groups De, n, β_0, l and ϵ based on the desired fluid and spring properties to be modelled.

2. Calculate the force $\boldsymbol{f} = [|\boldsymbol{y} - \boldsymbol{y}_W| - l]\bar{\boldsymbol{d}}$.

3. At each iteration r until converged, construct and solve the linear system [DGNS]. Given an initial guess $\boldsymbol{\mathcal{U}}^0(\boldsymbol{x}) = \boldsymbol{0}$ for all $\boldsymbol{x} \in \Omega$, the solutions $\boldsymbol{u}$ and p are obtained through the steps:

   - Calculate the basis functions for velocity $\left\{\hat{\varphi}_a(\boldsymbol{\xi})\right\}_{a=1}^{27}$ and pressure $\left\{\hat{\psi}_b(\boldsymbol{\xi})\right\}_{b=1}^{8}$ on the reference element. Also calculate the Jacobians $J^{(e)}(\boldsymbol{\xi})$ of the mapping from the reference element to each global mesh element $\hat{E} \to E^{(e)}$.

   - Construct the matrix blocks in the linear system [DGNS] using Gauss-Legendre quadrature to compute the required integrals.

   - Calculate β_S^r from equation (3.54). Then calculate the load vector integrals (3.52) numerically, using the sinh mapping when required.

- Solve the system using the MATLAB® backslash command "\", obtaining the solutions $\boldsymbol{\mathcal{U}}^r$ and $\mathcal{P}^r$ at all mesh nodes.
- Calculate the regularised stokeslet solutions $\boldsymbol{u}_S$ and p_S at each mesh node. Then calculate $\boldsymbol{u}^r = \boldsymbol{\mathcal{U}}^r + \boldsymbol{u}_S$ and $p^r = \mathcal{P}^r + p_S$.
- Stop iterating if $\|\boldsymbol{u}^r - \boldsymbol{u}^{r-1}\|_2 < 10^{-9}$. At the final iteration $r = r_{\max}$, set $\boldsymbol{u} = \boldsymbol{\mathcal{U}}^{r_{\max}} + \boldsymbol{u}_S$ and $p = \mathcal{P}^{r_{\max}} + p_S$.

4. Find $\boldsymbol{u}(\boldsymbol{y}(t), t)$ through interpolating to find $\boldsymbol{\mathcal{U}}^{r_{\max}}(\boldsymbol{y}(t), t)$, calculating $\boldsymbol{u}_S(\boldsymbol{y}(t), t)$ and taking the summation.

5. Time-step the the position $\boldsymbol{y}(t)$ via solving

$$\frac{d\boldsymbol{y}(t)}{dt} = \boldsymbol{u}(\boldsymbol{y}(t), t), \quad \boldsymbol{y}(0) = \boldsymbol{y}_0, \tag{3.62}$$

   using the Adams-Bashforth scheme (or Euler's method if $t = 0$).

6. Repeat steps 2–5 until the desired time $t = t_{\max}$ is reached. For this particular problem, we set $t_{\max} = 1.5$ and choose the time-step size $\Delta t = 3 \times 10^{-3}$, corresponding to $k = 500$ loops of the algorithm.

3.4.4 Results

To demonstrate the ideas of the method, specifically the slowly varying nature of the velocity perturbation $\boldsymbol{\mathcal{U}}$, we consider the velocity solutions $\boldsymbol{u}$, $\boldsymbol{u}_S$ and $\boldsymbol{\mathcal{U}}$ produced by a single regularised force with prescribed strength $\boldsymbol{f}$. We consider the domain $\Omega = [0,1] \times [0,1] \times [0,1]$ which contains a regularised force of strength $\boldsymbol{f} = (1,0,0)$ at the point $\boldsymbol{y} = (0.5, 0.5, 0.5)$. The regularisation parameter is set as $\epsilon = 0.01$ and we consider fluid parameters $\beta_0 = 2$, $\mathrm{De} = 1$ and $n = 0.5$ to simulate a shear-thinning fluid. In Figure 3.11a-c we plot the three velocity solutions (converged solutions after $N_{\mathrm{it}} = 9$ iterations). Figure 3.11a shows the velocity $\boldsymbol{u}_s$ calculated using the regularised stokeslet solution in the plane $x_3 = 0.5$. In Figure 3.11b we observe the perturbation solution $\boldsymbol{\mathcal{U}}$, found through the finite element method. Note that near

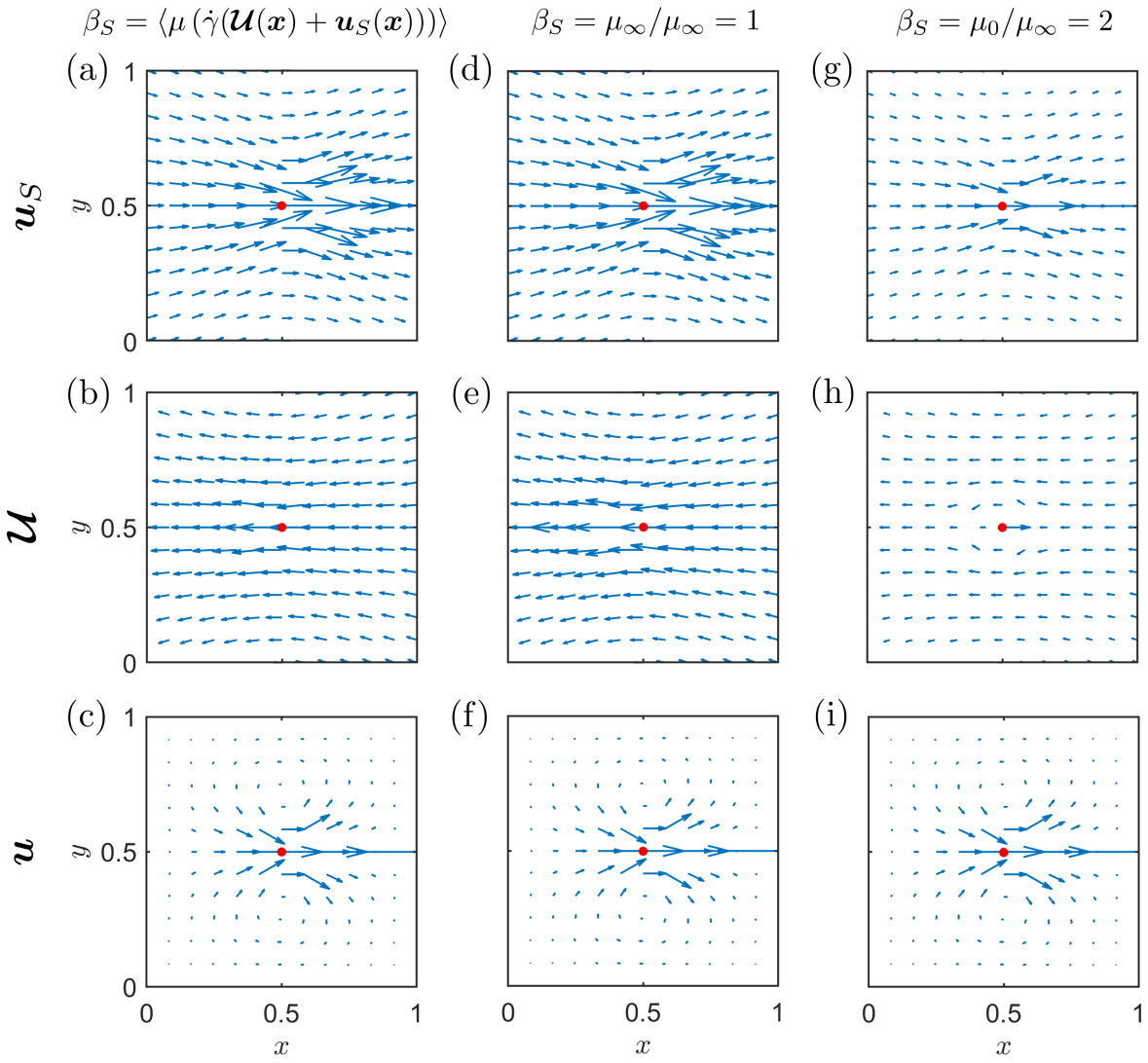


Figure 3.11: The velocity solutions $\boldsymbol{u}_S$, $\boldsymbol{\mathcal{U}}$ and $\boldsymbol{u}$, in the plane $x_3 = 0.5$ for a regularised force of strength $\boldsymbol{f} = (1, 0, 0)$ at the point $\boldsymbol{y} = (0.5, 0.5, 0.5)$ within a shear-thinning fluid. Here, $\epsilon = 0.01$ and the fluid parameters are $\beta_0 = 2$, De $= 1$ and $n = 0.5$. The domain is the unit cube $\Omega = [0, 1] \times [0, 1] \times [0, 1]$ which is meshed using $N_e = 216$ elements. Solutions are shown for three difference choices of β_S, (a-c) $\beta_S = \langle \mu(\dot{\gamma}(\boldsymbol{\mathcal{U}}(\boldsymbol{x}) + \boldsymbol{u}_S(\boldsymbol{x}))) \rangle$ where $\boldsymbol{x} \in \left\{ \boldsymbol{x} : (x_1 - y_1)^2 + (x_2 - y_2)^2 + (x_3 - y_3)^2 = \epsilon^2 \right\}$, (d-f) $\beta_S = \mu_\infty/\mu_\infty = 1$, and (g-i) $\beta_S = \mu_0/\mu_\infty = 2$.

the point of near-singularity $\boldsymbol{y}$, this solution remains slowly varying, in contrast to the rapidly varying solutions shown in Figure 3.11a. Figure 3.11c shows the summation of the velocity solutions, $\boldsymbol{u} = \boldsymbol{\mathcal{U}} + \boldsymbol{u}_S$, which is the full velocity solution to the problem accounting for the non-Newtonian nature of the fluid and the boundary conditions on $\partial\Omega$.

To quantify how rapidly varying each solution is, we calculate the absolute difference be-

tween the velocity solutions at each node of the mesh and the velocity at all adjacent nodes. For the regularised stokeslet solution $\boldsymbol{u}_S$, the maximum change in the x component of the velocity over adjacent nodes is $\Delta u_S = 2.8583$. Correspondingly, for the finite element solution $\boldsymbol{\mathcal{U}}$, $\Delta\boldsymbol{\mathcal{U}} = 0.0655$ and for the full solution $\boldsymbol{u}$ we have $\Delta u = 2.7928$. Therefore, the change in the velocity over neighbouring nodes in the finite element solution is approximately 45 times smaller than the change in $\boldsymbol{u}_S$ and $\boldsymbol{u}$. These results demonstrate the merit of formulating the problem in this way, in order to be able to calculate the finite element solution on a coarse mesh (here with only $N_e = 216$ elements).

To justify our choice of β_S as defined in equation (3.53), we also plot the three velocity solutions $\boldsymbol{u}_S$, $\boldsymbol{\mathcal{U}}$ and $\boldsymbol{u}$ for alternative choices of β_S. In Figures 3.11d-f, we plot the same velocity solutions as in Figures 3.11a-c but for $\beta_S = \mu_\infty/\mu_\infty = 1$. Similarly, in Figures 3.11g-i, we plot the solutions for $\beta_S = \beta_0 = \mu_0/\mu_\infty = 2$. We observe that in both cases, the perturbation solution $\boldsymbol{\mathcal{U}}$ can still be classified as slowly varying across the domain. We find that the change in the velocity solution $\boldsymbol{\mathcal{U}}$ over neighbouring nodes in the finite element solution is approximately 12 times smaller than the change in $\boldsymbol{u}_S$ and $\boldsymbol{u}$ (for both values of β_S). Compared to the results in Figures 3.11a-c, this indicates that choosing $\beta_S = \mu_\infty/\mu_\infty = 1$ or $\beta_S = \mu_0/\mu_\infty = 2$ does not yield as much of a benefit as choosing β_S via equation (3.53). Thus we choose β_S via equation (3.53) going forward, noting that this also does not affect our final velocity solution, as can be observed in Figures 3.11c,f,i.

Next, we explore the effects of shear-thinning rheology on the relaxation of a spring. We again consider the domain $\Omega = [0,1] \times [0,1] \times [0,1]$ and generate a mesh of the domain consisting of $N_e = 3375$ hexahedron elements. The domain contains a spring attached to the wall $\partial\Omega$ at the point $\boldsymbol{y}_W = (0, 0.5, 0.5)$, and extending to the point $\boldsymbol{y} = (0.5, 0.5, 0.5)$ within the fluid. The spring has a dimensionless resting length of $l = 0.25$ and we consider the effect of varying the dimensionless groups n, De and β_0 on the relaxation of the spring.

In Figure 3.12a, we plot the evolution of the x_1 component of the free end of the spring over time for $n \in [0.1, 1]$. Similarly, we plot the absolute value of the component of the velocity in the x_1 direction at the free end of the spring, $|u_1(\boldsymbol{y})|$, in Figure 3.12b. The Picard iterative

process converges over an average of $N_{\text{it}} = 7$ iterations over all timesteps and values of n. The relaxation of the spring is accelerated as the value of n decreases, i.e. as the fluid becomes more shear-thinning. This is demonstrated by the change in the position y_1 in Figure 3.12a, which is more rapid in the shear-thinning cases, meaning that the spring reaches its resting length l faster the lower the value of n. Further, Figure 3.12b shows that the velocity at the free end of the spring $\boldsymbol{y}$ is higher the lower the value of n toward the start of the simulation, i.e. for low t. At a certain point $t \approx 0.3$, this shifts and the velocity becomes lower the higher n. This is because, at this point, the force $\boldsymbol{f}$ prescribed by Hooke's law is lower the smaller the value of n, since the spring has relaxed further towards its rest state.

In Figures 3.12c and 3.12d, for various $\text{De} \in [0, 3]$, we plot the evolution of the free end of the spring and the x_1 component of the velocity at $\boldsymbol{y}$ respectively. The equivalent plots for varying $\beta_0 \in [1, 4]$ can be seen in Figures 3.12e and 3.12f. We again observe that increasing De, which corresponds to increasing the shear-thinning nature of the fluid, results in more rapid relaxation of the spring towards its rest state. As in the varying n case, a more shear-thinning fluid (higher De) also results in higher velocities initially but lower velocities for larger t, since at this point, the spring has relaxed further towards its rest state. For the results over β_0, increasing β_0 (increasing shear-thinning effects) hinders the relaxation of the spring. This is because increasing β_0 also corresponds to increasing the zero shear rate viscosity of the fluid, and fluids with an overall higher viscosity hinder relaxation.

The results presented in this section demonstrate that the HANS method can be applied to the simulation of an elastic spring in a shear-thinning fluid. In particular, the perturbation solutions are slowly varying across the domain and can therefore be calculated on a coarse mesh. Also, increasing the strength of the shear-thinning effects (decreasing n, increasing De) results in springs that relax faster towards their rest state. In the next section, we outline the HANS method for simulating sperm-like swimmers with flexible elastic flagella in shear-thinning fluids.

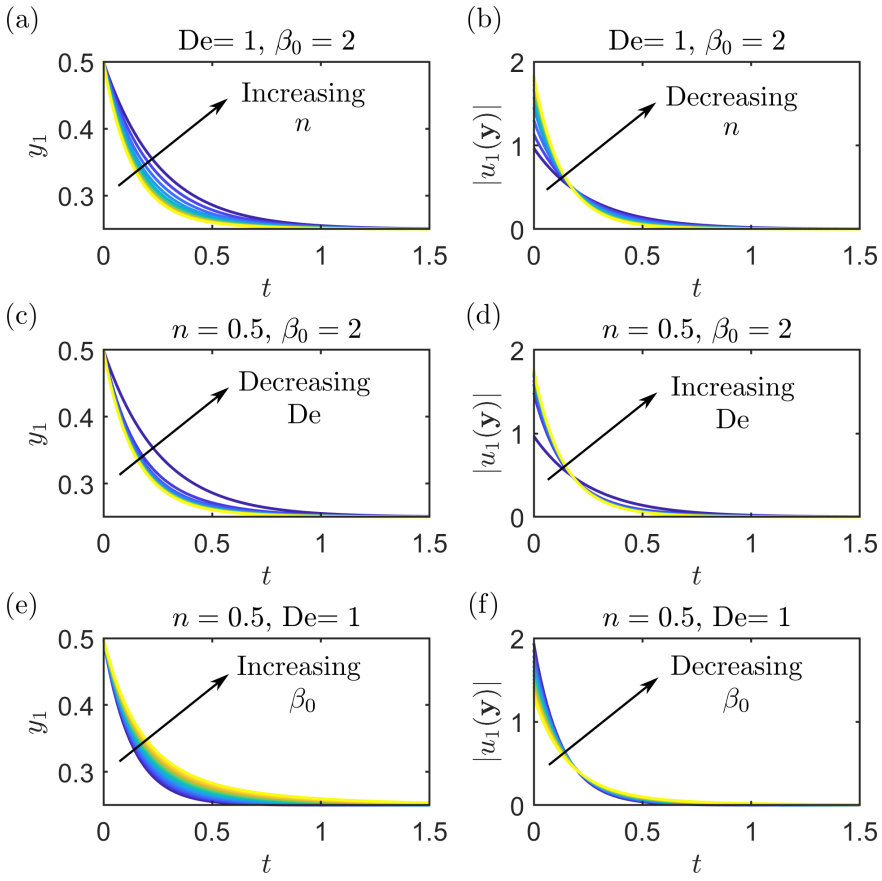


Figure 3.12: Relaxation of a single Hookean spring, located within the domain $\Omega = [0,1] \times [0,1] \times [0,1]$ and with resting length $l = 0.25$. The spring is attached to the wall of the domain at the point $\boldsymbol{y}_W = (0, 0.5, 0.5)$, and extends to a point $\boldsymbol{y} = (0.5, 0.5, 0.5)$ within the fluid. In (a), the x_1 component of the position of the free end of the spring y_1 is plotted over time for 10 equally spaced values of $n \in [0.1, 1]$. In (b), the absolute value of the velocity in the x_1 direction at the free end of the spring $|u_1(\boldsymbol{y})|$ is plotted over time for the values of n considered in (a). In (c) and (d), the equivalent figures as (a) and (b) are plotted, but for 13 equally spaced values of De $\in [0, 3]$. Finally, in (e) and (f), the analogous plots as (a) and (b) are plotted, but for 13 equally spaced values of $\beta_0 \in [1, 4]$. In all cases, the Newtonian solution ($n = 1$, De $= 0$ or $\beta_0 = 1$) is shown in blue, ranging to the most shear-thinning simulation in yellow. The remaining two shear-thinning parameters are fixed in each case, as indicated in the plot titles.

3.5 The hybrid method for sperm-like swimmers in generalised Newtonian fluids

In Section 3.4, we derived the hybrid approach for non-linear swimming (HANS), for solving the fluid flow equations associated with a generalised-Newtonian fluid in the presence of a single immersed force. Following summarising the derivation and implementations of this method, we studied the relaxation of a single Hookean spring within a shear-thinning fluid

using this framework. In particular, we found that the spring relaxes faster towards its rest state with decreasing shear-thinning index n or increasing Deborah number, corresponding to enhanced shear-thinning effects.

This section describes how the HANS method is formulated to study human spermatozoa within shear-thinning fluids. To model the cell itself, we consider a modification of the elastohydrodynamic model of a single sperm cell derived in Chapter 2. Applying the HANS method as described in Section 3.4 allows for the solution of the elastohydrodynamic problem in conjunction with the finite element solution for the unknown fluid velocity and pressure perturbations. This method then allows us to simulate a sperm cell within a shear-thinning fluid, the results for which will be discussed in Chapter 4.

To begin this section, we derive the continuous model equations and their dimensionless form. Following this, we describe the discretisation of the system and its representation via a linear system. Finally, we outline the implementation of the method and discuss convergence and suitable parameter choices for the problems we will consider in Chapter 4.

3.5.1 Problem formulation

We consider a single sperm cell situated within the bounded open domain $\Omega \in \mathbb{R}^3$ with a boundary $\partial\Omega$. The domain contains a generalised-Newtonian fluid, the rheology of which is modelled using the BCC4p constitutive law as given in equation (1.14). As in Chapter 2, we describe the flagellum via a time-varying curve $\boldsymbol{X}(s,t)$ where s is arclength along the flagellum with $0 \leq s \leq L$. The length $s \in [0, \ell]$ is considered active, representing the actuated principal piece of the flagellum, and the remaining length $s \in (\ell, L]$ is considered inactive to model the flagellum end piece (see Figure 2.1 of Chapter 2). As before, the flagellum can only bend in the xy-plane, and so the geometry of the cell can be formulated via the flagellum tangent angle $\theta(s,t)$ and the head angle $\phi(t)$, rather than the variable $\boldsymbol{X}(s,t)$. The flagellum is connected to the cell head at the point $\boldsymbol{X}_0(t)$, where the head is represented by an elliptical surface ∂H.

The geometry, kinematics and elasticity of the flagellum can be expressed as before via equations (2.1), (2.2) and (2.13) respectively. We again consider varying elastic flagellar stiff-

ness described by a function $E(s)$, the form of which is given in equation (2.12) and is included to model the tapering fibrous sheath surrounding the core of the flagellum. Actuation is again achieved through the active moment term $m(s,t) = m_0 \cos(ks - \omega t) H(\ell - s)$, where k is wavenumber, ω is radian frequency and $H(\ell - s)$ is a Heaviside function where $0 < \ell \leq L$ is the length of the active tail segment.

Modelling the head as undergoing rigid body motion around $\boldsymbol{X}_0(t)$ yields the head kinematics equation (2.3) and the head-flagellum coupling is again enforced via equation (2.16). A hydrodynamic force per unit length $-\boldsymbol{f}(s,t)$ is experienced by the entire flagellum, and a force per unit area $-\boldsymbol{\Phi}(\boldsymbol{Y},t)$ is experienced by the head. Since the entire cell is force and moment free, we again recover the equations for total force and moment balance, given in equations (2.14) and (2.15). We define the total force per unit volume exerted on the fluid by the cell as

$$\boldsymbol{F}(\boldsymbol{x},t) = \int_0^L \boldsymbol{f}\left(s',t\right) \phi_\epsilon\left(\boldsymbol{x} - \boldsymbol{X}\left(s',t\right)\right) ds' + \iint_{\partial H(t)} \boldsymbol{\Phi}(\boldsymbol{Y},t)\, \phi_\epsilon(\boldsymbol{x} - \boldsymbol{Y})\, dS_Y. \tag{3.63}$$

This choice again relates to the method of regularised stokeslets (Cortez, 2001; Cortez et al., 2005), as discussed in Section 1.4.3. Terms one and two in equation (3.63) represent the force per unit volume exerted by the flagellum and head onto the fluid respectively. We prescribe no-slip boundary conditions on the boundary $\partial\Omega$ and write the boundary value problem

$$\begin{aligned}
&\nabla \cdot \left[2\mu\left(\dot{\gamma}\left(\boldsymbol{u}(\boldsymbol{x},t)\right)\right) \boldsymbol{\varepsilon}\left(\boldsymbol{u}(\boldsymbol{x},t)\right)\right] - \nabla p(\boldsymbol{x},t) \\
&\qquad + \int_0^L \boldsymbol{f}\left(s',t\right) \phi_\epsilon\left(\boldsymbol{x} - \boldsymbol{X}\left(s',t\right)\right) ds' \\
&\qquad\quad + \iint_{\partial H(t)} \boldsymbol{\Phi}(\boldsymbol{Y},t)\, \phi_\epsilon(\boldsymbol{x} - \boldsymbol{Y})\, dS_Y = \boldsymbol{0} \text{ for } \boldsymbol{x} \in \Omega, \qquad (3.64a)
\end{aligned}$$

$$\nabla \cdot \boldsymbol{u} = 0 \text{ for } \boldsymbol{x} \in \Omega, \tag{3.64b}$$

$$\boldsymbol{u} = \boldsymbol{0} \text{ for } \boldsymbol{x} \in \partial\Omega, \tag{3.64c}$$

which is the system (1.16) restricted to the computational domain Ω, with $\boldsymbol{F}$ chosen as in equation (3.63). This is the boundary value problem for a single sperm cell swimming within a generalised-Newtonian fluid.

As in Section 3.4, we employ the HANS method and split the velocity and pressure solutions into two parts: a regularised stokeslet component that accounts for the rapidly varying nature of the solution, and a perturbation that is solved for using the finite element method and which is slowly varying across the domain. Following the derivation in Section 3.4, the full system for the unknown perturbations $\boldsymbol{\mathcal{U}}$ and $\mathcal{P}$ is given by system (3.43), where now

$$u_{S_i}(\boldsymbol{x},t) = \int_0^L S_{ij}^{\epsilon}\left(\boldsymbol{x},\boldsymbol{X}\left(s',t\right)\right) f_j\left(s',t\right) ds' + \iint_{\partial H(t)} S_{ij}^{\epsilon}(\boldsymbol{x},\boldsymbol{Y})\,\Phi_j(\boldsymbol{Y},t)\,dS_Y, \tag{3.65a}$$

$$p_S(\boldsymbol{x},t) = \int_0^L P_j^{\epsilon}\left(\boldsymbol{x},\boldsymbol{X}\left(s',t\right)\right) f_j\left(s',t\right) ds' + \iint_{\partial H(t)} P_j^{\epsilon}(\boldsymbol{x},\boldsymbol{Y})\,\Phi_j(\boldsymbol{Y},t)\,dS_Y. \tag{3.65b}$$

Here, $\boldsymbol{S}^{\epsilon}$ and $\boldsymbol{P}^{\epsilon}$ are the regularised stokeslet velocity and pressure tensors respectively, as defined in the system (1.32). These are the solutions to the Newtonian problem via the method of regularised stokeslets for a fluid of viscosity μ_S. In particular, the equation for the Newtonian velocity (3.65a) is identical to the boundary integral equation for the hydrodynamics in the end piece model (equation (2.4) in Chapter 2). Similarly, the boundary conditions on the wall of the domain are given by

$$\mathcal{U}_i(\boldsymbol{x},t) = -\int_0^L S_{ij}^{\epsilon}\left(\boldsymbol{x},\boldsymbol{X}\left(s',t\right)\right) f_j\left(s',t\right) ds' - \iint_{\partial H(t)} S_{ij}^{\epsilon}(\boldsymbol{x},\boldsymbol{Y})\,\Phi_j(\boldsymbol{Y},t)\,dS_Y, \text{ for } \boldsymbol{x}\in\partial\Omega. \tag{3.66}$$

Finally, the velocity of the flagellum ($\boldsymbol{X}(s,t)$) and head ($\boldsymbol{Y}(t)$) points are given in full by

$$\partial_t X_i(s,t) = \mathcal{U}_i\left(\boldsymbol{X}(s,t),t\right) + \int_0^L S_{ij}^{\epsilon}\left(\boldsymbol{X}(s,t),\boldsymbol{X}\left(s',t\right)\right) f_j\left(s',t\right) ds' + \iint_{\partial H(t)} S_{ij}^{\epsilon}\left(\boldsymbol{X}(s,t),\boldsymbol{Y}\right)\Phi_j(\boldsymbol{Y},t)\,dS_Y, \tag{3.67}$$

and

$$d_t Y_i(t) = \mathcal{U}_i\left(\boldsymbol{Y}(t),t\right) + \int_0^L S_{ij}^{\epsilon}\left(\boldsymbol{Y}(t),\boldsymbol{X}\left(s',t\right)\right) f_j\left(s',t\right) ds' + \iint_{\partial H(t)} S_{ij}^{\epsilon}\left(\boldsymbol{Y}(t),\boldsymbol{Y}\right)\Phi_j(\boldsymbol{Y},t)\,dS_Y, \tag{3.68}$$

where we have applied $u_i\left(\boldsymbol{X}\left(s,t\right),t\right)=\partial_t X_i\left(s,t\right)$ and $u_i\left(\boldsymbol{Y}\left(t\right),t\right)=d_t Y_i\left(t\right)$.

3.5.2 The dimensionless system

The model equations are non-dimensionalised with respect to characteristic length-scale L, time-scale ω^{-1}, force-scale $\mu_\infty\omega L^2$, velocity-scale $L\omega$ and pressure-scale $\mu_\infty\omega$. The elastic stiffness function is non-dimensionalised with respect to E_d, the distal stiffness value. The full dimensionless system (with dimensionless variables denoted with $\hat{\cdot}$) is given by

$$\begin{aligned}
\mathbf{0} &= \hat{\boldsymbol{\nabla}}\cdot\left[2\hat{\mu}\left(\hat{\dot{\gamma}}\left(\hat{\boldsymbol{\mathcal{U}}}\left(\hat{\boldsymbol{x}},\hat{t}\right)+\hat{\boldsymbol{u}}_S\left(\hat{\boldsymbol{x}},\hat{t}\right)\right)\right)\hat{\boldsymbol{\varepsilon}}\left(\hat{\boldsymbol{\mathcal{U}}}\left(\hat{\boldsymbol{x}},\hat{t}\right)\right)\right]\\
&\quad+\hat{\boldsymbol{\nabla}}\cdot\left[2\hat{\mu}\left(\hat{\dot{\gamma}}\left(\hat{\boldsymbol{\mathcal{U}}}\left(\hat{\boldsymbol{x}},\hat{t}\right)+\hat{\boldsymbol{u}}_S\left(\hat{\boldsymbol{x}},\hat{t}\right)\right)\right)\hat{\boldsymbol{\varepsilon}}\left(\hat{\boldsymbol{u}}_S\left(\hat{\boldsymbol{x}},\hat{t}\right)\right)\right]\\
&\quad-\hat{\boldsymbol{\nabla}}\hat{\mathcal{P}}\left(\hat{\boldsymbol{x}},\hat{t}\right)-\beta_S\hat{\nabla}^2\hat{\boldsymbol{u}}_S\left(\hat{\boldsymbol{x}},\hat{t}\right),\ \hat{\boldsymbol{x}}\in\hat{\Omega}, && (3.69a)\\
0 &= \hat{\boldsymbol{\nabla}}\cdot\hat{\boldsymbol{\mathcal{U}}}\left(\hat{\boldsymbol{x}},\hat{t}\right),\ \hat{\boldsymbol{x}}\in\hat{\Omega}, && (3.69b)\\
\hat{\mathcal{U}}_i\left(\hat{\boldsymbol{x}},\hat{t}\right) &= -\int_0^1\hat{S}_{ij}^{\hat{\epsilon}}\left(\hat{\boldsymbol{x}},\hat{\boldsymbol{X}}\left(\hat{s}',\hat{t}\right)\right)\hat{f}_j\left(\hat{s}',\hat{t}\right)d\hat{s}'\\
&\quad-\iint_{\partial\hat{H}(\hat{t})}\hat{S}_{ij}^{\hat{\epsilon}}\left(\hat{\boldsymbol{x}},\hat{\boldsymbol{Y}}\right)\hat{\Phi}_j\left(\hat{\boldsymbol{Y}},\hat{t}\right)dS_{\hat{\boldsymbol{Y}}},\ \hat{\boldsymbol{x}}\in\partial\hat{\Omega}, && (3.69c)\\
0 &= \hat{E}\left(\hat{s}\right)\partial_{\hat{s}}\theta\left(\hat{s},\hat{t}\right)+\boldsymbol{e}_3\cdot\mathcal{S}^4\int_{\hat{s}}^1\left[\hat{\boldsymbol{X}}\left(\hat{s}',\hat{t}\right)-\hat{\boldsymbol{X}}\left(\hat{s},\hat{t}\right)\right]\times\hat{\boldsymbol{f}}\left(\hat{s}',\hat{t}\right)d\hat{s}'\\
&\quad-\mathcal{M}\mathcal{S}^4\int_{\hat{s}}^1\cos\left(\hat{k}\hat{s}'-\hat{t}\right)H\left(\hat{\ell}-\hat{s}'\right)d\hat{s}', && (3.69d)\\
\mathbf{0} &= \int_0^1\hat{\boldsymbol{f}}\left(\hat{s}',\hat{t}\right)d\hat{s}'+\iint_{\partial\hat{H}(\hat{t})}\hat{\boldsymbol{\Phi}}\left(\hat{\boldsymbol{Y}},\hat{t}\right)dS_{\hat{\boldsymbol{Y}}}, && (3.69e)\\
0 &= \boldsymbol{e}_3\cdot\int_0^1\left[\hat{\boldsymbol{X}}\left(\hat{s}',\hat{t}\right)-\hat{\boldsymbol{X}}_0\left(\hat{t}\right)\right]\times\hat{\boldsymbol{f}}\left(\hat{s}',\hat{t}\right)d\hat{s}'\\
&\quad+\boldsymbol{e}_3\cdot\iint_{\partial\hat{H}(\hat{t})}\left[\hat{\boldsymbol{Y}}-\hat{\boldsymbol{X}}_0\left(\hat{t}\right)\right]\times\hat{\boldsymbol{\Phi}}\left(\hat{\boldsymbol{Y}},\hat{t}\right)dS_{\hat{\boldsymbol{Y}}}, && (3.69f)\\
\partial_{\hat{t}}\hat{X}_i\left(\hat{s},\hat{t}\right) &= \hat{\mathcal{U}}_i\left(\hat{\boldsymbol{X}}\left(\hat{s},\hat{t}\right),\hat{t}\right)+\int_0^1\hat{S}_{ij}^{\hat{\epsilon}}\left(\hat{\boldsymbol{X}}\left(\hat{s},\hat{t}\right),\hat{\boldsymbol{X}}\left(\hat{s}',\hat{t}\right)\right)\hat{f}_j\left(\hat{s}',\hat{t}\right)d\hat{s}'\\
&\quad+\iint_{\partial\hat{H}(\hat{t})}\hat{S}_{ij}^{\hat{\epsilon}}\left(\hat{\boldsymbol{X}}\left(\hat{s},\hat{t}\right),\hat{\boldsymbol{Y}}\right)\hat{\Phi}_j\left(\hat{\boldsymbol{Y}},\hat{t}\right)dS_{\hat{\boldsymbol{Y}}}, && (3.69g)\\
\partial_{\hat{t}}\hat{\boldsymbol{X}}\left(\hat{s},\hat{t}\right) &= d_{\hat{t}}\hat{\boldsymbol{X}}_0\left(\hat{t}\right)+\int_0^{\hat{s}}\partial_{\hat{t}}\theta\left(\hat{s}',\hat{t}\right)\left[-\sin\theta\left(\hat{s}',\hat{t}\right),\cos\theta\left(\hat{s}',\hat{t}\right),0\right]^T d\hat{s}', && (3.69h)\\
d_{\hat{t}}\hat{Y}_i\left(\hat{t}\right) &= \hat{\mathcal{U}}_i\left(\hat{\boldsymbol{Y}}\left(\hat{t}\right),\hat{t}\right)+\int_0^1\hat{S}_{ij}^{\hat{\epsilon}}\left(\hat{\boldsymbol{Y}}\left(\hat{t}\right),\hat{\boldsymbol{X}}\left(\hat{s}',\hat{t}\right)\right)\hat{f}_j\left(\hat{s}',\hat{t}\right)d\hat{s}'
\end{aligned}$$

$$+ \iint_{\partial \hat{H}(\hat{t})} \hat{S}_{ij}^{\hat{\epsilon}} \left(\hat{Y} \left(\hat{t} \right), \hat{Y} \right) \hat{\Phi}_j \left(Y, t \right) \, dS_{\hat{Y}}, \tag{3.69i}$$

$$d_{\hat{t}} \hat{Y} \left(\hat{t} \right) = d_{\hat{t}} \hat{\boldsymbol{X}}_0 \left(\hat{t} \right) + d_{\hat{t}} \hat{\phi} \left(\hat{t} \right) \, \boldsymbol{e}_3 \times \left[\hat{Y} \left(\hat{t} \right) - \hat{\boldsymbol{X}}_0 \left(\hat{t} \right) \right], \tag{3.69j}$$

where $0 \leq \hat{s} \leq 1$ and $\hat{t} \geq 0$. The dimensionless form of the elastic stiffness function $\hat{E}(\hat{s})$ is given via equation (2.19), the dimensionless form of the geometry equation is given in equation (2.20), and the dimensionless form of the head-flagellum boundary condition is given via equation (2.21). In addition, the dimensionless form of the BCC4p constitutive law is

$$\hat{\mu} \left(\hat{\dot{\gamma}} \left(\hat{\boldsymbol{U}} \left(\hat{\boldsymbol{x}}, \hat{t} \right) + \hat{\boldsymbol{u}}_S \left(\hat{\boldsymbol{x}}, \hat{t} \right) \right) \right) = 1 + \left[\beta_0 - 1 \right] \left[1 + \left[\mathrm{De} \, \hat{\dot{\gamma}} \left(\hat{\boldsymbol{U}} \left(\hat{\boldsymbol{x}}, \hat{t} \right) + \hat{\boldsymbol{u}}_S \left(\hat{\boldsymbol{x}}, \hat{t} \right) \right) \right]^2 \right]^{\frac{n-1}{2}}, \tag{3.70}$$

and we have that

$$\hat{u}_{S_i} \left(\hat{\boldsymbol{x}}, \hat{t} \right) = \int_0^1 \hat{S}_{ij}^{\hat{\epsilon}} \left(\hat{\boldsymbol{x}}, \hat{\boldsymbol{X}} \left(\hat{s}', \hat{t} \right) \right) \hat{f}_j \left(\hat{s}', \hat{t} \right) d\hat{s}' + \iint_{\partial \hat{H}(\hat{t})} \hat{S}_{ij}^{\hat{\epsilon}} \left(\hat{\boldsymbol{x}}, \hat{Y} \right) \hat{\Phi}_j \left(\hat{Y}, \hat{t} \right) dS_{\hat{Y}}, \tag{3.71a}$$

$$\hat{p}_S \left(\hat{\boldsymbol{x}}, \hat{t} \right) = \int_0^1 \hat{P}_j^{\hat{\epsilon}} \left(\hat{\boldsymbol{x}}, \hat{\boldsymbol{X}} \left(\hat{s}', \hat{t} \right) \right) \hat{f}_j \left(\hat{s}', \hat{t} \right) d\hat{s}' + \iint_{\partial \hat{H}(\hat{t})} \hat{P}_j^{\hat{\epsilon}} \left(\hat{\boldsymbol{x}}, \hat{Y} \right) \hat{\Phi}_j \left(\hat{Y}, \hat{t} \right) dS_{\hat{Y}}, \tag{3.71b}$$

with

$$\hat{S}_{ij}^{\hat{\epsilon}} \left(\hat{\boldsymbol{x}}, \hat{\boldsymbol{y}} \right) = \frac{1}{8\pi\beta_S} \left[\delta_{ij} \frac{\hat{r}^2 + 2\hat{\epsilon}^2}{\left[\hat{r}^2 + \hat{\epsilon}^2 \right]^{3/2}} + \frac{\hat{r}_i \hat{r}_j}{\left[\hat{r}^2 + \hat{\epsilon}^2 \right]^{3/2}} \right], \tag{3.72a}$$

$$\hat{P}^{\hat{\epsilon}} \left(\hat{\boldsymbol{x}}, \hat{\boldsymbol{y}} \right) = \frac{1}{4\pi} \left[\hat{r}_j \frac{2\hat{r}^2 + 5\hat{\epsilon}^2}{\left[\hat{r}^2 + \hat{\epsilon}^2 \right]^{5/2}} \right], \tag{3.72b}$$

where $\hat{r}_i = \hat{x}_i - \hat{y}_i$ and $\hat{r} = |\hat{\boldsymbol{x}} - \hat{\boldsymbol{y}}|$. As in Section 3.4, we have dimensionless groups $\mathrm{De} = \lambda\omega$ (Deborah number), $\beta_0 = \mu_0/\mu_\infty$ (zero-infinite shear rate viscosity ratio), $\beta_S = \mu_S/\mu_\infty$ (Newtonian-infinite shear rate viscosity ratio) and n (shear-thinning index). We also have the 'sperm number' $\mathcal{S} = L(\mu_\infty \omega / E_d)^{1/4}$, comparing viscous and elastic forces in the problem, the active-viscous ratio $\mathcal{M} = m_0/\mu_\infty \omega L^2$, and proximal-distal stiffness ratio ρ. Finally, we have the dimensionless regularisation parameter $\hat{\epsilon} = \epsilon/L$, active tail length $\hat{\ell} = \ell/L$ and wavenumber $\hat{k} = kL$. We drop the dimensionless 'hat' notation in what follows for clarity.

3.5.3 Solution method

The finite element weak formulation of the boundary value problem described in equations (3.69a–c) can be derived in the same way as in Section 3.4, and is given by system (3.44) with $\boldsymbol{u}_S$ and p_S defined as in (3.71). Unlike in the spring case, the forces involved in the calculation of the regularised stokeslet terms are unknown and must be solved for, along with the unknowns $\boldsymbol{X}_0(t)$, $\phi(t)$ and $\theta(s,t)$. Due to the dependence of the shear rate on $\boldsymbol{u}_S(\boldsymbol{x},t)$, which in turn depends on the unknown forces, the weak formulation is non-linear in $\boldsymbol{f}(s,t)$ and $\boldsymbol{\Phi}(\boldsymbol{Y},t)$. The system is also non-linear in the perturbation velocity $\boldsymbol{\mathcal{U}}(\boldsymbol{x},t)$ as before, and is linearised via a Picard iterative process, the steps of which follow:

1. Initialise with $r = 0$ and set

$$\begin{cases} \boldsymbol{\mathcal{U}}^0(\boldsymbol{x},t) = \boldsymbol{0} \text{ for every } \boldsymbol{x} \in \Omega, \\ \boldsymbol{\Phi}^0(\boldsymbol{Y},t) = \boldsymbol{0} \text{ for all } \boldsymbol{Y} \in \partial H, \\ \boldsymbol{f}^0(s,t) = \boldsymbol{0} \text{ for } 0 \leq s \leq 1. \end{cases} \tag{3.73}$$

2. Set $r = r + 1$.

3. Find $(\boldsymbol{\mathcal{U}}^r, \mathcal{P}^r) \in V(\Omega) \times L_0^2(\Omega)$, along with $\left(\boldsymbol{\Phi}^r(\boldsymbol{Y},t), \boldsymbol{f}^r(s,t)\right)$, such that $\forall\, (\boldsymbol{v}, q) \in W(\Omega) \times L_0^2(\Omega)$,

$$\begin{aligned} \boldsymbol{0} = &\int_\Omega 2\mu\left(\dot{\gamma}\left(\boldsymbol{\mathcal{U}}^{r-1} + \boldsymbol{u}_S^{r-1}\right)\right)\left[\boldsymbol{\varepsilon}\left(\boldsymbol{\mathcal{U}}^r\right) : \boldsymbol{\varepsilon}(\boldsymbol{v})\right] d\boldsymbol{x} - \int_\Omega \mathcal{P}^r\left[\nabla \cdot \boldsymbol{v}\right] d\boldsymbol{x} \\ &+ \int_\Omega \left\{ 2\mu\left(\dot{\gamma}\left(\boldsymbol{\mathcal{U}}^{r-1} + \boldsymbol{u}_S^{r-1}\right)\right)\left[\boldsymbol{\varepsilon}\left(\boldsymbol{u}_S^r\right) : \boldsymbol{\varepsilon}(\boldsymbol{v})\right] - \beta_S\left[\nabla \boldsymbol{u}_S^r : \nabla \boldsymbol{v}\right] \right\} d\boldsymbol{x}, \end{aligned} \tag{3.74a}$$

$$0 = \int_\Omega q\left[\nabla \cdot \boldsymbol{\mathcal{U}}^r\right] d\boldsymbol{x}, \tag{3.74b}$$

$$\begin{aligned} 0 = &\rho\kappa(0,t) - \boldsymbol{e}_3 \cdot \mathcal{S}^4 \iint_{\partial H(t)} \left[\boldsymbol{Y} - \boldsymbol{X}_0(t)\right] \times \boldsymbol{\Phi}^r(\boldsymbol{Y},t) dS_Y \\ &- \mathcal{M}\mathcal{S}^4 \int_0^1 \cos\left(ks' - t\right) H\left(\ell - s'\right) d\hat{s}', \end{aligned} \tag{3.74c}$$

$$\begin{aligned} 0 = &E(s)\, \partial_s \theta(s,t) + \boldsymbol{e}_3 \cdot \mathcal{S}^4 \int_s^1 \left[\boldsymbol{X}\left(s',t\right) - \boldsymbol{X}(s,t)\right] \times \boldsymbol{f}^r\left(s',t\right) ds' \\ &- \mathcal{M}\mathcal{S}^4 \int_s^1 \cos\left(ks' - t\right) H\left(\ell - s'\right) ds', \end{aligned} \tag{3.74d}$$

$$\mathbf{0} = \int_0^1 \boldsymbol{f}^r\left(s',t\right) ds' + \iint_{\partial H(t)} \boldsymbol{\Phi}^r\left(\boldsymbol{Y},t\right) dS_Y, \tag{3.74e}$$

$$\begin{aligned} 0 = \boldsymbol{e}_3 \cdot \int_0^1 \left[\boldsymbol{X}\left(s',t\right) - \boldsymbol{X}_0\left(t\right)\right] \times \boldsymbol{f}^r\left(s',t\right) ds' \\ + \boldsymbol{e}_3 \cdot \iint_{\partial H(t)} \left[\boldsymbol{Y} - \boldsymbol{X}_0\left(t\right)\right] \times \boldsymbol{\Phi}^r\left(\boldsymbol{Y},t\right) dS_Y, \end{aligned} \tag{3.74f}$$

$$\begin{aligned} \partial_t X_i\left(s,t\right) = \mathcal{U}_i^r\left(\boldsymbol{X}\left(s,t\right),t\right) + \int_0^1 S_{ij}^\epsilon\left(\boldsymbol{X}\left(s,t\right),\boldsymbol{X}\left(s',t\right)\right) f_j^r\left(s',t\right)\, ds' \\ + \iint_{\partial H(t)} S_{ij}^\epsilon\left(\boldsymbol{X}\left(s,t\right),\boldsymbol{Y}\right) \Phi_j^r\left(\boldsymbol{Y},t\right)\, dS_Y, \end{aligned} \tag{3.74g}$$

$$\partial_t \boldsymbol{X}\left(s,t\right) = d_t \boldsymbol{X}_0\left(t\right) + \int_0^s \partial_t\theta\left(s',t\right)\left[-\sin\theta\left(s',t\right),\cos\theta\left(s',t\right),0\right]^T ds', \tag{3.74h}$$

$$\begin{aligned} d_t Y_i\left(t\right) = \mathcal{U}_i^r\left(\boldsymbol{Y}\left(t\right),t\right) + \int_0^1 S_{ij}^\epsilon\left(\boldsymbol{Y}\left(t\right),\boldsymbol{X}\left(s',t\right)\right) f_j^r\left(s',t\right)\, ds' \\ + \iint_{\partial H(t)} S_{ij}^\epsilon\left(\boldsymbol{Y}\left(t\right),\boldsymbol{Y}\right) \Phi_j^r\left(\boldsymbol{Y},t\right)\, dS_Y, \end{aligned} \tag{3.74i}$$

$$d_t \boldsymbol{Y}\left(t\right) = d_t \boldsymbol{X}_0\left(t\right) + d_t\phi\left(t\right)\, \boldsymbol{e}_3 \times \left[\boldsymbol{Y}\left(t\right) - \boldsymbol{X}_0\left(t\right)\right], \tag{3.74j}$$

where $0 \leq \hat{s} \leq 1$, $\hat{t} \geq 0$, and

$$u_{S_i}^r\left(\boldsymbol{x},t\right) = \int_0^1 S_{ij}^\epsilon\left(\boldsymbol{x},\boldsymbol{X}\left(s',t\right)\right) f_j^r\left(s',t\right) ds' + \iint_{\partial H(t)} S_{ij}^\epsilon\left(\boldsymbol{x},\boldsymbol{Y}\right) \Phi_j^r\left(\boldsymbol{Y},t\right) dS_Y, \tag{3.75a}$$

$$p_S^r\left(\boldsymbol{x},t\right) = \int_0^1 P_j^\epsilon\left(\boldsymbol{x},\boldsymbol{X}\left(s',t\right)\right) f_j^r\left(s',t\right) ds' + \iint_{\partial H(t)} P_j^\epsilon\left(\boldsymbol{x},\boldsymbol{Y}\right) \Phi_j^r\left(\boldsymbol{Y},t\right) dS_Y. \tag{3.75b}$$

The form of the elastic stiffness function $E(s)$ is given via equation (2.19), the viscosity is described via the constitutive law (3.70), the regularised stokeslet kernels are defined in (3.72), and the shape of the flagellum is described via the geometry equation (2.20).

4. Calculate $\boldsymbol{u}^r = \boldsymbol{\mathcal{U}}^r + \boldsymbol{u}_S^r$ and $p^r = \mathcal{P}^r + p_S^r$.

5. Repeat steps 2–4 until converged.

3.5.4 Discretisation

As in the end piece model, the flagellum is discretised into $Q = N - 1$ straight-line segments of equal length $\Delta s = 1/Q$, as described in Section 2.2.3. The end points of each segment are

denoted $\boldsymbol{X}^{[n]}(t)$ for $n = 1, 2, \dots, N$ where $\boldsymbol{X}^{[1]}(t) := \boldsymbol{X}_0(t)$. At each iteration r, the force on the n^{th} segment, which is assumed to be acting at the segment midpoint $\tilde{\boldsymbol{X}}^{[n]}(t)$, is denoted $\tilde{\boldsymbol{f}}^{[n;r]}(t)$ for $n = 1, 2, \dots, Q$. The elliptical head surface ∂H is discretised via a set of nodes $\left\{\boldsymbol{Y}^{[1]}(t), \boldsymbol{Y}^{[2]}(t), \dots, \boldsymbol{Y}^{[M_h]}(t)\right\}$. The force per unit area exerted by the head on the fluid at these points at each iteration r is denoted $\left\{\boldsymbol{\Phi}^{[1;r]}(t), \boldsymbol{\Phi}^{[2;r]}(t), \dots, \boldsymbol{\Phi}^{[M_h;r]}(t)\right\}$. The discretised form of the regularised stokeslet solutions $\boldsymbol{u}_S^r(\boldsymbol{x}, t)$ and $p_S^r(\boldsymbol{x}, t)$ are given by

$$u_{S_i}^r(\boldsymbol{x}, t) = \sum_{n=1}^{Q} I_{ij}^{[n]}(\boldsymbol{x}, t)\tilde{f}_j^{[n;r]}(t) + \sum_{m=1}^{M_h} S_{ij}^{\epsilon}\left(\boldsymbol{x}, \boldsymbol{Y}^{[m]}(t)\right)\Phi_j^{[m;r]}(t), \tag{3.76a}$$

$$p_S^r(\boldsymbol{x}, t) = \sum_{n=1}^{Q} J_j^{[n]}(\boldsymbol{x}, t)\tilde{f}_j^{[n;r]}(t) + \sum_{m=1}^{M_h} P_j^{\epsilon}\left(\boldsymbol{x}, \boldsymbol{Y}^{[m]}(t)\right)\Phi_j^{[m;r]}(t), \tag{3.76b}$$

where the terms $I_{ij}^{[n]}(\boldsymbol{x}, t)$ and $J_j^{[n]}(\boldsymbol{x}, t)$ represent the segment integrals

$$I_{ij}^{[n]}(\boldsymbol{x}, t) := \int_{(n-1)\Delta s}^{n\Delta s} S_{ij}^{\epsilon}\left(\boldsymbol{x}, \tilde{\boldsymbol{X}}^{[n]}(t) + [s' - \tilde{s}^{[n]}]\left[\cos\tilde{\theta}^{[n]}(t), \sin\tilde{\theta}^{[n]}(t), 0\right]^T\right) ds', \tag{3.77a}$$

$$J_j^{[n]}(\boldsymbol{x}, t) := \int_{(n-1)\Delta s}^{n\Delta s} P_j^{\epsilon}\left(\boldsymbol{x}, \tilde{\boldsymbol{X}}^{[n]}(t) + [s' - \tilde{s}^{[n]}]\left[\cos\tilde{\theta}^{[n]}(t), \sin\tilde{\theta}^{[n]}(t), 0\right]^T\right) ds', \tag{3.77b}$$

which can be calculated analytically. Here $\tilde{s}^{[n]}$, denotes the arclength at the midpoint of the n^{th} segment and the angle connecting the points $\boldsymbol{X}^{[n]}(t)$ and $\boldsymbol{X}^{[n+1]}(t)$ is denoted $\tilde{\theta}^{[n]}(t)$ for $n = 1, 2, \dots, Q$. In a similar way to the derivation described in Section 2.2.3, the discrete form of the equations (3.74c–j) is given by

$$\begin{aligned} 0 = {} & \rho\left[\frac{\tilde{\theta}^{[1]}(t) - \phi(t)}{\Delta s}\right] - \delta_{i3}\mathcal{S}^4\sum_{m=1}^{M_h}\varepsilon_{ijk}\left[Y_j^{[m]}(t) - X_{0\,j}(t)\right]\Phi_k^{[m;r]} \\ & - \mathcal{M}\mathcal{S}^4\int_0^1 \cos(ks' - t)H(\ell - s')ds', \end{aligned} \tag{3.78a}$$

$$\begin{aligned} 0 = {} & E\left(s^{[n+1]}\right)\left[\frac{\tilde{\theta}^{[n+1]}(t) - \tilde{\theta}^{[n]}(t)}{\Delta s}\right] \\ & + \delta_{i3}\mathcal{S}^4\sum_{m=n}^{Q-1}\Delta s\varepsilon_{ijk}\left[\tilde{X}_j^{[m+1]}(t) - X_j^{[n+1]}(t)\right]\tilde{f}_k^{[m+1;r]} \\ & - \mathcal{M}\mathcal{S}^4\int_{s^{[n+1]}}^1 \cos(ks' - t)H(\ell - s')ds', \end{aligned} \tag{3.78b}$$

$$0 = \sum_{n=1}^{Q} \Delta s \tilde{f}_i^{[n;r]}(t) + \sum_{m=1}^{M_h} \Phi_i^{[m;r]}(t), \tag{3.78c}$$

$$\begin{aligned} 0 = {} & \delta_{i3} \sum_{n=1}^{Q} \Delta s \varepsilon_{ijk} \left[\tilde{X}_j^{[n]}(t) - X_{0j}(t) \right] \tilde{f}_k^{[n;r]}(t) \\ & + \delta_{i3} \sum_{m=1}^{M_h} \varepsilon_{ijk} \left[Y_j^{[m]}(t) - X_{0j}(t) \right] \Phi_k^{[m;r]}(t), \end{aligned} \tag{3.78d}$$

$$\begin{aligned} d_t \tilde{X}_i^{[n]}(t) = {} & \mathcal{U}_i^r \left(\boldsymbol{X}^{[n]}(t), t \right) + \sum_{m=1}^{Q} I_{ij}^{[m]} \left(\tilde{\boldsymbol{X}}^{[n]}(t), t \right) \tilde{f}_j^{[m;r]}(t) \\ & + \sum_{m=1}^{M_h} S_{ij}^{\epsilon} \left(\tilde{\boldsymbol{X}}^{[n]}(t), \boldsymbol{Y}^{[q]}(t) \right) \Phi_j^{[m;r]}(t), \end{aligned} \tag{3.78e}$$

$$\begin{aligned} d_t \tilde{\boldsymbol{X}}^{[n]}(t) = {} & d_t \boldsymbol{X}_0(t) + \sum_{m=1}^{n-1} \left\{ \Delta s d_t \tilde{\theta}^{[m]}(t) \left[-\sin \tilde{\theta}^{[m]}(t), \cos \tilde{\theta}^{[m]}(t), 0 \right]^T \right\} \\ & + \frac{\Delta s}{2} \partial_t \tilde{\theta}^{[n]}(t) \left[-\sin \tilde{\theta}^{[n]}(t), \cos \tilde{\theta}^{[n]}(t), 0 \right]^T, \end{aligned} \tag{3.78f}$$

$$\begin{aligned} d_t Y_i^{[m]}(t) = {} & \mathcal{U}_i^r \left(\boldsymbol{Y}^{[m]}(t), t \right) + \sum_{n=1}^{Q} I_{ij}^{[n]} \left(\boldsymbol{Y}^{[m]}(t), t \right) \tilde{f}_j^{[n;r]}(t) \\ & + \sum_{m=1}^{M_h} S_{ij}^{\epsilon} \left(\boldsymbol{Y}^{[m]}(t), \boldsymbol{Y}^{[q]}(t) \right) \Phi_j^{[m;r]}(t), \end{aligned} \tag{3.78g}$$

$$d_t \boldsymbol{Y}^{[m]}(t) = d_t \boldsymbol{X}_0(t) + d_t \phi(t) \boldsymbol{e}_3 \times [\boldsymbol{Y}^{[m]}(t) - \boldsymbol{X}_0^r(t)], \tag{3.78h}$$

for $n = 1, 2, \ldots, Q$ and $m = 1, 2, \ldots, M_h$ where ε_{ijk} is the Levi-Civita tensor, δ_{ij} is the Kronecker delta function and repeated indices are summed over. As shown in Section 2.2.3, we may eliminate the variables $\left\{ d_t \tilde{\boldsymbol{X}}^{[n]}(t) \right\}_{n=1}^{Q}$, $\left\{ d_t \boldsymbol{Y}^{[m]}(t) \right\}_{m=1}^{M_h}$, $\left\{ \boldsymbol{X}^{[n]}(t) \right\}_{n=1}^{N}$ and $\left\{ \tilde{\boldsymbol{X}}^{[n]}(t) \right\}_{n=1}^{Q}$ from the system. The remaining system is linear in $d_t \boldsymbol{X}_0(t)$, $\phi(t)$, $d_t \tilde{\theta}^{[1]}(t), \ldots, d_t \tilde{\theta}^{[Q]}(t)$, $\tilde{\boldsymbol{f}}^{[1;r]}(t), \ldots, \tilde{\boldsymbol{f}}^{[Q;r]}(t)$ and $\boldsymbol{\Phi}^{[1;r]}(t), \ldots, \boldsymbol{\Phi}^{[M_h;r]}(t)$, as well as the unknown velocity and pressure perturbation solutions.

Following the method in Sections 3.2 and 3.4, the domain Ω is partitioned into arbitrary polyhedera elements to form the domain Ω_h. The velocity $\boldsymbol{\mathcal{U}}$ and pressure $\mathcal{P}$ solutions are expanded in terms of piecewise polynomial basis functions $\{\varphi_n(\boldsymbol{x})\}_{n=1}^{N}$ and $\{\psi_m(\boldsymbol{x})\}_{m=1}^{M}$ as in equations (3.7) and (3.8) respectively. Given an initial discrete configuration of the cell

$$\boldsymbol{Z}_0 = \left[\boldsymbol{X}_0(0), \phi(0), \tilde{\theta}^{[1]}(0), \tilde{\theta}^{[2]}(0), \ldots, \tilde{\theta}^{[Q]}(0) \right]^T, \tag{3.79}$$

the full system can be expressed as an initial value problem

$$d_t Z = \mathcal{F}(Z, t), \quad Z(0) = Z_0, \tag{3.80}$$

where $Z(t) := \left[\boldsymbol{X}_0(t), \phi(t), \tilde{\theta}^{[1]}(t), \tilde{\theta}^{[2]}(t), \ldots, \tilde{\theta}^{[Q]}(t)\right]^T$. At each timestep and iteration, augmenting the problem with a vector of unknown head forces $\boldsymbol{\Phi}^r$, flagellum forces $\tilde{\boldsymbol{f}}^r$, nodal velocities $\boldsymbol{U}^r$ and nodal pressures $\boldsymbol{P}^r$, yields a linear system given by

$$\mathrm{A}^r \begin{bmatrix} d_t \boldsymbol{Z}^r \\ \boldsymbol{\Phi}^r \\ \tilde{\boldsymbol{f}}^r \\ \boldsymbol{U}^r \\ \boldsymbol{P}^r \end{bmatrix} = \boldsymbol{c}, \tag{3.81}$$

where

$$\mathrm{A}^r = \left[\begin{array}{c|c|c} 0 & \mathrm{A}_E & 0 \\ \hline \mathrm{A}_K & \mathrm{A}_H & \mathrm{A}_P \\ \hline 0 & \mathrm{A}_L^{r-1} & \mathrm{A}_{\mathrm{F}}^{r-1} \end{array}\right], \tag{3.82}$$

$$\boldsymbol{c} = \left[0, \rho\left(\frac{\tilde{\theta}^{[1]}(t) - \phi(t)}{\Delta s}\right) - \Lambda^{[1]}(t), E\left(s^{[2]}\right)\left(\frac{\tilde{\theta}^{[2]}(t) - \tilde{\theta}^{[1]}(t)}{\Delta s}\right) - \Lambda^{[2]}(t), \ldots, E\left(s^{[Q]}\right)\left(\frac{\tilde{\theta}^{[Q]}(t) - \tilde{\theta}^{[Q-1]}(t)}{\Delta s}\right) - \Lambda^{[Q]}(t), 0, 0, 0, \ldots, 0\right]^T. \tag{3.83}$$

The matrix block A_E encodes the elastodynamics of the problem. The first row corresponds to the total moment balance equation (3.78d), along with the first component of the vector $\boldsymbol{c}$. The second row of A_E, along with the second component of $\boldsymbol{c}$, corresponds to the enforcement of

the discrete moment boundary condition at the head-flagellum joint (equation (3.78a)), where $\Lambda^{[q]}(t)$ is defined as in equation (2.42). The next $Q-1$ rows of the matrix correspond to moment balance about each interior flagellum joint, i.e. the discrete elasticity equation (3.78b). The final two rows of A_E correspond to force balance in the x and y directions, i.e. equation (3.78c). Thus, the total size of A_E is $(Q+3)\times(3Q+3M_h)$.

The blocks A_K, A_H and A_P encode the discrete form of the kinematics ((3.78f) and (3.78h)) and hydrodynamics ((3.78e) and (3.78g)) equations. The kinematics block A_K is of size $(3Q+3M_h)\times(Q+3)$. The block A_H is a $(3Q+3M_h)\times(3Q+3M_h)$ stokeslet matrix, accounting for the 2nd and 3rd terms on the right hand side of the discrete hydrodynamics equations. This matrix consists of both analytic segment integrals for the flagellum terms and stokeslet evaluations for the head terms. The first term on the right hand side of the hydrodynamics equations is accounted for through the $(3Q+3M_h)\times(3N+M)$ block A_P. This block projects the value of the perturbation velocity $\boldsymbol{\mathcal{U}}^r(\boldsymbol{x},t)$ at the nodes of the finite element mesh to the solution evaluated at the segment midpoints and head points. This is achieved through interpolation via the velocity basis functions, as detailed in equation (3.22a).

Together, the blocks A_F^{r-1}, A_L^{r-1} form the discrete form of the weak formulation (3.74a–b). The matrix block A_F^{r-1} has the same form as the stiffness matrix Z in the [DGNS]. The size of A_F^{r-1} is $(3N+M)\times(3N+M)$. The block A_L^{r-1}, when multiplied by the vector of unknown forces, forms the load vector of the finite element system (i.e. $\boldsymbol{b}$ in [DGNS], where we note that $\boldsymbol{u}_S$ is now calculated per iteration). This block also applies the boundary conditions through applying the discrete form of equation (3.69c) to boundary nodes. The size of A_L^{r-1} is $(3N+M)\times(3Q+3M_h)$.

3.5.5 Implementation

The domain Ω is again divided into hexahedron elements to form a mesh. As in Sections 3.2 and 3.4, we generate a structured mesh, where in this case we choose to refined the mesh near the cell. Specifically, for a cell with a flagellum of dimensionless length $L=1$ and head radii

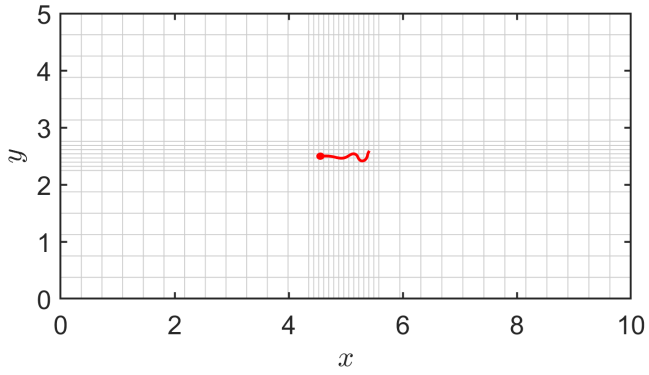


Figure 3.13: View in the xy-plane of an example hexahedron mesh of the domain $\Omega = [0, 10] \times [0, 5] \times [0, 5]$. The domain contains a sperm cell with a flagellum of dimensionless length $L = 1$ and dimensionless head radii $r_x = 0.0444$ and $r_y = 0.0356$. The mesh is more refined in a box surrounding the cell, the dimensions of which are give in equation (3.84).

$r_x = 0.0444$ and $r_y = 0.0356$, we refine the mesh in the region defined by the box

$$\left[X_1^{[1]}(t) - \frac{1}{4}, X_1^{[Q+1]}(t) + \frac{1}{6}\right] \times \left[X_2^{[1]}(t) - \frac{1}{6}, X_2^{[Q+1]}(t) + \frac{1}{6}\right] \times \left[X_3^{[1]}(t) - \frac{1}{6}, X_3^{[Q+1]}(t) + \frac{1}{6}\right]. \quad (3.84)$$

An example mesh can be seen in Figure 3.13. We choose to refine the mesh close to the cell since this is the region where the solution varies most rapidly, and where we desire the most accurate interpretation of the solution. Whilst this mesh is not truly body fitted since there is no requirement for finite element nodes on cell body, it does require re-meshing at each time-step as the cell evolves.

The basis functions for velocity $\{\varphi_n(\boldsymbol{x})\}_{n=1}^N$ and pressure $\{\psi_m(\boldsymbol{x})\}_{m=1}^M$ are again chosen to be piecewise quadratic and piecewise linear respectively, as discussed in detail in Section 3.2. Basis functions are calculated on the reference element and mapped to all other elements of the mesh as previously. The volume integrals that must be evaluated in order to construct the matrix block A_F^{r-1} are calculated numerically using a $5 \times 5 \times 5$ Gauss-Legendre quadrature rule, as before.

The matrix A_L^{r-1} has block form

$$\mathrm{A}_L^{r-1} = \left[\begin{array}{c|c} \mathrm{A}_L^{h,r-1} & \mathrm{A}_L^{f,r-1} \end{array}\right], \quad (3.85)$$

where $\mathrm{A}_L^{h,r-1}$ is a $(3N+M)\times 3M_h$ matrix multiplying the vector of unknown head forces per unit area $\boldsymbol{\Phi}^r$, and $\mathrm{A}_L^{f,r-1}$ is a $(3N+M)\times 3Q$ matrix multiplying the vector of unknown flagellum forces per unit length $\boldsymbol{f}^r$. The form of $\mathrm{A}_L^{h,r-1}$ is given by

$$\mathrm{A}_L^{h,r-1} = \left[\begin{array}{c|c|c} \mathrm{R}_{11}^{h,r-1} & \mathrm{R}_{12}^{h,r-1} & \mathrm{R}_{13}^{h,r-1} \\ \hline \mathrm{R}_{21}^{h,r-1} & \mathrm{R}_{22}^{h,r-1} & \mathrm{R}_{23}^{h,r-1} \\ \hline \mathrm{R}_{31}^{h,r-1} & \mathrm{R}_{32}^{h,r-1} & \mathrm{R}_{33}^{h,r-1} \\ \hline 0 & 0 & 0 \end{array}\right], \tag{3.86}$$

where

$$\begin{aligned}[\mathrm{R}_{ij}^{h,r-1}]_{nm} = \int_{\Omega_h} \left[\mu\left(\dot{\gamma}\left(\boldsymbol{\mathcal{U}}^{r-1}+\boldsymbol{u}_S^{r-1}\right)-\beta_S\right)\right] \sum_{k=1}^{3} \frac{\partial \varphi_n}{\partial x_k}\frac{\partial}{\partial x_k} S_{ij}\left(\boldsymbol{x}, \boldsymbol{Y}^{[m]}(t)\right) \\ + \mu\left(\dot{\gamma}\left(\boldsymbol{\mathcal{U}}^{r-1}+\boldsymbol{u}_S^{r-1}\right)\right) \sum_{k=1}^{3} \frac{\partial \varphi_n}{\partial x_k}\frac{\partial}{\partial x_i} S_{kj}\left(\boldsymbol{x}, \boldsymbol{Y}^{[m]}(t)\right) d\boldsymbol{x}, \\ \text{for } n = 1,2,\ldots,N, \quad b = 1,2,\ldots,M_h. \end{aligned} \tag{3.87}$$

Similarly, the block form of $\mathrm{A}_L^{f,r-1}$ is given by

$$\mathrm{A}_L^{f,r-1} = \left[\begin{array}{c|c|c} \mathrm{R}_{11}^{f,r-1} & \mathrm{R}_{12}^{f,r-1} & \mathrm{R}_{13}^{f,r-1} \\ \hline \mathrm{R}_{21}^{f,r-1} & \mathrm{R}_{22}^{f,r-1} & \mathrm{R}_{23}^{f,r-1} \\ \hline \mathrm{R}_{31}^{f,r-1} & \mathrm{R}_{32}^{f,r-1} & \mathrm{R}_{33}^{f,r-1} \\ \hline 0 & 0 & 0 \end{array}\right], \tag{3.88}$$

where

$$[\mathrm{R}_{ij}^{f,r-1}]_{nq} = \int_{\Omega_h} \left[\mu\left(\dot{\gamma}\left(\boldsymbol{\mathcal{U}}^{r-1}+\boldsymbol{u}_S^{r-1}\right)-1\right)\right] \sum_{k=1}^{3} \frac{\partial \varphi_n}{\partial x_k}\frac{\partial}{\partial x_k} I_{ij}^{[q]}(\boldsymbol{x}, t)$$

$$+ \mu \left(\dot{\gamma} \left(\boldsymbol{\mathcal{U}}^{r-1} + \boldsymbol{u}_S^{r-1} \right) \right) \sum_{k=1}^{3} \frac{\partial \varphi_n}{\partial x_k} \frac{\partial}{\partial x_i} I_{kj}^{[q]}(\boldsymbol{x}, t) d\boldsymbol{x},$$

$$\text{for } n = 1, 2, \ldots, N, \quad q = 1, 2, \ldots, Q, \quad (3.89)$$

with $I_{ij}^{[q]}(\boldsymbol{x}, t)$ defined as in (3.77a). Differentiating under the integral sign, the expression $\frac{\partial}{\partial x_k} I_{ij}^{[q]}(\boldsymbol{x}, t)$ can be written as

$$\frac{\partial}{\partial x_k} I_{ij}^{[q]}(\boldsymbol{x}, t) = \int_{(q-1)\Delta s}^{q\Delta s} \frac{\partial}{\partial x_k} S_{ij}^{\epsilon} \left(\boldsymbol{x}, \tilde{\boldsymbol{X}}^{[q]}(t) + [s' - \tilde{s}^{[q]}] \left[\cos \tilde{\theta}^{[q]}(t), \sin \tilde{\theta}^{[q]}(t), 0 \right]^T \right) ds'. \quad (3.90)$$

Note that both equations (3.87) and (3.90) require the derivatives of the regularised stokeslet kernel $\boldsymbol{S}^{\epsilon}$. To calculate these, we first write the regularised stokeslet kernel as

$$S_{ij}^{\epsilon}(\boldsymbol{x}, \boldsymbol{y}) = \frac{1}{8\pi\beta_S} \left[A_{ij}^{\epsilon}(\boldsymbol{x}, \boldsymbol{y}) + B_{ij}^{\epsilon}(\boldsymbol{x}, \boldsymbol{y}) \right], \quad (3.91)$$

where

$$A_{ij}^{\epsilon}(\boldsymbol{x}, \boldsymbol{y}) = \delta_{ij} \frac{r^2 + 2\epsilon^2}{[r^2 + \epsilon^2]^{3/2}}, \quad (3.92a)$$

$$B_{ij}^{\epsilon}(\boldsymbol{x}, \boldsymbol{y}) = \frac{r_i r_j}{[r^2 + \epsilon^2]^{3/2}}, \quad (3.92b)$$

are the isotropic and dyadic components respectively. We calculate

$$\frac{\partial}{\partial x_k} S_{ij}^{\epsilon}(\boldsymbol{x}, \boldsymbol{y}) = \frac{1}{8\pi\beta_S} \left[\frac{\partial}{\partial x_k} A_{ij}^{\epsilon}(\boldsymbol{x}, \boldsymbol{y}) + \frac{\partial}{\partial x_k} B_{ij}^{\epsilon}(\boldsymbol{x}, \boldsymbol{y}) \right], \quad (3.93)$$

where

$$\frac{\partial}{\partial x_k} A_{ij}^{\epsilon}(\boldsymbol{x}, \boldsymbol{y}) = -\frac{\delta_{ij} r_k [r^2 + 4\epsilon^2]}{r_{\epsilon}^5}, \quad (3.94a)$$

$$\frac{\partial}{\partial x_k} B_{ij}^{\epsilon}(\boldsymbol{x}, \boldsymbol{y}) = -\frac{3 r_i r_j r_k [1 - \delta_{ik}][1 - \delta_{jk}]}{r_{\epsilon}^5} + \frac{\delta_{ik} r_j + \delta_{jk} r_i}{r_{\epsilon}^5} \left[r_{\epsilon}^2 - \frac{3 r_k^2}{2^{\delta_{ik}\delta_{jk}}} \right], \quad (3.94b)$$

and $\frac{\partial}{\partial x_k} A_{ij}^{\epsilon}(\boldsymbol{x}, \boldsymbol{y})$ and $\frac{\partial}{\partial x_k} B_{ij}^{\epsilon}(\boldsymbol{x}, \boldsymbol{y})$ are rank-3 tensors with $r_{\epsilon} = \sqrt{r^2 + \epsilon^2}$.

The integral of the regularised stokeslet derivatives defined in (3.90) is calculated analyt-

ically, as described in Appendix D. The integrands in equations (3.87) and (3.89) are rapidly varying close to the swimmer (in the region defined by (3.84)) due to the presence of the kernel S^ϵ, and are therefore costly to integrate. We again use the sinh transform rule, as described in Section 3.4.3, to reduce the computational costs associated with evaluating these integrals. For elements further away from the swimmer (within the complement of (3.84) in Ω), Gauss-Legendre quadrature is sufficient to calculate these volume integrals.

To determine the number of quadrature points required in each direction, we examine the convergence of the volume integrals over each mesh element. Specifically, we consider a hexahedron mesh of the domain $\Omega = [0, 10] \times [0, 5] \times [0, 5]$ consisting of $N_e = 13718$ elements, as depicted previously in Figure 3.13. For dimensionless parameters

$$\mathcal{S} = 13, \quad \mathcal{M} = 0.027, \quad \ell = 0.95, \quad \epsilon = 0.01, \quad k = 4\pi, \quad \mathrm{De} = 1, \quad \beta_0 = 2, \quad n = 0.1, \tag{3.95}$$

we consider the value of the the integrals (3.87) and (3.89) over each mesh element at $t = 2\pi$, i.e. after one beat cycle. We calculate the value of the integrals per element using both standard Gauss-Legendre quadrature and the sinh method, summing integral values over each basis function and segment/head point.

In Figure 3.14a, we indicate via the colour of each element the number of Gauss-Legendre quadrature points per direction required to reduce the error in approximating the head integrals to 1×10^{-9}. Similarly, the number of quadrature points per direction in the sinh method required to reduce the head integral error to 1×10^{-9} is shown in Figure 3.14b. Figures 3.14c and 3.14d show the equivalent plots but for flagellum integrals. We observe that using the sinh transform significantly reduces the number of quadrature points per direction required in elements contained within the region defined in equation (3.84). Specifically, whilst the elements in this region require up to $P = 40^3$ quadrature points in the Gauss-Legendre case to reduce the error to under 1×10^{-9}, only up to $P = 10^3$ quadrature points are required in the sinh case for the same level of error. This corresponds to a reduction of 63000 quadrature points, with the construction of the integrals over all mesh elements taking only approximately 3.5% of the

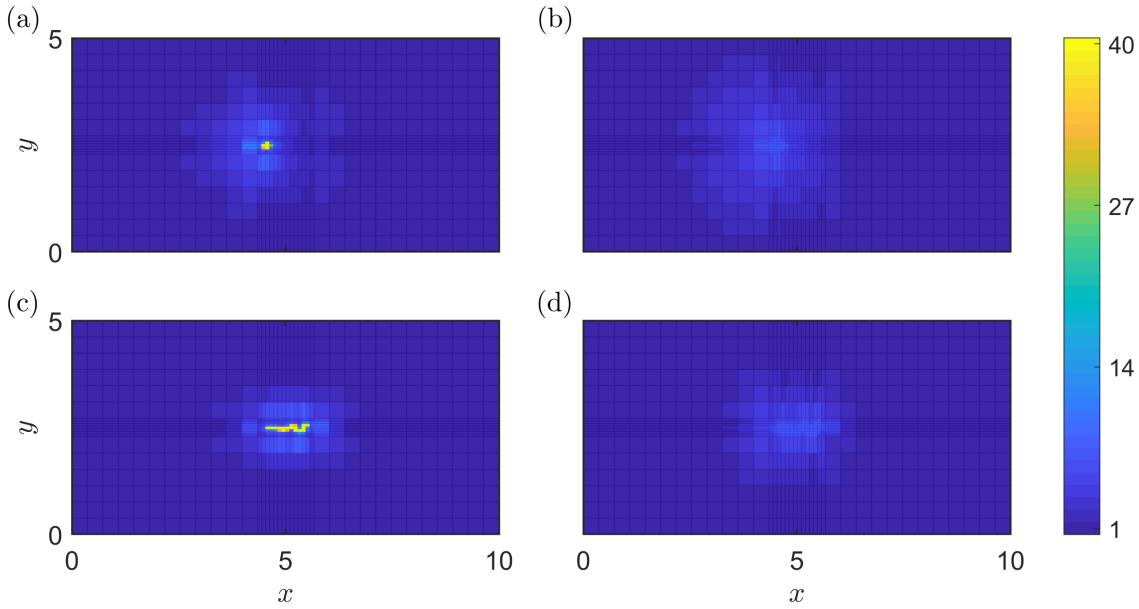


Figure 3.14: Convergence of the volume integrals (3.87) and (3.89) over a mesh of the domain $\Omega = [0, 10]\times[0, 5]\times[0, 5]$, consisting of $N_e = 13718$ elements and shown in the xy-plane. For the head integrals (3.89), the colour of each element in (a) shows the number of quadrature points per direction required to reduce the absolute error in approximating the integral using Gauss-Legendre quadrature to 1×10^{-9}, where the integral is summed over all basis functions and head points. Similarly, (b) shows the equivalent but for integrals approximated using the sinh method. (c) and (d) show convergence of the integrals over the flagellum segments, i.e. (3.87), summed over all basis function and flagellum segments and calculated using Gauss-Legendre and the sinh method respectively. Values are shown after one beat cycle, i.e. at $t = 2\pi$.

time spent in the Gauss-Legendre case (profiled in MATLAB®). Thus, in this inner region, we choose to evaluate integrals using the sinh method with $10 \times 10 \times 10$ quadrature points. In the outer region, defined as the the complement of (3.84) in Ω, we choose to use a $10 \times 10 \times 10$ Gauss-Legendre quadrature rule. Calculating these integrals allows for the construction of the matrix block A_L^{r-1}. The remaining matrix blocks A_E, A_K and A_H can be constructed from the form of the relevant discrete equations in system (3.78).

The parameters De, β_0 and n can again be chosen in the model depending on the desired shear-thinning properties of the fluid. The dimensionless group $\beta_S = \mu_S/\mu_\infty$ is again chosen in order for the regularised stokeslet component of the solution $\boldsymbol{u}_S(\boldsymbol{x}, t)$ to be the best approximation to the true solution near to the cell. This is in order for the perturbation solution $\boldsymbol{\mathcal{U}}(\boldsymbol{x}, t)$ to be slowly varying over the mesh. For each flagellum segment we choose a different value

of β_S, $\left\{\beta_S^q\right\}_{q=1}^{Q}$, chosen similarly to the spring case as the average of the dimensionless viscosity over a cylinder of radius ϵ surrounding the straight-line segment. For the head terms, β_S is similarly chosen to be the average of the dimensionless viscosity surrounding the head, a distance of ϵ away. In order for the system to be linear, we again require that these values of β_S are calculated from the viscosities at the previous iteration.

Given initial values $\boldsymbol{X}_0(0)$, $\{\tilde{\theta}^{[n]}(0)\}_{n=1}^{Q}$ and $\phi(0)$, the system (3.83) can be constructed and solved at each iteration r using the MATLAB® backslash command '\'. For a square m-by-m matrix A and a vector b consisting of m rows, applying the backslash command via $x = A \setminus b$ finds the solution to the linear system $Ax = b$. Once converged, the unknown vector $d_t \boldsymbol{Z}^{r_{\text{final}}}$ is integrated using the built in MATLAB® stiff ODE solver `ode23tb` and the velocity can be calculated at all mesh points. At any point in time, the sperm cell's position and shape can be reconstructed completely from $\boldsymbol{X}_0(t)$, $\{\tilde{\theta}^{[n]}(t)\}_{n=1}^{Q}$ and $\phi(t)$ through the discrete geometry equation (2.28) and the construction of the head from the point $\boldsymbol{X}_0(t)$ and angle $\phi(t)$. This allows for the simulation of a single sperm cell in a fluid modelled using the BCC4p constitutive law.

3.5.6 Numerical solver parameters and convergence

In this section, we discuss the choice of physical and numerical parameters that will be used when applying the HANS method to the simulation of sperm in shear-thinning fluids in Chapter 4. We consider a sperm cell with dimensionless flagellar length $L = 1$ and head radii $r_x = 0.0444$ and $r_y = 0.0356$. The fluid domain is given by the cuboidal channel $\Omega = [0, 10] \times [0, 5] \times [0, 5]$ in which boundary effects are negligible. The head-flagellum joint is initialised as $\boldsymbol{X}_0(0) = [5, 2.5, 2.5]^T$ and the flagellar shape is initialised in the form of a low-amplitude parabola, as in Chapter 2.

In what follows, we fix the dimensionless wavenumber $k = 4\pi$, which is typical of mammalian sperm flagella. We also fix the active-viscous parameter as $\mathcal{M} = 0.027$, a value chosen in order for all simulations to produce realistic beating motion. We will consider a variety of values of the viscous-elastic parameter $\mathcal{S}$, identical to the range considered in Chapter 2 i.e.

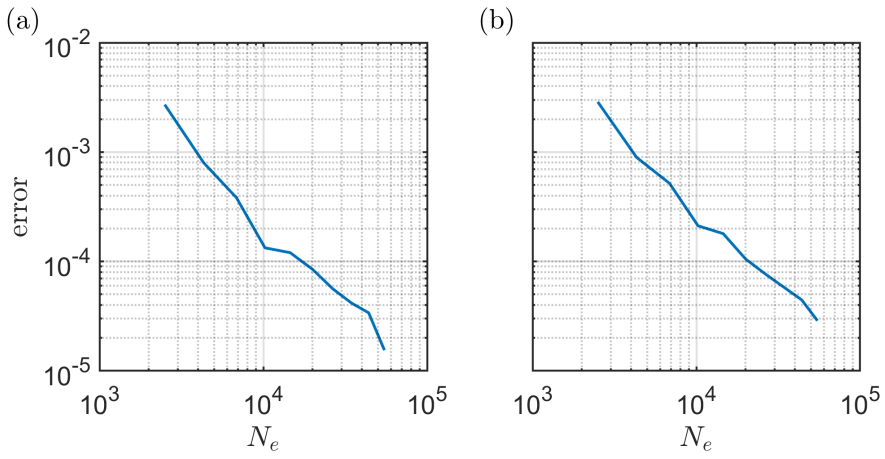


Figure 3.15: Convergence of the velocity solution (at $t = 2\pi$) over all mesh points with the number of mesh elements, corresponding to simulating a sperm cell within the domain $\Omega = [0, 10] \times [0, 10] \times [0, 10]$, with cell parameters $\mathcal{S} = 13$, $\mathcal{M} = 0.027$ and $\ell = 0.95$. For a fine mesh ($N_e = 67500$ elements), the plot shows the sum of the error over all refined mesh nodes, between the velocity solutions in this case and the interpolated velocity solutions for a less refined mesh with N_e elements. In (a), the fluid is Newtonian with parameters $(\mathrm{De}, \beta_0, n) = (1, 2, 1)$. In (b), the fluid is shear-thinning with $(\mathrm{De}, \beta_0, n) = (1, 2, 0.2)$.

$\mathcal{S} \in [9, 18]$. We also set $\rho = 36.4$ as in Chapter 2, $\epsilon = 0.01$, and set the dimensionless active tail length $\ell = 0.95$ unless otherwise stated. In this way, the end piece forms the most distal 5% of the flagellum, a value which is in line with experimental observations (Cummins and Woodall, 1985), and which is within the range found in Chapter 2 to optimise propulsion.

In our studies, we will consider the effect of varying the Deborah number $\mathrm{De} = \lambda\omega$, the zero-infinite shear rate viscosity ratio $\beta_0 = \mu_0/\mu_\infty$ and the shear-thinning index n, on the propulsion of sperm cells. We varying these parameters from the Newtonian cases, where either $\mathrm{De} = 0$, $\beta_0 = 1$ or $n = 1$ (note that these are not all equivalent Newtonian solutions since they result in different values of the viscosity in (3.70)). We consider parameter ranges $\mathrm{De} \in [0, 3]$, $\beta_0 \in [1, 6]$ and $n \in [0.2, 1]$, an extension of the range considered by Montenegro-Johnson et al. (2012, 2013) when modelling sperm in shear-thinning fluids.

To choose suitable numerical parameters for the model, we consider the convergence of the velocity solution with the number of mesh elements N_e, number of flagellum segments Q and number of head points N_h. To study the convergence of the solution with the finite element mesh, we start by calculating the total velocity solution ($\boldsymbol{u} = \boldsymbol{\mathcal{U}} + \boldsymbol{u}_S$) over a re-

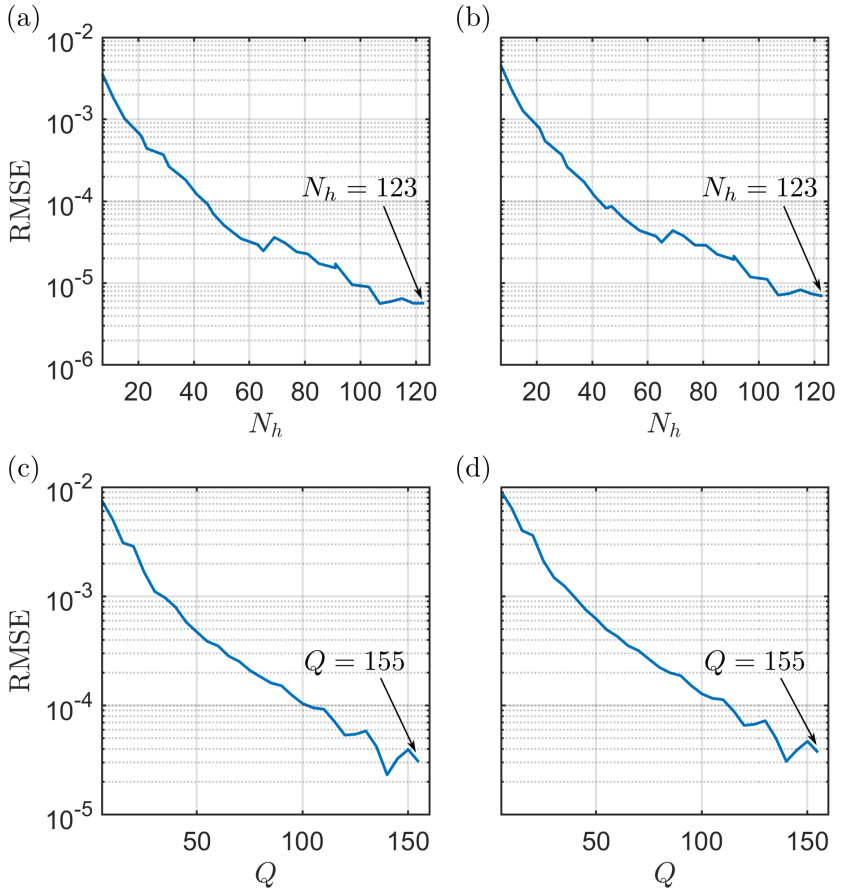


Figure 3.16: Convergence of the velocity solution with the number of head nodes N_h and number of flagellum segments Q. The plots show the root-mean-square-error (RMSE) between the velocity solution corresponding to a refined head/flagellum ($N_h = 125$ or $Q = 160$), and the solution calculated using a coarser head/flagellum discretisation, interpolated to the refined head/flagellum points. The velocity solution corresponds to $t = 2\pi$ and is that for a sperm cell within the domain $\Omega = [0, 10] \times [0, 10] \times [0, 10]$ with $\mathcal{S} = 13$, $\mathcal{M} = 0.027$ and $\ell = 0.95$. In (a), the fluid is Newtonian with parameters $(\mathrm{De}, \beta_0, n) = (1, 2, 1)$ and the convergence is shown with N_h. In (b), the fluid is shear-thinning with $(\mathrm{De}, \beta_0, n) = (1, 2, 0.2)$ and again convergence is shown with number of head nodes N_h. In (a) and (b) we set $Q = 60$. Finally, (c) and (d) show the equivalent plots but for convergence with the number of flagellar segments Q. Here we fix $N_h = 45$.

fined mesh, consisting of $N_e = 67500$ elements. The vector of velocity solutions over all mesh nodes in this case is denoted $\boldsymbol{u}_{\mathrm{ref}}$. We then solve the same problem over a series of less refined meshes (meshes with less than or equal to $N_e = 67500$ elements), consisting of between $N_e = 250$ and $N_e = 67500$ elements. For each less refined mesh (here we take $N_e \in \{250, 432, 686, 1024, 1458, 2000, 2662, 3456, 4394, 5488, 6750\}$), we interpolate the velocity perturbation component of the solution, $\boldsymbol{\mathcal{U}}$, to the refined mesh nodes using the shape func-

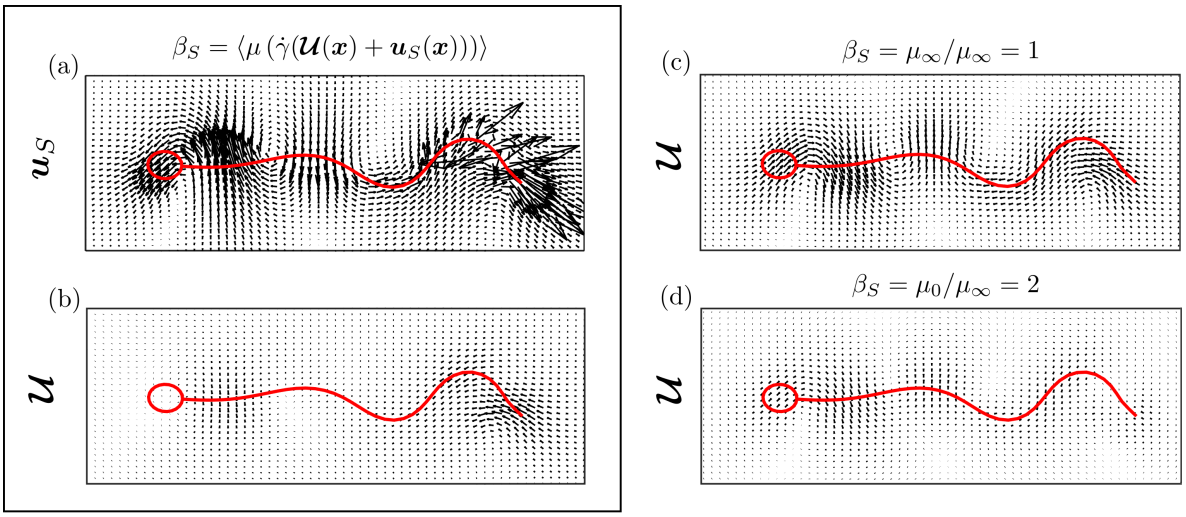


Figure 3.17: The instantaneous velocity solutions (plotted at $t = 2\pi$) (a) $\boldsymbol{u}_S(\boldsymbol{x}, t)$, the stokeslet solution, and, (b) $\boldsymbol{\mathcal{U}}(\boldsymbol{x}, t)$, the correction field, shown in the plane $z = 2.5$ surrounding a sperm cell with parameters $\mathcal{S} = 13$, $\mathcal{M} = 0.027$ and $\ell = 0.95$ where β_S is chosen as described in Section 3.5.5. The shear-thinning fluid is defined by the parameters $(\mathrm{De}, \beta_0, n) = (1, 2, 0.5)$. The solution $\boldsymbol{u}_S(\boldsymbol{x}, t)$ is rapidly varying across the fluid domain, however the perturbation solution $\boldsymbol{\mathcal{U}}(\boldsymbol{x}, t)$ is slowly varying by construction. Additional perturbation solutions are plotted for the same cell where now (c) $\beta_S = \mu_\infty/\mu_\infty = 1$, (d) $\beta_S = \mu_0/\mu_\infty = 2$, to demonstrate that the solutions in these cases are still slowly varying.

tion interpolation defined in equation (3.22). We then explicitly calculate the Newtonian component of the solution $\boldsymbol{u}_S$ at all refined mesh nodes via equation (3.76a). Taking the sum of these two components yields the total solution at all refined mesh points, based on interpolation from the solution calculated over a less refined mesh. This is denoted $\boldsymbol{u}_{N_e}$ for each N_e. For each less refined mesh, we calculate the error between the refined and less refined solution via $\|\boldsymbol{u}_{\mathrm{ref}} - \boldsymbol{u}_{N_e}\|_2$. We consider convergence in both the Newtonian case where $(\mathrm{De}, \beta_0, n) = (1, 2, 1)$, and a shear-thinning case where $(\mathrm{De}, \beta_0, n) = (1, 2, 0.2)$. In both cases, we solve over a single beat cycle, i.e. up to $t = 2\pi$. A plot of the error against the number of elements in the coarser mesh is given in Figure 3.15. The convergence in both the Newtonian and shear-thinning cases is similar, and in what follows we choose $N_e = 13718$ for all simulations, which reduces the error to under 1×10^{-4}.

In a similar way, we study the convergence of the solution with the number of head nodes N_h and flagellum segments Q. For convergence with N_h, we first calculate the velocity solution corresponding to a head discretised with $N_h = 125$ points. We then calculate the velocity

solutions corresponding to more coarsely discretised head, with $Q \in [7, 125]$. Interpolating to find the velocity solution at refined head points and calculate the root-mean-square-error (RMSE) between the solutions over all such points allows for the study of the convergence of the solution with N_h. We again consider the Newtonian case $(\mathrm{De}, \beta_0, n) = (1, 2, 1)$ and the shear-thinning case $(\mathrm{De}, \beta_0, n) = (1, 2, 0.2)$, with the change in RMSE over N_h plotted in Figures 3.16a and 3.16b respectively.

The convergence of the velocity solution with the number of flagellar segments Q is plotted in Figures 3.16c and 3.16d, for the above Newtonian and shear-thinning cases respectively. Again, the velocity solution is calculated for the refined case $Q = 160$, as well as for coarser flagellum discretisations where $Q \in [5, 160]$. The velocity solutions in the coarser cases are interpolated to find the velocity at the segment end points corresponding to the refined discretisation, and the RMSE between the solutions over all refined end points is calculated. Convergence with both N_h and Q is similar in the Newtonian and shear-thinning cases, and we choose $N_h = 45$ and $Q = 60$ for errors below 1×10^{-4} and 1×10^{-3} respectively.

To demonstrate the slowly varying nature of the velocity perturbation $\boldsymbol{\mathcal{U}}(\boldsymbol{x}, t)$ over the domain, we plot the solutions $\boldsymbol{u}_S(\boldsymbol{x}, t)$ and $\boldsymbol{\mathcal{U}}(\boldsymbol{x}, t)$ in the region surrounding a sperm cell with parameters $\mathcal{S} = 13$, $\mathcal{M} = 0.027$ and $\ell = 0.95$ in Figure 3.17a-b. Here, the sperm cell is swimming within a shear-thinning fluid where $(\mathrm{De}, \beta_0, n) = (1, 2, 0.5)$, and the solution is pictured at $t = 2\pi$ in the plane $z = 2.5$. Whilst the regularised stokeslet solution $\boldsymbol{u}_S(\boldsymbol{x}, t)$ varies very rapidly close to the cell, the perturbation solution $\boldsymbol{\mathcal{U}}(\boldsymbol{x}, t)$ is slowly varying across the region. To quantify this, we again calculate the absolute difference between the velocity solutions at each node of the mesh and all adjacent nodes. For the regularised stokeslet solution $\boldsymbol{u}_S$, the maximum change is observed in the y component of the velocity, and is given by $\Delta u_S = 1.8457$. Correspondingly, for the finite element solution $\boldsymbol{\mathcal{U}}$, we have $\Delta \mathcal{U} = 0.09039$. These quantities show that the change in the velocity over neighbouring nodes in the finite element solution is approximately 20 times smaller than the change in $\boldsymbol{u}_S$. As in Figure 3.11 of Section 3.4.4, we plot additional perturbation solutions in Figure 3.17c and Figure 3.17d for different choices of the parameter β_S, $\beta_S = \mu_\infty/\mu_\infty = 1$ and $\beta_S = \mu_0/\mu_\infty = 2$ respectively. This

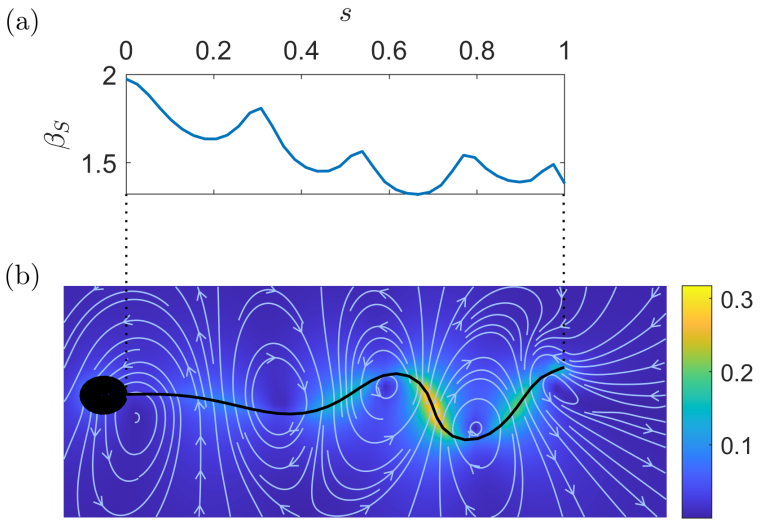


Figure 3.18: The variation in the Newtonian-infinite shear rate viscosity ratio $\beta_S = \mu_S/\mu_\infty$ with arclength s across the flagellum and the corresponding flagellar beat and surrounding flow fields (at $t = 10\pi$). (a) For each segment, the value β_S is approximated based on the average of the viscosity over a cylinder of radius $\epsilon = 0.01$ surrounding the segment. This value is plotted against arclength for a flagellum with $Q = 60$ segments. (b) The fluid magnitude surrounding the simulated sperm cell is indicated with a colourbar, with instantaneous fluid streamlines shown in white with arrows indicating direction.

demonstrates that the slowly varying assumption still holds for other choices of β_S, although we choose β_S as in 3.17a-b going forward. For the cell with parameters $\mathcal{S} = 13$, $\mathcal{M} = 0.027$ and $\ell = 0.95$, a plot of how the Newtonian-infinite shear rate viscosity ratio β_S varies with arclength s across the flagellum is shown in Figure 3.18a. The corresponding flagellar waveform and surrounding fluid velocity magnitude is given in Figure 3.18b, shown here at $t = 10\pi$.

We have now chosen suitable dimensionless parameter groups to explore, as well as suitable numerical parameters for appropriate convergence. We have also demonstrated the slowly varying nature of the velocity perturbation $\boldsymbol{\mathcal{U}}(\boldsymbol{x}, t)$, an important requirement of the HANS method. We now proceed to use the HANS method developed in this Chapter to study the effect of shear-thinning rheology on the propulsion of a single sperm cell in Chapter 4.

Chapter 4

How does shear-thinning rheology affect the propulsion of human sperm?

In this chapter, we use the HANS method developed in Chapter 3 to explore the effect of shear-thinning rheology on the propulsion of a single sperm cell with a flexible elastic flagellum. Results are presented for a cell situated within the domain $\Omega = [0, 10]\times[0, 5]\times[0, 5]$ containing a fluid modelling using the BCC4p constitutive law. The effect of shear-thinning rheology on propulsion is investigated through varying the shear-thinning index n, Deborah number $\mathrm{De} = \lambda\omega$ and zero-infinite shear rate viscosity ratio $\beta_0 = \mu_0/\mu_\infty$ and measuring the swimming speed and efficiency of cells. As in Chapter 2, Velocity Along a Line (VAL) is adopted as a measure of swimming speed, calculated via equation (2.43). Also, Lighthill Efficiency (η) is used to measure a cell's efficiency, as defined in equation (2.44). Across all simulations, VAL and η are measured after five cycles of the active moment function, corresponding to simulating cells over $t \in [0, 10\pi]$.

In Section 4.1, we study the effect of shear-thinning rheology on the propulsion of a sperm cell with fixed elastic properties. This corresponds to fixing the viscous-elastic parameter $\mathcal{S}$, where we choose $\mathcal{S} = 13$ to produce flagellar waveforms which resemble those of experimental observations of human sperm. As well as investigating the change in VAL and η over the shear-thinning parameters n, De and β_0, we analyse the variations in the flagellar waveform emerging from swimming in a BCC4p fluid. To distinguish the shear-thinning fluid effects on propulsion from the consequences of modified swimming gait, we simulate cells with a

prescribed beat in a Newtonian fluid. These waveforms correspond to the observed flagellar shape in a shear-thinning fluid, allowing us to compare the same beat in a BCC4p and Stokesian fluid. Finally, we further investigate the observed relationship between shear-thinning effects and propulsion through examining the flow fields surrounding swimmers, as well as flagellar force generation.

Following studying the effect of shear-thinning rheology on the propulsion of a sperm cell with fixed elastic properties, we examine the changes observed in a shear-thinning fluid for cells with varying viscous-elastic ratios S. In particular, in Section 4.2 we calculate VAL and η as a function of n, for various values of S. We again explore the flagellar beat patterns observed and compare the propulsive effectiveness of cells with the same beat in a shear-thinning and Newtonian fluid.

In Section 4.3, we explore how the presence of the mechanically inactive flagellar end piece affects propulsion in a shear-thinning fluid compared to the prior Newtonian results presented in Chapter 2. We explore the development of the flagellar waveform and the potential mechanisms behind the changes in swimming speed and efficiency observed. Finally, we discuss the possible implications of the results observed throughout this chapter and assess how they relate to previous observations of sperm in shear-thinning fluids.

4.1 The effect of shear-thinning rheology on propulsion for fixed viscous-elastic parameter S

In this section, we explore the effect of shear-thinning rheology on the propulsion of a single sperm cell of dimensionless length $L = 1$, swimming within a channel of ten body lengths in length ($10L$) and five body lengths wide and deep ($5L$). We choose the viscous-elastic parameter $S = 13$, active-viscous parameter $\mathcal{M} = 0.027$, wavenumber $k = 4\pi$, proximal-distal stiffness ratio $\rho = 36.4$ and active length $\ell = 0.95$ (or inactive end piece of length $L - \ell = 0.05$). These parameter choices are consistent with experimental observations of human sperm, as discussed previously in Section 3.5.6.

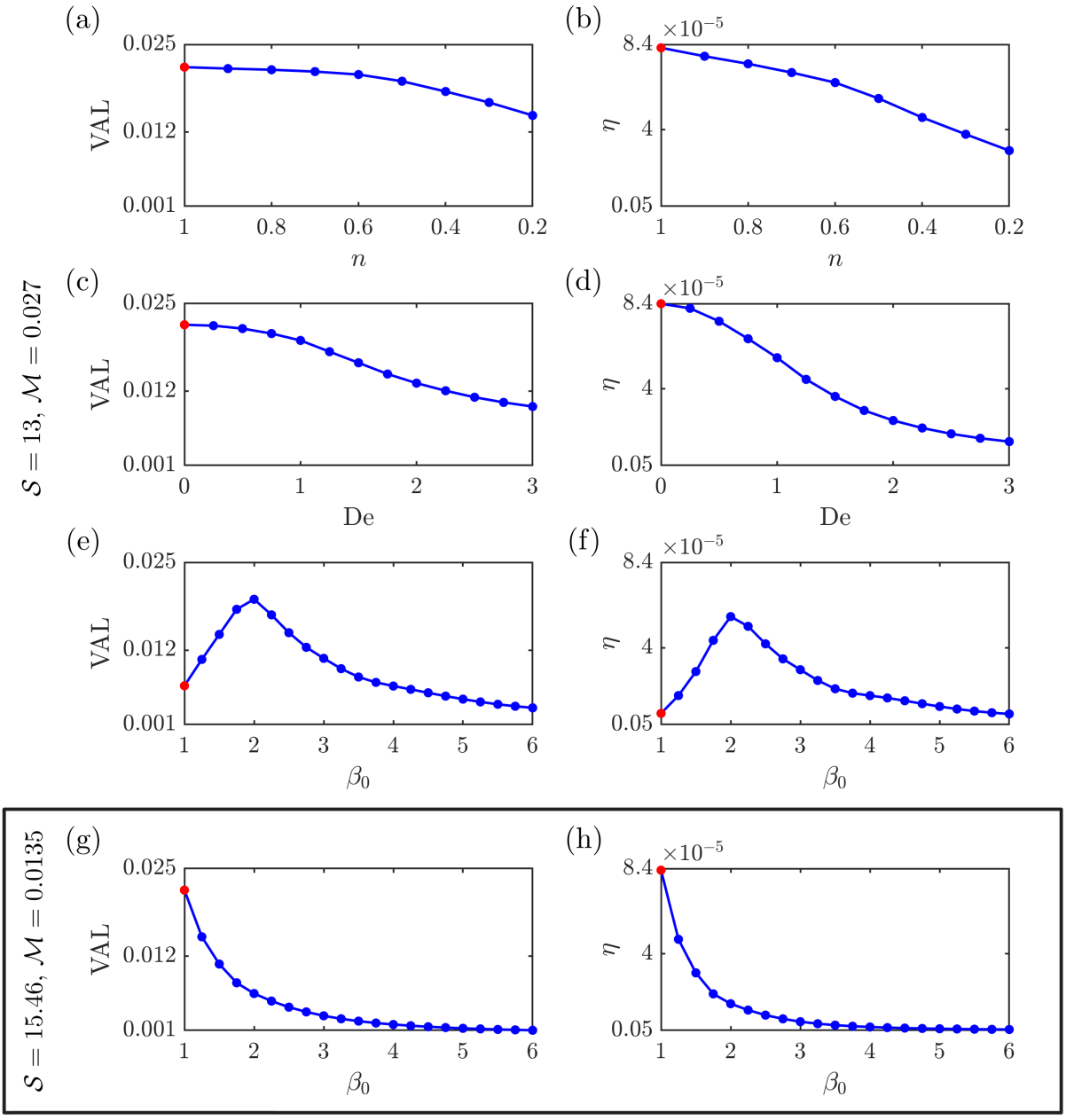


Figure 4.1: Results exploring the effect of shear-thinning rheology on the propulsion of a single human sperm cell with a flexible elastic flagellum. The impact of the shear-thinning index $n \in [0.2, 1]$ on (a) the swimming speed (VAL) and (b) the Lighthill efficiency (η) of the cell. Equivalently, (c) and (d) examine the effect of changing Deborah number $\mathrm{De} \in [0, 3]$ on swimming speed and efficiency, and (e) and (f) provide results for varying zero-infinite shear rate viscosity ratio $\beta_0 \in [1, 6]$. The Newtonian solutions, indicated by red dots, correspond to $n = 1$, $\mathrm{De} = 0$ and β_0. Across (a–f), $\mathcal{S} = 13$, $\mathcal{M} = 0.027$ and $\ell = 0.95$ and the remaining shear-thinning parameters are fixed as $n = 0.5$, $\mathrm{De} = 1$, or $\beta_0 = 2$ as appropriate. Panels (g) and (h) indicate the variation in VAL and η over $\beta_0 \in [1, 6]$ respectively for a cell with $\mathcal{S} = 15.46$ and $\mathcal{M} = 0.0135$ (remaining parameters fixed as in (a–f)). In this case the Newtonian solution $\beta_0 = 1$ is equivalence to that in (a–d).

In Figure 4.1a, we observe how swimming speed (VAL) changes with the value of the shear-thinning index $n \in [0.2, 1]$. Here, $n = 1$ corresponds to a Newtonian fluid with viscosity equal to the zero shear rate viscosity μ_0 and $n = 0.2$ corresponds to a strongly shear-thinning fluid. The remaining shear-thinning parameters are fixed as $\mathrm{De} = 1$ and $\beta_0 = 2$. The maximum swimming speed is obtained when $n = 1$, with VAL decreasing monotonically with decreasing n. This variation in swimming speed indicates that shear-thinning rheology impedes propulsion, with reductions in VAL of up to 66% observed over the values of $n < 1$ considered, compared to the Newtonian case. Figure 4.1b shows the same relationship between efficiency and shear-thinning index $n \in [0.2, 1]$. The sperm cell is more efficient in a Newtonian fluid than in a shear-thinning fluid for any $n < 1$. The cell is least efficient in a fluid of shear-thinning index $n = 0.2$, with a reduction in Lighthill efficiency of 35% compared to the Newtonian case for a fluid with viscosity μ_0.

The corresponding results for the variation in VAL and η with Deborah number $\mathrm{De} \in [0, 3]$ are presented in Figures 4.1c and 4.1d respectively. Here, $\mathrm{De} = 0$ corresponds to a Newtonian fluid with viscosity μ_0 in which the fluid relaxation time λ is effectively zero. The remaining shear-thinning parameters are fixed as $n = 0.5$ and $\beta_0 = 2$. Similarly to the results observed for varying n, the maximum swimming speed and efficiency occurs in a Newtonian fluid. Shear-thinning rheology is shown to always hinder propulsion, with increased shear-thinning effects (increased De) systematically reducing VAL and η. In particular, these results indicate that shear-thinning rheology can reduce swimming speed by up to 45% and decrease efficiency by 15% compared to a Newtonian fluid with viscosity μ_0.

In Figures 4.1e and 4.1f, we plot the variation in VAL and η with the value of the zero-infinite shear rate viscosity ratio $\beta_0 \in [1, 6]$. As a consequence of our non-dimensionalisation – choosing the infinite shear rate viscosity μ_∞ as the characteristic viscosity of the fluid – increasing β_0 corresponds to increasing the zero shear rate viscosity μ_0 with the infinite shear rate viscosity held constant. We also note that the fluid is Newtonian when $\beta_0 = 1$, corresponding to equal zero and infinite shear rate viscosities. The remaining shear-thinning parameters are fixed as $n = 0.5$ and $\mathrm{De} = 1$. In contrast to the n and De cases, these results indicate that shear-thinning

rheology can enhance propulsion. Specifically, from the Newtonian case $\beta_0 = 1$, VAL and η increase, reaching a peak at $\beta_0 = 2$. These peaks in VAL and η indicate enhanced swimming speed at $\beta_0 = 2$ of 290% compared to the Newtonian case, and correspondingly enhanced efficiency of 899%. Further increasing β_0 past $\beta_0 = 2$ leads to monotonic reductions in VAL and η from the corresponding peak values. With respect to efficiency, the value of η does not drop below the Newtonian value for $\beta_0 \in (1, 6)$, indicating that shear-thinning rheology is more efficient than swimming in a Newtonian fluid at the infinite shear rate viscosity (i.e. $\beta_0 = 1$). At $\beta_0 = 6$, the Newtonian and shear-thinning efficiency is approximately equal, suggesting that swimming in strongly shear-thinning fluids may result in no change in efficiency from the Newtonian case. The swimming speed is reduced past the Newtonian value for $\beta_0 > 4$, implying that whilst shear-thinning effects can enhance propulsion, highly shear-thinning fluids may hinder progress.

Physically, increasing the zero-infinite shear rate viscosity ratio $\beta_0 = \mu_0/\mu_\infty$ in our model corresponds to increasing the zero shear rate viscosity μ_0, or from a rheological perspective, increasing the value of the viscosity prior to the onset of shear-thinning. In this way, our results exploring the effect of β_0 on propulsion are not purely isolating the effect of shear-thinning rheology on propulsion, but are also incorporating the effect of an increase in the viscosity μ_0. On the other hand, increasing De corresponds to increasing fluid relaxation time and n itself defines the shear-thinning nature of the fluid. These parameters therefore likely better isolate the effect of shear-thinning rheology on propulsion than β_0.

Note that the Newtonian solutions in Figures 4.1a and 4.1c (and correspondingly Figures 4.1b and 4.1d) are equivalent, since in both cases the viscosity calculated using the dimensionless BCC4p equation (3.70) is equal to $\mu(\dot{\gamma}(\boldsymbol{u})) = 2$. However, the Newtonian solution $\beta_0 = 1$ in Figures 4.1e–f is not equivalent, since in this case $\mu(\dot{\gamma}(\boldsymbol{u})) = 1$. Therefore, these plots represent the variation from a Newtonian solution with a different fluid viscosity. The equivalent Newtonian solution to the results of Figure 4.1a–d for the $\beta_0 = 1$ case may be obtained by scaling the sperm number via $\mathcal{S} = (2)^{1/4}(13) = 15.46$, and the active-viscous ratio similarly as $\mathcal{M} = (2)^{-1}(0.0027) = 0.0135$. This corresponds to doubling both the zero and infinite shear

rate viscosity. These scaled results for swimming speed and efficiency as a function of β_0 are shown in Figure 4.1g and Figure 4.1h respectively. As β_0 increases, both the swimming speed and efficiency of the cell decrease monotonically. Thus for a cell with this particular choice of $\mathcal{S}$ and $\mathcal{M}$, shear-thinning effects decrease propulsive effectiveness compared to swimming in a Newtonian fluid at the infinite shear rate viscosity . This is in contrast to the results presented in Figures 4.1e–f, and indicates a likely sensitivity of the results to the choice of $\mathcal{S}$ and $\mathcal{M}$. We explore the effect of varying $\mathcal{S}$ later in Section 4.2.

In Figure 4.2, we plot the average work done ($\overline{W}$) by the cell over the fifth period, as used in the calculations of efficiency in Figure 4.1. In Figure 4.2a, we observe that $\overline{W}$ increases with decreasing n, indicating that cells require more work to progress through fluids with stronger shear-thinning rheology. Similarly, in Figure 4.2c, average work done increases with Deborah number De, eventually reaching a constant value past De ≈ 1.75. At this point, the fluid could be sufficiently thinned such that further thinning does not affect the average work done by the cell. In Figure 4.2e, we observe that increasing the zero-infinite shear rate viscosity ratio β_0 (physically, increasing μ_0 with μ_∞ held constant) leads to decreased $\overline{W}$, meaning that it is easier for the cell to progress through fluids of increased β_0. In Figure 4.1g, we plot the work done for the cell with a normalised Newtonian solution, i.e. the work done used in the calculation of η in Figure 4.1f. As discussed previously, this corresponds to parameter choices $\mathcal{S} = 15.46$ and $\mathcal{M} = 0.0135$. In this case, average work done decreases monotonically with increased β_0.

To attempt to explain this variation in average work $\overline{W}$, for each of the results presented in Figures 4.1a,c,e,g, we plot the average distal curvature over the fifth period $\langle \kappa_d \rangle$ in Figures 4.2b,d,f,h respectively. Here the distal curvature κ_d is taken to be the the average of the curvature $\partial\theta(s,t)/\partial s$ over the flagellar end piece, here of dimensionless length $L - \ell = 0.05$. The variation in the average distal curvature with each shear-thinning parameter shows good qualitative agreement with the average work done by the cell, indicating that the curvature of the end piece could be of particular importance when predicting the average work done by a sperm cell in a shear-thinning fluid. These results could further demonstrate the importance of the flagellar end piece in cell propulsion which will be discussed further in Section 4.3.

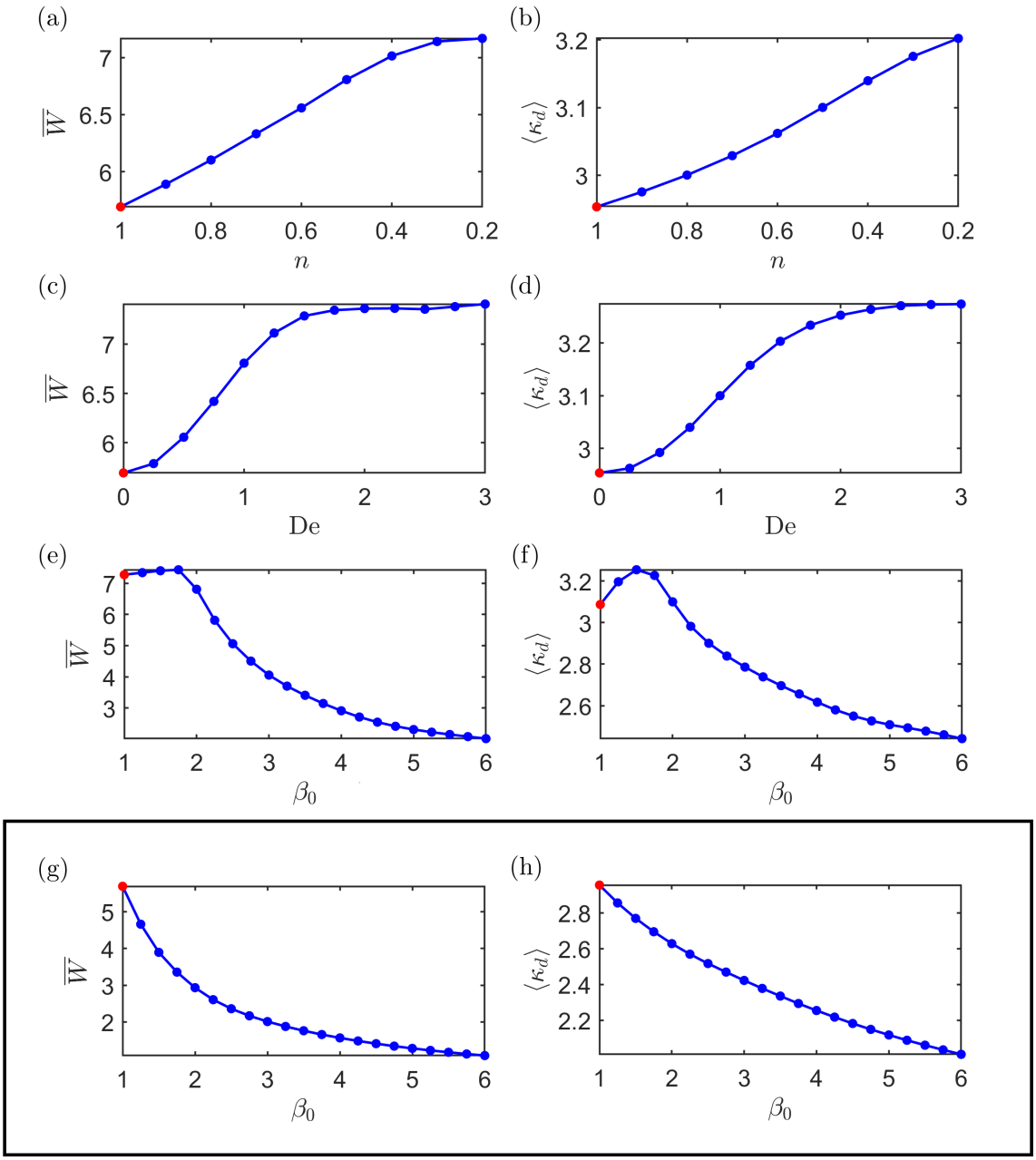


Figure 4.2: Results exploring the effect of shear-thinning rheology on average work done by a single human sperm cell and average distal flagellar curvature over $t \in [8\pi, 10\pi]$. The impact of the shear-thinning index $n \in [0.2, 1]$ on (a) the average work done by the cell over the fifth period $\overline{W}$ and (b) the average of the distal curvature over the fifth period ($\langle \kappa_d \rangle$). Equivalently, (c) and (d) examine the effect of changing Deborah number $\mathrm{De} \in [0, 3]$ on average work done and curvature, and (e) and (f) provide results for varying zero-infinite shear rate viscosity ratio $\beta_0 \in [1, 6]$. The Newtonian solutions, indicated by red dots, correspond to $n = 1$, $\mathrm{De} = 0$ and $\beta_0 = 1$. Across (a–f), $\mathcal{S} = 13$, $\mathcal{M} = 0.027$ and $\ell = 0.95$ and the remaining shear-thinning parameters are fixed as $n = 0.5$, $\mathrm{De} = 1$, or $\beta_0 = 2$ as appropriate. Panels (g) and (h) indicate the variation in $\overline{W}$ and $\langle \kappa_d \rangle$ over $\beta_0 \in [1, 6]$ respectively for a cell with $\mathcal{S} = 15.46$ and $\mathcal{M} = 0.0135$ (remaining parameters fixed as in (a–f)). In this case the Newtonian solution $\beta_0 = 1$ is equivalence to that in (a–d).

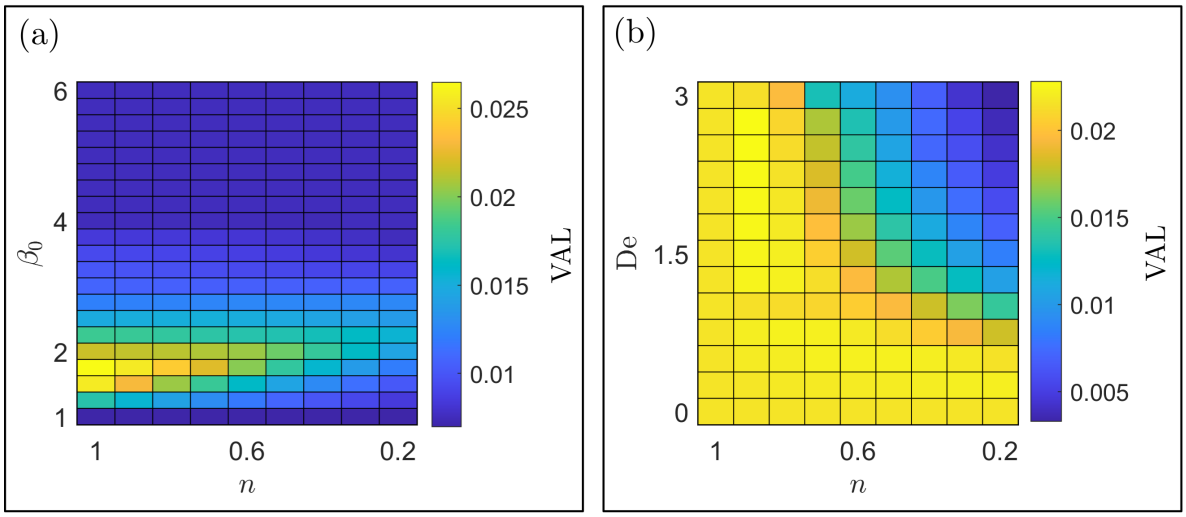


Figure 4.3: Results exploring the effect of shear-thinning rheology on swimming speed (VAL) and the relationship between the parameters $n \in [0.2, 1]$, De $\in [0, 3]$ and $\beta_0 \in [1, 6]$ and VAL. (a) The change in swimming speed VAL over n and β_0 and, (b) the change in VAL over n and De. In each case, swimming speed VAL is indicated by a colorbar with yellow corresponding to higher swimming speeds. Here, $\mathcal{S} = 13$, $\mathcal{M} = 0.027$ and $\ell = 0.95$ and the remaining shear-thinning parameters are fixed as $n = 0.5$, De $= 1$, or $\beta_0 = 2$ as appropriate

To further explore the relationship between the shear-thinning parameters n, De and β_0 and swimming speed, two-dimensional slices in the parameter space are provided in Figure 4.3 for a cell with $\mathcal{S} = 13$, $\mathcal{M} = 0.027$ and $\ell = 0.95$. In Figure 4.3a, the variation in VAL with $n \in [0.2, 1]$ and $\beta_0 \in [1, 6]$ is plotted. Across all values of β_0, the optimal swimming speed over n occurs at $n = 1$, indicating that for each β_0, the cell in a Newtonian fluid with viscosity equal to μ_0 is optimal. For high values of β_0, little change in VAL is observed over n. On the other hand, for each value of n, the optimal value of β_0 for propulsion can change. In particular, for decreased n (increased shear-thinning effects), the optimal β_0 increases, corresponding to an increase in the zero shear rate viscosity μ_0. Therefore with increased shear-thinning effects, a higher viscosity μ_0 results in more effective propulsion. In Figure 4.3b, we plot the variation in VAL across $n \in [0.2, 1]$ and De $\in [0, 3]$. We observe that in general, the closer the fluid is to Newtonian (the closer to $n = 1$ or De $= 0$), the faster the cell swims, as demonstrated previously.

The foregoing results indicate that shear-thinning rheology tends to hinder the propulsion of a single sperm cell with an elastic flagellum, compared to swimming in a Newtonian fluid

with the same zero shear rate viscosity. Propulsion can also be enhanced (compared to swimming at the infinite shear rate viscosity) for certain values of β_0, which incorporates both the effects of shear-thinning rheology for $\beta_0 > 1$ and also changing overall fluid viscosity. To better understand these changes, in the next section we analyse the flagellar beats for the most and least effective swimmers (in terms VAL), as well as exploring the differences in the flagellar waveform over fluid parameters $n \in [0.2, 1]$, $\mathrm{De} \in [0, 3]$ and $\beta_0 \in [1, 6]$.

4.1.1 Waveform development in shear-thinning fluids

For the results over the parameters n, De and β_0 presented in Figure 4.1a–f, overlaid timelapses of the flagellar beat over $t \in [8\pi, 10\pi]$ are given in Figures 4.4a,c,e. In each of these panels, corresponding to parameters n, De and β_0 respectively, the waveforms are plotted for the fastest (highest VAL) and slowest (lowest VAL) swimmers. Here, the most effective swimmers correspond to $n = 1$, $\mathrm{De} = 0$ and $\beta_0 = 2$. In these cases, a common flagellar beat emerges, exhibiting similar shaped flagellar envelopes. The flagellar waveforms exhibit sections in which the angle relative to the direction of propulsion is approximately $\pi/4$, indicating that these regions could be optimal for cell progress. The slowest swimmers occur when $n = 0.2$, $\mathrm{De} = 3$ or $\beta_0 = 6$, with greater variation in the flagellar beat observed in these cases. For the slowest cells over n and De, the flagellum exhibits a beat with an increasing tangent angle towards the distal end, reminiscent of experimental observations of sperm in shear-thinning fluids (Katz et al., 1978; Hyakutake et al., 2019) (see Figure 1.4 in Chapter 1). When $\beta_0 = 6$, the flagellum exhibits a low amplitude beat, likely impeded by the higher overall zero shear rate viscosity of the surrounding fluid.

In Figures 4.4b,d,f we plot the distribution in the flagellar tangent angles associated with the flagellar beats in Figures 4.4a,c,e, sampled at 100 time points over the beat $t \in [8\pi, 10\pi]$. For the best swimmers over n and De, we observe flagellar angles that are typically in the range of $-\pi/4$ to $\pi/4$, again indicating that cells exhibiting tangent angles within this range are generally better for propulsion. On the other hand, the worst swimmers over n and De demonstrate a larger range in tangent angles between $-\pi/2$ and $\pi/2$, which we infer to be

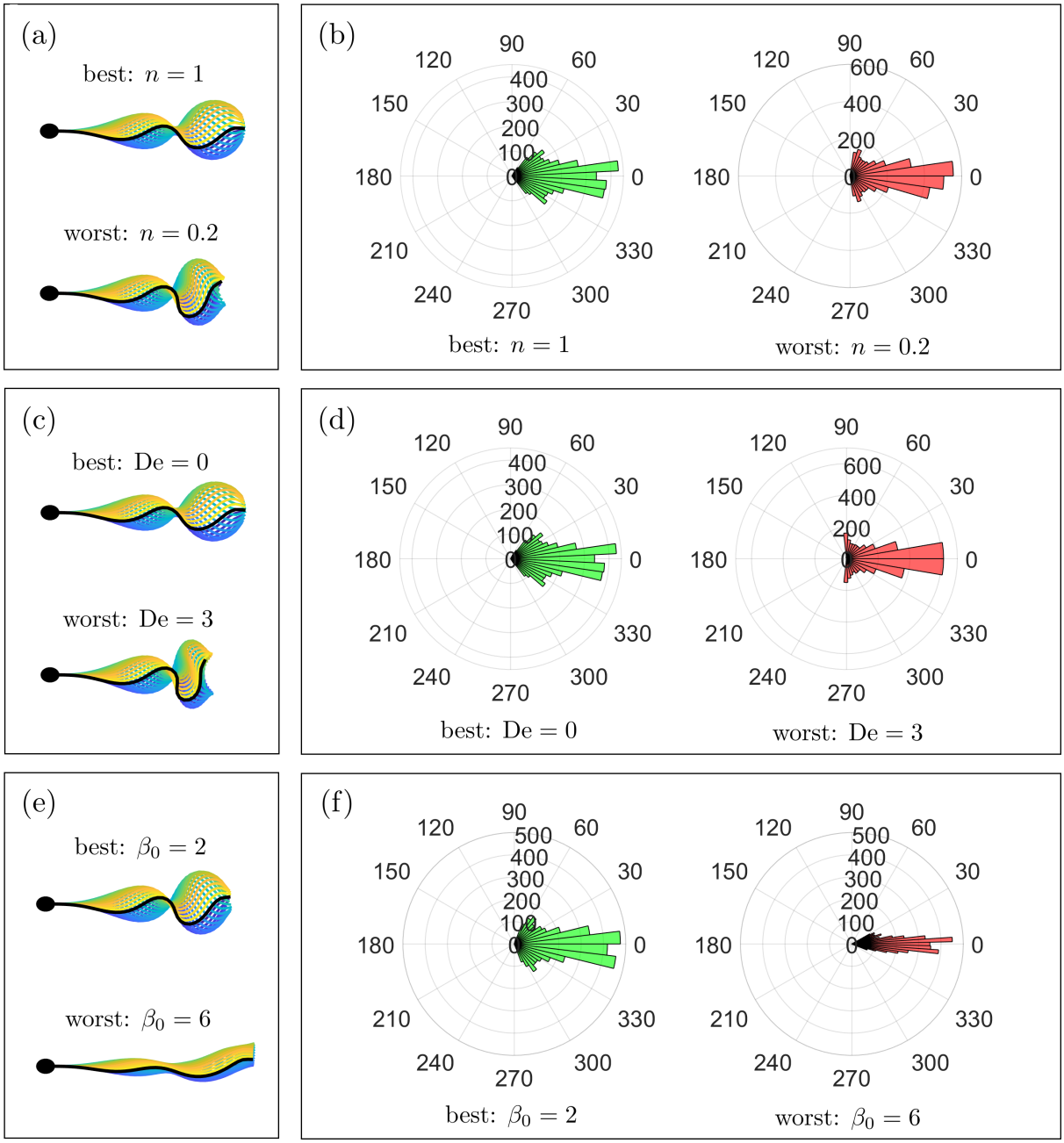


Figure 4.4: Results exploring the effect of shear-thinning rheology on flagellar waveform and the distribution of tangent angles over the beat $t \in [8\pi, 10\pi]$. (a) The flagellar waveform is shown for the best and worst swimmers (maximum and minimum VAL respectively) over $n \in [0.2, 1]$. The colour of the flagellum indicates progress through the beat, from blue to yellow, with the final waveform shown in black at $t = 10\pi$. In (b) the distribution of flagellar tangent angles across the beat are shown for the best and worst swimmers plotted in (a). In (c) and (d), the equivalent results are shown for the best and worst swimmers over De $\in [0, 3]$. Finally, in (e) and (f), the same is shown over $\beta_0 \in [1, 6]$. Across all simulations $\mathcal{S} = 13$, $\mathcal{M} = 0.027$ and $\ell = 0.95$ and the remaining shear-thinning parameters are fixed as $n = 0.5$, De $= 1$, or $\beta_0 = 2$ as appropriate.

detrimental to propulsion. For the best swimmer over β_0, we observe a similar range in tangent angle as in the best cases for n and De. The worst swimmer in this case exhibits a low amplitude beat, and a corresponding small range of tangent angles.

The variation in the flagellar waveform over the parameter ranges $n \in [0.2, 1]$, $\mathrm{De} \in [0, 3]$ and $\beta_0 \in [1, 6]$ is further examined in Figure 4.5. Here, the waveform is pictured at five points over the interval $t \in [8\pi, 10\pi]$ for each fluid parameter. For simulations over n and De, the Newtonian solutions (shown in yellow) are equivalent, and occur at $n = 1$ and $\mathrm{De} = 0$ respectively. As n decreases and De increases, the fluid becomes more shear-thinning, and the flagellar waveforms change significantly. Whilst in the proximal half of the flagellum little change is observed; in the distal half, the curvature and tangent angle of the flagellum increase with greater shear-thinning effects. Thus shear-thinning rheology can dramatically change the development of the flagellar waveform, resulting in beats that have much higher curvature relative to the Newtonian case. This change is again consistent with experimental observations of sperm in these fluids, as revealed by Katz et al. (1978); Hyakutake et al. (2019).

The variation in the waveform with the zero-infinite shear rate viscosity parameter β_0 is more dramatic and distinctive when compared with the n- and De-varying results. The Newtonian solution, shown in yellow and occurring at $\beta_0 = 1$, is associated with high curvature, particularly towards the distal end. When $\beta_0 = 6$, the waveform exhibits very low curvature and tangent angle throughout the flagellum. These changes are associated with the higher overall viscosity of the fluid as the parameter β_0 increases, as this corresponds to increasing the zero shear rate viscosity μ_0. The waveforms observed over varying β_0 exhibit changes throughout the length of the flagellum, rather than being confined to the distal half as in the n and De cases.

To examine these changes in curvature across the flagellum further, we plot the variation in curvature for the most and least effective swimmers considered in Figure 4.4, in Figure 4.6. As in our observations of the flagellar beat, we note that the optimum cells (in terms of swimming speed VAL), corresponding to $n = 1$, $\mathrm{De} = 0$ and $\beta_0 = 2$, result in similar curvature variation across the flagellum. In the $n = 1$ and $\mathrm{De} = 0$ cases, the curvatures are identical,

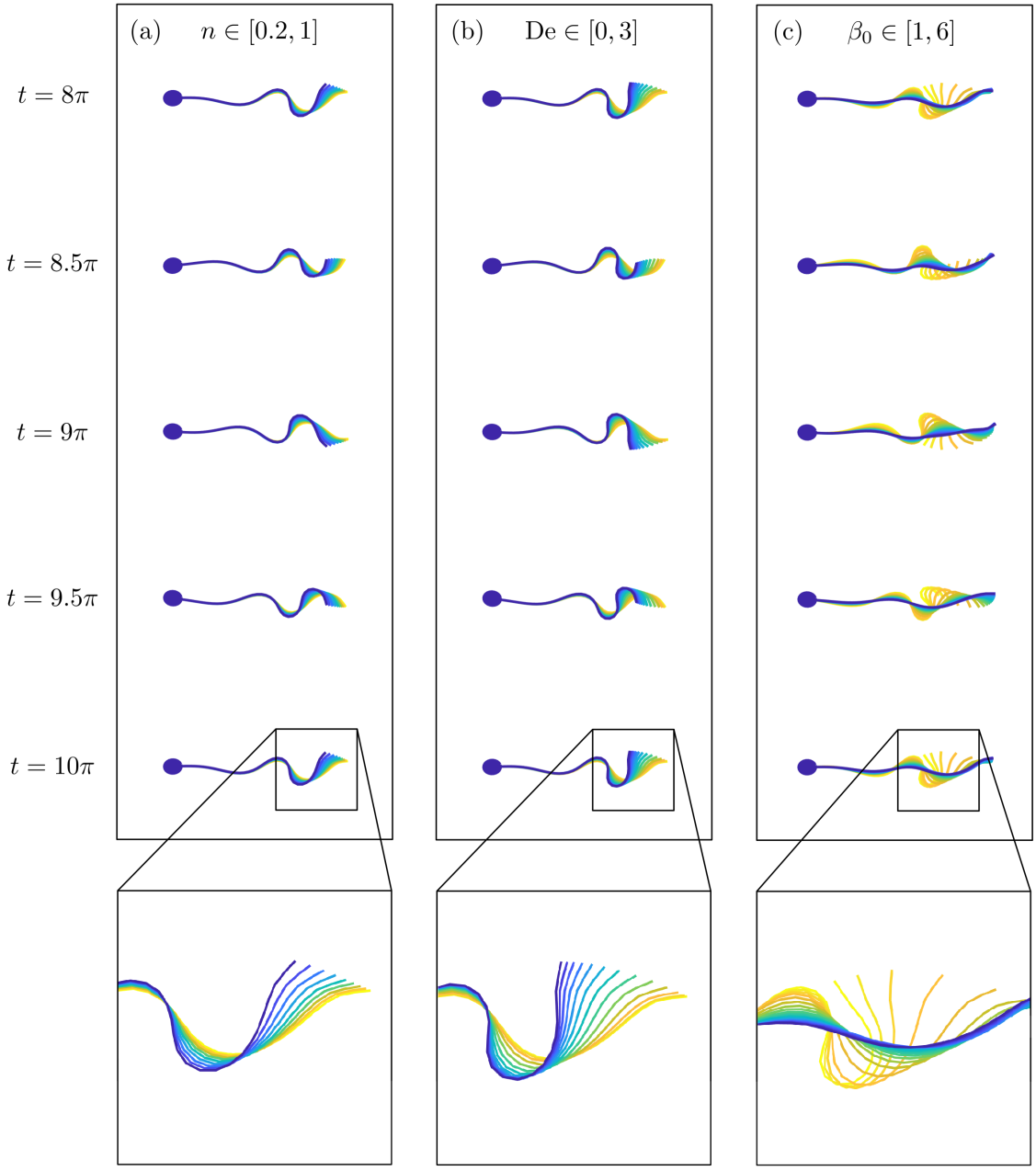


Figure 4.5: The flagellar waveform during the beat $t \in [8\pi, 10\pi]$, over parameter ranges (a) $n \in [0.2, 1]$, (b) De $\in [0, 3]$ and (c) $\beta_0 \in [1, 6]$. In each case, the waveform in the Newtonian case is shown in yellow, corresponding to $n = 1$, De $= 0$ or $\beta_0 = 1$ respectively. These waveforms are plotted ranging to blue, corresponding to the strongest shear-thinning effects and parameters $n = 0.2$, De $= 3$ or $\beta_0 = 6$. In each panel, a magnified image of distal flagellum is shown at $t = 10\pi$. Across all simulations $\mathcal{S} = 13$, $\mathcal{M} = 0.027$ and $\ell = 0.95$ and the remaining shear-thinning parameters are fixed as $n = 0.5$, De $= 1$, or $\beta_0 = 2$ as appropriate.

since these parameter choices correspond to the same solution. The $\beta_0 = 2$ case corresponds to a distinct parameter choice compared with the other two 'best' swimmers but results in

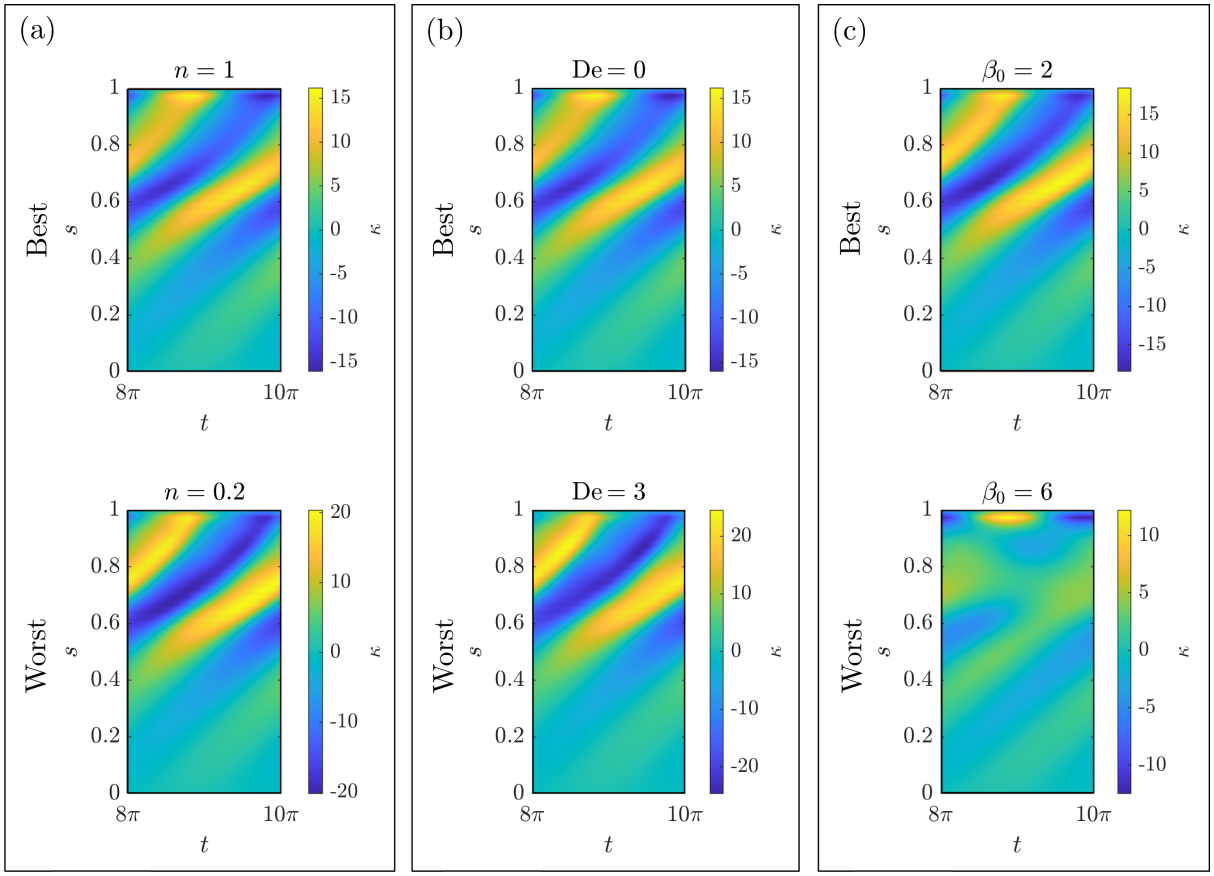


Figure 4.6: The flagellar curvature $\partial\theta(s,t)/\partial s$ for the best and worst swimmer (maximum and minimum VAL respectively), over the parameters (a) $n \in [0.2, 1]$, (b) De $\in [0, 3]$ and (c) $\beta_0 \in [1, 6]$. The curvature is plotted over a single beat $t \in [8\pi, 10\pi]$. Across all simulations $\mathcal{S} = 13$, $\mathcal{M} = 0.027$ and $\ell = 0.95$ and the remaining shear-thinning parameters are fixed as $n = 0.5$, De $= 1$, or $\beta_0 = 2$ as appropriate.

similar curvature. The least effective cells, corresponding to $n = 0.2$, De $= 3$ and $\beta_0 = 6$, differ somewhat significantly from the optimal cells. In the case of n and De, the curvature of the least effective cells is much greater than the curvature in the optimal cases. For the simulations over the β_0, the curvature for the least optimum cell is reduced compared to the $\beta_0 = 2$ case due to higher overall fluid viscosity.

The trajectories and maximum flagellar amplitude over the three shear-thinning parameters are given in Figure 4.7a–c for $n \in [0.2, 1]$, De $\in [0, 3]$ and $\beta_0 \in [1, 6]$ respectively. On the left of each panel, the flagellar trajectory is plotted over the beat $t \in [8\pi, 10\pi]$ from yellow (high shear-thinning effects) to blue (low shear-thinning effects). The Newtonian trajectories are plotted in black for each parameter. For the variation with n and De shown in Figures

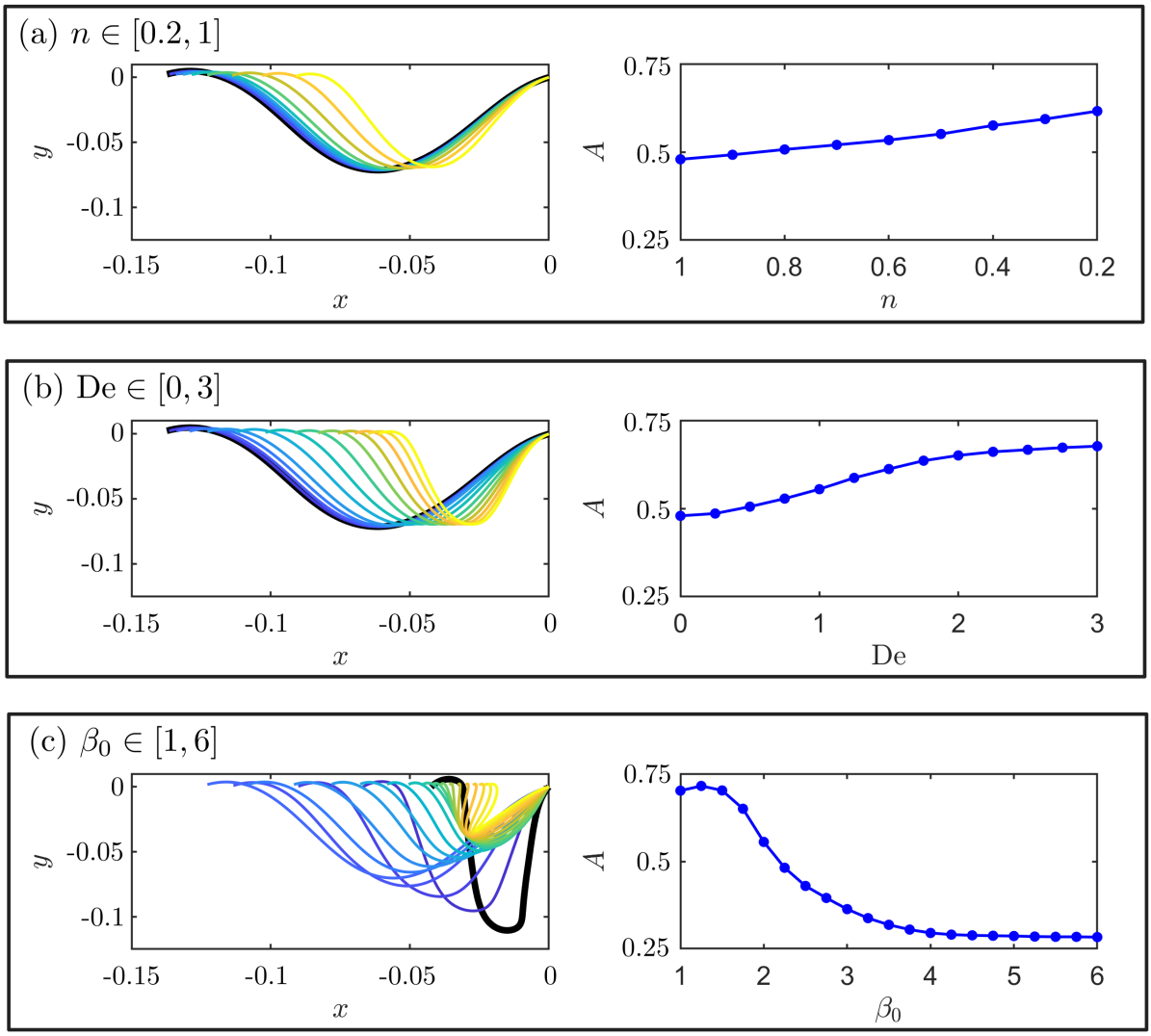


Figure 4.7: The variation in the trajectories of sperm cells and the maximum flagellar amplitude over shear-thinning parameters (a) $n \in [0.2, 1]$, (b) De $\in [0, 3]$ and (c) $\beta_0 \in [1, 6]$. In each case, the trajectory is plotted over the beat $t \in [8\pi, 10\pi]$ (left), where x and y represent the displacement of $\boldsymbol{X}_0(t)$ from $\boldsymbol{X}_0(t = 8\pi)$. The Newtonian case is plotted in black, with the remaining paths plotted from least shear-thinning (dark blue) to most shear-thinning (yellow). Maximum flagellar amplitude over the beat $t \in [8\pi, 10\pi]$ (right) is plotted via calculating the maximum displacement of the flagellum in the y direction from the y component of the head-flagella joint $\boldsymbol{X}_0(t)$ in the cell body frame. Across all simulations, the remaining shear-thinning parameters are fixed as $n = 0.5$, De $= 1$, or $\beta_0 = 2$ as appropriate.

4.7a and 4.7b respectively, the paths are of a similar shape in both the Newtonian and shear-thinning cases, with increased compression of the trajectories in the x direction observed as shear-thinning effects increase. For the paths over β_0 shown in Figures 4.7c, the shape changes more dramatically, notably with the cell 'back-tracking' on itself for high values of β_0, likely due to the skewed beat observed in Figure 4.4e. On the right of each panel, the maximum

flagellar amplitude over the beat A is plotted over the shear-thinning parameters, calculated as the maximum displacement of the flagellum in the y direction from the y component of the head-flagella joint $\boldsymbol{X}_0(t)$. With increasing n and De, the amplitude A increases as observed in Figure 4.5. Over β_0, A decreases, due to the increase in overall fluid viscosity.

4.1.2 Velocity fields and flagellar force generation

Returning to the best and worst cell for propulsion (in terms of swimming speed VAL) from the results in Figure 4.1, we plot the velocity fields associated with each cell in Figure 4.8. Whilst the region of high tangent angle associated with the worst case cells for n and De exhibit high fluid velocities, the optimal cells corresponding to parameters $n = 1$, $\mathrm{De} = 0$ and $\beta_0 = 2$ possess additional oblique regions, in which the tangent angle is approximately $\pi/4$. This likely confers additional thrust to the cells and generally results in higher fluid velocities across the flagellum. When $\beta_0 = 6$, corresponding to the least optimal cell in this case, fluid velocities are very small, likely due to the small amplitude motion of the flagellum and decreased thrust.

The force that the flagellum exerts on the surrounding fluid in the best and worst cases considered previously is shown in Figure 4.9. Here, the magnitude and direction of the force generation across the flagellum is indicated by arrows in Figure 4.9a–c (left), for the parameters n, De and β_0 respectively. In each of these panels, the optimum cell for swimming speed over these parameters is plotted on the top, with the least-optimal cell plotted on the bottom. In all cases, the force generation is strongest across the oblique regions of the flagellum, as well as over the end piece. Plotting the magnitude of the force across the flagellum for each parameter in Figures 4.9a–c (right) reveals that force generation is generally similar in the proximal portion of the flagellum, corresponding to the first peak in each of these plots. Past this point, force varies more significantly, with force generation in the optimum case exhibiting larger peaks and troughs, as expected. Therefore force generation can either increase or decrease in a shear-thinning fluid compared to a Newtonian fluid at different points along the flagellum, likely brought on by the changes to the flagellar waveform in these cases and the subsequent

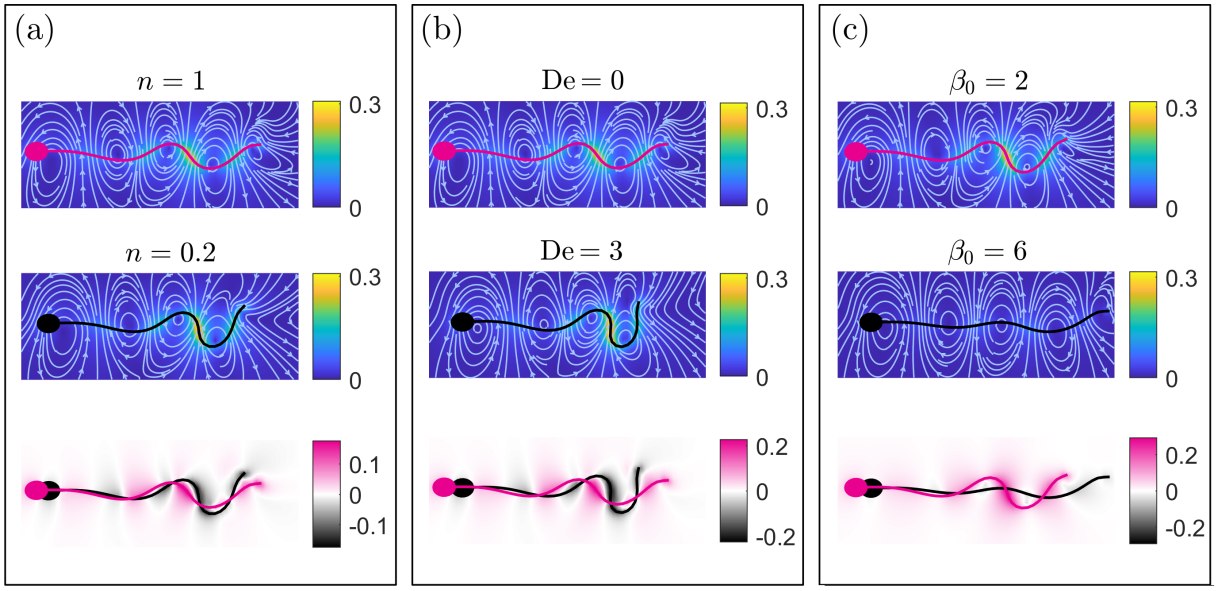


Figure 4.8: Comparison of the flow fields around a simulated sperm for best and worst swimmer (maximum and minimum VAL respectively), over the parameters (a) $n \in [0.2, 1]$, (b) $\mathrm{De} \in [0, 3]$ and (c) $\beta_0 \in [1, 6]$. The top of each column shows the best swimmer, with fluid magnitude indicated by the colorbar, and instantaneous fluid streamlines shown in white with arrows indicating direction. The middle of each column shows the worst swimmer, with fluid magnitude and streamlines indicated as above. The difference between flow fields is shown in the bottom of each column, where positive values correspond to the best swimmer having faster fluid velocity. Here the best and worst swimmers (heads and flagella) are plotted in pink and black respectively. Across all simulations $\mathcal{S} = 13$, $\mathcal{M} = 0.027$ and $\ell = 0.95$ and the remaining shear-thinning parameters are fixed as $n = 0.5$, $\mathrm{De} = 1$, or $\beta_0 = 2$ as appropriate.

increase or decrease in drag associated with the oblique regions of the flagellum.

4.1.3 Prescribed flagellar beat comparisons

We have observed that shear-thinning rheology tends to hinder the propulsion of a sperm-like swimmers with an elastic flagellum, and that the development of the flagellar beat depends heavily on the rheology of the fluid. To isolate the effects of the fluid itself, we simulate cells with the same waveform in a shear-thinning and Newtonian fluid. In this way, any changes in velocity or efficiency are due to the rheology of the fluid, rather than modified propulsion being a result of flagellar shape changes. For each of the simulations over $n \in [0.2, 1]$, $\mathrm{De} \in [0, 3]$ and $\beta_0 \in [1, 6]$ in Figure 4.1, the resulting flagellar beat is extracted between $t \in [0, 10\pi]$. In the Newtonian (Stokes flow) case, we prescribe the flagellar motion in the body frame, defined as

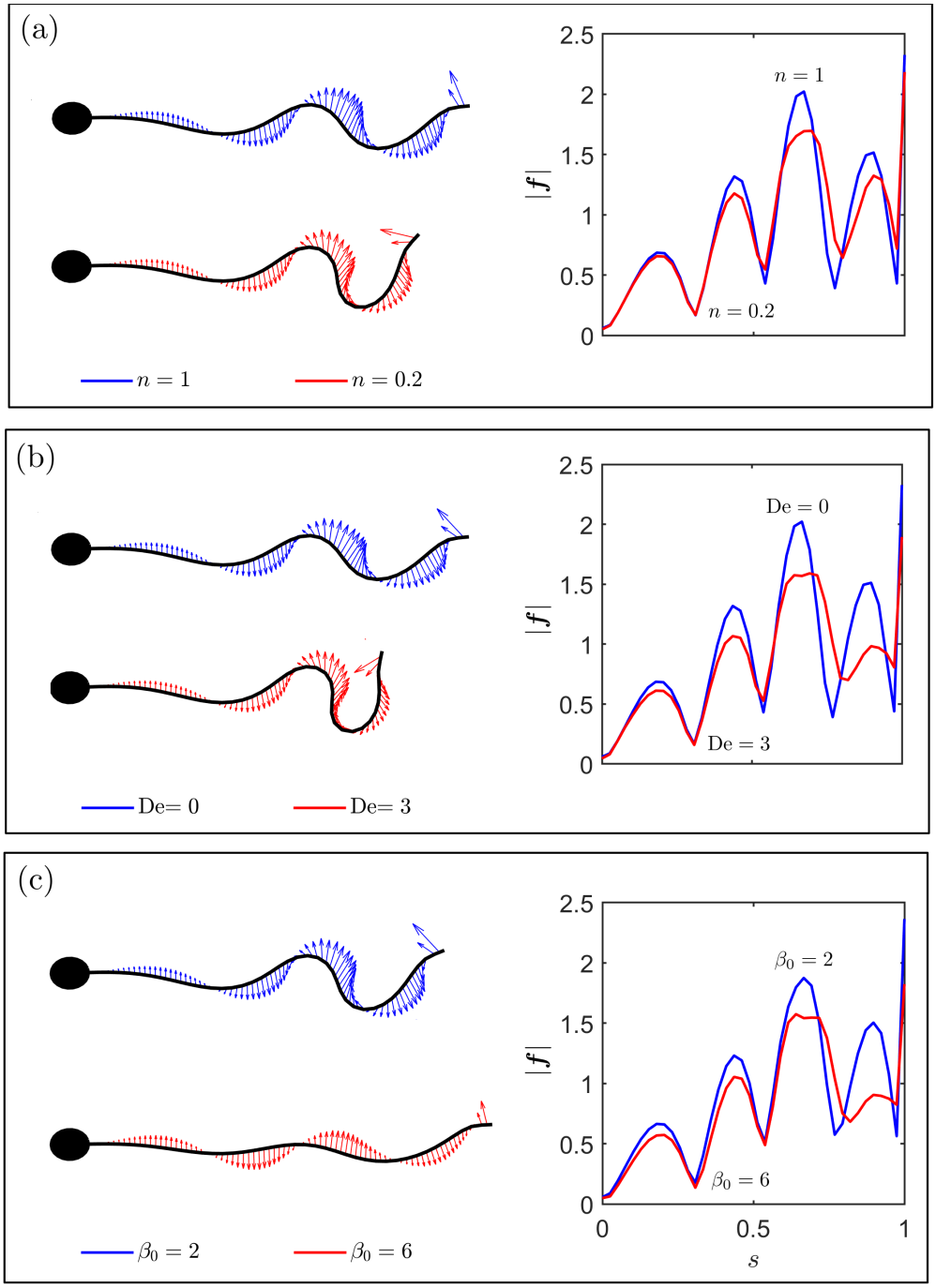


Figure 4.9: Comparison of the force generation of the flagellum for the best and worst swimmer (maximum and minimum VAL respectively), over the parameters (a) $n \in [0.2, 1]$, (b) De $\in [0, 3]$ and (c) $\beta_0 \in [1, 6]$. In (a), force generation is indicated by arrows showing strength and direction for a cell with $n = 1$ (top left) and $n = 0.2$ (bottom left). Arrows are scaled equally in the top and bottom diagrams. The magnitude of the flagellar force ($|\boldsymbol{f}|$) is plotted over arclength s (right). Similarly, (b) shows the same as (a) but for the cells corresponding to De $= 0$ (top left) and De $= 3$ (bottom left). The same is also true of (c), for cells corresponding to $\beta_0 = 2$ (top left) and $\beta_0 = 6$ (bottom left). Across all simulations $\mathcal{S} = 13$, $\mathcal{M} = 0.027$ and $\ell = 0.95$ and the remaining shear-thinning parameters are fixed as $n = 0.5$, De $= 1$, or $\beta_0 = 2$ as appropriate.

the frame in which the head of the sperm cell does not move. The subsequent fluid problem can be solved using the nearest-neighbour regularised stokeslet method (Gallagher and Smith, 2018), as detailed in Appendix E.

In Figure 4.10a, for each value of $n \in [0.2, 1]$, we compare the swimming speed of a cell with a flexible elastic flagellum in a fluid with shear-thinning index n (blue) with the swimming speed of a cell with the same beat in a Newtonian fluid (red). At $n = 1$, the two methods are consistent, as expected. For $n < 1$, the swimming speed in a Newtonian fluid, $\mathrm{VAL}_{\text{STb-Nf}}$, is always less than the swimming speed in a shear-thinning fluid VAL_{ST}. Therefore, for a cell with prescribed flagellar motion in a Newtonian and shear-thinning fluid, shear-thinning rheology always aids propulsion. This conclusion implies that the reduction in swimming speed with decreasing n observed in Figure 4.1a is likely a result of the shape changes associated with swimming in a shear-thinning fluid. Indeed, both $\mathrm{VAL}_{\text{STb-Nf}}$ and VAL_{ST} reduce with reducing n, indicating that in both the Newtonian and shear-thinning cases the change in the flagellar beat pattern with n impedes progress. In Figure 4.10b, we plot the difference between the swimming speeds, $\mathrm{VAL}_{\text{ST}} - \mathrm{VAL}_{\text{STb-Nf}}$, over $n \in [0.2, 1]$.

The equivalent results to Figures 4.10a and 4.10b for the swimming speeds over $\mathrm{De} \in [0, 3]$ are given in Figures 4.10c and 4.10d. As before, these results indicate that shear-thinning rheology in the absence of swimmer elasticity enhances propulsion, with the quantity $\mathrm{VAL}_{\text{ST}} - \mathrm{VAL}_{\text{STb-Nf}}$ remaining positive for all values of $\mathrm{De} \in (0, 3]$ considered. The results for the swimming speeds over $\beta_0 \in [1, 6]$ yield the same result, where in this case the swimming speeds $\mathrm{VAL}_{\text{STb-Nf}}$ and VAL_{ST} peak at $\mathrm{VAL}_{\text{STb-Nf}} = 1.75$ and $\mathrm{VAL}_{\text{ST}} = 2$ respectively.

Whilst in the Newtonian case, the cell experiences an environment of constant viscosity, we expect to see regions of thinned fluid surrounding the cell in a shear-thinning fluid. In Figure 4.11, we plot the viscosity surrounding a sperm cell corresponding to the HANS simulations in Figure 4.10a for shear-thinning indices $n = 0.2$, $n = 0.5$ and $n = 0.8$. For each value of n, the viscosity is plotted over three planes in order to examine the variation in viscosity in each direction. Over all n and each plane, we observe a region of thinned fluid surrounding the swimmer. This region generally grows in size with increased shear-thinning effects, with the

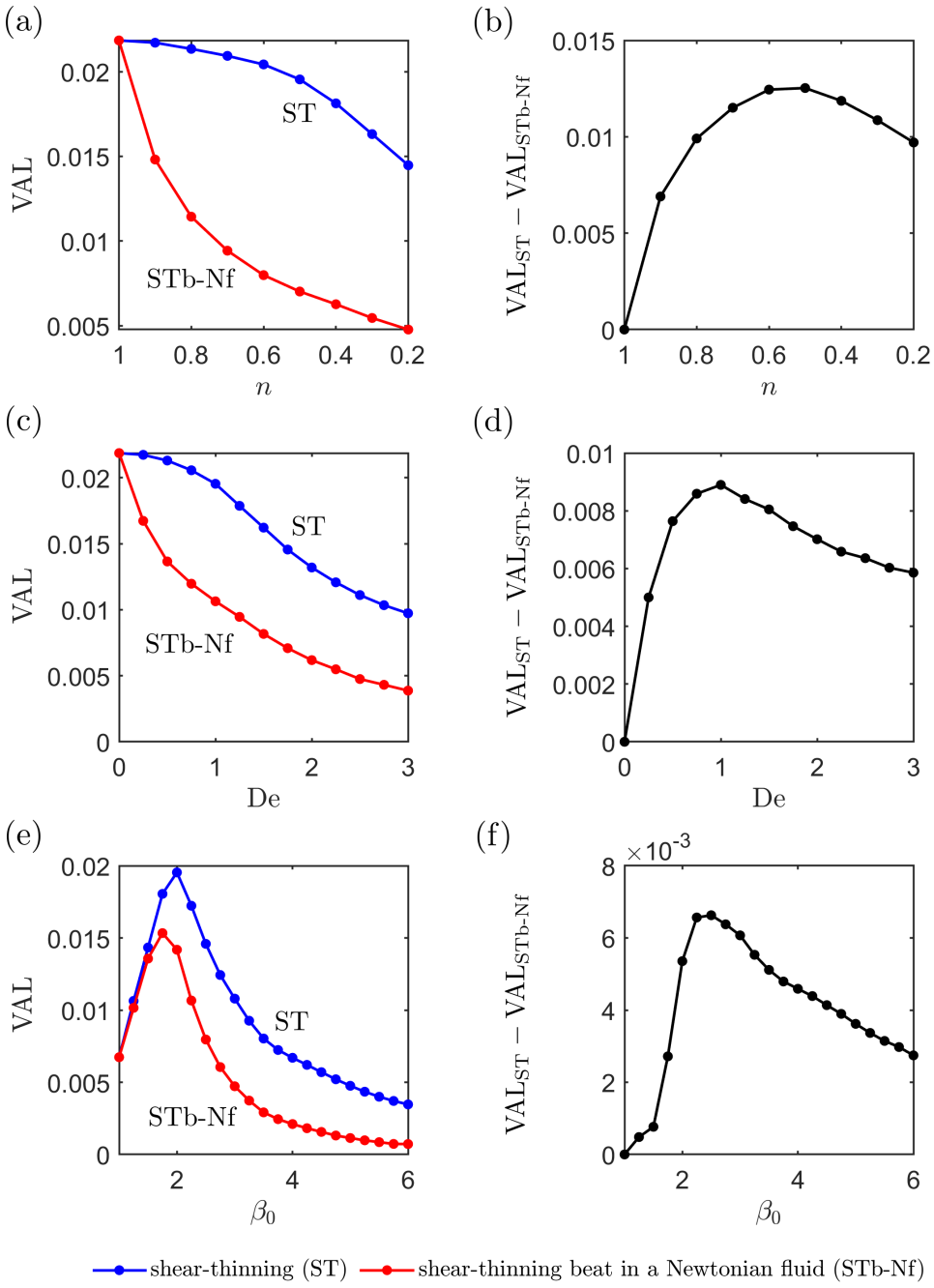


Figure 4.10: Results exploring the effect of shear-thinning rheology on propulsion of a sperm cell with fixed flagellar beat. (a) The effect of the shear-thinning index $n \in [0.2, 1]$ on swimming speed ($\mathrm{VAL_{ST}}$) for a cell simulated using the HANS method (blue). For each n, the swimming speed ($\mathrm{VAL_{STb\text{-}Nf}}$) of a cell with prescribed flagellar beat corresponding to the beat obtained via the HANS method and simulated within a Newtonian fluid is plotted in red. (b) The difference in swimming speeds between a cell simulated with shear-thinning index n and a cell with the same waveform within a Newtonian fluid. Panels (c) and (d) show analogous results to (a),(b) but over $\mathrm{De} \in [0, 3]$. Similarly, (e) and (f) show the corresponding results for $\beta_0 \in [1, 6]$. Across all simulations $\mathcal{S} = 13$, $\mathcal{M} = 0.027$ and $\ell = 0.95$ and the remaining shear-thinning parameters in the HANS simulation are fixed as $n = 0.5$, $\mathrm{De} = 1$, or $\beta_0 = 2$ as appropriate.

viscosity close to the swimmer reducing with smaller n. The thinned envelope surrounding the swimmer is reminiscent of that observed in other studies of swimmers in shear-thinning fluids (Montenegro-Johnson et al., 2013; Gagnon and Arratia, 2016). Similar results can be observed for the variation in the viscosity surrounding the swimmer with De, plotted in Figure 4.12 for De $= 3$, De $= 1.5$ and De $= 0.5$. Finally, the variation in the viscosity field with β_0 is plotted in Figure 4.13 for $\beta_0 = 2$, $\beta_0 = 4$ and $\beta_0 = 6$. Here, the layers of thinned fluid are more tightly packed around the flagellum for higher values of β_0.

In Figure 4.14, we plot the variation in the Newtonian-infinite shear rate viscosity β_S over arclength s for each of the shear-thinning parameters n, De and β_0. This corresponds to the change in the viscosity over arclength surrounding the flagellum over these parameter choices. For the variation over n and De plotted in 4.14a and 4.14b respectively, we observe that for all for $n < 1$ and De > 0 considered, viscosity decreases non-monotonically with arclength. As a result, the fluid surrounding the distal flagellum is significantly thinned compared to the fluid surrounding the proximal region, likely leading to a difference in drag across the two ends of the flagellum. With increased shear-thinning effects, the difference between the distal and proximal viscosities increases. For the results with changing β_0 indicated in Figure 4.14c, increasing β_0 results in a higher overall fluid viscosity surrounding the flagellum, and again an increase in the difference in viscosity between the proximal and distal ends.

In this section, we have shown how shear-thinning rheology tends to hinder progression of a single sperm cell in terms of swimming speed, efficiency and work done. We have also revealed that the variation in the work done by the cell over the various parameter ranges can be quantified via the average curvature of the distal flagellum over a beat. We have explored the fluid velocity and force generation of the flagellum, and uncovered that the shape changes associated with swimming in fluids with different rheologies is likely a significant factor in the differences in propulsion observed. To explore this further, we will now explore the effect of varying the viscous-elastic parameter S and observing how changes in the shear-thinning index n affect propulsion and waveform.

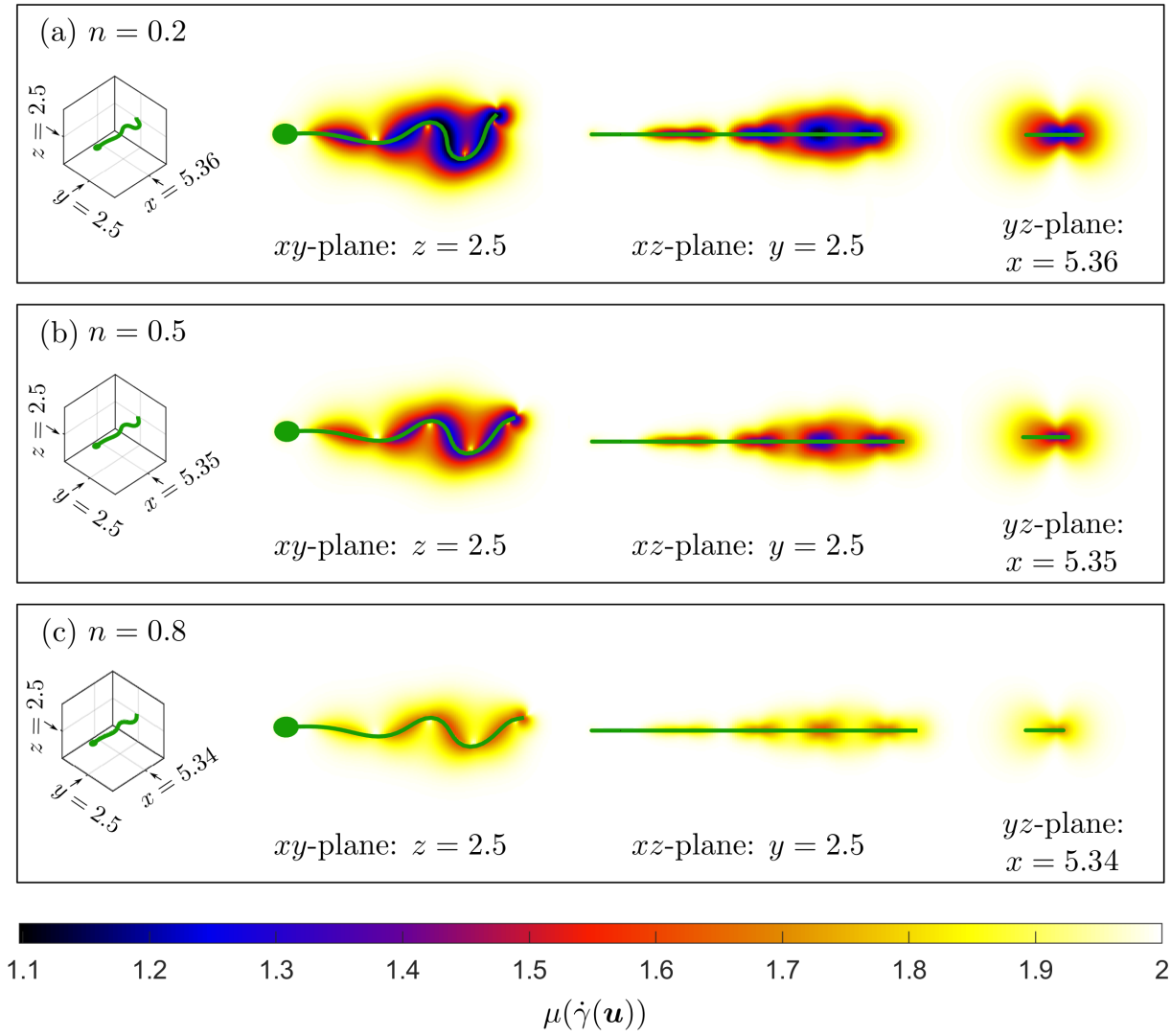


Figure 4.11: The viscosity $\mu(\dot{\gamma}(\boldsymbol{u}))$ surrounding a simulated sperm cell for (a) $n = 0.2$, (b) $n = 0.5$ and (c) $n = 0.8$. Here, the colorbar corresponds to the fluid viscosity, with lower viscosity regions indicated in black, and higher viscosity regions in white. For each value of n, the cell waveform and the surrounding viscosity is plotted in the planes $z = \bar{z}$ (left), $y = \bar{y}$ (middle) and $x = \bar{x}$ (right) where $\bar{x}$, $\bar{y}$ and $\bar{z}$ represent the mean position across the flagellum in each direction (values indicated in each panel). Across all simulations, $\mathcal{S} = 13$, $\mathcal{M} = 0.027$ and $\ell = 0.95$ and the remaining shear-thinning parameters are fixed as $\mathrm{De} = 1$ and $\beta_0 = 2$. The waveform and viscosity are plotted at $t = 10\pi$ (after five beats).

4.2 The effect of shear-thinning rheology on propulsion with varying viscous-elastic parameter $\mathcal{S}$

We next examine the effect of shear-thinning rheology on cells with varying viscous-elastic properties, corresponding to parameter values $\mathcal{S} \in [9, 18]$. Here, the parameters $\mathcal{M} = 0.027$

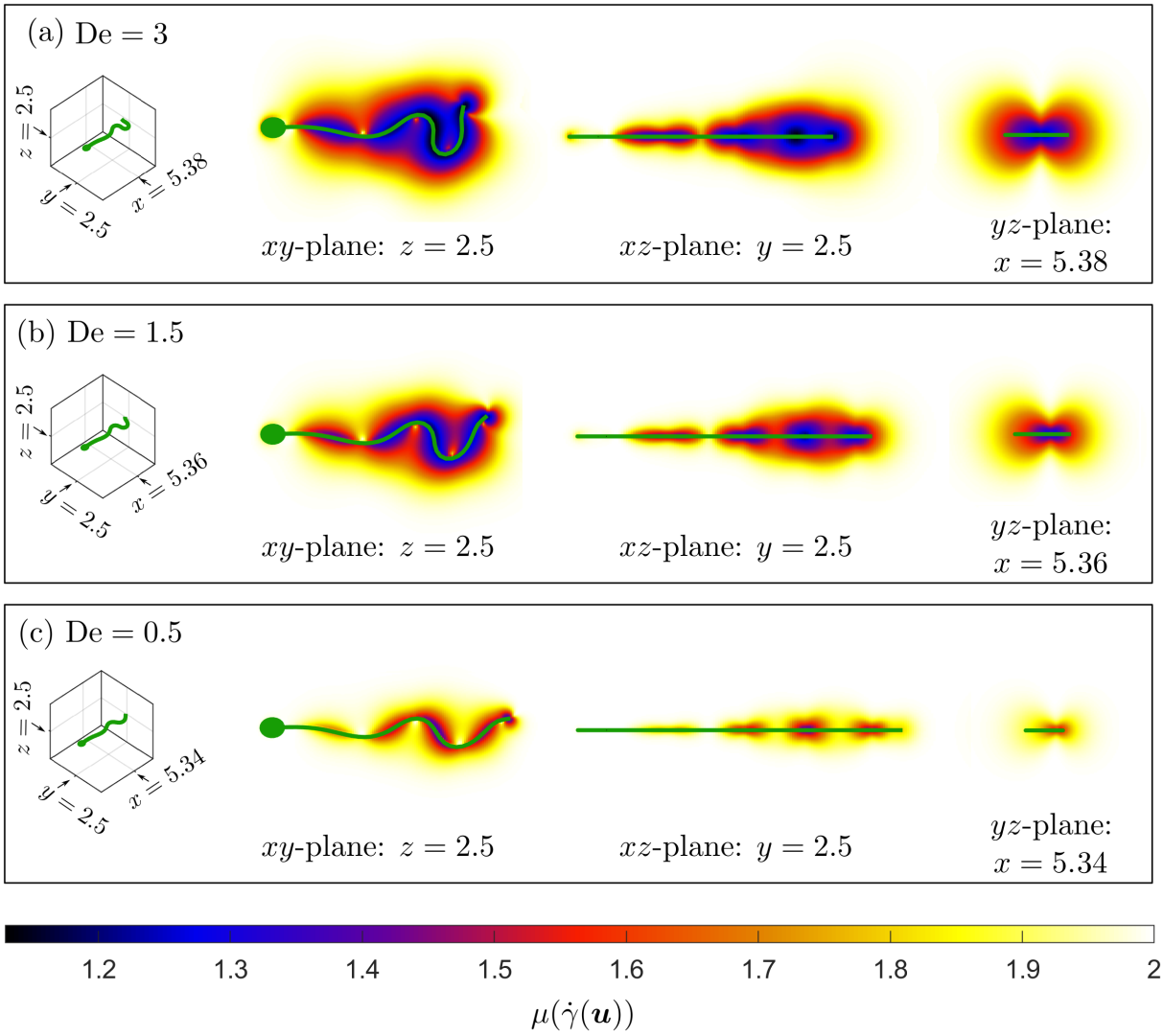


Figure 4.12: The viscosity $\mu(\dot{\gamma}(\boldsymbol{u}))$ surrounding a simulated sperm cell for (a) De = 3, (b) De = 1.5 and (c) De = 0.5. Here, the colorbar corresponds to the fluid viscosity, with lower viscosity regions indicated in black, and higher viscosity regions in white. For each value of De, the cell waveform and the surrounding viscosity is plotted in the planes $z = \bar{z}$ (left), $y = \bar{y}$ (middle) and $x = \bar{x}$ (right) where $\bar{x}$, $\bar{y}$ and $\bar{z}$ represent the mean position across the flagellum in each direction (values indicated in each panel). Across all simulations, $\mathcal{S} = 13$, $\mathcal{M} = 0.027$ and $\ell = 0.95$ and the remaining shear-thinning parameters are fixed as $n = 0.5$ and $\beta_0 = 2$. The waveform and viscosity are plotted at $t = 10\pi$ (after five beats).

and $\ell = 0.95$ are kept constant as before. In Figure 4.15a (left), we plot the variation in the swimming speed (VAL) with $\mathcal{S}$, for nine different values of the shear-thinning index $n \in [0.2, 1]$. The Newtonian case where $n = 1$ (corresponding to a fluid with viscosity μ_0) is shown in black, with the remaining values $n \in [0.2, 0.9]$ plotted from yellow ($n = 0.2$) to dark blue ($n = 0.9$). For $\mathcal{S} \in [9, 13]$, swimming speed decreases as the fluid becomes more shear-thinning (decreased

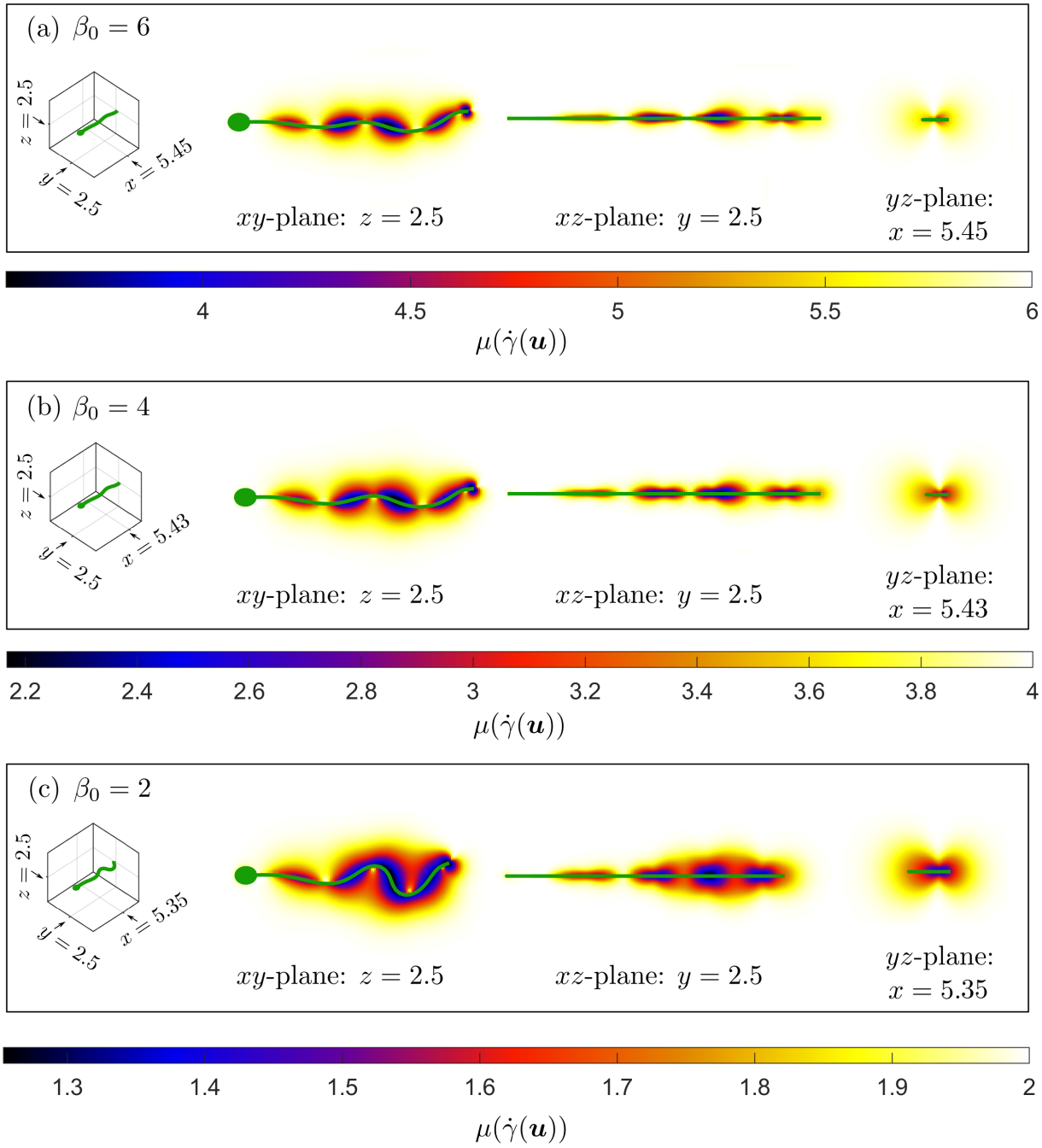


Figure 4.13: The viscosity $\mu(\dot{\gamma}(\boldsymbol{u}))$ surrounding a simulated sperm cell for (a) $\beta_0 = 2$, (b) $\beta_0 = 4$ and (c) $\beta_0 = 6$. Here, the colorbar corresponds to the fluid viscosity, with lower viscosity regions indicated in black, and higher viscosity regions in white. For each value of β_0, the cell waveform and the surrounding viscosity is plotted in the planes $z = \bar{z}$ (left), $y = \bar{y}$ (middle) and $x = \bar{x}$ (right) where $\bar{x}$, $\bar{y}$ and $\bar{z}$ represent the mean position across the flagellum in each direction (values indicated in each panel). Across all simulations, $\mathcal{S} = 13$, $\mathcal{M} = 0.027$ and $\ell = 0.95$ and the remaining shear-thinning parameters are fixed as $n = 0.5$ and $\mathrm{De} = 1$. The waveform and viscosity are plotted at $t = 10\pi$ (after five beats).

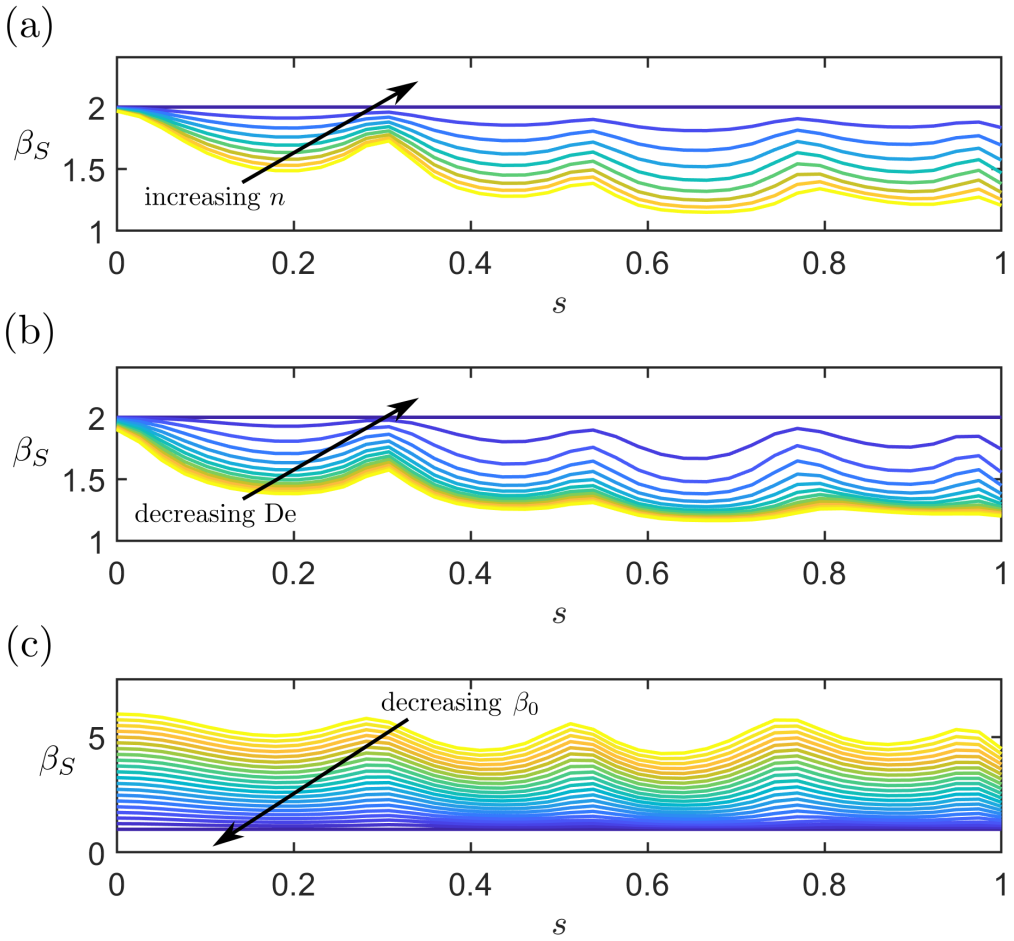


Figure 4.14: The variation in the viscosity ratio β_S with arclength s along the flagellum over shear-thinning parameters (a) $n \in [0.2, 1]$, (b) De $\in [0, 3]$ and (c) $\beta_0 = [1, 6]$. Results are plotted at $t = 10\pi$ for a cell with $\mathcal{S} = 13$, $\mathcal{M} = 0.027$ and $\ell = 0.95$. In each panel, yellow represents the most strongly shear-thinning case, ranging to blue for the Newtonian solution. Arrows are plotted to show the change in the shear-thinning parameters across each panel. Across all panels, the remaining shear-thinning parameters are fixed as $n = 0.5$, De $= 1$ and $\beta_0 = 2$ as appropriate.

n), with more substantial decreases observed with increased $\mathcal{S}$ within this interval. This indicates that for low-to-moderate viscous-elastic parameter $\mathcal{S}$, shear-thinning rheology impairs propulsion compared to swimming in a Newtonian fluid of the same zero shear rate viscosity. For $\mathcal{S} \in [14, 18]$, we observe an increase in VAL for $n \in [0.8, 0.9]$, and no change in VAL for $n = 0.9$ compared to the Newtonian swimming speed. For $n \in [0.2, 0.8]$, we observe substantial decreases in VAL compared to the equivalent Newtonian values, with larger decreases observed for larger values of $\mathcal{S}$. This indicates that for moderate-to-large viscous-elastic pa-

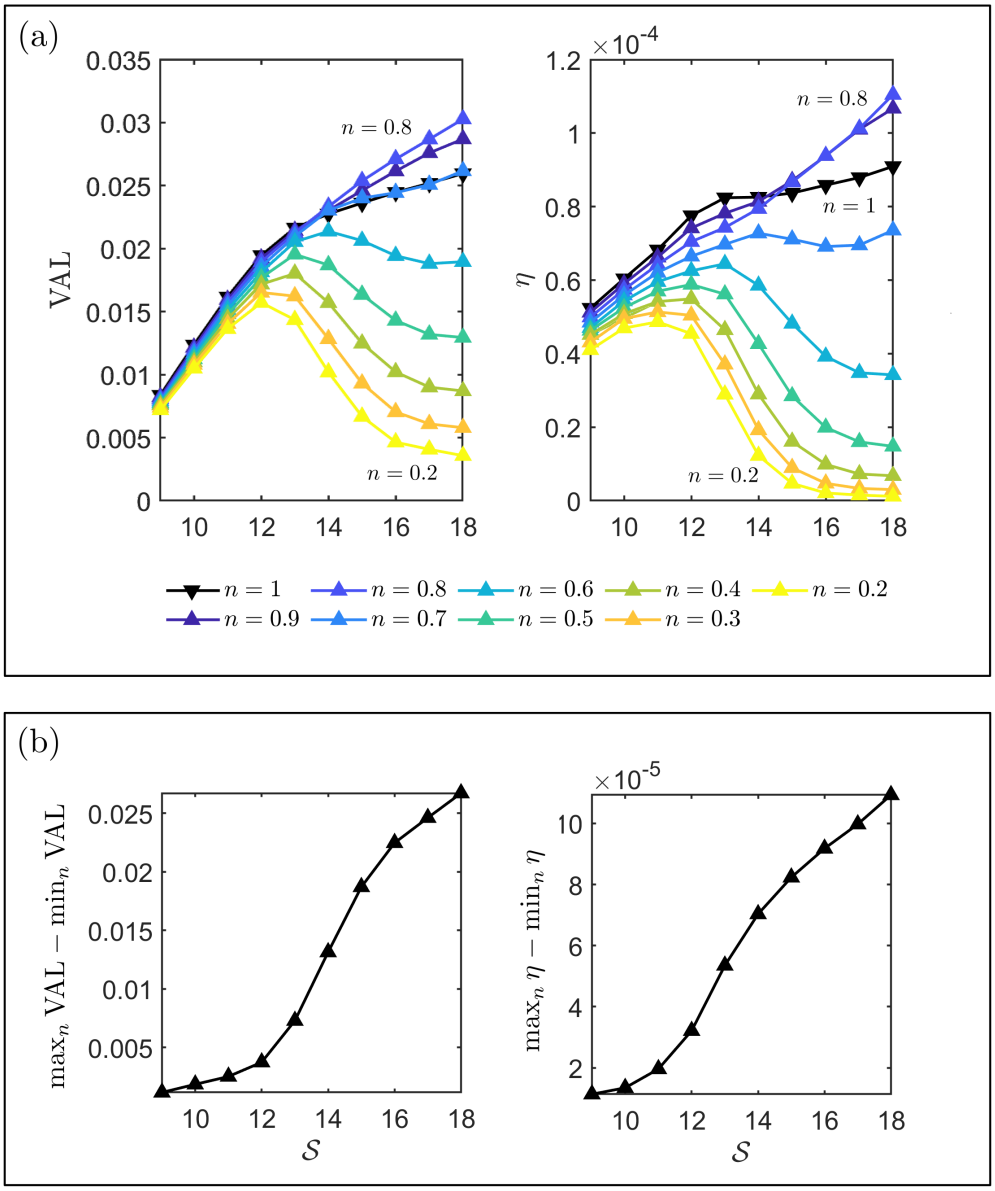


Figure 4.15: The effect of shear-thinning rheology on the propulsion of a single human sperm over varying viscous-elastic parameter values $\mathcal{S} \in [9, 18]$. (a) The swimming speed (VAL, left panel) and the Lighthill efficiency (η, right panel) over $\mathcal{S} \in [9, 18]$, plotted for nine values of $n \in [0.2, 1]$. Here, the solutions for a Newtonian fluid (where $n = 1$) are plotted in black, with the solutions for the remaining values of $n \in [0.2, 0.9]$ plotted from yellow ($n = 0.2$) to dark blue ($n = 0.9$). In (b), the difference between the maximum and minimum VAL across all values of n is plotted over $\mathcal{S} \in [9, 18]$ (left panel). Similarly, the difference between the maximum and minimum observed efficiency η across all values of n is plotted over $\mathcal{S} \in [9, 18]$ (right panel). The remaining shear-thinning parameters are fixed as $\mathrm{De} = 1$ and $\beta_0 = 2$.

rameter $\mathcal{S}$, weakly shear-thinning fluids yield an increase in swimming speed, whilst strong shear-thinning effects can impede progress compared to swimming in a Newtonian fluid with viscosity μ_0.

To further illustrate the range in swimming speed (VAL) observed over $\mathcal{S} \in [9, 18]$, the difference between the maximum and minimum VAL over $n \in [0.2, 1]$ is plotted as a function of $\mathcal{S}$ in Figure 4.15b (left). The range in VAL observed increases with $\mathcal{S}$, indicating that a higher viscous-elastic ratio (or a more 'floppy' flagellum) leads to greater propulsive changes in a shear-thinning fluid.

In Figure 4.15a (right), we plot the variation in the Lighthill efficiency (η) with $\mathcal{S}$, for nine different values of the shear-thinning index $n \in [0.2, 1]$. Analogous to Figure 4.15a, we plot the variation in the Newtonian efficiency with $\mathcal{S}$ in black, with the equivalent results for $n \in [0.2, 0.9]$ plotted from yellow ($n = 0.2$) to dark blue ($n = 0.9$). We observe that for $\mathcal{S} \in [9, 14]$, efficiency decreases with increased shear-thinning effects, whereas for $\mathcal{S} \in [15, 18]$ we observe an increase in efficiency for weakly shear-thinning fluids ($n \in [0.8, 0.9]$), as in Figure 4.15a. Fluids with $n \in [0.2, 0.8]$ again yield a decrease in efficiency, with the range in efficiency over $n \in [0.2, 1]$ increasing with greater $\mathcal{S}$ (shown in Figure 4.15b (right)).

To further analyse the observed changes in propulsive effectiveness over n and $\mathcal{S}$, we examine the variation in the flagellar waveform over these parameters in Figure 4.16. At times $t = 9\pi$ and $t = 10\pi$, we plot the change in the flagellar shape over $n \in [0.2, 1]$ for ten values of $\mathcal{S} \in [9, 18]$. For each $(\mathcal{S}, t)$ pair, the waveform in the Newtonian ($n = 1$) case is shown in yellow, ranging to the strongly shear-thinning case ($n = 0.2$) shown in blue. For smaller values of S, corresponding to stiffer flagella, little change is observed in the waveform over n. With increasing $\mathcal{S}$, the modifications to the waveform in a shear-thinning fluid become more pronounced. The proximal half of the flagellum exhibits little change in curvature across all values of n and $\mathcal{S}$ explored, however the distal half of the flagellum exhibits large changes to the curvature and tangent angle for moderate-to-high $\mathcal{S}$. These changes likely explain the degree of variation in propulsion with $\mathcal{S}$ observed in Figure 4.15.

For each $(\mathcal{S}, n)$ pair, we again extract the flagellar beat between $t \in [0, 10\pi]$ and simulate a cell with prescribed flagellar beat in the body frame in a Newtonian fluid, allowing for the calculation of the swimming speed $\mathrm{VAL}_{\text{STb-Nf}}$ in each case. For nine equally spaced values of $n \in [0.2, 1]$, we plot the difference between the swimming speed in a shear-thinning and

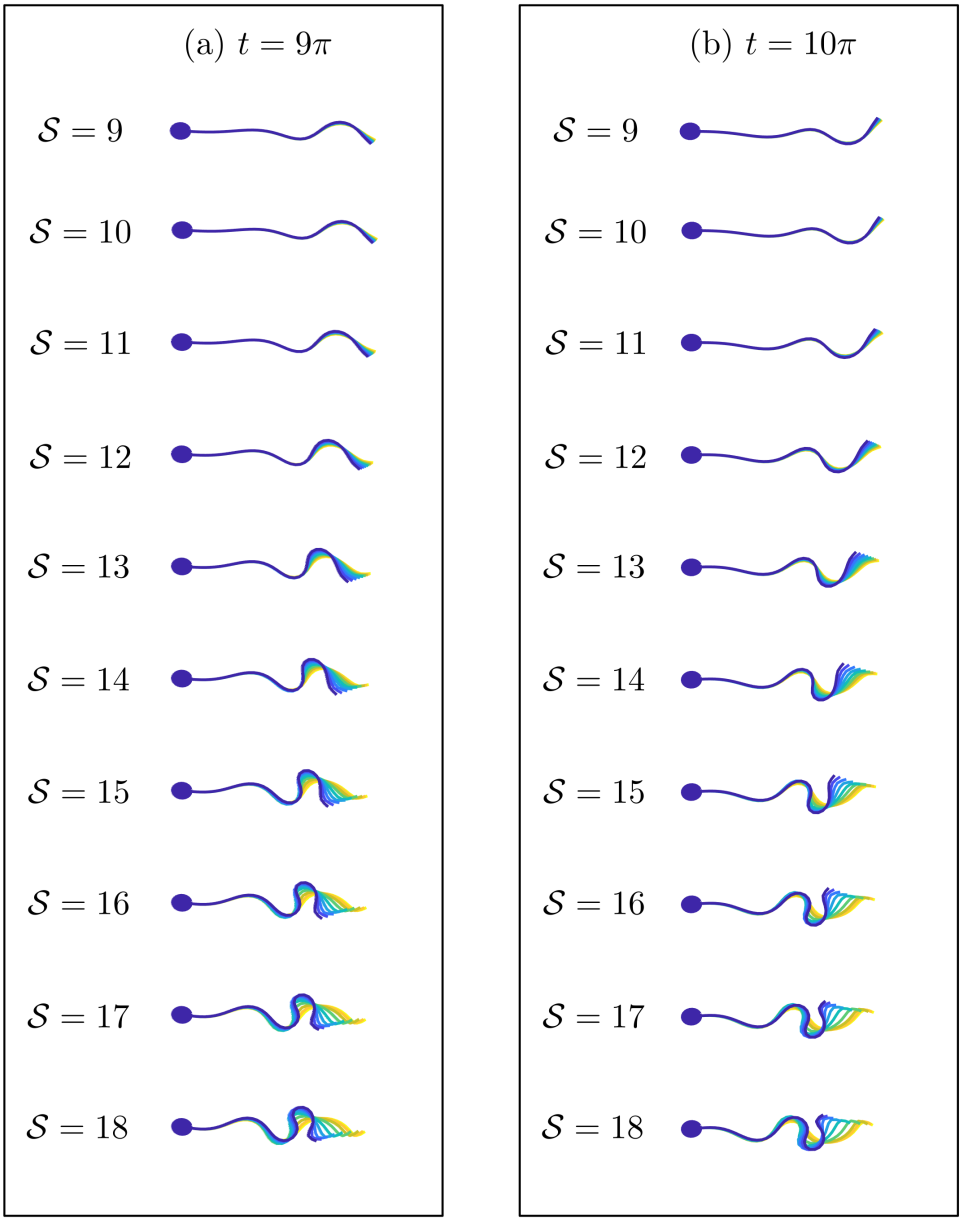


Figure 4.16: The effect of shear-thinning rheology on flagellar waveform over varying viscous-elastic parameter values $\mathcal{S} \in [9, 18]$. At two points over the beat (a) $t = 9\pi$ and (b) $t = 10\pi$, the variation in flagellar shape over $n \in [0.2, 1]$ is plotted for ten values of $\mathcal{S} \in [9, 18]$. For each $(\mathcal{S}, t)$ pair, the waveform in the Newtonian case ($n = 1$) is shown in yellow, ranging to the waveform in a strongly shear-thinning fluid ($n = 0.2$), which is plotted in blue. The remaining shear-thinning parameters are fixed as De $= 1$ and $\beta_0 = 2$.

Newtonian fluid with the same beat, $\text{VAL}_{\text{ST}} - \text{VAL}_{\text{STb-Nf}}$, over $\mathcal{S} \in [9, 18]$, in Figure 4.17. The difference in VAL corresponding to $n = 1$ in the HANS simulation is zero across all values of $\mathcal{S} \in [9, 18]$ (shown in black). This demonstrates that the solution using both methods in the Newtonian case ($n = 1$) is consistent over all $\mathcal{S} \in [9, 18]$, as expected. The difference in

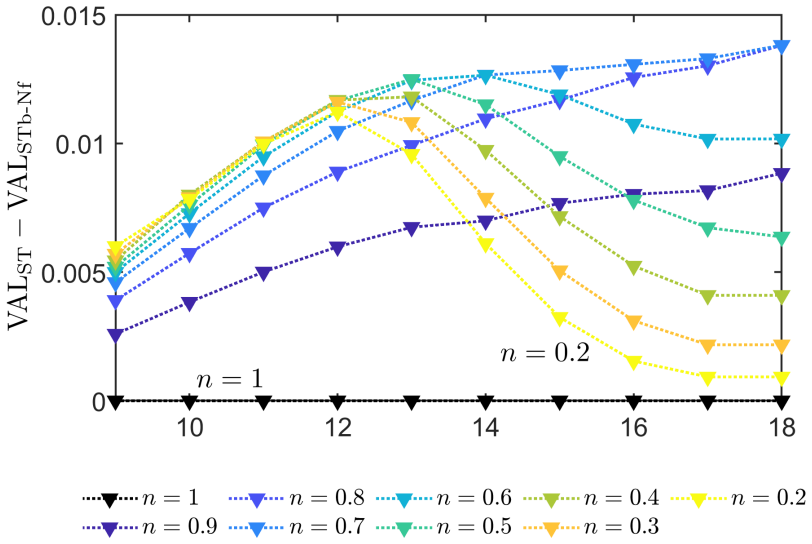


Figure 4.17: The effect of shear-thinning rheology on the propulsion of a single human sperm cell with a fixed flagellar beat over varying viscous-elastic parameter values $\mathcal{S} \in [9, 18]$. For each of the simulations in Figure 4.15a, i.e. for every combination of $n \in [0.2, 1]$ and $\mathcal{S} \in [9, 18]$, the flagellar beat is extracted between $t \in [0, 10\pi]$. The extracted beat is used to prescribe the flagellar motion in the body frame of a sperm cell in a Newtonian fluid. The difference in swimming speed between the results plotted in Figure 4.15a and for the same waveform in a Newtonian fluid, $\mathrm{VAL_{ST}} - \mathrm{VAL_{STb\text{-}Nf}}$, is plotted over $\mathcal{S} \in [9, 18]$ for nine values of $n \in [0.2, 1]$. The results for $n \in [0.2, 0.9]$ are plotted from yellow ($n = 0.2$) to dark blue ($n = 0.9$). When $n = 1$, the two solutions methods coincide (shown in black).

VAL over $n \in [0.2, 0.9]$ in the HANS simulation are plotted from yellow ($n = 0.2$) to dark blue ($n = 0.9$). Notably, all values are greater than zero, indicating that for the shear-thinning beats considered, propulsion is always enhanced in a shear-thinning fluid compared to swimming in a Newtonian fluid of viscosity μ_0.

4.3 The effect of the inactive end piece on propulsion in shear-thinning fluids

In Chapter 2, we discussed how the presence of the inactive flagellar end piece enhances propulsion of sperm cells in a Newtonian fluid, compared to cells with a fully-active flagellum. In particular, we found that across the parameter ranges considered, the presence of the end piece always increases swimming speed and efficiency of cells. The optimal inactive

length depends on both the viscous-active parameter $\mathcal{S}$ and the dimensionless waveform k, and is between $2-18\%$ of the total flagellar length. In this section, we explore the effect of the inactive flagellar end piece on propulsion in a shear-thinning fluid. Specifically, for two values of the viscous-elastic parameter $\mathcal{S} \in \{13, 18\}$ and for $k = 4\pi$, we consider simulating a fully-active cell and a cell with an inactive distal region of length $L - \ell = 0.05$ in fluids of varying shear-thinning parameter $n \in [0.2, 1]$. Whilst a detailed study exploring a fine gradation in the values of $\mathcal{S}$, k, and ℓ would be beneficial, the high number of simulations and large run-time of simulating in shear-thinning fluids means that this is beyond the scope of this thesis. Nevertheless, the results provided in this section provide insight into the effect of the flagellar end piece in shear-thinning fluids, building on the results in Chapter 2.

In Figure 4.18a (left), for viscous-elastic parameter value $\mathcal{S} = 13$, we compare the relationship between the swimming speed (VAL) and the shear-thinning index n for a fully-active cell ($\ell = 1$) and a cell with an inactive distal region ($\ell = 0.95$). In both cases, we observe a reduction in VAL with increased shear-thinning effects (smaller n), in agreement with our previous observations of the effect of shear-thinning rheology. In the Newtonian case ($n = 1$), we observe that the cell with an inactive end piece (blue) leads to an approximately 17% increase in VAL compared to a fully-active cell (red), comparable to the levels of swimming enhancement observed in Chapter 2. As n decreases, the difference between VAL for the cell with an inactive end piece and the fully-active cell decreases, and at $n = 0.2$ only a small 2% increase in swimming speed is observed for cells with an end piece. This indicates that in fluids with stronger shear-thinning effects, the presence of the end piece yields less of an advantage to cells. Similarly in Figure 4.18a (right) we plot the change in the efficiency η with n for the cell with $\ell = 1$ (fully-active) and $\ell = 0.95$ (inactive end piece). We again observe that whilst the cell with the inactive distal region is always more efficient, the beneficial effect of swimming with an end piece on efficiency decreases with stronger shear-thinning effects. By contrast, in the Newtonian case the cell with $\ell = 0.95$ leads to an approximately 67% increase in η, at $n = 0.2$ the increase only 5%.

In Figures 4.18b, the equivalent results to Figure 4.18a are shown for a cell with viscous-

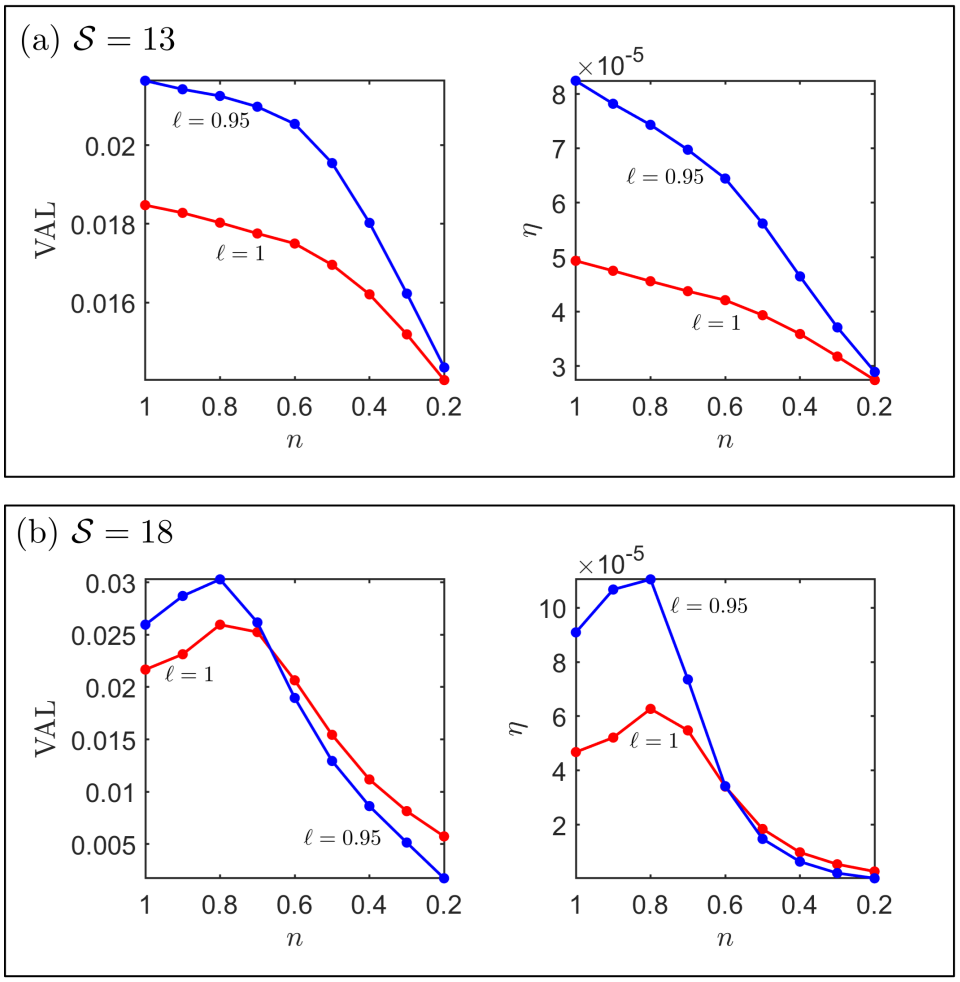


Figure 4.18: The effect of the flagellar end piece on the propulsion of a single human sperm cell in a shear-thinning fluid. (a) The effect of shear-thinning index $n \in [0.2, 1]$ on the swimming speed (VAL, left plot) and the Lighthill efficiency (η, right plot) are plotted for a fully-active cell (red) and a cell with an inactive end piece of length $L - \ell = 0.05$ (blue). Here, $\mathcal{S} = 13$. Panel (b) shows the equivalent results for swimming speed and efficiency for a cell with $\mathcal{S} = 18$. The remaining shear-thinning parameters are fixed as De $= 1$ and $\beta_0 = 2$, and VAL and η are calculated after five cycles of the active moment.

elastic parameter $\mathcal{S} = 18$. Again, in the Newtonian case when $n = 1$, we observe that both the swimming speed VAL and the efficiency η are larger for a cell with an end piece that for a cell with a fully-active flagellum. In both cases, decreasing n (increased shear-thinning effects) again leads to a reduction in both VAL and η, with the difference between the results for $\ell = 0.95$ and $\ell = 1$ again decreasing. Unlike the $\mathcal{S} = 13$ case, this eventually leads to a regime in which the fully-active cell swims faster and more efficiently that the cell with a passive distal region. Therefore, for approximately $n < 0.6$, the presence of the end piece hinders propulsion

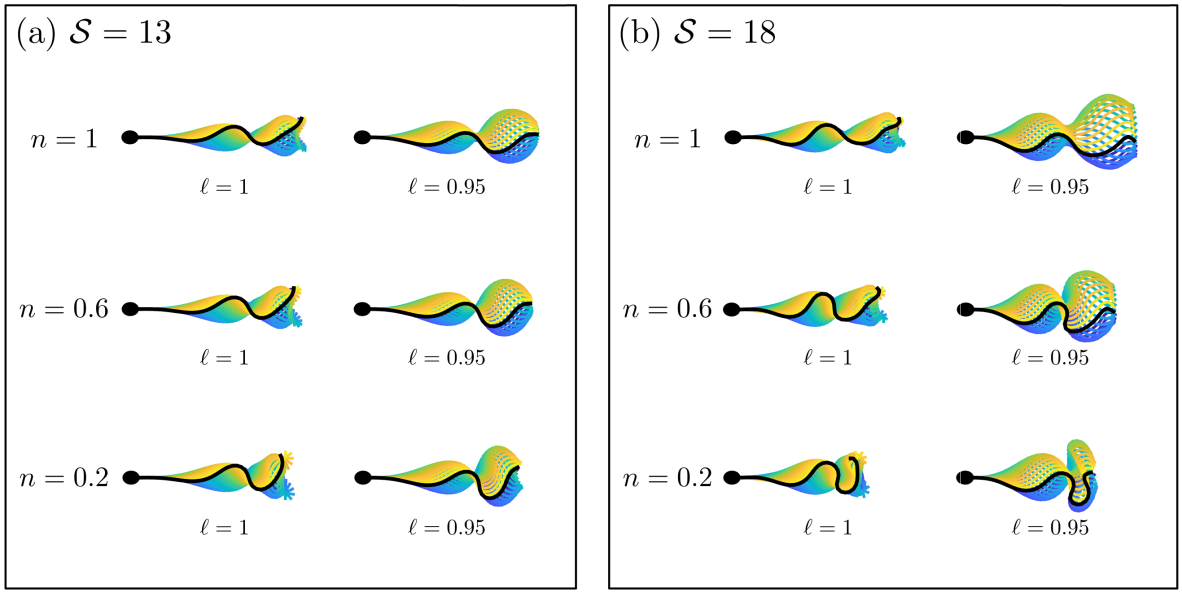


Figure 4.19: The flagellar waveform for fully-active ($\ell = 1$) cells and cells with an inactive end piece ($\ell = 0.95$) for three value of the shear-thinning index $n \in \{1, 0.6, 0.2\}$ and (a) $\mathcal{S} = 13$ and (b) $\mathcal{S} = 18$. The color of the flagellum indicates progress through a single beat ($t \in [8\pi, 10\pi]$), from blue to yellow, with the final waveform shown in black at $t = 10\pi$. The remaining shear-thinning parameters are set as De $= 1$ and $\beta_0 = 2$.

in a shear-thinning fluid. Whilst in the Newtonian case the presence of the end piece leads to an increase in VAL and η of ΔVAL $= 0.0043$ (20%) and $\Delta\eta = 4.4130 \times 10^{-5}$ (94%) respectively, in the most strongly shear-thinning case ($n = 0.2$), the presence of the end piece decreases these measures by ΔVAL $= 0.0040$ (70%) and $\Delta\eta = 2.5123 \times 10^{-6}$ (91%) respectively. These percentage changes indicate that the presence of the end piece can have a significant effect on propulsion in both Newtonian and shear-thinning fluids.

To further explore the effect of the end piece in shear-thinning fluids, we compare the flagellar beat in the $\ell = 1$ and $\ell = 0.95$ cases, as well as the surrounding fluid velocity. In Figure 4.19a, we plot the change in the flagellar envelope over $t \in [8\pi, 10\pi]$ for three values of the shear-thinning index $n = \{1, 0.6, 0.2\}$, for the cell where $\mathcal{S} = 13$. The equivalent results for the cell with $\mathcal{S} = 18$ are plotted in Figure 4.19b. In both cases, the waveform is plotted from blue (corresponding to $t = 8\pi$) to yellow, with the final waveform ($t = 10\pi$) plotted in black. In Chapter 2 (see Figures 2.13 and 2.15) we observed that the inclusion of the flagellar end piece could have a significant effect on flagellar waveform in a Newtonian fluid. Here, we observe a similar difference between the waveforms in the fully-active ($\ell = 1$) and partially-inactive

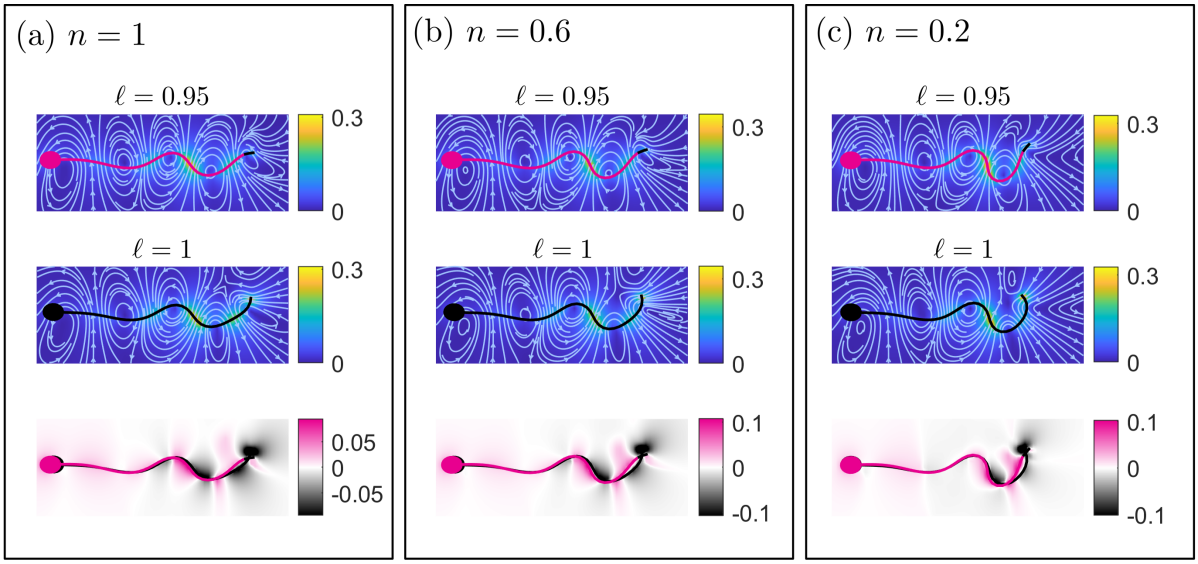


Figure 4.20: Comparison of the flow fields around a simulated sperm cell with and without an inactive end piece for three values of the shear-thinning index (a) $n = 1$, (b) $n = 0.6$ and (c) $n = 0.2$. In each case, the top panel indicates a cell with $\ell = 0.95$ and the bottom panel indicates a fully-active cell with $\ell = 1$. Fluid magnitude is indicated by a colorbar, and instantaneous fluid streamlines are shown in white with arrows indicating direction. The difference between flow fields is shown in the bottom of each panel, where positive values correspond to the cell with the inactive end piece having faster fluid velocity. Here, $\mathcal{S} = 13$ and the remaining shear-thinning parameters are set as $\mathrm{De} = 1$ and $\beta_0 = 2$.

($\ell = 0.95$) cases in both a Newtonian fluid (here $k = 4\pi$ and $\mathcal{M} = 0.027$ rather than $\mathcal{M} = \mathcal{M}_{\mathrm{VAL}}$ or $\mathcal{M} = \mathcal{M}_\eta$ as in Chapter 2) and in shear-thinning fluids. Similarly to the results presented in Chapter 2, the inclusion of the end piece tends to reduce the curvature and tangent angle in the distal portion of the flagellum, resulting in significant changes to the flagellar envelope, i.e. the shape the flagellum traces out over a full beat cycle.

For each of the final waveforms in Figure 4.19, the associated velocity fields are plotted in Figure 4.20 for cells with $\mathcal{S} = 13$, and Figure 4.21 for cells with $\mathcal{S} = 18$. For each $(\mathcal{S}, n)$ pair, the difference between the flow fields in the $\ell = 1$ and $\ell = 0.95$ cases is also indicated in these figures. In the Newtonian case, the increase in swimming speed and efficiency for cells with an inactive end piece can again be attributed to the formation of additional oblique regions of the flagellum which confer additional thrust. In Figure 4.20, we also observe that for $n < 1$ the cell with an end piece tends to always be moving more 'obliquely' than the fully-active case, although the Newtonian $n = 1$ case appears to be the most optimal. Contrastingly, in Figure

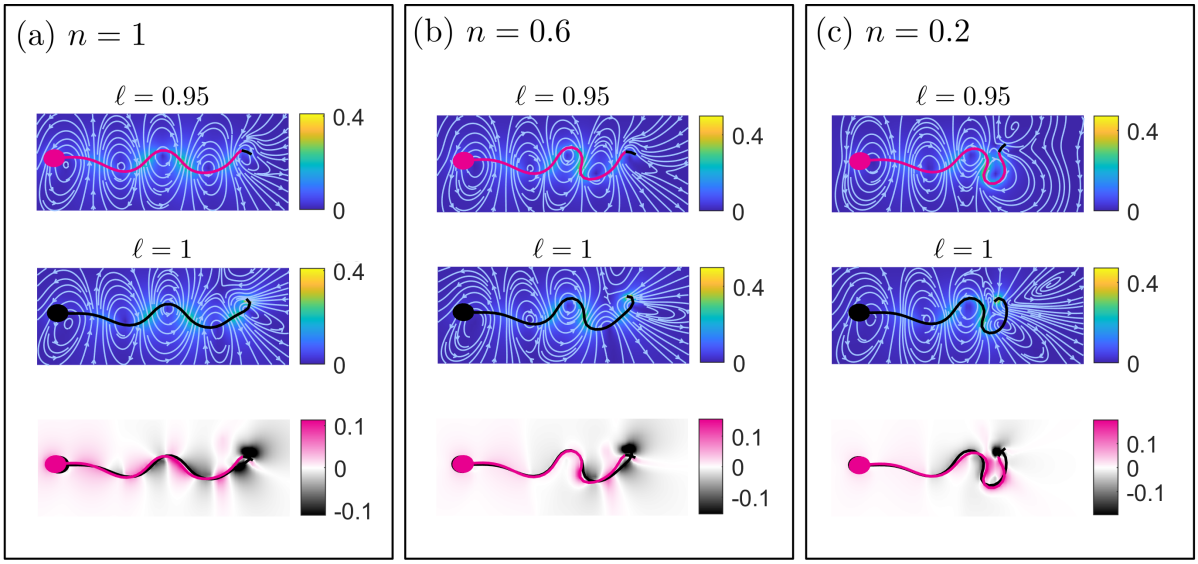


Figure 4.21: Comparison of the flow fields around a simulated sperm cell with and without an inactive end piece for three values of the shear-thinning index (a) $n = 1$, (b) $n = 0.6$ and (c) $n = 0.2$. In each case, the top panel indicates a cell with $\ell = 0.95$ and the bottom panel indicates a fully-active cell with $\ell = 1$. Fluid magnitude is indicated by a colorbar, and instantaneous fluid streamlines are shown in white with arrows indicating direction. The difference between flow fields is shown in the bottom of each panel, where positive values correspond to the cell with the inactive end piece having faster fluid velocity. Here, $S = 18$ and the remaining shear-thinning parameters are set as $\mathrm{De} = 1$ and $\beta_0 = 2$.

4.21, the end piece does not appear to aid in the formation of these oblique regions for $n = 0.6$ and $n = 0.2$ i.e. in a shear-thinning fluid. Whilst neither the $\ell = 1$ or $\ell = 0.95$ flagellar shape are close to optimal in these cases, the velocity associated with the fully-active cells appears to generally be slightly higher than that of the cells possessing an inactive end piece.

4.4 Discussion

In this chapter, we have used the hybrid method for non-linear swimming (HANS) to simulate sperm cells with flexible, elastic flagella in shear-thinning fluids modelled via the BCC4p constitutive law. Our results provide evidence that shear-thinning rheology tends to hinders propulsion of flexible swimmers (over all $\mathrm{De} \in [0, 3]$ and $n \in [0.2, 1]$ considered), with reductions in swimming speed and efficiency of up to 66% and 35% observed respectively, compared to swimming in a Newtonian fluid with viscosity equal to the zero shear rate viscosity μ_0. Enhanced swimming may occur in shear-thinning fluids with differing zero and infinite shear

rate viscosity ($\beta_0 = \mu_0/\mu_\infty > 1$), compared to swimming in a Newtonian fluid at the infinite shear rate viscosity. In this case a peak increase in swimming speed of 290% and efficiency of 899% is seen when $\beta_0 = 2$.

We have shown that the development of the flagellar waveform depends heavily on the shear-thinning properties of the fluid. To de-couple the effects of swimming gait and fluid rheology, we prescribed the observed shear-thinning beats in a Newtonian fluid and solved the resulting fluid problem. We uncovered that for swimmers with the same gait, the cell in the shear-thinning fluid always swims faster than the cell in a Newtonian fluid (see Figure 4.10). Therefore, shear-thinning rheology in the absence of swimmer elasticity aids propulsion. This enhancement may be due to a confinement-like effect, where swimmers propel faster when contained in a region of low viscosity fluid, surrounded by a region of high viscosity fluid (see Figures 4.11, 4.12 and 4.13). This was the mechanism proposed by Li and Ardekani (2015); Man and Lauga (2015); Gómez et al. (2017); Demir et al. (2020) for swimming enhancement in shear-thinning fluids for rigid swimmers with prescribed beat kinematics. Alternatively, this swimming enhancement could also be explained by the tapering fluid viscosity along the flagellum (see Figure 4.14). This could result in reduced drag over the distal portion of the tail due to the thinner fluid surrounding it, as previously observed by Montenegro-Johnson et al. (2012).

In view of the fact that the flagellar beat does indeed emerge from the interaction of active moment, elasticity and viscous resistance, we deduce that physiologically accurate sperm cells are likely mostly hindered by shear-thinning rheology. Thus we suggest that the mechanism by which propulsion of sperm cells are hindered in a shear-thinning fluid compared to a Newtonian fluid of the same zero shear rate viscosity is via shape changes due to the fluid-flagellum interactions which result in sub-optimal waveforms for progression. Similar to the results presented in Chapter 2, we note that cells possessing addition 'oblique' regions towards the distal end of the flagellum, where the absolute angle relative to the direction of propulsion is approximately $\pi/4$, swim the most efficiently. Over the parameter ranges considered, we observe that in general these regions tend to develop in cells swimming in Newtonian fluids (see

Figure 4.8), thus aiding propulsion in these types of fluids. Similar effects are uncovered for cells with varying viscous-elastic properties (quantified through $\mathcal{S}$), with larger shape changes observed for more 'floppy' flagella (higher $\mathcal{S}$). We also observe that the inactive flagellar end piece does not always aid propulsion in a shear-thinning fluid as it does in a Newtonian fluid, although the beneficial effects of the end piece are still in general greater than the drawbacks.

In our simulations, we considered the parameter ranges $n \in [0.2, 1]$, $\mathrm{De} := \lambda\omega \in [0, 3]$ and $\beta_0 := \mu_0/\mu_\infty \in [1, 6]$, an extension of the range considered by Montenegro-Johnson et al. (2012, 2013) when modelling sperm in two-dimensional shear-thinning fluids. It is, however, likely that the range of shear-thinning effects experienced by sperm are much larger. Montenegro-Johnson (2013) note that through fitting rheological data of cervical mucus from Lai et al. (2007) to the BCC4p constitutive law, it follows that the expected values of the viscosity ratio β_0 and fluid relaxation time λ could on occasion be an order of magnitude larger than those considered. Therefore, the results presented in this thesis likely represent a restricted parameter set, with larger ranges inviting an opportunity for further study. It should, however, be noted that stronger shear-thinning effects invoke elevated simulation times, due to the increase in the level of non-linearity of the problem and a subsequent raise in the number of iterations require for solution convergence.

From our conclusion that human sperm swim less efficiently in shear-thinning fluids than Newtonian fluids, it could be inferred that cells are unoptimised for swimming in their natural environments, such as biological fluids like cervical mucus. This would imply that sperm cells have not evolved to swim efficiently in non-Newtonian fluids, which may seem counter-intuitive. It could be that cells are more heavily optimised for other stages of their journey through the female reproductive tract; for example the process of penetrating between fluids of different viscosities as encountered when traversing between semen and cervical mucus. It might also be that our notion of optimal swimming in terms of the fastest or most energy efficient cell is oversimplified. Collective swimming has been shown to influence the propulsive characteristics of individual swimmers (Woolley et al., 2009), and therefore it may be that fast swimming of all sperm may not be optimal for one cell to succeed in reaching the egg.

On the other hand, sperm may be doing the best they can in biological fluids that are inherently shear-thinning and highly viscous due to high polymer concentrations. To develop a full view of how sperm behave in cervical mucus, viscoelastic effects may well also need to incorporated. It may be that the combination of both shear-thinning rheology and viscoelasticity leads to behaviour that helps explain why sperm have evolved the way they have. Further to this, different results may be observed when considering non-planar beats, rather than the planar dynamics considered in this thesis. In this case, the effect of three-dimensional flagellar twist, for example, could result in the entanglement of polymer fibres within mucus, potentially altering the effect of complex fluids on propulsion compared to the planar case.

Our results present a first study into the effect of shear-thinning rheology on sperm cells with elastic flagella including three-dimensional fluid dynamics. Previous studies of sperm cells in two-dimensional shear-thinning fluids (Montenegro-Johnson et al., 2012, 2013) found that shear-thinning rheology aids sperm progression. Whilst this conclusion is in stark contrast to our own observations that shear-thinning rheology tends to hinder propulsion, we note that the studies of Montenegro-Johnson et al. (2012, 2013) considered prescribed beat kinematics and two-dimensional fluid dynamics. Indeed, we observe that prescribing the shear-thinning flagellar beat in a Newtonian fluid always results in faster and more efficient swimming in a shear-thinning fluid (Figure 4.10), indicating that the fluid rheology itself aids propulsion in the absence of flagella elasticity. In this way, the results observed agree with the observations of Montenegro-Johnson et al. (2012, 2013), although we note a direct comparison has not been made.

A study that considered filament elasticity but for mechanically actuated filaments rather than human sperm was that of Qin et al. (2021). Studying swimming speed over a range of sperm number $\mathcal{S}$, Qin et al. (2021) observed that for strong actuation, shear-thinning rheology hinders propulsion, and for weak actuation, it often aids cells. Whilst it is not immediately clear whether our results fall into the strong or weakly actuated regime, we note that we also uncover that the presence of flagllar elasticity and shape changes can lead to reduced propulsion in the shear-thinning case. Qin et al. (2021) observe that the choice of $\mathcal{S}$ can also

determine whether shear-thinning rheology helps or hinders cells, a conclusion that we also observe, with the effect of shear-thinning rheology on propulsion becoming more pronounced with increased $\mathcal{S}$ (Figure 4.15). Interestingly, Qin et al. (2021) observe the opposite effect, with increased filament stiffness (higher $\mathcal{S}$) leading to striking changes in swimming speed with Deborah number (termed Carreau number in Qin et al. (2021)). The restricted range of De and $\mathcal{S}$ considered ($\mathrm{De} \in [0, 0.1]$ and $\mathcal{S} \in [0, 10]$) and the physical differences between the filament system and a human sperm cell are plausibly the reason for these differences in behaviours.

Other theoretical and experimental results (see Table 1.3 of Section 1.5.2) for microswimmers in shear-thinning fluids demonstrate varying degrees of swimming enhancement or inhibition compared to swimmers in Newtonian fluids. Many factors play a role in swimming in shear-thinning fluids, including swimming gait, elasticity of filaments/flagella and fluid properties. Whilst our work aims to understand the behaviour of sperm in shear-thinning fluids, it is clear that further work to explore the transitions between these different behaviours would be beneficial in order to attempt to unify these studies. We anticipate that the methods developed in this chapter could aid in these future investigations since the hybrid method has been developed with extensibility in mind.

In this chapter, we have explored the effect of shear-thinning rheology on the propulsion of human sperm cells with flexible, elastic flagella. We now conclude by summarising the methodology and results presented in this thesis, as well as outlining potential further directions for the models developed.

Chapter 5

Conclusion

The study of human sperm, from both an experimental and theoretical perspective, has been a thriving area of research for at least the last 60 years. As methods of imaging and cell tracking have developed, so too have a variety of numerical techniques for modelling sperm, including simulating cells with different structural properties and in complex fluids. In this thesis, we addressed several areas where our understanding of sperm propulsion could be further improved. In particular, we first explored the effect of the inactive flagellar end piece on the propulsion of human spermatozoa, providing evidence that its presence increases the swimming speed and efficiency of cells in Newtonian fluids. Following this, we developed a hybrid computational approach for solving the non-linear equations associated with sperm in shear-thinning fluids, and explored the effect of this complex rheology on propulsion and the development of the flagellar waveform.

This chapter concludes by summarising the methods developed and the results presented from both mathematical and biological perspectives. We also discuss possible future extensions to the the techniques described and outline how they could further develop our understanding of human sperm propulsion.

5.1 Summary of methodology and results

In Chapter 2, we explored the role of the mechanically inactive flagellar end piece in cell propulsion and waveform development. Whilst the existence of this region was identified

over 60 years ago (Gray, 1955), it has received relatively little attention, likely since it lacks the internal axoneme structure responsible for generating active bending (Zabeo et al., 2019). Nevertheless, the presence (or indeed the removal) of the end piece has been shown to have a significant effect on flagellar waveform, particularly towards the distal end (Omoto and Brokaw, 1982). We developed an elastohydrodynamic model of a single sperm cell within a Newtonian fluid, with a prescribed length of inactive distal flagellum. We utilised the method of regularised stokeslets (Cortez, 2001; Cortez et al., 2005) to describe the hydrodynamics of the problem via a boundary integral formulation. Considering planar bending in the xy-plane and the forces and moments acting across an infinitesimal segment of the flagellum (Walker et al., 2019; Schoeller et al., 2021), we derived an expression for the elastic behaviour of the cell. Choosing the prescribed active moment function as a sinusoidal travelling wave convolved with a Heaviside function allowed us to simulate cells with an actuated flagellar principal piece and an inactive end piece.

Through varying the end piece's length and comparing to simulations with a fully active flagellum, we demonstrated that an inactive distal region confers significant advantages to cell propulsion. Specifically, cells with an end piece swim up to 72% faster and 438% more efficiently than those with a fully active flagellum of the same total length. Cells were simulated over a broad spectrum of wavenumbers and viscous-elastic parameter choices, corresponding to the approximate physiological range for human sperm in the female reproductive tract. Across all parameters, cell motility was optimised when between 2–18% of the distal flagellum was inactive.

We also examined the differences in the development of the flagellar waveform in the fully-active and optimally-active cases. We observed that optimally-active cells, all of which possess an inactive end piece, produced flagellar waveforms that are much more qualitatively similar to experimentally observed waveforms than fully-active cells. Examining the fluid velocity surrounding these swimmers, we hypothesised that an additional 'oblique' region of the flagellum associated with the end piece could be responsible for the enhanced propulsion observed through conferring extra thrust. The inclusion of the inactive region could be an important

avenue to explore in the design of more efficient artificial microswimmers. Also, combining the model with flagellum tracking software could enable more accurate sperm analysis for use in a clinical setting.

Following the exploration of the flagellar end piece, we focused our study on the effect of shear-thinning rheology on the propulsion of sperm. Whilst the effect of complex fluid properties such as viscoelasticity on sperm has been studied reasonably broadly, relatively little attention has been given to modelling sperm in shear-thinning fluids. In particular, studying the effects of shear-thinning rheology on sperm with flexible elastic flagella has not been investigated. In this case, the flagellar waveform emerges due to the interactions between the flagellum and surrounding complex fluid. To explore the effect of shear-thinning rheology on cells with flexible flagella, we developed the hybrid method for non-linear swimming (HANS). This method was built with extensibility and computational efficiency in mind.

For a given boundary value problem associated with a swimmer situated within a domain containing a generalised-Newtonian fluid, the HANS method is implemented by first splitting the velocity and pressure solutions into two components. The first of these is a Newtonian approximation to the fluid flow surrounding the swimmer, derived using the method of regularised stokeslets. This solution accounts for the rapidly varying nature of the fluid flow surrounding the swimmer, and as such, the remaining velocity and pressure components are slowly varying across the computational domain. These remaining solutions account for the non-Newtonian nature of the fluid and can be solved for using the finite element method on a coarse structured mesh.

Before outlining the steps of the HANS method, we began by deriving the finite element method for the boundary value problem of a generalised-Newtonian fluid within a given computational domain, without the presence of a swimmer. After verifying the implementation through comparison of the FEM solution with a semi-analytic solution for the problem of pressure-driven flow in a cylindrical pipe, we introduced the HANS method for the problem of a single relaxing Hookean spring in a shear-thinning fluid. This involved the numerical calculation of rapidly varying integrals involving the regularised stokeslet kernel. The com-

putational costs associated with calculating these integrals was diminished using appropriate 'sinh' mappings to reduce the number of quadrature points required to calculate the solution within a given degree of error. Following the HANS implementation for the single spring problem, we derived the equivalent method for simulating a sperm cell with a flexible elastic flagellum and planar beat within a three-dimensional shear-thinning fluid. In particular, this involved combining the elastohydrodynamic method developed in Chapter 2 with the finite element implementation discussed in Chapter 3.

In Chapter 4, we used the HANS method to explore the effect of shear-thinning rheology on the propulsion of sperm. Examining the swimming speed (VAL) and efficiency (η) of cells over varying shear-thinning index n, Deborah number De and zero-infinite shear rate viscosity ratio β_0, we found that in general shear-thinning rheology hinders propulsion of flexible swimmers compared to swimming in a Newtonian fluid of the same zero shear-rate viscosity. However, simulating the same beats in a Newtonian fluid indicates that sperm with a prescribed beat always swim slower in a Newtonian fluid. These results suggest that shear-thinning rheology enhances propulsion for a given swimmer with a prescribed waveform, but that the shape changes resulting from the interactions of an elastic flagellum with a shear-thinning fluid result in decreased propulsion. Analysis of the flagellar waveforms and surrounding fluid velocity indicates that cells that possess flagellar regions moving obliquely through the fluid with an angle of approximately $\pi/4$ swim the fastest and the most efficiently.

Exploring the effect of varying the viscous-elastic ratio $\mathcal{S}$ and examining the propulsion of cells in fluid with various shear-thinning indices n, we uncover similar effects. Cells are usually hindered by shear-thinning rheology, although for high $\mathcal{S} > 14$ and $n \in [0.8, 0.9]$, cells can swim faster or at the same speed as in a Newtonian fluid with the same zero shear-rate viscosity. The effect of shear-thinning rheology on propulsion and flagellar waveform also becomes more pronounced with increasing $\mathcal{S}$. Again, simulating cells with the same flagellar beat in Newtonian fluid yields decreased swimming speed compared to a shear-thinning fluid. Therefore we again revealed that whilst shear-thinning rheology enhances propulsion, the flagellar shape changes uncovered when simulating cells with flexible flagellar in shear-

thinning fluids can hinder propulsion.

Finally, we explored the combined effect of shear-thinning rheology and the inactive flagellar end piece. Simulating cells over $n \in [0.2, 1]$ with and without an end piece for two values of the viscous-elastic parameter $\mathcal{S}$ indicated that whilst the end piece consistently increased propulsion in a Newtonian fluid, there are specific regimes within a shear-thinning fluid in which propulsion with an inactive distal region is decreased.

5.2 Future directions

A primary focus of the HANS method is the extensibility of the framework. The HANS method could be used to model different fluid constitutive laws and other model swimmers with additional future work. One natural extension would be to model fully three-dimensional swimmers within shear-thinning fluids. Whilst we have considered three-dimensional fluid dynamics, the model discussed in this thesis have involved sperm with a planar flagellar beat. Therefore, implementing a non-planar cell model would provide further biological accuracy. Three-dimensional flagellar beats could be used to model the helical flagella of bacteria which frequently encounter complex fluids in their natural biological environments. Examples include bacteria producing extracellular polymer substances (EPS) during the formation and growth of biofilms (Wilking et al., 2011), the bacterium *Pseudomonas aeruginosa* targeting the respiratory system (occupied by mucus) of patients with Cystic Fibrosis to mount an infection (Gómez and Prince, 2007), and the bacterium *Helicobacter pylori* moving through a layer of mucus which coats the stomach in order to form ulcers (Montecucco and Rappuoli, 2001; Celli et al., 2009).

As well as exhibiting shear-thinning effects, biological fluids such as cervical mucus also display viscoelastic properties (Lai et al., 2009). The HANS method could be augmented to include the effects of viscoelasticity along with shear-thinning rheology. In this case, the Cauchy stress tensor takes the form $\boldsymbol{\sigma} = -p\boldsymbol{I} + \boldsymbol{\tau}$. Here, $\boldsymbol{\tau}$ is the deviatoric stress tensor expressed via both a Newtonian contribution from the solvent ($\boldsymbol{\tau}_s$) and a polymeric contribution to the stress

($\boldsymbol{\tau}_p$). To include the elasticity of the fluid in the model, we could use the Giesekus constitutive law (Giesekus, 1982), as discussed in Section 1.5.2. The resulting system of equations would be solved as before using the HANS method in conjunction with the equation describing fluid elasticity, allowing for the simulation of human sperm with flexible elastic flagella in fluids with both viscoelasticity and shear-thinning properties. The effects of both these fluid properties on sperm is yet to be explored from a theoretical perspective, and as such the HANS method could provide a useful tool for furthering our understanding of sperm propulsion in biologically realistic fluid environments.

The HANS method could be extended to study the penetration of sperm cells between fluids of different viscosities or shear-thinning properties. This step-change in viscosities is a barrier that sperm must overcome in vivo, in particular when penetrating between semen and cervical mucus in natural reproduction. A recent study by López et al. (2021) reveals experimentally that the swimming speed of helical swimmers travelling across a viscosity gradient can increase or decrease, depending on the type of swimming employed and the direction of travel relative to the viscosity gradient. The effect of this scenario on the propulsion of human sperm is not yet well understood. It could, for example, present a challenge that only the strongest cells can overcome, therefore acting as a selection mechanism for the best swimmers. Contrastingly, it could be a barrier that multiple cells must work together to conquer. As well as modelling the penetration of sperm between fluids with different viscosities and shear-thinning properties, the effect of the inactive end piece on the ease of penetration could also be explored. This could further uncover whether the presence of the end piece always aids sperm cells.

With the methods developed, we have provided insight into how factors such as the inactive flagellar end piece and shear-thinning rheology can affect propulsion. Specifically, we have demonstrated that the inactive flagellar end piece always aids the propulsion of human sperm in Newtonian fluids, although it may sometimes impede propulsion in a shear-thinning fluid, depending on the degree of the shear-thinning effects and the viscous-elastic parameter $\mathcal{S}$. Shear-thinning rheology tends to reduce the swimming speed and efficiency of human

sperm cells, although increases can also be observed for moderate values of the zero-infinite shear rate viscosity ratio β_0 and for sufficiently floppy flagella in weakly shear-thinning fluids. An appreciation of how these physical processes impact the swimming speed and efficiency of sperm could aid in the design of artificial microswimmers, which should be build in order to maximise these properties. Furthermore, understanding the characteristic of sperm cells that swim the most optimally could help in the selecting of sperm cells in assisted reproductive technologies. For example, cells that possess an undamaged end piece or those with properties that aid in progression through a certain type of fluid might be chosen, with the aim of ultimately increasing the chances of successful outcomes for couples suffering from infertility.

Bibliography

L. Alvarez, B. M. Friedrich, G. Gompper, and U. B. Kaupp. The computational sperm cell. *Trends Cell Biol.*, 24(3):198–207, 2014. doi: https://doi.org/10.1016/j.tcb.2013.10.004.

J. D. Anderson and J. Wendt. *Computational fluid dynamics*, volume 206. Springer, 1995.

W. A. Anderson and P. Personne. The form and function of spermatozoa: a comparative view. *The functional anatomy of the spermatozoon*, pages 3–14, 1975. doi: https://doi.org/10.1016/B978-0-08-018006-9.50006-0.

V. Angeles, F. A. Godínez, J. A. Puente-Velazquez, R. Mendez-Rojano, E. Lauga, and R. Zenit. Front-back asymmetry controls the impact of viscoelasticity on helical swimming. *Phys. Rev. Fluids*, 6(4):043102, 2021.

C. R. Austin. Evolution of human gametes: spermatozoa. *See Grudzinskas & Yovich*, 1995:1–19, 1995.

I. Babuška. The finite element method with lagrangian multipliers. *Numer. Math.*, 20(3):179–192, 1973. doi: https://doi.org/10.1007/BF01436561.

J. M. Baltz, D. F. Katz, and R. A. Cone. Mechanics of sperm-egg interaction at the zona pellucida. *Biophys. J.*, 54(4):643–654, 1988. doi: https://doi.org/10.1016/S0006-3495(88)83000-5.

J. Baranger and K. Najib. Analyse numerique des ecoulements quasi-newtoniens dont la viscosite obeit a la loi puissance ou la loi de carreau. *Numer. Math.*, 58(1):35–49, 1990. doi: https://doi.org/10.1007/BF01385609.

H. A. Barnes, J. F. Hutton, and K. Walters. *An introduction to rheology*, volume 3. Elsevier, 1989.

C. L. Barratt, V. Kay, and S. K. Oxenham. The human spermatozoon–a stripped down but refined machine. *J. Biol.*, 8(63), 2009. doi: https://doi.org/10.1186/jbiol167.

J. W. Barrett and W. B. Liu. Finite element error analysis of a quasi-newtonian flow obeying the carreau or power law. *Numer. Math.*, 64(1):433–453, 1993. doi: https://doi.org/10.1007/BF01388698.

H. C. Berg. The rotary motor of bacterial flagella. *Annu. Rev. Biochem.*, 72(1):19–54, 2003.

R. B. Bird, R. C. Armstrong, and O. Hassager. *Dynamics of polymeric liquids. Vol. 1: Fluid mechanics*. Wiley, 2nd edition, 1987.

J. R. Blake and A. T. Chwang. Fundamental singularities of viscous flow. *J. Eng. Math.*, 8(1): 23–29, 1974. doi: https://doi.org/10.1007/BF02353701.

J. Boivin, L. Bunting, J. A. Collins, and K. G. Nygren. International estimates of infertility prevalence and treatment-seeking: potential need and demand for infertility medical care. *Hum. Reprod.*, 22(6):1506–1512, 2007. doi: https://doi.org/10.1093/humrep/dem046.

F. Brezzi. On the existence, uniqueness and approximation of saddle-point problems arising from lagrangian multipliers. *RAIRO Anal. Numer.*, 8:129 – 151, 1974. doi: https://doi.org/10.1051/m2an/197408R201291.

L. J. Burkman. The motility of human spermatozoa before and after capacitation. *See Grudzinskas & Yovich*, 1995:122–39, 1995.

L. Carichino and S. D. Olson. Emergent three-dimensional sperm motility: coupling calcium dynamics and preferred curvature in a Kirchhoff rod model. *Math. Med. Biol.*, 2018. ISSN 1477-8599. doi: 10.1093/imammb/dqy015.

P. J. Carreau. Rheological equations from molecular network theories. *Trans. Soc. Rheol.*, 16 (1):99–127, 1972. doi: https://doi.org/10.1122/1.549276.

J. P. Celli, B. S. Turner, N. H. Afdhal, S. Keates, I. Ghiran, C. P. Kelly, R. H. Ewoldt, G. H. McKinley, P. So, S. Erramilli, et al. Helicobacter pylori moves through mucus by reducing mucin viscoelasticity. *PNAS*, 106(34):14321–14326, 2009.

F. Ceric, D. Silva, and P. Vigil. Ultrastructure of the human periovulatory cervical mucus. *J. Electron Microsc. Tech.*, 54(5):479–484, 2005.

A. T. Chwang and T. Y. Wu. Hydromechanics of low-reynolds-number flow. part 2. singularity method for stokes flows. *J. Fluid Mech.*, 67(4):787–815, 1975. doi: https://doi.org/10.1017/S0022112075000614.

R. Cortez. The method of regularized stokeslets. *SIAM J. Sci. Comput.*, 23(4):1204–1225, 2001. doi: https://doi.org/10.1137/S106482750038146X.

R. Cortez, L. Fauci, and A. Medovikov. The method of regularized stokeslets in three dimensions: analysis, validation, and application to helical swimming. *Phys. Fluids*, 17(3):031504, 2005. doi: https://doi.org/10.1063/1.1830486.

R. Coy and H. Gadêlha. The counterbend dynamics of cross-linked filament bundles and flagella. *J. R. Soc. Interface*, 14(130):20170065, 2017. doi: https://doi.org/10.1098/rsif.2017.0065.

M. M. Cross. Rheology of non-newtonian fluids: a new flow equation for pseudoplastic systems. *J. Colloid Interface Sci.*, 20(5):417–437, 1965. doi: https://doi.org/10.1016/0095-8522(65)90022-X.

M. Crouzeix and P-A. Raviart. Conforming and nonconforming finite element methods for solving the stationary stokes equations i. *RAIRO Anal. Numer.*, 7(R3):33–75, 1973. doi: https://doi.org/10.1051/m2an/197307R300331.

J. M. Cummins and P. F. Woodall. On mammalian sperm dimensions. *Reproduction*, 75(1):153–175, 1985. doi: https://doi.org/10.1530/jrf.0.0750153.

M. Dasgupta, B. Liu, H. C. Fu, M. Berhanu, K. S. Breuer, T. R. Powers, and A. Kudrolli. Speed of a swimming sheet in newtonian and viscoelastic fluids. *Phys. Rev. E*, 87(1):013015, 2013.

E. Demir, N. Lordi, Y. Ding, and O. S. Pak. Nonlocal shear-thinning effects substantially enhance helical propulsion. *Phys. Rev. Fluids*, 5(11):111301, 2020. doi: https://doi.org/10.1103/PhysRevFluids.5.111301.

R. D. Dresdner and D. F. Katz. Relationships of mammalian sperm motility and morphology to hydrodynamic aspects of cell function. *Biol. Reprod.*, 25(5):920–930, 1981. doi: https://doi.org/10.1095/biolreprod25.5.920.

R. Dreyfus, J. Baudry, M. L. Roper, M. Fermigier, H. A. Stone, and J. Bibette. Microscopic artificial swimmers. *Nature*, 437(7060):862, 2005. doi: https://doi.org/10.1038/nature04090.

E. Z. Drobnis, A. I. Yudin, G. N. Cherr, and D. F. Katz. Kinematics of hamster sperm during penetration of the cumulus cell matrix. *Gamete Res.*, 21(4):367–383, 1988. doi: https://doi.org/10.1002/mrd.1120210406.

J. Espinosa-Garcia, E. Lauga, and R. Zenit. Fluid elasticity increases the locomotion of flexible swimmers. *Phys. Fluids*, 25(3):031701, 2013. doi: https://doi.org/10.1063/1.4795166.

D. W. Fawcett. The mammalian spermatozoon. *Dev. Biol.*, 44(2):394–436, 1975. doi: https://doi.org/10.1016/0012-1606(75)90411-X.

B. M. Friedrich, I. H. Riedel-Kruse, J. Howard, and F. Jülicher. High-precision tracking of sperm swimming fine structure provides strong test of resistive force theory. *J. Exp. Biol.*, 213(8):1226–1234, 2010. doi: https://doi.org/10.1242/jeb.039800.

H. C. Fu, C. W. Wolgemuth, and T. R. Powers. Swimming speeds of filaments in nonlinearly viscoelastic fluids. *Phys. Fluids*, 21(3):033102, 2009. doi: https://doi.org/10.1063/1.3086320.

G. R. Fulford, D. F. Katz, and R. L. Powell. Swimming of spermatozoa in a linear viscoelastic fluid. *Biorheology*, 35(4-5):295–309, 1998. doi: https://doi.org/10.1016/S0006-355X(99)80012-2.

H. Gadêlha, E. A. Gaffney, D. J. Smith, and J. C. Kirkman-Brown. Nonlinear instability in flagellar dynamics: a novel modulation mechanism in sperm migration? *J. R. Soc. Interface*, 7 (53):1689–1697, 2010. doi: https://doi.org/10.1098/rsif.2010.0136.

E. A. Gaffney, H. Gadêlha, D. J. Smith, J. R. Blake, and J. C. Kirkman-Brown. Mammalian sperm motility: observation and theory. *Annu. Rev. Fluid. Mech.*, 43(1):501–528, 2011. doi: https://doi.org/10.1146/annurev-fluid-121108-145442.

D. A. Gagnon and P. E. Arratia. The cost of swimming in generalized newtonian fluids: experiments with c. elegans. *J. Fluid Mech.*, 800:753–765, 2016. doi: https://doi.org/10.1017/jfm.2016.420.

D. A. Gagnon and T. D. Montenegro-Johnson. Thrifty swimming with shear-thinning: a note on out-of-plane effects for undulatory locomotion through shear-thinning fluids. *ANZIAM J.*, 59(4):443–454, 2018. doi: https://doi.org/10.1017/S1446181118000032.

D. A. Gagnon, N. C. Keim, and P. E. Arratia. Undulatory swimming in shear-thinning fluids: experiments with c. elegans. *J. Fluid Mech.*, 758:R3, 2014. doi: https://doi.org/10.1017/jfm.2014.539.

M. T. Gallagher and D. J. Smith. Meshfree and efficient modeling of swimming cells. *Phys. Rev. Fluids*, 3(5):053101, 2018. doi: https://doi.org/10.1103/PhysRevFluids.3.053101.

M. T. Gallagher, D. J. Smith, and J. C. Kirkman-Brown. CASA: tracking the past and plotting the future. *Reprod. Fertil. Dev.*, 30(6):867–874, 2018. doi: https://doi.org/10.1071/RD17420.

M. T. Gallagher, G. Cupples, E. H Ooi, J. C. Kirkman-Brown, and D. J. Smith. Rapid sperm capture: high-throughput flagellar waveform analysis. *Hum. Reprod.*, 34(7):1173–1185, 06 2019a. doi: https://doi.org/10.1093/humrep/dez056.

M. T. Gallagher, R. A. J. Wain, S. Dari, J. P. Whitty, and D. J. Smith. Non-identifiability of parameters for a class of shear-thinning rheological models, with implications for haematological

fluid dynamics. *J. Biomech.*, 85:230–238, 2019b. doi: https://doi.org/10.1016/j.jbiomech.2019.01.036.

H. Giesekus. A simple constitutive equation for polymer fluids based on the concept of deformation-dependent tensorial mobility. *J. Non-Newton. Fluid*, 11(1-2):69–109, 1982.

F. A. Godínez, L. Koens, T. D. Montenegro-Johnson, R. Zenit, and E. Lauga. Complex fluids affect low-reynolds number locomotion in a kinematic-dependent manner. *Exp. Fluids*, 56 (5):1–10, 2015.

R. E. Goldstein, E. Lauga, A. I. Pesci, and M. R. E. Proctor. Elastohydrodynamic synchronization of adjacent beating flagella. *Phys. Rev. Fluids*, 1(7):073201, 2016. doi: https://doi.org/10.1103/PhysRevFluids.1.073201.

M. I. Gómez and A. Prince. Opportunistic infections in lung disease: Pseudomonas infections in cystic fibrosis. *Curr. Opin. Pharmacol.*, 7(3):244–251, 2007.

S. Gómez, F. A. Godínez, E. Lauga, and R. Zenit. Helical propulsion in shear-thinning fluids. *J. Fluid Mech.*, 812, 2017. doi: https://doi.org/10.1017/jfm.2016.807.

J. Gray. The movement of sea-urchin spermatozoa. *J. Exp. Biol.*, 32(4):775–801, 1955. doi: https://doi.org/10.1242/jeb.32.4.775.

J. Gray and G. J. Hancock. The propulsion of sea-urchin spermatozoa. *J. Exp. Biol.*, 32(4):802–814, 1955. doi: https://doi.org/10.1242/jeb.32.4.802.

H. Guo, L. Fauci, M. Shelley, and E. Kanso. Bistability in the synchronization of actuated microfilaments. *J. Fluid Mech.*, 836:304–323, 2018. doi: https://doi.org/10.1017/jfm.2017.816.

A. L. Hall-McNair, T. D. Montenegro-Johnson, H. Gadêlha, D. J. Smith, and M. T. Gallagher. Efficient implementation of elastohydrodynamics via integral operators. *Phys. Rev. Fluids*, 4 (11):113101, 2019. doi: https://doi.org/10.1103/PhysRevFluids.4.113101.

G. J. Hancock. The self-propulsion of microscopic organisms through liquids. *Proc. R. Soc. A*, 217(1128):96–121, 1953. doi: https://doi.org/10.1098/rspa.1953.0048.

W. V. Holt and A. Fazeli. Do sperm possess a molecular passport? mechanistic insights into sperm selection in the female reproductive tract. *Mol. Hum. Reprod.*, 21(6):491–501, 2015. doi: https://doi.org/10.1093/molehr/gav012.

T. Hyakutake, K. Sato, and K. Sugita. Study of bovine sperm motility in shear-thinning viscoelastic fluids. *J. Biomech.*, 88:130–137, 2019.

V. Ierardi, A. Niccolini, M. Alderighi, A. Gazzano, F. Martelli, and R. Solaro. AFM characterization of rabbit spermatozoa. *Microsc. Res. Tech.*, 71(7):529–535, 2008. doi: https://doi.org/10.1002/jemt.20584.

A. Iserles. *A first course in the numerical analysis of differential equations*. Number 44. Cambridge university press, 2009.

S. Ishijima. Modulatory mechanisms of sliding of nine outer doublet microtubules for generating planar and half-helical flagellar waves. *Mol. Hum. Reprod.*, 25(6):320–328, 2019. doi: https://doi.org/10.1093/molehr/gaz012.

K. Ishimoto and E. A. Gaffney. Boundary element methods for particles and microswimmers in a linear viscoelastic fluid. *J. Fluid Mech.*, 831:228–251, 2017.

K. Ishimoto and E. A. Gaffney. Hydrodynamic clustering of human sperm in viscoelastic fluids. *Sci. Rep.*, 8(1):1–11, 2018.

K. Ishimoto, H. Gadêlha, E. A. Gaffney, D. J. Smith, and J. Kirkman-Brown. Coarse-graining the fluid flow around a human sperm. *Phys. Rev. Lett.*, 118(12):124501, 2017. doi: https://doi.org/10.1103/PhysRevLett.118.124501.

R. Jeanneret, M. Contino, and M. Polin. A brief introduction to the model microswimmer *Chlamydomonas reinhardtii*. *Eur. Phys. J.*, 225:2141–2156, 06 2016. doi: https://doi.org/10.1140/epjst/e2016-60065-3.

R. E. Johnson. An improved slender-body theory for stokes flow. *J. Fluid Mech.*, 99(2):411–431, 1980. doi: https://doi.org/10.1017/S0022112080000687.

R. E. Johnson and C. J. Brokaw. Flagellar hydrodynamics. a comparison between resistive-force theory and slender-body theory. *Biophys. J.*, 25(1):113–127, 1979. doi: https://doi.org/10.1016/S0006-3495(79)85281-9.

S. Jung. Caenorhabditis elegans swimming in a saturated particulate system. *Phys. Fluids*, 22 (3):031903, 2010.

D. F. Katz, R. N. Mills, and T. R. Pritchett. The movement of human spermatozoa in cervical mucus. *Reproduction*, 53(2):259–265, 1978. doi: https://doi.org/10.1530/jrf.0.0530259.

D. F. Katz, T. D. Bloom, and R. H. Bondurant. Movement of bull spermatozoa in cervical mucus. *Biol. Reprod.*, 25(5):931–937, 1981.

D. F. Katz, E. Z. Drobnis, and J. W. Overstreet. Factors regulating mammalian sperm migration through the female reproductive tract and oocyte vestments. *Gamete Res.*, 22(4):443–469, 1989.

R. B. Kimsey and A. Spielman. Motility of lyme disease spirochetes in fluids as viscous as the extracellular matrix. *J. Infect. Dis.*, 162(5):1205–1208, 1990.

C. Kuhn III and W. Engleman. The structure of the tips of mammalian respiratory cilia. *Cell Tissue Res.*, 186(3):491–498, 1978. doi: https://doi.org/10.1007/BF00224937.

D. Kuzmin and J. Hämäläinen. Finite element methods for computational fluid dynamics: a practical guide. *SIAM Rev*, 57(4):642, 2015. doi: https://doi.org/10.1137/1.9781611973617.

S. K. Lai, D. E. O'Hanlon, S. Harrold, S. T. Man, Y-Y Wang, R. Cone, and J. Hanes. Rapid transport of large polymeric nanoparticles in fresh undiluted human mucus. *PNAS*, 104(5):1482–1487, 2007.

S. K. Lai, Y-Y. Wang, D. Wirtz, and J. Hanes. Micro-and macrorheology of mucus. *Adv. Drug Deliv. Rev.*, 61(2):86–100, 2009. doi: https://doi.org/10.1016/j.addr.2008.09.012.

L. D. Landau and E. M. Lifshitz. *Theory of elasticity*. Pergamon Press, Oxford, 3rd edn, 1986.

E. Lauga. Propulsion in a viscoelastic fluid. *Phys. Fluids*, 19(8):083104, 2007. doi: https://doi.org/10.1063/1.2751388.

C. Li, B. Qin, A. Gopinath, P. E. Arratia, B. Thomases, and R. D. Guy. Flagellar swimming in viscoelastic fluids: role of fluid elastic stress revealed by simulations based on experimental data. *J. R. Soc. Interface*, 14(135):20170289, 2017.

G. Li and A. M. Ardekani. Undulatory swimming in non-newtonian fluids. *J. Fluid Mech.*, 784, 2015. doi: https://doi.org/10.1017/jfm.2015.595.

J. Lighthill. *Mathematical biofluiddynamics*. SIAM, 1975. doi: https://doi.org/10.1137/1.9781611970517.

M. J. Lighthill. Aquatic animal propulsion of high hydromechanical efficiency. *J. Fluid Mech.*, 44(2):265, 1970. doi: https://doi.org/10.1017/S0022112070001830.

J. Lin and D. Nicastro. Asymmetric distribution and spatial switching of dynein activity generates ciliary motility. *Science*, 360(6387):eaar1968, 2018. doi: https://doi.org/10.1126/science.aar1968.

B. Liu, T. R. Powers, and K. S. Breuer. Force-free swimming of a model helical flagellum in viscoelastic fluids. *PNAS*, 108(49):19516–19520, 2011.

C. E. López, J. Gonzalez-Gutierrez, F. Solorio-Ordaz, E. Lauga, and R. Zenit. Dynamics of a helical swimmer crossing viscosity gradients. *Phys. Rev. Fluids*, 6(8):083102, 2021.

H. A. Lorentz. A general theorem concerning the motion of a viscous fluid and a few consequences derived from it. *Zittingsverlag Akad. Wet. Amsterdam*, 5:168–175, 1896.

K. E. Machin. Wave propagation along flagella. *J. Exp. Biol.*, 35(4):796–806, 1958. doi: https://doi.org/10.1242/jeb.35.4.796.

P. S. Mafunda, L. Maree, A. Kotze, and G. van der Horst. Sperm structure and sperm motility of the african and rockhopper penguins with special reference to multiple axonemes of the

flagellum. *Theriogenology*, 99:1–9, 2017. doi: https://doi.org/10.1016/j.theriogenology.2017.05.009.

Y. Man and E. Lauga. Phase-separation models for swimming enhancement in complex fluids. *Phys. Rev. E*, 92(2):023004, 2015.

J. C. Maxwell. Iv. on the dynamical theory of gases. *Philos. Trans. R. Soc.*, (157):49–88, 1867.

C. Montecucco and R. Rappuoli. Living dangerously: how helicobacter pylori survives in the human stomach. *Nat. Rev. Mol. Cell Biol.*, 2(6):457–466, 2001.

T. D. Montenegro-Johnson. *Microscopic swimming in biological fluids*. PhD thesis, University of Birmingham, 2013.

T. D. Montenegro-Johnson. Microtransformers: Controlled microscale navigation with flexible robots. *Phys. Rev. Fluids*, 3(6):062201, 2018. doi: https://doi.org/10.1103/PhysRevFluids.3.062201.

T. D. Montenegro-Johnson, A. A. Smith, D. J. Smith, D. Loghin, and J. R. Blake. Modelling the fluid mechanics of cilia and flagella in reproduction and development. *Eur. Phys. J. E*, 35 (111):1–17, 2012. doi: https://doi.org/10.1140/epje/i2012-12111-1.

T. D. Montenegro-Johnson, D. J. Smith, and D. Loghin. Physics of rheologically enhanced propulsion: different strokes in generalized stokes. *Phys. Fluids*, 25(8):081903, 2013. doi: https://doi.org/10.1063/1.4818640.

T. D. Montenegro-Johnson, H. Gadêlha, and D. J. Smith. Spermatozoa scattering by a microchannel feature: an elastohydrodynamic model. *R. Soc. Open Sci.*, 2(3):140475, 2015.

T. D. Montenegro-Johnson, D. A. Gagnon, P. E. Arratia, and E. Lauga. Flow analysis of the low reynolds number swimmer c. elegans. *Phys. Rev. Fluids*, 1(5):053202, 2016. doi: https://doi.org/10.1103/PhysRevFluids.1.053202.

A. Morozov and S. E. Spagnolie. Introduction to complex fluids. In *Complex fluids in biological systems*, pages 3–52. Springer, 2015.

G. P. Muldowney and J. J. L. Higdon. A spectral boundary element approach to three-dimensional stokes flow. *J. Fluid Mech.*, 298:167–192, 1995. doi: https://doi.org/10.1017/S0022112095003260.

C. V. Neal, A. L. Hall-McNair, J. Kirkman-Brown, D. J Smith, and M. T. Gallagher. Doing more with less: the flagellar end piece enhances the propulsive effectiveness of human spermatozoa. *Phys. Rev. Fluids*, 5(7):073101, 2020.

D. R. Nelson, R. Guidetti, and L. Rebecchi. Tardigrada. In *Ecology and classification of North American freshwater invertebrates*, pages 455–484. Elsevier, 2010.

S. Nonaka, Y. Tanaka, Y. Okada, S. Takeda, A. Harada, Y. Kanai, M. Kido, and N. Hirokawa. Randomization of left–right asymmetry due to loss of nodal cilia generating leftward flow of extraembryonic fluid in mice lacking KIF3B motor protein. *Cell*, 95(6):829–837, 1998. doi: https://doi.org/10.1016/s0092-8674(00)81705-5.

E. J. Nyström. Über die praktische auflösung von integralgleichungen mit anwendungen auf randwertaufgaben. *Acta Math.*, 54:185–204, 1930.

E. Odeblad. The functional structure of human cervical mucus. *Acta Obstet. Gynecol. Scand.*, 47(sup1):57–79, 1968.

J. T. Oden. A general theory of finite elements. ii. applications. *Int. J. Numer. Meth. Eng.*, 1(3): 247–259, 1969. doi: https://doi.org/10.1002/nme.1620010304.

J. T. Oden. Finite-element analogue of navier-stokes equation. *Jo. Eng. Mech. Div.*, 96(4):529–534, 1970. doi: https://doi.org/10.1061/JMCEA3.0001264.

S. S. Olmsted, J. L. Padgett, A. I. Yudin, K. J. Whaley, T. R. Moench, and R. A. Cone. Diffusion of macromolecules and virus-like particles in human cervical mucus. *Biophys. J.*, 81(4):1930–1937, 2001.

C. K. Omoto and C. J. Brokaw. Structure and behaviour of the sperm terminal filament. *J. Cell. Sci.*, 58(1):385–409, 1982. doi: https://doi.org/10.1242/jcs.58.1.385.

N. Phan-Thien, T. Tran-Cong, and M. Ramia. A boundary-element analysis of flagellar propulsion. *J. Fluid Mech.*, 184:533–549, 1987. doi: https://doi.org/10.1017/S0022112087003008.

C. Pozrikidis. *Boundary integral and singularity methods for linearized viscous flow*. Cambridge University Press, 1992. doi: https://doi.org/10.1017/CBO9780511624124.

J. A. Puente-Velázquez, F. A. Godínez, E. Lauga, and R. Zenit. Viscoelastic propulsion of a rotating dumbbell. *Microfluid Nanofluidics*, 23(9):1–7, 2019.

E. M. Purcell. Life at low reynolds number. *Am. J. Phys.*, 45(1):3–11, 1977.

B. Qin, A. Gopinath, J. Yang, J. P. Gollub, and P. E. Arratia. Flagellar kinematics and swimming of algal cells in viscoelastic fluids. *Sci. Rep.*, 5(1):1–7, 2015.

K. Qin, Z. Peng, Y. Chen, H. Nganguia, L. Zhu, and O. S. Pak. Propulsion of an elastic filament in a shear-thinning fluid. *Soft Matter*, 17(14):3829–3839, 2021. doi: https://doi.org/10.1039/D0SM02130J.

Z. Qu and K. S. Breuer. Effects of shear-thinning viscosity and viscoelastic stresses on flagellated bacteria motility. *Phys. Rev. Fluids*, 5(7):073103, 2020.

M. Ramia, D. L. Tullock, and N. Phan-Thien. The role of hydrodynamic interaction in the locomotion of microorganisms. *Biophys. J.*, 65(2):755–778, 1993. doi: https://doi.org/10.1016/S0006-3495(93)81129-9.

E. E. Riley and E. Lauga. Enhanced active swimming in viscoelastic fluids. *EPL*, 108(3):34003, 2014. doi: https://doi.org/10.1209/0295-5075/108/34003.

E. E. Riley and E. Lauga. Empirical resistive-force theory for slender biological filaments in shear-thinning fluids. *Phys. Rev. E*, 95(6):062416, 2017. doi: https://doi.org/10.1103/PhysRevE.95.062416.

S. F. Schoeller, A. K. Townsend, T. A. Westwood, and E. E. Keaveny. Methods for suspensions of passive and active filaments. *J. Comput. Phys.*, 424:109846, 2021.

X. N. Shen and P. E. Arratia. Undulatory swimming in viscoelastic fluids. *Phys. Rev. Lett.*, 106 (20):208101, 2011.

D. J. Smith. A boundary element regularized stokeslet method applied to cilia-and flagella-driven flow. *Proc. R. Soc. A*, 465(2112):3605–3626, 2009. doi: https://doi.org/10.1098/rspa.2009.0295.

D. J. Smith. A nearest-neighbour discretisation of the regularized stokeslet boundary integral equation. *J. Comput. Phys.*, 358:88–102, 2018. doi: https://doi.org/10.1016/j.jcp.2017.12.008.

D. J. Smith, E. A. Gaffney, and J. R. Blake. Discrete cilia modelling with singularity distributions: application to the embryonic node and the airway surface liquid. *Bull. Math. Biol.*, 69(5): 1477–1510, 2007. doi: https://doi.org/10.1007/s11538-006-9172-y.

D. J. Smith, E. A. Gaffney, and J. R. Blake. Mathematical modelling of cilia-driven transport of biological fluids. *Proc. R. Soc. A*, 465(2108):2417–2439, 2009a. doi: https://doi.org/10.1098/rspa.2009.0018.

D. J. Smith, E. A. Gaffney, H. Gadêlha, N. Kapur, and J. C. Kirkman-Brown. Bend propagation in the flagella of migrating human sperm, and its modulation by viscosity. *Cytoskeleton*, 66 (4):220–236, 2009b. doi: https://doi.org/10.1002/cm.20345.

A. J. Sobrero and J. MacLeod. The immediate postcoital test. *Fertil. Steril.*, 13(2):184–189, 1962.

S. E. Spagnolie, B. Liu, and T. R. Powers. Locomotion of helical bodies in viscoelastic fluids: enhanced swimming at large helical amplitudes. *Phys. Rev. Lett.*, 111(6):068101, 2013.

S. S. Suarez and X. Dai. Hyperactivation enhances mouse sperm capacity for penetrating viscoelastic media. *Biol. Reprod.*, 46(4):686–691, 1992.

S. S. Suarez and A. A. Pacey. Sperm transport in the female reproductive tract. *Hum. Reprod. Update*, 12(1):23–37, 2006. doi: https://doi.org/10.1093/humupd/dmi047.

C. Taylor and P. Hood. A numerical solution of the navier-stokes equations using the finite element technique. *Comput. Fluids*, 1(1):73–100, 1973. doi: https://doi.org/10.1016/0045-7930(73)90027-3.

G. I. Taylor. Analysis of the swimming of microscopic organisms. *Proc. R. Soc. A*, 209(1099): 447–461, 1951. doi: https://doi.org/10.1098/rspa.1951.0218.

J. Teran, L. Fauci, and M. Shelley. Viscoelastic fluid response can increase the speed and efficiency of a free swimmer. *Phys. Rev. Lett.*, 104(3):038101, 2010. doi: https://doi.org/10.1103/PhysRevLett.104.038101.

B. Thomases and R. D. Guy. Mechanisms of elastic enhancement and hindrance for finite-length undulatory swimmers in viscoelastic fluids. *Phys. Rev. Lett.*, 113(9):098102, 2014. doi: https://doi.org/10.1103/PhysRevLett.113.098102.

B. Thomases and R. D. Guy. The role of body flexibility in stroke enhancements for finite-length undulatory swimmers in viscoelastic fluids. *J. Fluid Mech.*, 825:109–132, 2017. doi: https://doi.org/10.1017/jfm.2017.383.

C-k. Tung, F. Ardon, A. Roy, D. L. Koch, S. Suarez, and M. Wu. Emergence of upstream swimming via a hydrodynamic transition. *Phys. Rev. Lett.*, 114:108102, 2015. doi: 10.1103/PhysRevLett.114.108102.

C-k. Tung, C. Lin, B. Harvey, A. G. Fiore, F. Ardon, M. Wu, and S. S. Suarez. Fluid viscoelasticity promotes collective swimming of sperm. *Sci. Rep.*, 7(1):1–9, 2017.

J. R. Vélez-Cordero and E. Lauga. Waving transport and propulsion in a generalized newtonian fluid. *J. Non-Newton. Fluid*, 199:37–50, 2013. doi: https://doi.org/10.1016/j.jnnfm.2013.05.006.

G. G. Vernon and D. M. Woolley. Basal sliding and the mechanics of oscillation in a mammalian sperm flagellum. *Biophys. J.*, 87(6):3934–3944, 2004. doi: https://doi.org/10.1529/biophysj.104.042648.

S. Vogel. *Life in Moving Fluids: The Physical Biology of Flow-Revised and Expanded Second Edition*. Princeton University Press, 2020.

B. J. Walker, K. Ishimoto, H. Gadêlha, and E.A,A. Gaffney. Filament mechanics in a half-space via regularised stokeslet segments. *J. Fluid Mech.*, 879:808–833, 2019.

M. Werner and L. W. Simmons. Insect sperm motility. *Biol. Rev.*, 83(2):191–208, 2008. doi: https://doi.org/10.1111/j.1469-185X.2008.00039.x.

WHO. Who laboratory manual for the examination and processing of human semen. 2010.

J. N. Wilking, T. E. Angelini, A. Seminara, M. P. Brenner, and D. A. Weitz. Biofilms as complex fluids. *MRS Bull.*, 36(5):385–391, 2011.

D. P. Wolf, L. Blasco, M. A.. Khan, and M. Litt. Human cervical mucus. ii. changes in viscoelasticity during the ovulatory menstrual cycle. *Fertil. Steril.*, 28(1):47–52, 1977.

D. P. Wolf, L. Blasco, M. A. Khan, and M. Litt. Human cervical mucus. iv. viscoelasticity and sperm penetrability during the ovulatory menstrual cycle. *Fertil. Steril.*, 30(2):163–169, 1978.

D. M. Woolley. Motility of spermatozoa at surfaces. *Reproduction*, 126(2):259–270, 2003. doi: https://doi.org/10.1530/rep.0.1260259.

D. M. Woolley, D. A. Carter, and G. N. Tilly. Compliance in the neck structures of the guinea pig spermatozoon, as indicated by rapid freezing and electron microscopy. *J. Anat.*, 213(3): 336–341, 2008. doi: https://doi.org/10.1111/j.1469-7580.2008.00919.x.

D. M. Woolley, R. F. Crockett, W. D. I. Groom, and S. G. Revell. A study of synchronisation between the flagella of bull spermatozoa, with related observations. *J. Exp. Biol.*, 212(14): 2215–2223, 2009.

R. Yanagimachi. Mammalian fertilization. *The physiology of reproduction*, 1994.

K. Yasuda. *Investigation of the analogies between viscometric and linear viscoelastic properties of polystyrene fluids*. PhD thesis, Massachusetts Institute of Technology, 1979.

W. S. Yeung, V. K. Ng, E. Y. Lau, and P. C. Ho. Human oviductal cells and their conditioned medium maintain the motility and hyperactivation of human spermatozoa in vitro. *Hum. Reprod.*, 9(4):656–660, 1994. doi: https://doi.org/10.1093/oxfordjournals.humrep.a138566.

G. K. Youngren and A. Acrivos. Stokes flow past a particle of arbitrary shape: a numerical method of solution. *J. Fluid Mech.*, 69(2):377–403, 1975. doi: https://doi.org/10.1017/S0022112075001486.

A. I. Yudin, F. W. Hanson, and D. F. Katz. Human cervical mucus and its interaction with sperm: a fine-structural view. *Biol. Reprod.*, 40(3):661–671, 1989.

D. Zabeo, J. T. Croft, and J. L. Höög. Axonemal doublet microtubules can split into two complete singlets in human sperm flagellum tips. *FEBS Lett.*, 593(9):892–902, 2019. doi: https://doi.org/10.1002/1873-3468.13379.

O. C. Zienkiewicz and Y. K. Cheung. Finite elements in the solution of field problems. *The Engineer*, 220(5722):507–510, 1965.

Appendices

Appendix A

Basis function mapping from the reference element in the finite element solver

The velocity and pressure basis functions on the reference element $\hat{E}$ are denoted as $\left\{\hat{\varphi}_a(\boldsymbol{\xi})\right\}_{a=1}^{27}$ and $\left\{\hat{\psi}_b(\boldsymbol{\xi})\right\}_{b=1}^{8}$ respectively. These basis functions are mapped to the physical mesh elements $E^{(e)}$ when calculating the integrals required for construction of the system (3.9). Following Kuzmin and Hämäläinen (2015), this mapping can be written as

$$\boldsymbol{F} : \hat{E} \to E^{(e)}, \quad \boldsymbol{F}(\boldsymbol{\xi}) = \boldsymbol{x}, \tag{A.1}$$

such that the vertices the reference element $\hat{E}$ are mapped to the vertices of the physical element $E^{(e)}$. Consider the coordinates of the velocity nodes of the physical element $E^{(e)}$, denoted as $\left\{\boldsymbol{x}_a^{(v,e)}\right\}_{a=1}^{27}$. We define that

$$\boldsymbol{F}(\boldsymbol{\xi}) = \sum_{a=1}^{27} \hat{\varphi}_a(\boldsymbol{\xi}) \boldsymbol{x}_a^{(v,e)} = \boldsymbol{x}, \tag{A.2}$$

or component-wise

$$x_1(\boldsymbol{\xi}) = \sum_{a=1}^{27} \hat{\varphi}_a(\boldsymbol{\xi}) x_{1a}^{(v,e)}, \tag{A.3a}$$

$$x_2(\boldsymbol{\xi}) = \sum_{a=1}^{27} \hat{\varphi}_a(\boldsymbol{\xi}) x_{2a}^{(v,e)}, \tag{A.3b}$$

$$x_3(\boldsymbol{\xi}) = \sum_{a=1}^{27} \hat{\varphi}_a(\boldsymbol{\xi}) x_{3a}^{(v,e)}. \tag{A.3c}$$

Thus, to calculate an integral of a general function $f(\boldsymbol{x})$ over the element $E^{(e)}$ we perform

$$\int_{E^{(e)}} f(\boldsymbol{x}) d\boldsymbol{x} = \int_{\hat{E}} f(x_1(\boldsymbol{\xi}), x_2(\boldsymbol{\xi}), x_3(\boldsymbol{\xi})) |J^{(e)}(\boldsymbol{\xi})| d\boldsymbol{\xi}, \tag{A.4}$$

where $|J^{(e)}(\boldsymbol{\xi})|$ is the determinant of the Jacobian matrix of the transformation, defined by

$$\left[J^{(e)}(\boldsymbol{\xi})\right]_{ij} = \frac{\partial x_i}{\partial \xi_j} \text{ for } i, j = 1, 2, 3. \tag{A.5}$$

The entries of this Jacobian matrix can be found through differentiating the equations in system (A.3). Given the mapping $\boldsymbol{F}$, we define

$$\varphi_a^{(e)}(\boldsymbol{x}) := \hat{\varphi}_a(\boldsymbol{\xi}), \quad a = 1, 2, \ldots, 27, \tag{A.6}$$

where $\varphi_a^{(e)}(\boldsymbol{x})$ represents the a^{th} global velocity basis function on the element $E^{(e)}$. Using a similar transformation argument we may write that

$$\psi_b^{(e)}(\boldsymbol{x}) := \hat{\psi}_b(\boldsymbol{\xi}), \quad b = 1, 2, \ldots, 8, \tag{A.7}$$

where $\psi_j^{(e)}(\boldsymbol{x})$ represents the b^{th} pressure basis function on the element $E^{(e)}$. Finally, note that from the chain rule

$$\frac{\partial \hat{\varphi}_a}{\partial \xi_i} = \left[J^{(e)}(\boldsymbol{\xi})\right]_{ij} \frac{\partial \varphi_a^{(e)}}{\partial x_j}, \quad a = 1, 2, \ldots, 27, \tag{A.8}$$

which then allows the calculation of

$$\frac{\partial \varphi_a^{(e)}}{\partial x_i} = \left[\left(J^{(e)}(\boldsymbol{\xi})\right)^{-1}\right]_{ij} \frac{\partial \hat{\varphi}_a}{\partial \xi_j}, \quad a = 1, 2, \ldots, 27. \tag{A.9}$$

The equations (A.6), (A.7) and (A.9) allow us to calculate all integrals in terms of the basis functions defined on the reference element. Let us for example consider the following integral

$$\int_{E^{(e)}} \psi_a^{(e)} \frac{\partial \varphi_b^{(e)}}{\partial \boldsymbol{x}_i} d\boldsymbol{x}, \tag{A.10}$$

for some $i \in \{1, 2, 3\}$, $a \in \{1, 2, \dots, M\}$ and $b \in \{1, 2, \dots, N\}$. We may transform this to

$$\int_{\hat{E}} \hat{\psi}_a \left\{ \left[\left(J^{(e)} \right)^{-1} \right]_{i1} \frac{\partial \hat{\varphi}_b}{\partial \xi_1} + \left[\left(J^{(e)} \right)^{-1} \right]_{i2} \frac{\partial \hat{\varphi}_b}{\partial \xi_2} + \left[\left(J^{(e)} \right)^{-1} \right]_{i3} \frac{\partial \hat{\varphi}_b}{\partial \xi_3} \right\} |J^{(e)}| d\boldsymbol{\xi}, \tag{A.11}$$

which is an integral entirely on the reference element, where the dependencies of the Jacobian and basis functions on $\boldsymbol{\xi}$ have been dropped for brevity.

Appendix B

Velocity basis functions on the reference element in the finite element solver

The twenty-seven tri-quadratic velocity basis functions on the reference element $\hat{E} = [-1,1] \times [-1,1] \times [-1,1]$ are given by

$$\hat{\varphi}_1(\boldsymbol{\xi}) = \frac{1}{8}\xi_1(\xi_1 - 1)\xi_2(\xi_2 - 1)\xi_3(\xi_3 - 1), \tag{B.1}$$

$$\hat{\varphi}_2(\boldsymbol{\xi}) = \frac{1}{4}\xi_1(\xi_1 - 1)(1 - \xi_2^2)\xi_3(\xi_3 - 1), \tag{B.2}$$

$$\hat{\varphi}_3(\boldsymbol{\xi}) = \frac{1}{8}\xi_1(\xi_1 - 1)\xi_2(\xi_2 + 1)\xi_3(\xi_3 - 1), \tag{B.3}$$

$$\hat{\varphi}_4(\boldsymbol{\xi}) = \frac{1}{4}\xi_1(\xi_1 - 1)\xi_2(\xi_2 + 1)(1 - \xi_3^2), \tag{B.4}$$

$$\hat{\varphi}_5(\boldsymbol{\xi}) = \frac{1}{8}\xi_1(\xi_1 - 1)\xi_2(\xi_2 + 1)\xi_3(\xi_3 + 1), \tag{B.5}$$

$$\hat{\varphi}_6(\boldsymbol{\xi}) = \frac{1}{4}\xi_1(\xi_1 - 1)(1 - \xi_2^2)\xi_3(\xi_3 + 1), \tag{B.6}$$

$$\hat{\varphi}_7(\boldsymbol{\xi}) = \frac{1}{8}\xi_1(\xi_1 - 1)\xi_2(\xi_2 - 1)\xi_3(\xi_3 + 1), \tag{B.7}$$

$$\hat{\varphi}_8(\boldsymbol{\xi}) = \frac{1}{4}\xi_1(\xi_1 - 1)\xi_2(\xi_2 - 1)(1 - \xi_3^2), \tag{B.8}$$

$$\hat{\varphi}_9(\boldsymbol{\xi}) = \frac{1}{2}\xi_1(\xi_1 - 1)(1 - \xi_2^2)(1 - \xi_3^2), \tag{B.9}$$

$$\hat{\varphi}_{10}(\boldsymbol{\xi}) = \frac{1}{4}(1 - \xi_1^2)\xi_2(\xi_2 - 1)\xi_3(\xi_3 - 1), \tag{B.10}$$

$$\hat{\varphi}_{11}(\boldsymbol{\xi}) = \frac{1}{2}(1 - \xi_1^2)(1 - \xi_2^2)\xi_3(\xi_3 - 1), \tag{B.11}$$

$$\hat{\varphi}_{12}(\boldsymbol{\xi}) = \frac{1}{4}(1 - \xi_1^2)\xi_2(\xi_2 + 1)\xi_3(\xi_3 - 1), \tag{B.12}$$

$$\hat{\varphi}_{13}(\boldsymbol{\xi}) = \frac{1}{2}(1-\xi_1^2)\xi_2(\xi_2+1)(1-\xi_3^2), \tag{B.13}$$

$$\hat{\varphi}_{14}(\boldsymbol{\xi}) = \frac{1}{4}(1-\xi_1^2)\xi_2(\xi_2+1)\xi_3(\xi_3+1), \tag{B.14}$$

$$\hat{\varphi}_{15}(\boldsymbol{\xi}) = \frac{1}{2}(1-\xi_1^2)(1-\xi_2^2)\xi_3(\xi_3+1), \tag{B.15}$$

$$\hat{\varphi}_{16}(\boldsymbol{\xi}) = \frac{1}{4}(1-\xi_1^2)\xi_2(\xi_2-1)\xi_3(\xi_3+1), \tag{B.16}$$

$$\hat{\varphi}_{17}(\boldsymbol{\xi}) = \frac{1}{2}(1-\xi_1^2)\xi_2(\xi_2-1)(1-\xi_3^2), \tag{B.17}$$

$$\hat{\varphi}_{18}(\boldsymbol{\xi}) = (1-\xi_1^2)(1-\xi_2^2)(1-\xi_3^2), \tag{B.18}$$

$$\hat{\varphi}_{19}(\boldsymbol{\xi}) = \frac{1}{8}\xi_1(\xi_1+1)\xi_2(\xi_2-1)\xi_3(\xi_3-1), \tag{B.19}$$

$$\hat{\varphi}_{20}(\boldsymbol{\xi}) = \frac{1}{4}\xi_1(\xi_1+1)(1-\xi_2^2)\xi_3(\xi_3-1), \tag{B.20}$$

$$\hat{\varphi}_{21}(\boldsymbol{\xi}) = \frac{1}{8}\xi_1(\xi_1+1)\xi_2(\xi_2+1)\xi_3(\xi_3-1), \tag{B.21}$$

$$\hat{\varphi}_{22}(\boldsymbol{\xi}) = \frac{1}{4}\xi_1(\xi_1+1)\xi_2(\xi_2+1)(1-\xi_3^2), \tag{B.22}$$

$$\hat{\varphi}_{23}(\boldsymbol{\xi}) = \frac{1}{8}\xi_1(\xi_1+1)\xi_2(\xi_2+1)\xi_3(\xi_3+1), \tag{B.23}$$

$$\hat{\varphi}_{24}(\boldsymbol{\xi}) = \frac{1}{4}\xi_1(\xi_1+1)(1-\xi_2^2)\xi_3(\xi_3+1), \tag{B.24}$$

$$\hat{\varphi}_{25}(\boldsymbol{\xi}) = \frac{1}{8}\xi_1(\xi_1+1)\xi_2(\xi_2-1)\xi_3(\xi_3+1), \tag{B.25}$$

$$\hat{\varphi}_{26}(\boldsymbol{\xi}) = \frac{1}{4}\xi_1(\xi_1+1)\xi_2(\xi_2-1)(1-\xi_3^2), \tag{B.26}$$

$$\hat{\varphi}_{27}(\boldsymbol{\xi}) = \frac{1}{2}\xi_1(\xi_1+1)(1-\xi_2^2)(1-\xi_3^2). \tag{B.27}$$

Appendix C

Element-wise construction of the global matrix blocks in the finite element solver

Recall the element-wise construction of the integral

$$[B_1]_{nm} = \int_{\Omega_h} \psi_n \frac{\partial \varphi_m}{\partial x_1} d\boldsymbol{x}, \quad n = 1, 2, \ldots, M, \quad m = 1, 2, \ldots, N, \tag{C.1}$$

given by

$$[B_1]_{nm} = \int_{\Omega_h} \psi_n \frac{\partial \varphi_m}{\partial x_1} d\boldsymbol{x} = \sum_e \left[B_1^{(e)}\right]_{nm}, \quad \left[B_1^{(e)}\right]_{nm} = \int_{E^{(e)}} \psi_n \frac{\partial \varphi_m}{\partial x_1} d\boldsymbol{x}, \tag{C.2}$$

where $\left[B_1^{(e)}\right]_{nm} \neq 0$ if and only if n and m are also nodes of the element $E^{(e)}$. Following Kuzmin and Hämäläinen (2015), the correspondence between the global and local node numbers can be defined though the mapping H given by

$$n = H(e, a), \quad m = H(e, b), \quad a = 1, 2, \ldots, 8, \quad b = 1, 2, \ldots, 27, \tag{C.3}$$

where a and b represent the local node numbers i.e. the numbering within each element. In this way, the only non-zero entries of $B_1^{(e)}$ are given by

$$\left[B_1^{(e)}\right]_{ab} = \int_{E^{(e)}} \psi_a^{(e)} \frac{\partial \varphi_b^{(e)}}{\partial x_1} d\boldsymbol{x}, \quad a = 1, 2, \ldots, 8, \quad b = 1, 2, \ldots, 27. \tag{C.4}$$

Using equations (A.6), (A.7) and (A.9), we can calculate integrals of this form using only the basis functions defined on the reference element. For each element, this results in a 8×27 matrix, the entries of which can be used to update the global matrix B_1 via

$$\left[B_1\right]_{H(e,a),H(e,b)} = \left[B_1\right]_{H(e,a),H(e,b)} + \left[B_1^{(e)}\right]_{ab}. \tag{C.5}$$

Appendix D

Calculation of stokeslet velocity derivatives in the hybrid solver

We calculate the integral

$$\frac{\partial}{\partial x_k} I_{ij}^{[q]}(\boldsymbol{x}, t) = \int_{(q-1)\Delta s}^{q\Delta s} \frac{\partial}{\partial x_k} S_{ij}^{\epsilon}\left(\boldsymbol{x}, \tilde{\boldsymbol{X}}^{[q]}(t) + [s' - \tilde{s}^{[q]}]\left[\cos\tilde{\theta}^{[q]}(t), \sin\tilde{\theta}^{[q]}(t), 0\right]^T\right) ds', \tag{D.1}$$

analytically for each segment q. Following the method outlined by Smith (2009), we perform the coordinate transformation $x_i^L = \left[x_j - \tilde{X}^{[q]}(t)\right]\Theta_{ij}$ where $\boldsymbol{\Theta}$ is a rotation matrix with entries given by

$$\boldsymbol{\Theta} = \begin{bmatrix} \cos\tilde{\theta}^{[q]}(t) & -\sin\tilde{\theta}^{[q]}(t) & 0 \\ \sin\tilde{\theta}^{[q]}(t) & \cos\tilde{\theta}^{[q]}(t) & 0 \\ 0 & 0 & 1 \end{bmatrix}, \tag{D.2}$$

such that the first row is given by the tangent to the qth segment and the remaining rows form a orthogonal basis. Applying this transformation yields the integrals in the 'local' frame, given by

$$\frac{\partial}{\partial x_k} I_{ij}^{L\,[q]}\left(\boldsymbol{x}, \tilde{s}^{[q]}\right) = \int_{-\Delta s}^{\Delta s} \frac{\partial}{\partial x_k} S_{ij}^{\epsilon}\left(\boldsymbol{x}^L, s'\boldsymbol{e}_1\right) ds'. \tag{D.3}$$

In this way, the integral in the original coordinate system is given by

$$\frac{\partial}{\partial x_k} I_{ij}^{[q]}\left(\boldsymbol{x}, \tilde{s}^{[q]}\right) = \Theta_{li}\Theta_{mj}\Theta_{nk}\frac{\partial}{\partial x_k} I_{ij}^{L\,[q]}\left(\boldsymbol{x}, \tilde{s}^{[q]}\right). \tag{D.4}$$

We denote the definite local integrals via $\frac{\partial}{\partial x_k} I_{ij}^{L\,[q]}\left(\boldsymbol{x}, \tilde{s}^{[q]}\right) = \left[J_{ijk}^{L\,[q]}\left(\boldsymbol{x}^L, s'\right)\right]_{-\Delta s}^{\Delta s}$ where $J_{ijk}^{L\,[q]}(\boldsymbol{x}^L, s')$ are the corresponding indefinite integrals. Writing (x, y, z) for $\left(x_1^L, x_2^L, x_3^L\right)$, s for s' and $\alpha = y^2 + z^2 + \epsilon^2$ for brevity, we write

$$J_{ijk}^{L\,[q]} = \frac{1}{8\pi\mu_S}\left[\mathcal{A}_{ijk}^{L\,[q]} + \mathcal{B}_{ijk}^{L\,[q]}\right], \tag{D.5}$$

and calculate that

$$\mathcal{A}_{ij1}^{L\,[q]} = -\delta_{ij}\frac{\left[[x-s]^2 + \alpha + \epsilon^2\right]}{\left[[x-s]^2 + \alpha\right]^{3/2}} \tag{D.6}$$

$$\mathcal{A}_{ij2}^{L\,[q]} = \delta_{ij}\frac{[x-s]\,y}{\alpha^2\left[[x-s]^2 + \alpha\right]^{3/2}}\left[\alpha^2 + \alpha\left[3\epsilon^2 + [x-s]^2\right] + 2\epsilon^2[x-s]^2\right], \tag{D.7}$$

$$\mathcal{A}_{ij3}^{L\,[q]} = \delta_{ij}\frac{[x-s]\,z}{\alpha^2\left[[x-s]^2 + \alpha\right]^{3/2}}\left[\alpha^2 + \alpha\left[3\epsilon^2 + [x-s]^2\right] + 2\epsilon^2[x-s]^2\right]. \tag{D.8}$$

We also have that

$$\mathcal{B}_{111}^{L\,[q]} = -\frac{[x-s]^2}{\left[[x-s]^2 + \alpha\right]^{3/2}}, \tag{D.9}$$

$$\mathcal{B}_{121}^{L\,[q]} = -\frac{[x-s]\,y}{\left[[x-s]^2 + \alpha\right]^{3/2}}, \tag{D.10}$$

$$\mathcal{B}_{131}^{L\,[q]} = -\frac{[x-s]\,z}{\left[[x-s]^2 + \alpha\right]^{3/2}}, \tag{D.11}$$

$$\mathcal{B}_{221}^{L\,[q]} = -\frac{y^2}{\left[[x-s]^2 + \alpha\right]^{3/2}}, \tag{D.12}$$

$$\mathcal{B}_{231}^{L\,[q]} = -\frac{yz}{\left[[x-s]^2 + \alpha\right]^{3/2}}, \tag{D.13}$$

$$\mathcal{B}_{331}^{L\,[q]} = -\frac{z^2}{\left[[x-s]^2 + \alpha\right]^{3/2}}, \tag{D.14}$$

where $\mathcal{B}^{L[q]}_{211} = \mathcal{B}^{L[q]}_{121}$, $\mathcal{B}^{L[q]}_{311} = \mathcal{B}^{L[q]}_{131}$ and $\mathcal{B}^{L[q]}_{321} = \mathcal{B}^{L[q]}_{231}$, and

$$\mathcal{B}^{L[q]}_{112} = \frac{[x-s]^3 y}{\alpha \left[[x-s]^2 + \alpha\right]^{3/2}}, \tag{D.15}$$

$$\mathcal{B}^{L[q]}_{122} = \frac{[x-s]^2 + \alpha - y^2}{\left[[x-s]^2 + \alpha\right]^{3/2}}, \tag{D.16}$$

$$\mathcal{B}^{L[q]}_{132} = -\frac{yz}{\left[[x-s]^2 + \alpha\right]^{3/2}}, \tag{D.17}$$

$$\mathcal{B}^{L[q]}_{222} = -\frac{[x-s]\, y}{\alpha^2 \left[[x-s]^2 + \alpha\right]^{3/2}} \left[2\alpha \left[\alpha + [x-s]^2\right] - y^2 \left[3\alpha + 2[x-s]^2\right]\right], \tag{D.18}$$

$$\mathcal{B}^{L[q]}_{232} = -\frac{z[x-s]}{\alpha^2 \left[[x-s]^2 + \alpha\right]^{3/2}} \left[\alpha \left[\alpha + [x-s]^2\right] - y^2 \left[3\alpha + 2[x-s]^2\right]\right], \tag{D.19}$$

$$\mathcal{B}^{L[q]}_{332} = \frac{[x-s]\, yz^2}{\alpha^2 \left[[x-s]^2 + \alpha\right]^{3/2}} \left[2[x-s]^2 + 3\alpha\right], \tag{D.20}$$

where $\mathcal{B}^{L[q]}_{212} = \mathcal{B}^{L[q]}_{122}$, $\mathcal{B}^{L[q]}_{312} = \mathcal{B}^{L[q]}_{132}$ and $\mathcal{B}^{L[q]}_{322} = \mathcal{B}^{L[q]}_{232}$, and

$$\mathcal{B}^{L[q]}_{113} = \frac{[x-s]^3 z}{\alpha \left[[x-s]^2 + \alpha\right]^{3/2}}, \tag{D.21}$$

$$\mathcal{B}^{L[q]}_{123} = -\frac{yz}{\left[[x-s]^2 + \alpha\right]^{3/2}}, \tag{D.22}$$

$$\mathcal{B}^{L[q]}_{133} = \frac{[x-s]^2 + y^2 + \epsilon^2}{\left[[x-s]^2 + \alpha\right]^{3/2}}, \tag{D.23}$$

$$\mathcal{B}^{L[q]}_{223} = \frac{[x-s]\, y^2 z}{\alpha^2 \left[[x-s]^2 + \alpha\right]^{3/2}} \left[3\alpha + 2[x-s]^2\right], \tag{D.24}$$

$$\mathcal{B}^{L[q]}_{233} = -\frac{[x-s]\, y}{\alpha^2 \left[[x-s]^2 + \alpha\right]^{3/2}} \left[\alpha \left[\alpha + [x-s]^2\right] - z^2 \left[3\alpha + 2[x-s]^2\right]\right], \tag{D.25}$$

$$\mathcal{B}^{L[q]}_{333} = -\frac{[x-s]\, z}{\alpha^2 \left[[x-s]^2 + \alpha\right]^{3/2}} \left[2\alpha \left[\alpha + [x-s]^2\right] - z^2 \left[3\alpha + 2[x-s]^2\right]\right], \tag{D.26}$$

where $\mathcal{B}^{L[q]}_{213} = \mathcal{B}^{L[q]}_{123}$, $\mathcal{B}^{L[q]}_{313} = \mathcal{B}^{L[q]}_{133}$ and $\mathcal{B}^{L[q]}_{323} = \mathcal{B}^{L[q]}_{233}$.

Appendix E

Solving problems involving prescribed flagellar motion using the nearest-neighbour method

In Chapter 4, we compare the swimming speed of a sperm cell with a flexible elastic flagellum in a shear-thinning (solved using the HANS method), to the speed of a cell with the same prescribed flagellar beat in a Newtonian fluid. To solve the prescribed beat problem, we first recall that for a swimmer with surface D within a fluid obeying the Stokes flow equations (1.8), the fluid velocity u_i at the point $\boldsymbol{x}$ can be approximated via the method of regularised stokeslets by

$$u_i(\boldsymbol{x}) \approx -\int_D S_{ij}^{\epsilon}(\boldsymbol{x}, \boldsymbol{X}) f_j(\boldsymbol{X}) dS_{\boldsymbol{X}}. \tag{E.1}$$

The error in this approximation is discussed in Section 1.4.2, with the expression treated as exact in what follows. Following Gallagher and Smith (2018), to model a cell with prescribed beat kinematics, we prescribe the swimmers deformation in the body frame. In this frame of reference, the head and flagellum of the cell do not translate or rotate. For a cell with given flagellar shape $\boldsymbol{\xi}$ and motion $\dot{\boldsymbol{\xi}}$ in the body frame, we transform to the laboratory frame, which is stationary. In this way, the laboratory frame velocities are given by

$$\dot{\boldsymbol{x}} = \boldsymbol{U} + \boldsymbol{\omega} \times (\boldsymbol{x} - \boldsymbol{x}_0) + \boldsymbol{B} \cdot \dot{\boldsymbol{x}}, \tag{E.2}$$

where $\boldsymbol{x}_0$ is the body frame origin and $\boldsymbol{B}$ is a matrix of basis vectors of the body frame. The terms $\boldsymbol{U}$ and $\boldsymbol{\omega}$ represent the rigid body velocity and angular velocity of the swimmer respectively.

Applying the non-slip condition $\boldsymbol{u}(\boldsymbol{x}) = \dot{\boldsymbol{x}}$ in equation (E.1) and closing the system via imposing zero net force and moment on the swimmer, we require that

$$-U_i - \epsilon_{ikj}\omega_j(x_k - x_{0k}) - \int_D S^{\epsilon}_{ij}(\boldsymbol{x}, \boldsymbol{X}) f_j(\boldsymbol{X}) dS_X = B_{ij}\dot{\xi}_j, \tag{E.3a}$$

$$\int_D f_i(\boldsymbol{X}) dS_X = 0, \tag{E.3b}$$

$$\int_D \epsilon_{ikj} X_k f_j(\boldsymbol{X}) dS_X = 0, \tag{E.3c}$$

where ϵ_{ijk} is the Levi-Civita symbol and repeated indicies are summed over. The unknowns of this problem are the surface force $\boldsymbol{f}(\boldsymbol{X})$ for $\boldsymbol{X} \in D$, the rigid body velocity $\boldsymbol{U}$ and the angular velocity $\boldsymbol{\omega}$.

The sperm cells considered in Chapter 4 are situated within the dimensionless fluid domain $\Omega = [0, 10] \times [0, 5] \times [0, 5]$ with no-slip boundary conditions applied on the domain boundary $\partial\Omega$. The prescribed beat swimming problem involving the inclusion of this boundary becomes

$$-U_i - \epsilon_{ikj}\omega_j(x_k - x_{0k}) - \int_{D\cup\partial\Omega} S^{\epsilon}_{ij}(\boldsymbol{x}, \boldsymbol{X}) f_j(\boldsymbol{X}) dS_X = B_{ij}\dot{\xi}_j \text{ for } \boldsymbol{x} \in D, \tag{E.4a}$$

$$-\int_{D\cup\partial\Omega} S^{\epsilon}_{ij}(\boldsymbol{x}, \boldsymbol{X}) f_j(\boldsymbol{X}) dS_X = 0 \text{ for } \boldsymbol{x} \in \partial\Omega, \tag{E.4b}$$

$$\int_D f_i(\boldsymbol{X}) dS_X = 0, \tag{E.4c}$$

$$\int_D \epsilon_{ikj} X_k f_j(\boldsymbol{X}) dS_X = 0. \tag{E.4d}$$

The system may be solved using the nearest-neighbour method (NEAREST), as described in Gallagher and Smith (2018). In particular, we discretise the swimmer via a set of force points $\left\{\boldsymbol{x}^{[1]}, \boldsymbol{x}^{[2]}, \dots, \boldsymbol{x}^{[M_T]}\right\}$ and quadrature points $\left\{\boldsymbol{X}^{[1]}, \boldsymbol{X}^{[2]}, \dots, \boldsymbol{X}^{[M_Q]}\right\}$, and the boundary by force points $\left\{\boldsymbol{x}^{[M_T+1]}, \boldsymbol{x}^{[M_T+2]}, \dots, \boldsymbol{x}^{[M_T+N_T]}\right\}$ and quadrature points $\left\{\boldsymbol{x}^{[M_Q+1]}, \boldsymbol{x}^{[M_Q+2]}, \dots, \boldsymbol{x}^{[M_Q+N_Q]}\right\}$. Full details of the discretisation are given in Section 2.2.3. For the prescribed beat simulations pro-

vided in Chapter 4, we set $M_T = (Q + 1) + N_h$ and $M_Q = 4((Q + 1) + N_h)$. Here, $Q = 60$ is the number of flagellar segments used in the discresitaion of the flagellum in the HANS method and $N_h = 45$ is the number of points used to discretise the head (see Section 3.5.6). Thus, we discretise such that the NEAREST cell force discretisation and the HANS cell discretisation are identical. We discretise the boundary via $N_T = 642$ equally spaced force points and $N_Q = 10892$ equally spaced quadrature points.

The swimmers trajectory may be computed through solving an initial value problem for the evolution of the body frame origin $\boldsymbol{x}_0$ and the body frame basis vectors forming $\boldsymbol{B}$, as detailed in Gallagher and Smith (2018). Thus the location of the cell in the laboratory frame can be calculated, and the swimming speed, VAL, may be computed via equation (2.43).